Nicola Barbieri

Tests of fundamental physics
with cosmological observables

Supervisor: Dr. Massimiliano Lattanzi
Co-advisor: Dr. Martina Gerbino

Department of Physics
and Earth Sciences,
University of Ferrara

Doctoral course in Physics

Cycle XXXVII

Coordinator: Prof. Paolo Lenisa

NICOLA BARBIERI

Tests of FUNDAMENTAL PHYSICS *with* COSMOLOGICAL OBSERVABLES

Scientific/Disciplinary Sector (SDS) FIS/02

A thesis submitted in satisfaction of the requirements for the degree of

Doctor of Philosophy

Department of Physics and Earth Sciences
Faculty of Physics
University of Ferrara

Supervisor
Dr. Massimiliano Lattanzi

Co-advisor
Dr. Martina Gerbino

November 2024

Nicola Barbieri: *Tests of fundamental physics with cosmological observables*, © November 2024

SUPERVISOR:
Dr. Massimiliano Lattanzi

CO-SUPERVISOR:
Dr. Martina Gerbino

LOCATION:
Ferrara (IT)
Dipartimento di Fisica e Scienze della Terra,
Università degli Studi di Ferrara, Via G. Saragat 1, I-44122

WEBSITE:
https://www.fe.infn.it/cosmologia/

E-MAIL:
nicola.barbieri@unife.it (academic)
nicola.barbieri.mn@gmail.com (personal)

COVER IMAGE:
Section of the 2018 Planck map of the temperature anisotropies of the CMB [Aghanim et al., 2020a].
BACK COVER IMAGE:
Slice of dark matter density field from Millenium Simulation [Springel et al., 2005].

There must be no barriers to freedom of inquiry.
There is no place for dogma in science.
The scientist is free, and must be free to ask any question,
to doubt any assertion, to seek for any evidence,
to correct any errors.

— J. Robert Oppenheimer, 1949

ABSTRACT

This thesis investigates the interplay between fundamental physics and cosmological observables, offering a comprehensive examination of how cutting–edge cosmological data can constrain extensions of current theories. The work begins with a detailed exploration of the standard framework of particle cosmology, encompassing the thermal history of the Universe, the inflationary paradigm, and neutrino phenomenology. In the second part, particular emphasis is placed on non–standard neutrino physics in the early Universe. Specifically, we study their behavior in very low reheating scenarios and their optical activity when the neutrino sector is extended with non–standard interactions. Finally, the focus moves to the late Universe observables, extending the study to signatures of primordial oscillatory features in the Large–Scale Structure (LSS) of the Universe, employing advanced techniques in perturbation theory and N–body simulations to assess their imprints on observables. The results of this work contribute to the refinement of theoretical understanding of the Universe's evolution, highlighting potential deviations in standard predictions and offering insights into physical mechanisms possibly opening new avenues for future observations to test models of physics Beyond the Standard Model (BSM).

SOMMARIO

Questa tesi indaga l'interazione tra fisica fondamentale e osservabili cosmologiche, offrendo un esame completo di come i dati cosmologici all'avanguardia possano vincolare estensioni delle attuali teorie. Il lavoro inizia con un'analisi dettagliata del quadro standard della cosmologia delle particelle, che include la storia termica dell'Universo, il paradigma inflazionario e la fenomenologia dei neutrini. Nella seconda parte, viene posta particolare enfasi sulla fisica non–standard dei neutrini nell'Universo primordiale. In particolare, studiamo il loro comportamento in scenari di low reheating e la loro attività ottica quando il settore dei neutrini è esteso con interazioni non–standard. Infine, l'attenzione si sposta sugli osservabili dell'Universo tadivo, estendendo lo studio a segnature di features primordiali oscillatorie nella LSS dell'Universo, utilizzando tecniche avanzate di teoria delle perturbazioni e simulazioni N–body per valutarne le impronte sugli osservabili. I risultati di questo lavoro contribuiscono alla comprensione teorica dell'evoluzione dell'Universo, evidenziando potenziali deviazioni dalle predizioni standard e offrendo approfondimenti su meccanismi fisici che potrebbero aprire nuove strade per future osservazioni volte a testare i modelli di fisica BSM.

PUBLICATIONS

The content of this thesis is based on the following publications:

Ballardini, M. and N. Barbieri (Nov. 2024). "Refining the nonlinear modelling of primordial oscillatory features." In: arXiv: 2411.02261 [astro-ph.CO].

Barbieri, N., N. Bartolo, M. Lattanzi, and M. Zarei (2025a). "Testing neutrino NSI through CMB polarization." In preparation.

Barbieri, N., T. Brinckmann, S. Gariazzo, M. Lattanzi, S. Pastor, and O. Pisanti (Jan. 2025b). "Current constraints on cosmological scenarios with very low reheating temperatures." In: arXiv: 2501.01369 [astro-ph.CO].

Calabrese, E. et al. (Mar. 2025). "The Atacama Cosmology Telescope: DR6 Constraints on Extended Cosmological Models." In: arXiv: 2503.14454 [astro-ph.CO].

CONTENTS

LIST OF FIGURES

LIST OF TABLES

PREFACE

Cosmology has emerged as a precision science, driven by an unprecedented wealth of high-resolution data and advances in theoretical modeling. Observations of the Cosmic Microwave Background (CMB) anisotropies by missions like the COsmic Background Explorer (COBE) [Boggess et al., 1992; Smoot, 1999], the Wilkinson Microwave Anisotropy Probe (WMAP) [Bennett et al., 2003; 2013], and Planck [Aghanim et al., 2020a; Tauber et al., 2006] have provided critical insights into the early Universe's dynamics, including its energy content, thermal history, and geometry. These measurements have solidified the ΛCDM paradigm as the standard model of cosmology, achieving sub–percent level precision in almost all of its six parameters. This framework, when coupled with the Standard Model (SM) of particle physics, forms the foundation for our understanding of the Universe's evolution and composition.

Despite these successes, significant gaps remain in our knowledge. The ΛCDM model requires dark matter and dark energy to explain observations, yet their fundamental nature remains elusive. Likewise, the discovery that neutrinos possess mass, as revealed by flavor oscillation experiments, challenges the SM's original formulation, which assumes massless neutrinos. These and other puzzles, such as the physics driving cosmic inflation, the baryon asymmetry of the Universe, and the mechanism of neutrino mass generation, point to the existence of physics Beyond the Standard Model (BSM).

Neutrinos offer a unique bridge between cosmology and particle physics. As relics of the early Universe, neutrinos influence both the background expansion and the growth of perturbations. Their properties, such as the sum of their masses (Σm_ν) and the effective number of relativistic species ($N_{\rm eff}$), leave imprints on the CMB and the Large–Scale Structure (LSS) of the Universe. Current cosmological constraints already compete with laboratory experiments in sensitivity, with the sum of neutrino masses constrained to $\Sigma m_\nu < 0.12\,\text{eV}$ at the 95% confidence level [Aghanim et al., 2020c]. Future missions, including Simons Observatory[1] [Galitzki et al., 2018], CMB-S4[2] [Abazajian et al., 2016], LiteBIRD [Matsumura et al., 2014] and *Euclid*[3] [Laureijs et al., 2011], aim to refine these bounds further, potentially resolving questions about the absolute neutrino mass scale, mass ordering, and non–standard neutrino interactions.

In addition to the insights provided by early–Universe observables, like the CMB, late–Universe measurements offer an equally compelling window

1 https://simonsobservatory.org/
2 https://cmb-s4.org/
3 https://www.euclid-ec.org/

into cosmology and fundamental physics. The LSS refers to the distribution of matter on cosmic scales, encompassing structures such as galaxies, galaxy clusters, and voids. These structures form as a result of the gravitational amplification of initial density perturbations, which are seeded in the early Universe and evolve through complex nonlinear interactions. Current LSS surveys, such as those from the Dark Energy Survey (DES) [Becker et al., 2016], the Dark Energy Spectroscopic Instrument (DESI) [Adame et al., 2024c], the Baryon Oscillation Spectroscopic Survey (BOSS) and extended Baryon Oscillation Spectroscopic Survey (eBOSS) [Dawson et al., 2013; 2016], and the Kilo–Degree Survey (KiDS) [Kuijken et al., 2015], have significantly advanced our understanding of the Universe's matter content and its large-scale distribution. These surveys have constrained parameters such as the total matter density and the growth rate of structure, offering additional tests of the ΛCDM model and its extensions. Future projects like the Vera C. Rubin Observatory's Legacy Survey of Space and Time (LSST)[4] [Ivezić et al., 2019], the *Euclid* mission[5] [Laureijs et al., 2011], and the Square Kilometer Array Observatory (SKAO)[6] [Bacon et al., 2020] promise to map the LSS with groundbreaking precision, covering larger volumes and probing smaller scales.

By combining early– and late–Universe observables, cosmology now stands at the forefront of testing new physics. The interplay between theoretical advances and observational precision offers unprecedented opportunities to probe fundamental questions about the Universe's origin, evolution, and the physics that governs it. The goal of this work is to contribute to this effort by developing and refining theoretical and analytical tools necessary to interpret the upcoming influx of high–precision cosmological data. In this thesis we try to address key challenges in modeling and analyzing phenomena that leave imprints on observables, bridging gaps between theoretical predictions and observational capabilities. Such advancements are essential to fully exploit the potential of future surveys and to uncover signatures of physics BSM.

The work is organized as follows:

FIRST CHAPTER talks about the standard cosmological model, ΛCDM, which provides the current framework for describing the Universe's large–scale structure and evolution. We begin by describing the foundations of modern cosmology, discussing the Cosmological Principle and the mathematical description of geometry and dynamics of the expanding Universe through the Friedmann equations. The chapter further examines the matter–energy content of the Universe, highlighting the roles of its most important components. The main events in the Universe's thermal history are also described, emphasizing key transitions. Finally,

4 https://rubinobservatory.org/
5 https://www.euclid-ec.org/
6 https://www.skao.int/en

we introduce the shortcomings of the ΛCDM model and explain how the inflationary paradigm provides compelling solutions to all of them.

SECOND CHAPTER talks about neutrino physics and its relevance in the quest for extensions of the SM. The chapter starts with a historical introduction to the development of the neutrino concept and its experimental discovery. It then discusses how puzzling experimental evidence led to the discovery of neutrino oscillations and how they are physically modeled. We finally focus on the incompatibility of these observations with the SM, emphasizing the need for extensions and examining some candidates of interest for the subsequent chapters.

THIRD CHAPTER addresses the problem of neutrino production in scenarios with very low reheating temperatures. The chapter begins by discussing the problem of computing neutrino distribution functions throughout the decoupling process and the dynamics of a simple reheating model. It then shows how non–thermal neutrinos influence cosmological probes like Big Bang Nucleosynthesis (BBN) and the CMB, and carries out a detailed data analysis to derive bounds on the reheating temperature. A new statistical approach is also discussed, along with comparisons to previous works. This chapter is based on the results reported in [Barbieri et al., 2025b].

FOURTH CHAPTER talks about the optical activity of neutrino Non–Standard Interactions (NSI) in the early Universe. It shows how, thanks to Quantum Field Theory (QFT) techniques, it is possible to study the evolution of the density matrix of a system of photons, representing the case of the CMB. Focusing on a simple phenomenological model, it discusses consequences at the level of both forward scattering and collisions, carrying out detailed calculations of the evolution equations. In the end, it makes some considerations about signatures in observables like CMB linear polarization and cosmic birefringence. This chapter is based on the results reported in [Barbieri et al., 2025a].

FIFTH CHAPTER talks about the role of neutrino self–interactions in cosmology and their implications for cosmological observations. The chapter begins with an overview of neutrino properties and their significance in the standard cosmological model. It then introduces the framework of non–standard interactions (NSI) and explores their phenomenology in limiting scenarios involving massless and very heavy mediators. Using data from the Atacama Cosmology Telescope (ACT) DR6 and other cosmological probes, the chapter presents detailed analyses of neutrino self–interactions and derives constraints on their coupling strengths. This chapter is based on the results reported in [Calabrese et al., 2025].

SIXTH CHAPTER talks about the study of features in the primordial power spectrum. It begins by discussing the basic technicalities of the Time–

Slice Perturbation Theory (TSPT) formalism, which is the core of the methodology of this study. Then, it specifies the formalism for including primordial oscillatory features, discussing compatibility with results in the literature and extending the description to include novel contributions such as induced mixed oscillations and new oscillatory templates. Finally, it shows a comparison between the analytical results and N–body simulations. This chapter is based on the results reported in [Ballardini and Barbieri, 2024].

Part I

FUNDAMENTALS

In this part, the foundational concepts of modern cosmology and neutrino physics are presented. Special attention is dedicated to the thermal history of the Universe, the inflationary paradigm, neutrino oscillations and the neutrino mass problem. The choice of topics and the disucssion has been tailored to be propedeutic to the technical analysis of the following chapters.

1 INTRODUCTION TO ΛCDM COSMOLOGY

This chapter provides an overview of the basic aspects concerning the ΛCDM model, the standard cosmological framework for understanding the properties and the evolution of our Universe. In section 1.1, we introduce the foundational principles of modern cosmology. The mathematical framework underlying the ΛCDM model is then established through the geometry, dynamics of the spacetime and the matter–energy content of the Universe. In section 1.2, we explore the thermal history of the Universe, tracing its evolution from the earliest moments and developing the basic mathematical tools to study equilibrium thermodynamics in the expanding Universe. In section 1.3, we move beyond equilibrium processes, including BBN and CMB formation. These processes are critical for linking theoretical predictions with cosmological observations and set the stage for subsequent chapters. Finally, in section 1.4, we introduce the inflationary paradigm, a cornerstone of modern cosmology that addresses key shortcomings of the hot Big Bang model.

This chapter aims to establish the theoretical and observational framework for the ΛCDM model, providing essential context for the more specialized discussions in later chapters. For readers seeking deeper insights, we refer to standard textbook and major reviews in the field [Baumann, 2022; Dodelson, 2003; Kolb and Turner, 2019; Piattella, 2018; Rubakov and Gorbunov, 2017].

1.1 FOUNDATIONS OF MODERN COSMOLOGY

At the dawn of the 20th century, the groundwork was laid for constructing a scientific framework capable of describing the Universe on a cosmological scale. In the absence of robust empirical evidence, theorists adopted guiding principles to aid in the formulation of such theories. By leveraging symmetry principles, the degrees of freedom in a system could be significantly reduced, simplifying its mathematical modeling and analysis.

1.1.1 The Cosmological Principle

In cosmology, simplification was achieved by adopting a principle rooted in the Copernican Principle, which asserts that the Earth does not occupy a central or privileged position in the Universe. With the advent of Einstein's theory of relativity, this principle required a broader interpretation. Relativity highlighted the importance of the observer and their reference frame, making

the notion of the Earth as a central reference system untenable. Consequently, the Copernican Principle was reformulated within the framework of relativity into the following statement:

> *Every comoving observer perceives the Universe, at a fixed time in their own reference frame, as homogeneous and isotropic.*

This reformulation is known as the *Cosmological Principle*.

A *comoving observer* is defined as one who remains stationary with respect to the geometry of the Universe. Operationally, such an observer detects the CMB radiation as isotropic to within a few parts per million, except for intrinsic anisotropies, which are on the order of a few micro-Kelvin. This implies that the reference frame of a comoving observer acts as a privileged system of reference. In the late 1960s and early 1970s, a dipole anisotropy was observed in the CMB radiation, which has an average temperature of 2.725 K [Fixsen, 2009]. This anisotropy appears as a slightly "hotter" region in one direction and a "cooler" region in the opposite direction, with temperature variations on the order of one part in a thousand. The detection of this anisotropy indicates that the Earth is not in a comoving reference frame aligned with the average mass-energy distribution of the Universe. Even after accounting for the Earth's motion around the Sun, the Sun's motion relative to the center of the Milky Way, and the Milky Way's motion with respect to the Local Group of galaxies, a residual dipole anisotropy in the CMB remains. This residual anisotropy is attributed to the Doppler effect caused by the peculiar velocity of the Local Group relative to a reference frame at rest with the CMB, or equivalently, relative to a comoving observer. This velocity is approximately $600\,\mathrm{km\,s^{-1}}$. The presence of this non-zero kinematic dipole demonstrates a violation of global Lorentz invariance in cosmology.

The terms *homogeneous* and *isotropic*, as used here, refer to the large-scale distribution of mass-energy. This perspective corresponds to observing the Universe at low spatial resolution.

The concept of *cosmic time* is defined as the proper time experienced by comoving observers. The Cosmological Principle, while abstract and potentially idealized, is an extremely useful tool. It can be compared to Galileo's principle of inertia: the principle itself is straightforward, but additional factors—such as friction in mechanics or small anisotropies and inhomogeneities in cosmology—must be accounted for to accurately describe reality. Despite these complexities, the principle remains invaluable as it significantly simplifies the equations governing the dynamics of the Universe.

The Cosmological Principle is based on two foundational assumptions. The isotropy of the Universe is well-supported by observations, including the isotropy of the CMB, the uniform abundance of elements such as deuterium and helium, and the statistical isotropy of galaxy clustering. Homogeneity, on the other hand, is a philosophical assumption, as it cannot be experimentally verified on large scales due to the limited capacity for direct exploration. There is no guarantee that our cosmological descriptions apply universally;

indeed, even the laws of physics might differ in regions of the Universe beyond our cosmological horizon. To understand spatial homogeneity better, one can reference a theorem from General Relativity, which demonstrates that isotropy around all comoving observers at a fixed time implies homogeneity. The validity of this assumption ultimately rests on the agreement between its consequences and observational evidence.

1.1.2 Geometry and Dynamics of the Expanding Universe

Observations have conclusively established that the Universe is expanding. This expansion enables the Universe to be described as spatially homogeneous and isotropic, while evolving over time. Within the framework of differential geometry, this description implies that spacetime can be represented as a series of spacelike slices, with each slice corresponding to a maximally symmetric three–dimensional space. Mathematically, the four–dimensional spacetime manifold $\mathcal{M}_4$ can be decomposed as $\mathcal{M}_4 = \mathbb{R} \times \Sigma$, where $\mathbb{R}$ represents the time dimension, and Σ is a maximally symmetric three–manifold.

Under these assumptions, the spacetime metric is given by the Friedmann–Robertson–Walker (FRW) metric

$$\mathrm{d}s^2 = -\mathrm{d}t^2 + a^2(t)\left[\frac{\mathrm{d}r^2}{1-kr^2} + r^2\left(\mathrm{d}\theta^2 + \sin^2\theta\,\mathrm{d}\phi^2\right)\right], \tag{1.1}$$

where (r, θ, ϕ) are the comoving polar coordinates, and $a(t)$ is the scale factor that relates proper distances to comoving coordinates. The curvature parameter k can be normalized to $+1$, -1, or 0, representing positive, negative, or zero spatial curvature, respectively. Observations strongly suggest that the Universe is extremely close to flat. Therefore, it is common practice to assume $k = 0$ in many analyses.

The time coordinate t corresponds to the cosmic time, defined as the proper time experienced by comoving observers. It is often useful to introduce the conformal time τ, which is defined by

$$\mathrm{d}\tau = \frac{\mathrm{d}t}{a(t)}\,. \tag{1.2}$$

In terms of conformal time, the flat FRW metric simplifies to a static Minkowski metric, scaled by the conformal factor $a(\tau)$

$$\mathrm{d}s^2 = a^2(\tau)\left[-\mathrm{d}\tau^2 + \mathrm{d}r^2 + r^2\left(\mathrm{d}\theta^2 + \sin^2\theta\,\mathrm{d}\phi^2\right)\right]. \tag{1.3}$$

The dynamics of the expansion is governed by the time evolution of the scale factor $a(t)$, which is determined by solving Einstein's field equations

$$G_{\mu\nu} \equiv R_{\mu\nu} - \frac{1}{2}Rg_{\mu\nu} = 8\pi G T_{\mu\nu}\,. \tag{1.4}$$

Here, the Einstein tensor $G_{\mu\nu}$ encodes spacetime curvature, depending on the metric and its derivatives, while the stress–energy tensor $T_{\mu\nu}$ represents the energy and matter content of the Universe. For compatibility with the symmetries of the FRW metric, the stress–energy tensor must be diagonal with isotropic spatial components. The simplest form is the stress–energy tensor of a perfect fluid

$$T^{\mu}_{\nu} = (\rho + p)u^{\mu}u_{\nu} + p\delta^{\mu}_{\nu} = \mathrm{diag}(-\rho, p, p, p) \,, \tag{1.5}$$

where ρ is the energy density, p is the pressure, and $u^{\mu} = (1, 0, 0, 0)$ is the four-velocity in comoving coordinates, where the fluid is stationary.

Energy and momentum conservation, expressed by $\nabla_{\mu}T^{\mu\nu} = 0$, leads to the continuity equation

$$\dot{\rho} = -3H(\rho + p) \,, \tag{1.6}$$

where $H = \dot{a}/a$ is the Hubble parameter. This equation describes the energy exchange between the expanding Universe and its constituents. Applying Einstein's equations to the FRW metric results in the Friedmann equations

$$H^2 = \frac{8\pi G}{3}\rho - \frac{k}{a^2} \,, \tag{1.7}$$

$$\frac{\ddot{a}}{a} = -\frac{4\pi G}{3}(\rho + 3p) \,. \tag{1.8}$$

These equations govern the evolution of the scale factor. The first equation relates the expansion rate to the energy density and curvature, while the second describes the acceleration or deceleration of the expansion. Together with the continuity equation, these form a complete system of equations, though only two are independent due to the Bianchi identities.

By using the continuity equation to track how ρ evolves with a during different epochs, the first Friedmann equation can be solved to determine $a(t)$. The second Friedmann equation then reveals whether the expansion is accelerating or decelerating. For example, during epochs dominated by radiation or matter, where $\rho + 3p > 0$, the expansion decelerates. Conversely, epochs dominated by a cosmological constant or a slowly rolling scalar field, where $\rho + 3p < 0$, exhibit accelerated expansion, as observed during inflation and the current Dark Energy era. It is important to highlight the connection between the geometry of the Universe and its density. To formalize this link, we define the critical density as

$$\rho_{\mathrm{crit}} = \frac{3H^2}{8\pi G} \,, \tag{1.9}$$

where ρ_{crit} represents the density required for the Universe to have a flat geometry. Additionally, we introduce the dimensionless density parameter

$$\Omega \equiv \frac{\rho}{\rho_{\mathrm{crit}}} \,, \tag{1.10}$$

which describes the ratio of the actual energy density ρ to the critical density ρ_{crit}. Using these definitions, the first Friedmann equation can be expressed in an alternative form

$$\Omega - 1 = \frac{k}{a^2 H^2} \,, \tag{1.11}$$

where k is the curvature parameter. Since $a^2 H^2 > 0$, the sign of k is determined by the sign of $\Omega - 1$. Thus, the geometry of the Universe is directly tied to the value of Ω: a flat Universe corresponds to $\Omega = 1$, while $\Omega > 1$ and $\Omega < 1$ indicate closed and open geometries, respectively.

1.1.3 Matter Content of the Universe

The Universe consists of various components, which can be categorized based on their contribution to pressure. These components dictate the dynamics of the Universe's evolution and are outlined as follows.

MATTER The term "matter" refers to all forms of matter for which the pressure is negligible compared to the energy density, $|P| \ll \rho$. For a gas composed of non–relativistic particles, where the energy density is dominated by mass, the pressure P is negligible. Under the assumption $P = 0$, the continuity equation leads to the relation

$$\rho \propto a^{-3} \,. \tag{1.12}$$

This scaling describes the dilution of the energy density of matter due to the Universe's expansion, where the volume evolves as $V \propto a^3$. The majority of the Universe's matter content is attributed to dark matter, hypothesized to be a massive, invisible, and as–yet unidentified particle species. Despite extensive research, the precise nature of dark matter remains unknown. In contrast, ordinary matter, comprising nuclei and electrons, is often referred to as baryonic matter. While this terminology is not strictly accurate—-since electrons are leptons—-it remains common usage because the bulk of ordinary matter's mass resides within nuclei.

RADIATION Radiation refers to components for which the pressure equals one-third of the energy density, $P = 1/3\,\rho$. This condition characterizes relativistic particles, where the energy density is dominated by kinetic energy, with momentum significantly exceeding mass. In such cases, the continuity equation gives

$$\rho \propto a^{-4} \,. \tag{1.13}$$

The additional factor of a^{-1} reflects the redshifting of energy, $E \propto a^{-1}$, as the Universe expands. As massless particles, photons are inherently relativistic and are still observable today as the CMB radiation. Similarly, neutrinos

initially behaved as radiation due to their high energies, but as the Universe expanded and cooled, their small masses began to influence their dynamics, leading to a transition toward matter–like behavior. Additionally, the early Universe may have produced a background of gravitational waves, or gravitons, which current experimental efforts aim to detect.

VACUUM ENERGY Recent observations reveal that matter and radiation alone are insufficient to fully describe the Universe's evolution. Instead, a mysterious component with negative pressure, $P = -\rho$, dominates the current epoch. This component results in an energy density that remains constant

$$\rho \propto a^0 \,. \tag{1.14}$$

Since this energy density does not dilute with the expansion of the Universe, energy must effectively be created as the Universe grows. QFT predicts the existence of vacuum energy, described by the stress-energy tensor

$$T^{\mu\nu}_{\text{vac}} = \rho_{\text{vac}} g^{\mu\nu} \,. \tag{1.15}$$

This expression implies a negative pressure, $P_{\text{vac}} = -\rho_{\text{vac}}$. However, the theoretical value of ρ_{vac} predicted by QFT is vastly larger than the observed value, with a discrepancy of approximately

$$\frac{\rho_{\text{vac}}}{\rho_{\text{obs}}} \sim 10^{120} \,. \tag{1.16}$$

This enormous mismatch represents one of the most significant unresolved challenges in modern physics. In response, alternative explanations have been proposed, including models of time–varying dark energy and modifications to general relativity. While these approaches offer intriguing possibilities, they remain speculative and lack robust experimental or observational support.

Summarizing, the behavior of cosmological fluids is often characterized by a constant equation of state,

$$w = P/\rho \,. \tag{1.17}$$

For different components, the energy density evolves according to

$$\rho \propto a^{-3(1+w)} \,, \tag{1.18}$$

which results in the following scaling relations

$$\rho \propto \begin{cases} a^{-3} & \text{(matter)} \,, \\ a^{-4} & \text{(radiation)} \,, \\ a^0 & \text{(vacuum energy)} \,. \end{cases} \tag{1.19}$$

By analyzing the evolution of the energy densities of different components, it becomes clear that the Universe experienced an early phase dominated by

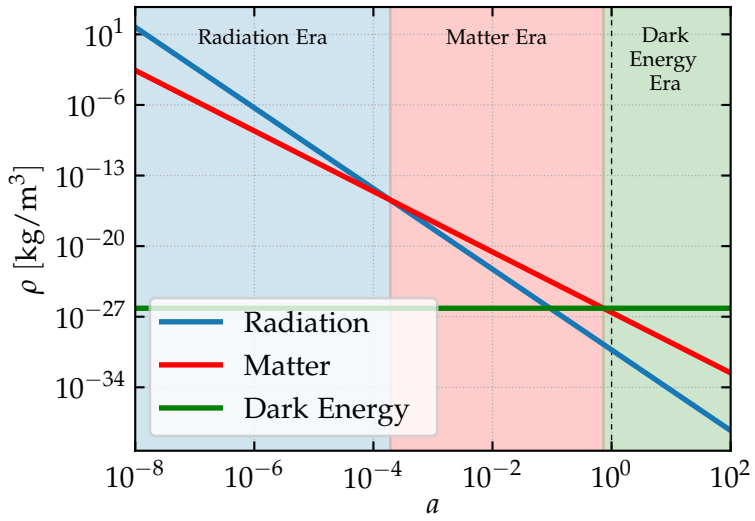

Figure 1.1: Evolution of energy density of constituents of the Universe as a function of the scale factor. The dashed line represent the scale factor today (in the normalization where $a_0 \equiv 1$).

radiation. Later, during the epoch of matter–radiation equality, the energy densities of matter and radiation became comparable, marking the transition to a matter–dominated phase. In recent times, the expansion of the Universe has been driven predominantly by the Cosmological Constant, or an equivalent form of Dark Energy with similar present–day characteristics. This progression is illustrated in fig. 1.1, which shows the evolution of the energy densities of radiation, matter, and the cosmological constant as functions of the scale factor.

For a flat Universe, the Friedmann eq. (1.7), combined with the continuity equation, eq. (1.6), can be integrated to determine the time evolution of the scale factor

$$a(t) \propto \begin{cases} t^{2/3(1+w)} & w \neq -1 \,, \\ e^{Ht} & w = -1 \,. \end{cases} \tag{1.20}$$

Using this relation, the evolution of the scale factor during the distinct phases of the Universe can be explicitly determined

$$a(t) \propto \begin{cases} t^{1/2} & \text{radiation domination} \,, \\ t^{2/3} & \text{matter domination} \,, \\ e^{Ht} & \text{cosmological constant} \,. \end{cases} \tag{1.21}$$

1.2 THERMAL HISTORY OF THE UNIVERSE

1.2.1 Statistical Mechanics in the Expanding Universe

A fundamental aspect of understanding the thermal history of the Universe lies in comparing the *rate of interactions*, Γ, with the *rate of expansion*, H. When $\Gamma \gg H$, the time scale for particle interactions is much shorter than the characteristic expansion time scale

$$t_c \equiv \frac{1}{\Gamma} \ll t_H \equiv \frac{1}{H} \,. \tag{1.22}$$

Under these conditions, *local thermal equilibrium* is established before the effects of the expansion become significant. However, as the Universe cools, the rate of interactions may decline more rapidly than the expansion rate. When $t_c \sim t_H$, particles decouple from the thermal bath. Different particle species may exhibit varying interaction rates, leading to their decoupling at distinct times.

We have strong observational evidence, such as the perfect blackbody spectrum of the CMB, that the early Universe was in local thermal equilibrium. The SM predicts thermal equilibrium for temperatures above 100 GeV. To describe this state and the subsequent evolution of the Universe, it is necessary to revisit some fundamental aspects of equilibrium thermodynamics, suitably generalized to account for an expanding Universe.

Statistical mechanics is the art of translating microscopic laws into an understanding of the macroscopic world. We will briefly review this approach for a gas of weakly interacting particles. It is convenient to describe the system in phase space, where the gas is characterized by the positions and momenta of all particles. In quantum mechanics, the momentum eigenstates of a particle in a volume $V = L^3$ have a discrete spectrum. The density of states in momentum space $\{\mathbf{p}\}$ is then $L^3/h^3 = V/h^3$, and the state density in phase space $\{\mathbf{x}, \mathbf{p}\}$ is

$$\frac{1}{h^3} \,. \tag{1.23}$$

If the particle has g internal degrees of freedom (e.g., spin), the density of states becomes

$$\frac{g}{h^3} = \frac{g}{(2\pi)^3} \,. \tag{1.24}$$

To determine the number density of a gas of particles, we need to understand how the particles are distributed among the momentum eigenstates. This information is encapsulated in the *(phase space) distribution function*, $f(\mathbf{x}, \mathbf{p}, t)$. Due to homogeneity, the distribution function is, in fact, independent of the position $\mathbf{x}$. Moreover, isotropy requires that the momentum dependence is only on the magnitude of the momentum, $p \equiv |\mathbf{p}|$. We typically leave the

time dependence implicit; it will manifest as the temperature dependence of the distribution functions. The particle density in phase space is the product of the density of states and the distribution function. The *number density* of particles (in real space) is then obtained by integrating over momentum

$$n = \frac{g}{(2\pi)^3} \int d^3p\, f(p) \,. \tag{1.25}$$

To compute the *energy density* of a gas of particles, we must weigh each momentum eigenstate by its energy. In the early Universe, particles were *weakly interacting* to a good approximation. This assumption allows us to neglect interaction energies between particles and express the energy of a particle with mass m and momentum p as $E(p) = \sqrt{m^2 + p^2}$. The *energy density* is then obtained by integrating over momentum

$$\rho = \frac{g}{(2\pi)^3} \int d^3p\, f(p) E(p) \,. \tag{1.26}$$

Similarly, the *pressure* is defined as

$$P = \frac{g}{(2\pi)^3} \int d^3p\, f(p) \frac{p^2}{3E} \,. \tag{1.27}$$

THE CONCEPT OF THERMAL EQUILIBRIUM A system of particles is said to be in *kinetic equilibrium* if energy and momentum are exchanged efficiently among the particles. In this state of maximum entropy, the distribution functions are given by the *Fermi-Dirac* and *Bose-Einstein* distributions

$$f(p) = \frac{1}{e^{[E(p)-\mu]/T} \pm 1} \,, \tag{1.28}$$

where the $+$ sign applies to fermions, and the $-$ sign applies to bosons. At low temperatures, $T \ll E - \mu$, both distribution functions approximate the *Maxwell-Boltzmann* distribution

$$f(p) \simeq e^{-[E(p)-\mu]/T} \,. \tag{1.29}$$

The equilibrium distribution functions depend on two parameters: the *temperature*, T, and the *chemical potential*, μ, which may vary with temperature. As the Universe expands, T and $\mu(T)$ evolve in a manner that ensures the continuity equations for energy density ρ and particle number density n are satisfied. Each particle species i-—characterized by potentially distinct m_i, μ_i, and T_i-—has its own distribution function f_i and thus its own n_i, ρ_i, and P_i.

If a species i is in *chemical equilibrium*, its chemical potential μ_i is related to the chemical potentials μ_j of the other species it interacts with. For instance, if a species 1 interacts with species 2, 3, and 4 via the reaction $1 + 2 \leftrightarrow 3 + 4$, then chemical equilibrium requires

$$\mu_1 + \mu_2 = \mu_3 + \mu_4 \,. \tag{1.30}$$

This relation is known as the *Saha equation*. Since the number of photons is not conserved (e.g., double Compton scattering $e^- + \gamma \leftrightarrow e^- + \gamma + \gamma$ occurs in equilibrium at high temperatures), it follows that $\mu_\gamma = 0$. This implies that if the chemical potential of a particle X is μ_X, then the chemical potential of its corresponding antiparticle $\overline{X}$ is

$$\mu_{\overline{X}} = -\mu_X \,. \tag{1.31}$$

To demonstrate this, consider particle-antiparticle annihilation, $X + \overline{X} \leftrightarrow \gamma + \gamma$.

Finally, *thermal equilibrium* is achieved for species that are both in kinetic and chemical equilibrium. In this state, these species share a common temperature, $T_i = T$. Strictly speaking, the Universe can never truly be in equilibrium since the FRW spacetime does not possess a time-like Killing vector. However, this is physics, not mathematics: if the expansion is slow enough, particles have sufficient time to settle close to local equilibrium (and, since the Universe is homogeneous, the local values of thermodynamic quantities are also global values).

Following the previous discussion, we now summarize the key results of thermal equilibrium statistical mechanics in an expanding Universe. The number density of a particle species with mass m in equilibrium at temperature T is given by

$$n(T) = \frac{g}{(2\pi)^3} \int d^3p \, \frac{1}{\exp\left(\sqrt{p^2 + m^2}/T\right) \pm 1} \,, \tag{1.32}$$

where g is the number of internal degrees of freedom of the species, and the sign $+$ $(-)$ applies to fermions (bosons). In the relativistic limit, $T \gg m$, this simplifies to

$$n(T) = \frac{\zeta(3)}{\pi^2} g T^3 \times \begin{cases} 1 & \text{bosons} \,, \\ 3/4 & \text{fermions} \,. \end{cases} \tag{1.33}$$

Similarly, the energy density is defined as

$$\rho(T) = \frac{g}{(2\pi)^3} \int d^3p \, \frac{\sqrt{p^2 + m^2}}{\exp\left(\sqrt{p^2 + m^2}/T\right) \pm 1} \,, \tag{1.34}$$

which, in the relativistic limit $T \gg m$, reduces to

$$\rho(T) = \frac{\pi^2}{30} g T^4 \times \begin{cases} 1 & \text{bosons} \,, \\ 7/8 & \text{fermions} \,. \end{cases} \tag{1.35}$$

Using the above equation and accounting for the fact that different species can have distinct temperatures T_i if some have decoupled from the cosmological plasma, the total energy density in relativistic species can be expressed as

$$\rho_{\rm rad} = \frac{\pi^2}{30} g_*(T) T^4 \,, \tag{1.36}$$

where g_* represents the effective number of relativistic degrees of freedom, defined as

$$g_*(T) = \sum_{i=\text{bosons}} g_i \left(\frac{T_i}{T}\right)^4 + \frac{7}{8} \sum_{i=\text{fermions}} g_i \left(\frac{T_i}{T}\right)^4 . \tag{1.37}$$

Finally, in the relativistic limit, the pressure can be readily derived using the relation $P(T) = \rho(T)/3$, consistent with the equation of state introduced earlier for radiation.

Similar computations can also be performed in the opposite limit, i.e., $T \ll m$, when particles are non-relativistic. Starting with the number density, we find

$$n(T) = g \left(\frac{mT}{2\pi}\right)^{3/2} e^{-m/T} . \tag{1.38}$$

This result demonstrates that when particles transition from the ultra-relativistic to the non-relativistic regime, their number density becomes exponentially suppressed, regardless of whether they are fermions or bosons. This behavior is reminiscent of the Maxwell-Boltzmann distribution. For the energy density, it can be shown that it is related to the number density by

$$\rho(T) = \left[m + \frac{3}{2}T\right] n(T) . \tag{1.39}$$

However, in the limit of interest, the second term is subdominant, yielding the intuitive result

$$\rho(T) = mn(T) . \tag{1.40}$$

Similarly, the pressure is found to be

$$P(T) = n(T)T , \tag{1.41}$$

which aligns with the equation of state introduced earlier for pressureless matter. Specifically

$$P(T) = n(T)T \ll mn(T) = \rho(T) , \tag{1.42}$$

in the non-relativistic limit.

Another quantity that is extremely useful in describing the thermal history of the Universe is the entropy S, which remains conserved during the adiabatic expansion of the Universe. Entropy can be defined in terms of other thermodynamic quantities as

$$S \equiv \frac{\rho + P}{T} a^3 . \tag{1.43}$$

Using previous results, the total entropy for a collection of different particle species can be expressed as

$$S = \frac{2\pi^2}{45} g_{*s}(T) a^3 T^3 , \tag{1.44}$$

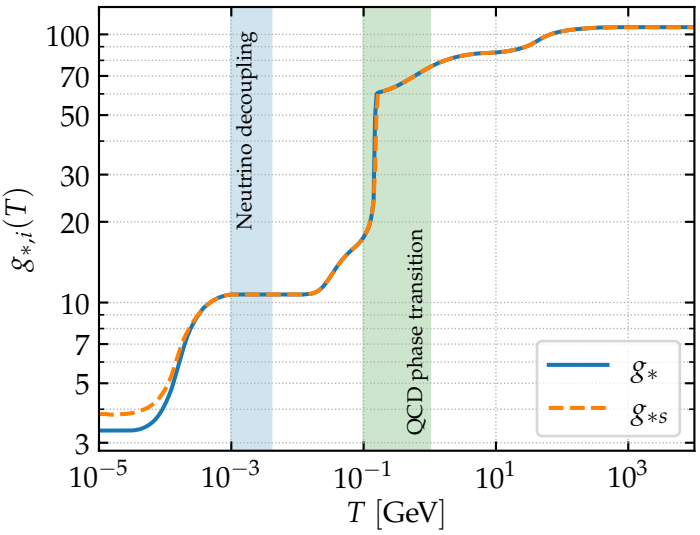

Figure 1.2: Temperature dependence of the number of relativistic degrees of freedom in the SM. The dashed line shows the same for the number of effective degrees of freedom in entropy.

where we have introduced the effective number of degrees of freedom in entropy

$$g_{*s}(T) = \sum_{i=\text{bosons}} g_i \left(\frac{T_i}{T}\right)^3 + \frac{7}{8} \sum_{i=\text{fermions}} g_i \left(\frac{T_i}{T}\right)^3 . \tag{1.45}$$

Notice that, as long as all particle species are in equilibrium at the same temperature T, $g_*(T) = g_{*s}(T)$. This condition holds at temperatures $T \gtrsim 1\,\text{MeV}$. However, as discussed in section 1.3.1, neutrinos decouple from the cosmological plasma at $T \sim 1\,\text{MeV}$. Shortly thereafter, when the temperature of the Universe falls below the electron mass ($m_e = 0.511\,\text{MeV}$), electron-positron annihilations occur. As a result, cosmic neutrinos acquire a slightly lower temperature compared to particles that remain in equilibrium with the cosmological plasma. This leads to $g_*(T \lesssim m_e) \neq g_{*s}(T \lesssim m_e)$, as illustrated in fig. 1.2, which shows g_* and g_{*s} as functions of the temperature T. Moreover, the conservation of entropy implies the relation

$$T \propto g_{*s}^{-1/3}(T)\, a^{-1} , \tag{1.46}$$

which, away from mass thresholds (where g_{*s} remains approximately constant), yields the expected scaling $T \propto a^{-1}$. This result is consistent with the behavior predicted by comparing the equation of state for radiation in Friedmann models with the Stefan-Boltzmann law.

1.2.2 A brief history of the Universe

The thermal history of the universe describes key epochs that shaped its evolution from a hot, dense plasma to the structured cosmos we observe

today. By combining insights from multiple references, this section presents a comprehensive, detailed, and scientifically rigorous narrative.

- **Planck Epoch and Limitations:** At $t < t_{\mathrm{Pl}} \sim 1 \times 10^{-43}\,\mathrm{s}$ and $T > T_{\mathrm{Pl}} \sim 1 \times 10^{19}\,\mathrm{GeV}$, the Universe existed in a state of extreme density and temperature, referred to as the Planck epoch. In this regime, quantum gravitational effects dominate, rendering classical theories such as General Relativity inadequate for providing a reliable description. Beyond this epoch, we lack a consistent theory of quantum gravity to describe the Universe's behavior. Consequently, descriptions of this era remain speculative, and this thermal history begins after the Planck epoch.

- **Inflation and Reheating:** Evidence suggests that the Universe underwent an early period of accelerated expansion, referred to as *inflation*, which resolved the horizon, flatness, and monopole problems inherent in the standard Big Bang model. Inflation also produced quantum fluctuations that were stretched to cosmic scales, seeding the primordial density perturbations observable in the CMB and LSS. The inflationary phase ended with the *reheating* process, during which the energy stored in the inflaton field was transferred to particles, creating a hot thermal plasma that signaled the beginning of the radiation-dominated era.

- **Baryogenesis:** The Universe exhibits an observed baryon asymmetry, quantified by the baryon-to-photon ratio $\eta \sim 10^{-9}$. According to relativistic QFT, every particle species should have a corresponding antiparticle with the same mass and decay rates but opposite charges. Consequently, the initial state of the Universe would have contained equal numbers of particles and antiparticles, resulting in mutual annihilation and a radiation-dominated Universe. However, the predominance of matter observed today indicates the presence of a mechanism for dynamically generating a baryon–antibaryon asymmetry, known as *baryogenesis*. This mechanism relies on Sakharov's conditions, which require processes that violate baryon number, CP symmetry, and thermal equilibrium. Although numerous baryogenesis models have been proposed, experimental confirmation of these processes remains elusive.

- **Electroweak Phase Transition:** At $T \sim 100\,\mathrm{GeV}$, the electroweak force underwent spontaneous symmetry breaking, transitioning from $\mathrm{SU}(2)_L \times \mathrm{U}(1)_Y$ to $\mathrm{U}(1)_{\mathrm{Q}}$. This symmetry breaking, mediated by the Higgs mechanism, endowed elementary particles with mass, including the gauge bosons $W^{\pm}$ and Z^0, while the photon remained massless. Furthermore, this transition marked the emergence of the weak interaction as a short-ranged force.

- **Quantum ChromoDynamics (QCD) Phase Transition:** As the Universe cooled to $T \sim 150\,\mathrm{MeV}$, the strong interaction underwent a phase

transition known as the *QCD phase transition*. During this epoch, quarks and gluons, which were asymptotically free at high energies, became confined into hadrons such as baryons (e.g., protons and neutrons) and mesons. This confinement significantly reduced the number of relativistic degrees of freedom in the plasma.

- **Neutrino Decoupling:** At $T \sim 1\,\mathrm{MeV}$, the interaction rate of neutrinos fell below the expansion rate of the Universe, causing neutrinos to decouple from the thermal plasma. From that point onward, neutrinos free–streamed through the Universe, forming a relic background.

- **Electron-Positron Annihilation:** When the temperature dropped to $T \sim 0.511\,\mathrm{MeV}$, electrons and positrons became non-relativistic and annihilated predominantly into photons via $e^+e^- \to 2\gamma$. The energy released during this annihilation heated the photon background but not the neutrinos, resulting in the present–day temperature ratio

$$T_\gamma / T_\nu \sim \left(\frac{11}{4}\right)^{1/3} . \tag{1.47}$$

- **Big Bang Nucleosynthesis (BBN):** Around $T \sim 0.1\,\mathrm{MeV}$ ($t \sim 3\,\mathrm{min}$), nuclear reactions in the cooling plasma led to the synthesis of light elements, including hydrogen (^{1}H), helium (^{4}He), deuterium (^{2}H), and trace amounts of lithium (^{7}Li). The predicted abundances of these elements are in excellent agreement with observational data, making BBN a cornerstone of the Hot Big Bang model.

- **Radiation-Matter Equality:** At $T \sim 0.75\,\mathrm{eV}$, the energy density of radiation, dominated by photons and neutrinos, equaled the energy density of matter, primarily composed of dark matter and baryons. This transition marked the end of the radiation–dominated era and the beginning of the matter–dominated era, during which density perturbations grew under the influence of gravity.

- **Recombination:** At $T \sim 0.3\,\mathrm{eV}$, free electrons combined with protons to form neutral hydrogen atoms via the process $e^- + p \to \mathrm{H} + \gamma$. This process, known as *recombination*, significantly reduced the Universe's opacity to photons, leading to the decoupling of matter and radiation.

- **Photon Decoupling:** Following recombination, photons decoupled from matter and began free-streaming through the Universe. These decoupled photons form the CMB, a relic radiation that provides a snapshot of the Universe at $t \sim 380\,000\,\mathrm{yr}$. The properties of the CMB, such as its temperature anisotropies, encode critical information about the early conditions and composition of the Universe.

- **Structure Formation:** Much later, gravitational collapse amplified the primordial density perturbations seeded during inflation, leading to

the formation of galaxies, galaxy clusters, and cosmic filaments. This hierarchical structure formation was driven by the interplay between dark matter, baryonic matter, and dark energy.

1.3 BEYOND EQUILIBRIUM: THE UNIVERSE BELOW 1 MeV

1.3.1 Neutrino decoupling

Below a temperature of $T \sim 30 - 40$ MeV, the leading processes contributing to neutrino equilibrium are scattering with electrons and positrons[1] and pair conversions $\nu_\alpha \bar{\nu}_\alpha \leftrightarrow e^+ e^-$. This is because, at first perturbative order in the weak coupling constant, all interactions involve only two particles, and at these temperatures, reactions involving more massive particles are energetically forbidden.

As long as the temperature remains smaller than the W and Z boson masses (focusing on the low–energy regime), the thermally averaged cross–section times velocity is approximately

$$\langle \sigma v \rangle \simeq G_{\mathrm{F}}^2 E^2 \simeq G_{\mathrm{F}}^2 T^2 \,. \tag{1.48}$$

This allows us to estimate the interaction rate as

$$\Gamma = n_e \langle \sigma v \rangle \simeq G_{\mathrm{F}}^2 T^5 \,. \tag{1.49}$$

On the other hand, from the first Friedmann equation, the Hubble parameter during the radiation–dominated epoch is given by

$$H(T) = \left(\frac{4\pi^3}{45}\right)^{1/2} g_*^{1/2}(T) \, \frac{T^2}{M_{\mathrm{pl}}} \,, \tag{1.50}$$

which, combined with the interaction rate estimate in eq. (1.49), gives an approximate decoupling temperature

$$T_{\nu,\mathrm{d}} \simeq \left(\frac{\sqrt{g_*}}{G_{\mathrm{F}}^2 M_{\mathrm{pl}}}\right)^{1/3} \sim g_*^{1/6} \text{ MeV} \,. \tag{1.51}$$

We observe that T_{d} is very weakly dependent on the number of relativistic degrees of freedom g_* and is of the order of MeV (a more precise calculation gives $T_{\mathrm{dec}} \sim 1.5$ MeV [Escudero, 2019]). After decoupling, neutrinos free–stream along geodesics and approximately preserve the *relativistic Fermi-Dirac* distribution, even after becoming non–relativistic at later times. The physical momentum of a particle scales as $p \propto a^{-1}$. It is therefore convenient to define

1 There is also a baryonic component; however, since it is much smaller than the leptonic one, we can safely neglect its contribution.

the time-independent combination $q \equiv ap$, so that the neutrino number density becomes

$$n_\nu \propto a^{-3} \int d^3q \, \frac{1}{\exp(q/aT_\nu) + 1} \, . \tag{1.52}$$

After decoupling, particle number conservation requires $n_\nu \propto a^{-3}$. This is consistent with eq. (1.52) only if the neutrino temperature evolves as $T_\nu \propto a^{-1}$. As long as the photon temperature T_γ scales in the same way, we still have $T_\nu = T_\gamma$.

Shortly after the neutrinos decouple, the temperature drops below the electron mass, and electron–positron annihilation occurs $e^+ + e^- \leftrightarrow \gamma + \gamma$. The energy density and entropy of the electrons and positrons are transferred to the photons but not to the decoupled neutrinos. As a result, the photons are "heated" (their temperature does not decrease as much) relative to the neutrinos. To quantify this effect, we consider the change in the effective number of degrees of freedom in entropy. Neglecting neutrinos and other decoupled species, which conserve their entropy separately, we have

$$g_{*s}^{\rm th} = \begin{cases} 2 + \dfrac{7}{8} \times 4 = \dfrac{11}{2} & T \gtrsim m_e \, , \\ 2 & T \lesssim m_e \, . \end{cases} \tag{1.53}$$

Since, in equilibrium, $g_{*s}^{\rm th}(aT_\gamma)^3$ remains constant, we find that aT_γ increases after electron–positron annihilation, $T \lesssim m_e$, by a factor $(11/4)^{1/3}$, while aT_ν remains unchanged. This implies that the neutrino temperature is slightly lower than the photon temperature after e^+e^- annihilation,

$$T_\nu = \left(\frac{4}{11}\right)^{1/3} T_\gamma \, . \tag{1.54}$$

For $T \ll m_e$, the effective number of relativistic species (in energy density and entropy) is therefore

$$g_* = 2 + \frac{7}{8} \times 2N_{\rm eff} \left(\frac{4}{11}\right)^{4/3} = 3.36 \, , \tag{1.55}$$

$$g_{*s} = 2 + \frac{7}{8} \times 2N_{\rm eff} \left(\frac{4}{11}\right) = 3.94 \, , \tag{1.56}$$

where we introduce the parameter $N_{\rm eff}$ as the *effective number of neutrino species* in the Universe. If neutrino decoupling were instantaneous, we would have $N_{\rm eff} = 3$. However, neutrino decoupling was not fully complete when e^+e^- annihilation began, so some of the energy and entropy leaked to the neutrinos. Taking this into account raises the effective number of neutrinos to $N_{\rm eff} = 3.044$. Notice that the Planck collaboration constraint is $N_{\rm eff} = 2.99^{+0.34}_{-0.33}$ at 95% CL [Aghanim et al., 2020c]. This still leaves room for the possibility that $N_{\rm eff} \neq 3.044$, providing an avenue for cosmology to discover new physics BSM.

COSMIC NEUTRINO BACKGROUND The relation eq. (1.54) holds to the present day. The Cosmic Neutrino Background (CNB) therefore has a slightly lower temperature, $T_{\nu,0} = 1.95\,\mathrm{K}$, than the CMB, $T_0 = 2.73\,\mathrm{K}$. The number density of neutrinos is

$$n_\nu = \frac{3}{4} N_{\rm eff} \times \frac{4}{11} n_\gamma \,, \tag{1.57}$$

corresponding to approximately 112 neutrinos cm^{-3} per flavor. The present energy density of neutrinos depends on whether the neutrinos are relativistic or non–relativistic today. It was once believed that neutrinos were massless, in which case

$$\rho_\nu = \frac{7}{8} N_{\rm eff} \left(\frac{4}{11}\right)^{4/3} \rho_\gamma \quad \Rightarrow \quad \Omega_\nu h^2 \simeq 1.7 \times 10^{-5} \quad (m_\nu = 0) \,. \tag{1.58}$$

However, neutrino oscillation experiments have since demonstrated that neutrinos have mass. The minimum sum of the neutrino masses is $\sum m_{\nu,i} \gtrsim 60\,\mathrm{meV}$. Massive neutrinos behave as radiation–like particles in the early Universe and as matter–like particles in the late Universe. The energy density of massive neutrinos, $\rho_\nu = \sum m_{\nu,i} n_{\nu,i}$, corresponds to

$$\Omega_\nu h^2 \simeq \frac{\sum m_{\nu,i}}{94\,\mathrm{eV}} \,. \tag{1.59}$$

By requiring that neutrinos do not overclose the Universe, i.e., $\Omega_\nu < 1$, we obtain a cosmological upper bound on the sum of the neutrino masses, $\sum m_{\nu,i} < 15\,\mathrm{eV}$.

1.3.2 Big Bang Nucleosynthesis

BBN stands as one of the strongest pillars of modern cosmology, offering a comprehensive explanation for the formation of light elements in the early Universe. This process occurred within the first few minutes following the Big Bang and represents the earliest epoch in cosmic history for which we possess direct observational evidence. The remarkable success of BBN in predicting the primordial abundances of light nuclei, particularly deuterium and helium–4, provides compelling support for the Hot Big Bang model, serving as a valuable probe of the Universe's initial conditions. BBN describes the sequence of nuclear reactions that took place as the Universe cooled from temperatures of several MeV to approximately $10^{-2}\,\mathrm{MeV}$. During this period, the primordial plasma was composed of relativistic photons, neutrinos, electrons, and their antiparticles, along with non–relativistic protons and neutrons. In the early stages, the high temperatures ensured that nuclear reactions were balanced by photodisintegration, preventing the formation of stable nuclei. As the Universe expanded and the temperature decreased, nuclear reactions began to dominate, enabling the formation of light nuclei. This transition marked the departure from thermal equilibrium and the freeze-out

of the primordial element abundances. The relative abundances of these light elements were dictated by the interplay between nuclear reaction rates, the expansion rate of the Universe, and particle decays.

A crucial process in BBN is the decoupling of neutrons and protons, which establishes the conditions for subsequent nucleosynthesis. At high temperatures $T \gtrsim 1\,\mathrm{MeV}$, weak interactions such as $p + e^- \leftrightarrow n + \nu_e$ maintained the neutron-to-proton ratio in thermal equilibrium, which can be approximated as

$$\frac{n_n}{n_p} = \exp\left(-\frac{\Delta m}{T}\right), \tag{1.60}$$

where $\Delta m \simeq 1.3\,\mathrm{MeV}$ represents the neutron–proton mass difference. As the Universe cooled, these interactions became inefficient around a temperature of $T_{n,\mathrm{dec}} \simeq 0.8\,\mathrm{MeV}$. At this freeze-out temperature, the neutron-to-proton ratio was approximately $n_n/n_p\big|_{T_{n,\mathrm{dec}}} \simeq 0.2$. After decoupling, neutrons were no longer replenished, and their abundance began to decline due to the expansion of the Universe and neutron decay, which has a lifetime of $\tau_n \simeq 881\,\mathrm{s}$. The evolving neutron fraction can be expressed as

$$\left.\frac{n_n}{n_p}\right|_{t>t_{n,\mathrm{dec}}} = \left.\frac{n_n}{n_p}\right|_{t_{n,\mathrm{dec}}} \exp\left(-\frac{t - t_{n,\mathrm{dec}}}{\tau_n}\right). \tag{1.61}$$

In the absence of nuclear interactions, this expression would remain valid indefinitely, and neutrons would eventually vanish from the Universe. However, once helium forms, neutrons bound within helium nuclei become stable, halting their decay.

The formation of light nuclei began once the temperature dropped sufficiently for deuterium to become stable against photodisintegration. The abundance of deuterium, which forms via the reaction $p + n \to d + \gamma$, is governed by the Saha equation

$$\frac{n_d}{n_p n_n} = \frac{g_d}{g_p g_n}\left(\frac{2\pi m_d}{m_p m_n T}\right)^{3/2} \exp\left(\frac{B_d}{T}\right), \tag{1.62}$$

where $B_d \simeq 2.2\,\mathrm{MeV}$ is the binding energy of deuterium. The exponential dependence on temperature emphasizes the sensitivity of deuterium formation to the photon energy, which must drop below B_d for stable nuclei to form. To estimate the abundance of deuterium, we approximate the neutron density with the baryon density and express this in terms of the photon temperature and the baryon-to-photon ratio

$$\eta_B \equiv \frac{n_\mathrm{b}}{n_\gamma} \simeq 5.5 \times 10^{-10}\left(\frac{\Omega_\mathrm{b} h^2}{0.02}\right). \tag{1.63}$$

The smallness of the baryon-to-photon ratio η_B inhibits deuterium production until the temperature drops significantly below the binding energy B_d. The temperature must decrease sufficiently for $e^{B_d/T}$ to compete with $\eta_B \simeq 10^{-9}$.

This phenomenon is often referred to as the "deuterium bottleneck." An order-one abundance of deuterium begins to form around $T_{\rm NUC} \simeq 0.06\,\text{MeV}$.

As the abundance of deuterium increased, it acted as a catalyst for the synthesis of heavier nuclei. Reactions such as $d + d \to {}^3\text{He}$ and $d + d \to {}^4\text{He}$ occurred rapidly. The majority of the available neutrons were ultimately bound into helium-4, the most stable and tightly bound of the light nuclei. The helium-4 mass fraction, denoted X_4, can be estimated as

$$X_4 = \frac{4n_{^4\text{He}}}{n_B} \simeq 2\frac{n_n/n_p}{1 + n_n/n_p}\,. \tag{1.64}$$

Using the neutron-to-proton ratio at nucleosynthesis, while accounting for neutron decay, we find $X_4 \simeq 0.25$, indicating that approximately 25% of the baryonic mass of the Universe was converted into helium-4. This prediction aligns remarkably well with observations of primordial helium in low-metallicity regions of the Universe.

BBN remains one of the most robust validations of the Hot Big Bang model. Observations of primordial abundances, particularly those of ^{4}He, deuterium, and ^{7}Li, offer invaluable insights into the early Universe. For example, the *deuterium-to-hydrogen ratio*, D/H, serves as a sensitive probe of the baryon-to-photon ratio, independently corroborating results from CMB studies. Likewise, the helium-4 mass fraction, $Y_p \equiv 4n_{\rm He}/n_{\rm b}$, constrains the number of relativistic species, providing information on neutrino physics and the possibility of new light particles. Despite its successes, BBN also presents unresolved challenges. The observed abundance of lithium-7, for instance, is significantly lower than theoretical predictions, a discrepancy commonly referred to as the *lithium problem*. Addressing this issue may necessitate new physics beyond the Standard Model or a more precise understanding of nuclear reaction rates. In summary, BBN not only reinforces the Big Bang model but also serves as a critical link between particle physics, nuclear astrophysics, and cosmology, offering a unique perspective on the Universe's earliest moments.

1.3.3 Photon decoupling

An important milestone in the early Universe's history is the formation of the first atoms. At temperatures exceeding approximately 1 eV, the Universe remained a plasma of free electrons and nuclei. Photons were tightly coupled to the electrons through Compton scattering, which, in turn, interacted strongly with protons via Coulomb scattering. As a result, there was very little neutral hydrogen. When the temperature dropped sufficiently, electrons and nuclei combined to form neutral atoms, in a process referred to as *recombination*. The density of free electrons decreased sharply, causing the photon mean free path to grow rapidly, eventually exceeding the horizon distance. At this point, photons *decoupled* from matter, rendering the Universe transparent. These photons are observed today as the *cosmic microwave background*

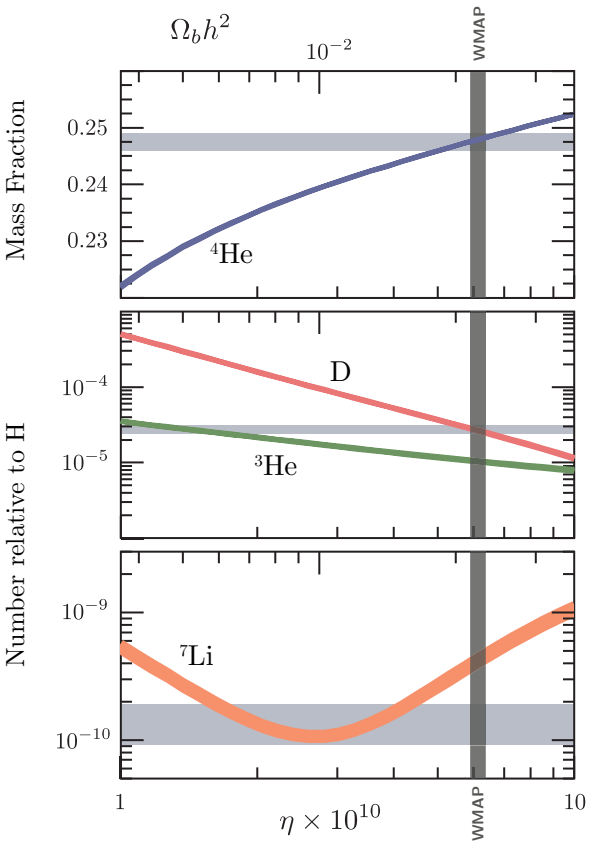

Figure 1.3: Theoretical predictions for the abundances of the four lightest nuclei. Colored bands indicate the error on theoretical calculations, while grey bands represents the most updated observational constraints. Figure taken from Baumann (2022), partially adapted from Pitrou et al. (2018).

(CMB). Let us begin with the regime $T > 1\,\text{eV}$. During this time, baryons and photons remained in equilibrium through electromagnetic reactions such as $e^- + p^+ \leftrightarrow \text{H} + \gamma$. Since $T < m_i$ ($i = e, p, \text{H}$), equilibrium abundances are described by eq. (1.38), with $\mu_p + \mu_e = \mu_\text{H}$ (noting that $\mu_\nu = 0$). To eliminate the dependence on the chemical potentials, we consider the ratio[2]

$$\left(\frac{n_\text{H}}{n_e n_p}\right)_\text{eq} = \frac{g_\text{H}}{g_e g_p}\left(\frac{m_\text{H}}{m_e m_p}\frac{2\pi}{T}\right)^{3/2} e^{\left[m_p + m_e - m_\text{H}\right]/T} . \tag{1.66}$$

In the prefactor, we can approximate $m_\text{H} \simeq m_p$, but the small difference between m_H and $m_p + m_e$ in the exponential is critical: it corresponds to the binding energy of hydrogen,

$$B_\text{H} \equiv m_p + m_e - m_\text{H} = 13.6\,\text{eV} . \tag{1.67}$$

The internal degrees of freedom are $g_p = g_e = 2$ and $g_\text{H} = 4$[3]. Additionally, since the Universe is electrically neutral, we have $n_e = n_p$. Substituting this into the eq. (1.66) simplifies it to

$$\left(\frac{n_\text{H}}{n_e^2}\right)_\text{eq} = \left(\frac{2\pi}{m_e T}\right)^{3/2} e^{B_\text{H}/T} . \tag{1.68}$$

We aim to follow the *free electron fraction*, defined as the ratio

$$X_e \equiv \frac{n_e}{n_b} , \tag{1.69}$$

where n_b is the baryon density. To simplify the discussion, we ignore all nuclei other than protons (since over 90% of nuclei by number are protons). The total baryon number density can then be approximated as $n_b \simeq n_p + n_\text{H} = n_e + n_\text{H}$, leading to

$$\frac{1 - X_e}{X_e^2} = \frac{n_\text{H}}{n_e^2} n_b . \tag{1.70}$$

Substituting eq. (1.63), we obtain the so–called *Saha equation*:

$$\frac{1 - X_e}{X_e^2} = \left(\frac{2\zeta(3)}{\pi^2}\right)\eta\left(\frac{2\pi}{m_e T}\right)^{3/2} e^{B_\text{H}/T} . \tag{1.71}$$

In fig. 1.4 we illustrate the redshift evolution of the free electron fraction, as predicted by both the Saha approximation and a more exact numerical

2 Let us recall here the formula for the number density of non–relativistic particles with a non–zero chemical potential, namely

$$n(T, \mu) = g\left(\frac{mT}{2\pi}\right)^{3/2} e^{(\mu - m)/T} . \tag{1.65}$$

3 The spins of the electron and proton in a hydrogen atom can be aligned or anti-aligned, yielding one singlet state and one triplet state, so $g_\text{H} = 1 + 3 = 4$.

treatment (discussed below). While the Saha approximation accurately identifies the onset of recombination—-our primary focus here—-it is inadequate for determining the relic density of electrons after freeze-out. We define, by convention, the recombination temperature $T_{\rm rec}$ as the temperature where $X_e = 10^{-1}$, i.e., when 90% of electrons have combined with protons to form hydrogen[4]. This yields

$$T_{\rm rec} \simeq 0.3\,{\rm eV} \simeq 3600\,{\rm K}\,. \tag{1.72}$$

The reason that $T_{\rm rec} \ll B_{\rm H} = 13.6\,{\rm eV}$ is that there are very many photons for each hydrogen atom, $\eta \sim 10^{-9} \ll 1$. Even when $T < B_{\rm H}$, the high–energy tail of the photon distribution contains photons with energy $E > B_{\rm H}$, enabling them to ionize hydrogen atoms.

Photons are strongly coupled to the primordial plasma through their interactions with electrons, $e^- + \gamma \leftrightarrow e^- + \gamma$, with an interaction rate given by

$$\Gamma_\gamma \simeq n_e \sigma_T\,, \tag{1.73}$$

where $\sigma_T \simeq 2 \times 10^{-3}\,{\rm MeV}^{-2}$ is the Thomson cross–section. Since $\Gamma_\gamma \propto n_e$, the interaction rate decreases as the density of free electrons declines. Photons and electrons decouple roughly when the interaction rate falls below the expansion rate,

$$\Gamma_\gamma(T_{\rm dec}) \sim H(T_{\rm dec})\,. \tag{1.74}$$

Using the first Friedmann equation (during matter domination) and writing the expansion rate as

$$H(T_{\rm dec}) = H_0 \sqrt{\Omega_m} \left(\frac{T_{\rm dec}}{T_0}\right)^{3/2}\,, \tag{1.75}$$

we obtain

$$X_e(T_{\rm dec}) T_{\rm dec}^{3/2} \sim \frac{\pi^2}{2\zeta(3)} \frac{H_0 \sqrt{\Omega_m}}{\eta \sigma_T T_0^{3/2}}\,. \tag{1.76}$$

Finally, using the Saha equation for $X_e(T_{\rm dec})$, we find

$$T_{\rm dec} \sim 0.27\,{\rm eV}\,. \tag{1.77}$$

Although $T_{\rm dec}$ is close to $T_{\rm rec}$, the ionization fraction decreases significantly between recombination and decoupling, transitioning from $X_e(T_{\rm rec}) \simeq 0.1$ to $X_e(T_{\rm dec}) \simeq 0.01$. This demonstrates that a high degree of neutrality is required for the Universe to become transparent to photon propagation. After decoupling, photons travel freely. Observations of the CMB today allow us to probe the conditions at recombination.

4 Let us stress that there is no profound reason behind this choice, it is purely arbitrary.

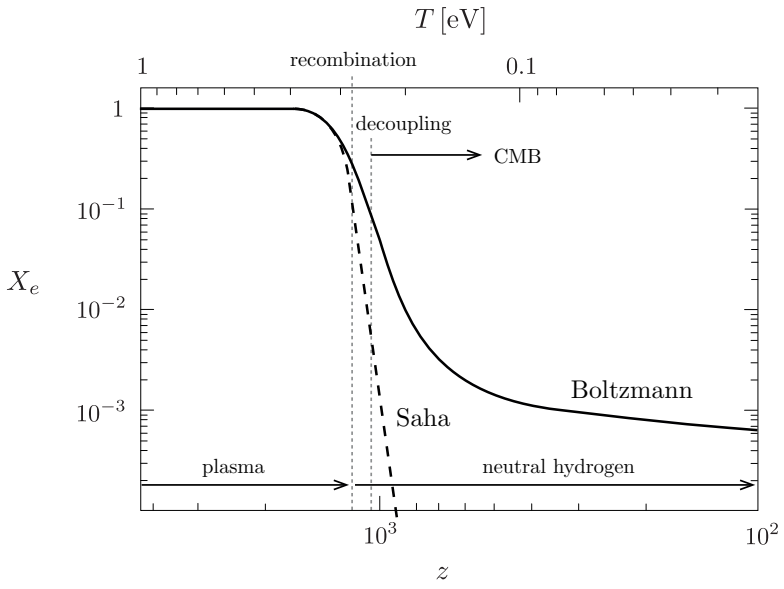

Figure 1.4: Free electron fraction as a function of redshift. The dashed line represents the solution obtained with the Saha approximation while the solid one and a more exact numerical treatment (see section 1.3.4). Figure taken from Baumann (2022).

THE COSMIC MICROWAVE BACKGROUND The CMB is a gas of non–interacting photons, predicted by the Hot Big Bang theory and discovered in 1964. The number density of CMB photons is approximately 400 per cubic centimeter. The energy distribution of these photons follows an almost perfect black–body spectrum. The CMB temperature is [Fixsen, 2009]

$$T_0 = 2.7255 \pm 0.0006\,\mathrm{K}\,. \tag{1.78}$$

The temperature of photons observed from different directions on the celestial sphere is uniform to a precision better than 10^{-4} (excluding the dipole component, see below). This remarkable uniformity provides strong evidence for the homogeneity and isotropy of the Universe. Nevertheless, the temperature does exhibit slight directional dependence. The angular anisotropy of the CMB temperature has been measured and is of the order $\delta T/T_0 \sim 10^{-4} \div 10^{-5}$.

We will repeatedly refer to CMB temperature and polarization anisotropies, as they encode extensive information about both the present and early Universe and can be measured with remarkable precision. The existence of the CMB implies the presence of a special reference frame in our Universe: the frame in which the gas of photons is at rest. The solar system moves relative to this frame in the direction of the Hydra constellation. This motion produces the dipole component of the observed CMB anisotropy,

$$\delta T_{\mathrm{dipole}} = 3.346\,\mathrm{mK}\,. \tag{1.79}$$

The present Universe is transparent to CMB photons[5]: their mean free path far exceeds the horizon size H_0^{-1}. However, this was not the case in the early Universe, where photons interacted actively with matter.

Since the CMB temperature T depends on the direction $\mathbf{n}$ on the celestial sphere, it is convenient to decompose it using spherical harmonics $Y_{\ell m}(\mathbf{n})$. These functions form a basis for the functions defined on a sphere, and this decomposition serves as the closest analog to Fourier decomposition. The temperature fluctuation δT in the direction $\mathbf{n}$ is defined as

$$\delta T(\mathbf{n}) = T(\mathbf{n}) - T_0 - \delta T_{\text{dipole}} \,, \tag{1.80}$$

and can be expressed as

$$\delta T(\mathbf{n}) = \sum_{\ell,m} a_{\ell m} Y_{\ell m}(\mathbf{n}) \,, \tag{1.81}$$

where the coefficients $a_{\ell m}$ satisfy the relation $a^*_{\ell m} = (-1)^m a_{\ell,-m}$, ensuring the reality of the temperature field. The multipoles ℓ correspond to fluctuations with a characteristic angular size π/ℓ. Current measurements can analyze angular scales ranging from the largest observable sizes down to less than 0.1° ($\ell \sim 1000$, see fig. 1.5).

Observational data are consistent with the property that temperature fluctuations $\delta T(\mathbf{n})$ are Gaussian random fields, meaning that the coefficients $a_{\ell m}$ are statistically independent for different ℓ and m

$$\langle a_{\ell m} a^*_{\ell' m'} \rangle = C_\ell \delta_{\ell\ell'} \delta_{mm'} \,, \tag{1.82}$$

where the brackets denote averaging over an ensemble of Universes similar to ours. In an isotropic Universe, the coefficients $C_{\ell m}$ are independent of m, so $C_{\ell m} \equiv C_\ell$. These coefficients determine the correlation of temperature fluctuations in different directions

$$\langle \delta T(\mathbf{n}_1) \delta T(\mathbf{n}_2) \rangle = \sum_\ell \frac{2\ell+1}{4\pi} C_\ell P_\ell(\cos\theta) \,, \tag{1.83}$$

where P_ℓ are the Legendre polynomials, which are functions of the angle θ between the vectors $\mathbf{n}_1$ and $\mathbf{n}_2$.

The quantity

$$D_\ell \equiv \frac{\ell(\ell+1) C_\ell}{2\pi} \,, \tag{1.84}$$

represents the contribution to the fluctuation for a unit interval of multipoles. This quantity is typically shown as in fig. 1.5. Importantly, the measurement of CMB temperature anisotropies provides not just a single value, but a large dataset comprising the values of C_ℓ for different ℓ. These values are influenced by numerous parameters of the present and early Universe, making their measurement an invaluable source of cosmological information. Further insights are obtained from measurements of CMB polarization.

5 This is not entirely true in certain regions of the Universe. For example, photons scatter off hot gas ($T \sim 10\,\text{keV}$) in galaxy clusters, gaining energy. Consequently, the CMB appears slightly

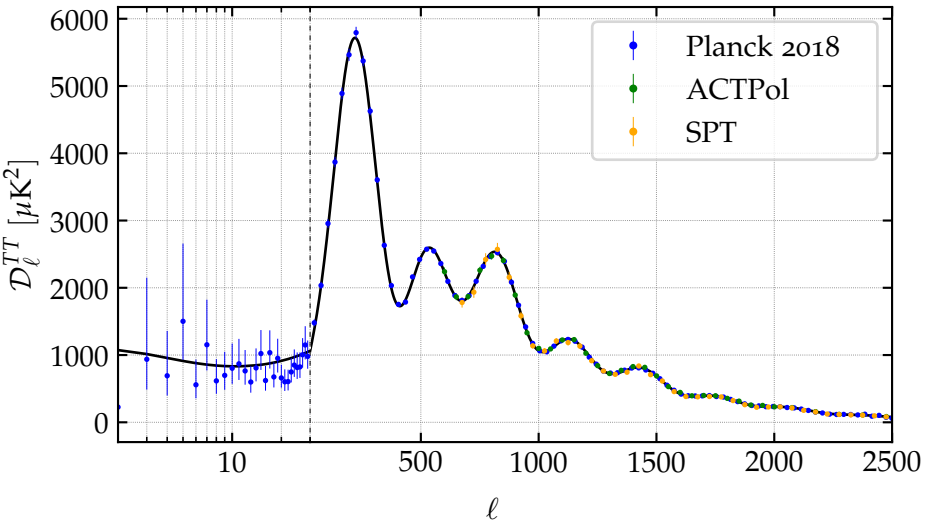

Figure 1.5: Power spectrum of CMB temperature anisotropies. Scattered points represent some of the most advanced measurements currently available. Note how different experiments, with distinct angular resolutions, probe distinct parts of the spectrum.

1.3.4 The Boltzmann equation

Throughout much of its early history, the Universe's components remained in thermal equilibrium, making an equilibrium description a highly accurate approximation. However, there have been several significant deviations from this state of equilibrium, including events such as neutrino decoupling, the decoupling of background radiation, primordial nucleosynthesis, and, on the more speculative side, phenomena like inflation, baryogenesis, and the decoupling of relic Weakly–Interacting Massive Particles (WIMPs). Without these departures from thermal equilibrium, the current state of the Universe would be entirely determined by its present temperature. These nonequilibrium processes, however, have left behind critical relics: the light elements, the neutrino background, a net baryon number, relic WIMPs, and more.

Once a particle species becomes completely decoupled from the plasma, its evolution follows straightforward rules: the number density of particles decreases as a^{-3}, and particle momenta scale as a^{-1}. While the evolution of the phase space distribution is simple for species in thermal equilibrium or fully decoupled, the transition during the decoupling process is much more complex. The key factor in determining whether a particle species remains coupled or becomes decoupled is the comparison between its interaction rate and the Universe's expansion rate

$$\Gamma \gtrsim H \quad \text{(coupled)}\,, \quad \Gamma \lesssim H \quad \text{(decoupled)}\,. \tag{5.1}$$

warmer in the directions of these clusters. This phenomenon, known as the Sunyaev–Zeldovich effect, is subtle but detectable in observations.

Here, Γ represents the interaction rate for the processes maintaining the species in thermal equilibrium.

Although this rule of thumb is often surprisingly accurate, a proper treatment of decoupling requires following the microscopic evolution of the particle's phase space distribution function $f(p,x)$. This evolution is governed by the Boltzmann equation, expressed as

$$\mathbb{L}[f] = \mathbb{C}[f] \,, \tag{1.85}$$

where $\mathbb{C}$ is the collision operator, and $\mathbb{L}$ represents the Liouville operator.

In the familiar non–relativistic context, the Liouville operator for a particle species' phase space density corresponds to the total time derivative. The covariant, relativistic generalization of the Liouville operator is given by

$$\mathbb{L} = p^\mu \frac{\partial}{\partial x^\mu} - \Gamma^\mu_{\nu\rho} p^\nu p^\rho \frac{\partial}{\partial p^\mu} \,. \tag{1.86}$$

As expected, gravitational effects appear in this equation exclusively through the affine connection. For the FRW model, where the phase space density is spatially homogeneous and isotropic, the Liouville operator simplifies to

$$\mathbb{L}[f(E,t)] = E\frac{\partial f}{\partial t} - \frac{\dot{R}}{R}|\mathbf{p}|^2 \frac{\partial f}{\partial E} \,, \tag{1.87}$$

where the Christoffel symbols are calculated using the metric given in eq. (1.1).

The collision term for the process $\psi + a + b + \cdots \leftrightarrow i + j + \cdots$ is expressed as

$$\begin{aligned}\mathbb{C}[f] = -\frac{1}{2}\int & d\Pi_a d\Pi_b \cdots d\Pi_i d\Pi_j \cdots \\ & \times (2\pi)^4 \delta^4\left(p_\psi + p_a + p_b + \cdots - p_i - p_j - \cdots\right) \\ & \times \Big[\left|\mathcal{M}_{\psi ab\to ij\cdots}\right|^2 f_a f_b \cdots f_\psi (1 \pm f_i)(1 \pm f_j)\cdots \\ & \quad - \left|\mathcal{M}_{ij\cdots\to\psi ab\cdots}\right|^2 f_i f_j \cdots (1 \pm f_a)(1 \pm f_b)\cdots\left(1 \pm f_\psi\right)\Big] \,,\end{aligned} \tag{1.88}$$

where f_i, f_j, f_a, f_b, $\cdots$ represent the phase space densities of species i, j, $\cdots$, a, b, $\cdots$, and f_ψ is the phase space density of ψ, the species whose evolution is under consideration. The terms $(+)$ and $(-)$ correspond to bosons and fermions, respectively. The quantity $d\Pi$ is defined as

$$d\Pi \equiv \frac{g}{(2\pi)^3}\frac{d^3p}{2E} \,, \tag{1.89}$$

where g represents the number of internal degrees of freedom. The four–dimensional delta function enforces the conservation of energy and momentum, while the squared matrix element, $\left|\mathcal{M}_{\psi ab\to ij\cdots}\right|^2$, describes the process $\psi + a + b + \cdots \leftrightarrow i + j + \cdots$. This matrix element is averaged over the initial and final spins and incorporates appropriate symmetry factors to account for identical particles in the initial or final states.

In many physical problems involving the early Universe, two well–motivated approximations significantly simplify eq. (1.88). The first is the assumption of CP invariance, which ensures that

$$\left|\mathcal{M}_{\psi ab\cdots\to ij\cdots}\right|^2 = \left|\mathcal{M}_{ij\cdots\to\psi ab\cdots}\right|^2 \equiv |\mathcal{M}|^2 \,. \tag{1.90}$$

The second simplification involves adopting Maxwell–Boltzmann statistics for all particle species instead of Fermi–Dirac for fermions and Bose–Einstein for bosons. In situations where neither Bose condensation nor Fermi degeneracy is relevant, the blocking and stimulated emission factors can be approximated as $1 \pm f \simeq 1$. Under this assumption, the phase space density for any species in kinetic equilibrium simplifies to

$$f_i(E_i) \simeq \exp[-(E_i - \mu_i)/T] \,. \tag{1.91}$$

Using the definition of the number density in terms of the phase space distribution, eq. (1.25), and performing an integration by parts, the Boltzmann equation can be expressed as

$$\frac{dn_\psi}{dt} + 3Hn_\psi = \int d\Pi_\psi \, \mathbb{C}[f] \,. \tag{1.92}$$

It is important to note that in the absence of collisions, where $\mathbb{C}[f] = 0$, the equation reduces to the expected dilution of number density caused by the Universe's expansion. Specifically,

$$0 = \frac{dn_\psi}{dt} + 3Hn_\psi = \frac{1}{a^3}\frac{d}{dt}\left(n_\psi a^3\right) \,. \tag{1.93}$$

This reflects the conservation of the particle number in an expanding volume.

As we have already stressed, the explicit expression of the collision term depends on the process under consideration. Given that all subsequent applications will focus on $2 \to 2$ scattering processes, let us now focuse on the case of the binary scattering

$$\psi + a \leftrightarrow i + j \,. \tag{1.94}$$

By applying the approximations discussed earlier, the last line of eq. (1.88) simplifies to

$$\begin{aligned}&\left[f_a f_\psi (1 \pm f_i)(1 \pm f_j) - f_i f_j (1 \pm f_a)(1 \pm f_\psi)\right] \\ &\quad \to e^{-\left(E_\psi + E_a\right)/T}\left[e^{\left(\mu_\psi + \mu_a\right)/T} - e^{\left(\mu_i + \mu_j\right)/T}\right] \,,\end{aligned} \tag{1.95}$$

where we have used the conservation of energy, $E_\psi + E_a = E_i + E_j$. To proceed, it is convenient to define the equilibrium number density for each species

$$n_i^{(0)} \equiv \frac{g_i}{(2\pi)^3}\int d^3\mathbf{p}\, e^{-E_i/T} \,, \tag{1.96}$$

where g_i denotes the internal degrees of freedom. Using this definition, each factor of $e^{\mu_i/T}$ can be rewritten as $n_i/n_i^{(0)}$. This allows the last line of eq. (1.88) to be reformulated as

$$e^{-\left(E_\psi+E_a\right)/T}\left[\frac{n_\psi n_a}{n_\psi^{(0)} n_a^{(0)}}-\frac{n_i n_j}{n_i^{(0)} n_j^{(0)}}\right] . \tag{1.97}$$

We now define the thermally averaged cross–section as

$$\langle\sigma v\rangle \equiv \frac{\int d^3\mathbf{p}_\psi d^3\mathbf{p}_a e^{-\left(E_\psi+E_a\right)/T}\sigma v_{\rm rel}}{\int d^3\mathbf{p}_\psi e^{-E_\psi/T}\int d^3\mathbf{p}_a e^{-E_a/T}} , \tag{1.98}$$

where the total cross–section times the relative velocity, $\sigma v_{\rm rel}$, can be calculated using tools from QFT

$$\sigma v_{\rm rel} \equiv \frac{1}{2E_\psi}\frac{1}{2E_a}\int d\Pi_i d\Pi_j (2\pi)^4\delta^{(4)}\left(p_\psi+p_a-p_i-p_j\right)|\mathcal{M}|^2 , \tag{1.99}$$

with $v_{\rm rel}$ being the Møller velocity, defined as [Cannoni, 2014]

$$v_{\rm rel} \equiv \frac{1}{2E_\psi E_a}\sqrt{\left(p_\psi\cdot p_a\right)^2-m_\psi^2 m_a^2} . \tag{1.100}$$

Finally, the Boltzmann equation takes the form

$$\frac{1}{a^3}\frac{d}{dt}\left(n_\psi a^3\right) = -n_\psi^{(0)} n_a^{(0)}\left\langle\sigma v_{\rm rel}\right\rangle\left[\frac{n_\psi n_a}{n_\psi^{(0)} n_a^{(0)}}-\frac{n_i n_j}{n_i^{(0)} n_j^{(0)}}\right] . \tag{1.101}$$

A qualitative insight into eq. (1.101) is worth noting. The left–hand side is approximately of the order n_ψ/t. Since the characteristic cosmological time scale is H^{-1}, this term scales as $n_\psi H$. On the other hand, the right–hand side is of the order $n_\psi n_a\left\langle\sigma v_{\rm rel}\right\rangle$. Consequently, if the reaction rate $\Gamma = n_a\left\langle\sigma v_{\rm rel}\right\rangle$ is significantly greater than the expansion rate H, the terms on the right–hand side will dominate those on the left. The only way to maintain equality in this scenario is for the individual terms on the right–hand side to cancel each other out. This implies that when reaction rates are large,

$$\frac{n_\psi n_a}{n_\psi^{(0)} n_a^{(0)}} = \frac{n_i n_j}{n_i^{(0)} n_j^{(0)}} . \tag{1.102}$$

From eq. (1.96), this condition is equivalent to $\mu_\psi+\mu_a = \mu_1+\mu_2$. This is the so–called Saha equation, which describes the condition of chemical equilibrium. Conversely, in the regime of very low reaction rates, eq. (1.101) reduces to the limiting case described by eq. (1.93), thereby capturing the free–streaming behavior of the relic abundance for the particle species in question.

1.4 THE INFLATIONARY PARADIGM

1.4.1 Shortcomings of the Hot Big Bang Model

THE FLATNESS PROBLEM The spatial curvature of the Universe is characterized by the curvature density parameter, defined as

$$\Omega_k \equiv -\frac{k}{H^2 a^2} \,, \tag{1.103}$$

where k is the curvature constant, H is the Hubble parameter, and a denotes the scale factor. Observations from the latest Planck data impose tight constraints on its present value [Aghanim et al., 2020c]

$$\Omega_{k0} = 0.0007 \pm 0.0019 \,, \tag{1.104}$$

with a 68% confidence level. These results provide strong evidence that $|\Omega_{k0}| < 1$.

While the current constraints on the curvature density parameter provide valuable insights into the present–day geometry of the Universe, their implications for the early Universe reveal a perplexing issue. Starting from the definition of Ω_k, one can express it as

$$|\Omega_k| = \left| -\frac{k}{H^2 a^2} \right| = \left| -\frac{k}{H^2 a^2} \frac{H_0^2 a_0^2}{H_0^2 a_0^2} \right| = |\Omega_{k0}| \frac{H_0^2}{H^2 a^2} < \frac{H_0^2}{H^2 a^2} \,, \tag{1.105}$$

where the normalization $a_0 = 1$ has been used. During earlier epochs, as $a \to 0$ and the Universe was radiation–dominated, the factor $H_0^2 / H^2 a^2$ scaled approximately as a^2, implying

$$\frac{H_0^2}{H^2 a^2} \sim a^2 \to 0 \,. \tag{1.106}$$

This means that as we trace the evolution of the Universe backward in time, the value of Ω_k approaches zero with increasing precision. For instance, at the epoch of radiation–matter equality, corresponding to $z \sim 10^4$, we find $\Omega_k < 10^{-4}$. At the time of BBN, approximately $z \sim 10^{10}$, $\Omega_k < 10^{-16}$. Extrapolating further to the Planck epoch, at $z \sim 10^{32}$, yields $\Omega_k < 10^{-60}$. Such an extraordinarily small value in the early Universe presents a significant challenge. To explain the observed Ω_{k0} today, the value of Ω_k at the Planck scale must have been fine–tuned to an accuracy of 60 significant digits. This level of precision appears highly unnatural, exemplifying a case of fine–tuning, where theoretical parameters must adopt highly specific values without any apparent natural mechanism to enforce them. Although fine–tuning does not necessarily invalidate a theory, it often signals the need for an underlying explanation that is not yet understood. In many cases, fine–tuning is regarded as an indication of ad hoc assumptions, motivating the search for more natural and fundamental explanations.

The flatness problem was first addressed by Guth (1981), who proposed a profound yet straightforward resolution. The key lies in eq. (1.103): if the Hubble parameter H remains approximately constant for an extended period, then $\Omega_k \propto 1/a^2$. As a result, an early phase of the Universe where H is nearly constant could drive Ω_k to extremely small values, eliminating the need for fine–tuning. This phase, marked by an almost constant Hubble parameter and exponential growth of the scale factor, is referred to as *inflation*. Inflation must occur before the radiation–dominated era to preserve the successful predictions of the standard Big Bang model. Quantitatively, if H is constant, the scale factor evolves as

$$H = \text{const.} \quad \Longrightarrow \quad a \propto e^{Ht} \,. \tag{1.107}$$

This exponential growth exponentially suppresses Ω_k. To illustrate this, consider the curvature parameter at the beginning of inflation

$$\frac{|k|}{a_i^2 H_i^2} = \mathcal{O}(1) \,, \tag{1.108}$$

where the subscript i denotes the onset of inflation. At the end of inflation, denoted by subscript f, the scale factor increases by a factor e^N, where N is the number of e–folds during inflation, defined by

$$N \equiv \ln \frac{a_f}{a_i} = \int_{t_i}^{t_f} dt\, H(t) \,. \tag{1.109}$$

Consequently

$$\frac{|k|}{a_f^2 H_f^2} = \frac{|k|}{a_i^2 H_i^2} e^{-2N} \sim e^{-2N} \,. \tag{1.110}$$

Extrapolating this result to the present–day gives

$$|\Omega_{k0}| = \frac{|k|}{H_0^2} = \frac{|k|}{a_f^2 H_f^2} \left(\frac{a_f H_f}{H_0}\right)^2 \sim e^{-2N} \left(\frac{a_f H_f}{H_0}\right)^2 \,. \tag{1.111}$$

For $|\Omega_{k0}| < 1$, the following condition must be satisfied

$$\frac{a_f H_f}{H_0} < e^N \,. \tag{1.112}$$

Assuming inflation ends during the radiation–dominated era, the scale factor can be approximated as

$$a_f \sim \Omega_{r0}^{1/4} \sqrt{\frac{H_0}{H_f}} \,, \tag{1.113}$$

which leads to

$$e^N > \Omega_{r0}^{1/4} \left(\frac{\rho_f}{\rho_0}\right)^{1/4} = \frac{\rho_f^{1/4}}{0.037\, h\, \text{eV}} \,, \tag{1.114}$$

where ρ_f is the energy density at the end of inflation. To remain consistent with BBN, ρ_f must exceed $1\,\mathrm{MeV}^4$, which requires $N > 17$. At higher energy scales, such as the Planck scale, $N > 68$, while for Grand Unified Theory (GUT) scales, $N > 62$. Thus, inflation offers an elegant and natural solution to the flatness problem by dynamically driving Ω_k to negligibly small values, eliminating the necessity for extreme fine–tuning.

THE HORIZON PROBLEM The horizon problem is a core challenge in cosmology, stemming from the observed isotropy of the CMB radiation. Specifically, regions of the CMB sky that are causally disconnected—-owing to the finite speed of light and the Universe's finite age-—exhibit remarkably uniform temperatures. This level of isotropy is difficult to explain within the framework of the standard Big Bang model without introducing an additional mechanism.

To analyze the horizon problem quantitatively, we consider the proper particle–horizon distance, which represents the maximum distance a signal could have traveled in the Universe since its beginning. It is defined as

$$d_H = a(t) \int_0^t \frac{dt'}{a(t')} = a \int_0^a \frac{da'}{H(a')a'^2} \,. \tag{1.115}$$

In a Universe dominated by matter and radiation, this expression simplifies to:

$$d_H = \frac{2a}{H_0 \Omega_{m0}} \left(\sqrt{\Omega_{m0} a + \Omega_{r0}} - \sqrt{\Omega_{r0}} \right), \tag{1.116}$$

where H_0 is the Hubble parameter today, and Ω_{m0} and Ω_{r0} denote the present–day density parameters for matter and radiation, respectively. The angular diameter distance, which connects physical distances to their corresponding angular scales on the sky, is given by:

$$d_A = a(t) \int_t^{t_0} \frac{dt'}{a(t')} = a \int_a^1 \frac{da'}{H(a')a'^2} \,. \tag{1.117}$$

During the matter– and radiation–dominated eras, the angular diameter distance simplifies to

$$d_A = \frac{2a}{H_0 \Omega_{m0}} \left(\sqrt{\Omega_{m0} + \Omega_{r0}} - \sqrt{\Omega_{m0} a + \Omega_{r0}} \right) \,. \tag{1.118}$$

The ratio d_H/d_A quantifies the angular size of the particle horizon on the sky for a given scale factor

$$\frac{d_H}{d_A} = \frac{\sqrt{\Omega_{m0} a + \Omega_{r0}} - \sqrt{\Omega_{r0}}}{\sqrt{\Omega_{m0} + \Omega_{r0}} - \sqrt{\Omega_{m0} a + \Omega_{r0}}} \,. \tag{1.119}$$

As $a \to 0$, this ratio approaches zero, reflecting the extremely small size of the particle horizon in the early Universe. At the time of recombination, when $a_{\mathrm{rec}} \simeq 10^{-3}$, the ratio is approximately

$$\frac{d_H}{d_A}(a_{\mathrm{rec}} = 10^{-3}) \simeq 0.018 \,. \tag{1.120}$$

This corresponds to an angular scale of roughly 1° on the CMB sky. Consequently, the observable CMB sky at recombination is divided into approximately $4\pi/(0.018)^2 \sim 10^4$ regions that are causally disconnected.

This raises a pivotal question: if the early Universe contained causally disconnected regions, what mechanism could explain the observed isotropy of the CMB? The inflationary paradigm offers a natural resolution to this horizon problem. During an inflationary phase, the scale factor grows exponentially, and the particle–horizon distance during this period is given by

$$d_H \simeq \frac{a}{a_f H_f}\left(e^N - 1\right) , \tag{1.121}$$

where N is the number of e–folds of inflation, and H_f represents the approximately constant Hubble parameter during inflation. For small a, the angular diameter distance scales as $d_A \sim a/H_0$, resulting in

$$\frac{d_H}{d_A} \sim \frac{H_0}{a_f H_f} e^N . \tag{1.122}$$

To address the horizon problem, the condition $d_H > d_A$ must be satisfied, leading to

$$\frac{a_f H_f}{H_0} < e^N . \tag{1.123}$$

This requirement is identical to the condition needed to resolve the flatness problem. Thus, inflation provides a unified framework to address both the flatness and horizon problems, offering a coherent solution to these fundamental cosmological challenges.

UNWANTED RELICS After a Spontaneous Symmetry Breaking (SSB), such as one associated with a GUT, the formation of certain objects known as *topological defects* may occur. These defects are classified based on the nature of the symmetry breaking and their dimensionality: magnetic monopoles (0–dimensional), cosmic strings (1–dimensional), domain walls (2–dimensional), and textures (3–dimensional). Although it is very propedeutic for this discussion, it is worth mentioning that the type of relics that are affected by the phenomenology considered in this paragraph is not limited only to the cases of topological defects. From a more general point of view, this classification can also be extended to include, for instance, particles such as gravitinos (with spin 3/2 and $m \simeq 100\,\mathrm{GeV}$) and moduli (with spin 0 and $m \simeq 100\,\mathrm{GeV}$). Due to their weak interactions, these relics, produced during the primordial Universe, can persist until the present day, potentially leading to an overclosure of the Universe with $\Omega_X \gg 1$.

The phenomenon of SSB in the primordial Universe can be intuitively understood by examining the effects of finite temperature on particle propagation. Consider a theory built in the vacuum $\langle\varphi\rangle = 0$ with a potential of the form

$$V(\varphi) = \frac{\lambda}{4}(\varphi^2 - \sigma^2)^2 . \tag{1.124}$$

In this setup, the mass term is given by $m^2 \equiv V''(\langle\varphi\rangle) = -\lambda\sigma^2$, which corresponds to an imaginary mass. This indicates an exponentially growing solution, where φ evolves until it reaches the true vacuum state of the theory. However, if the field ϕ interacts with a thermal bath, these interactions dampen the exponential growth. This damping effect assigns the ϕ field a temperature–dependent "plasma mass", which, by dimensional reasoning, can be expressed as $m^2_{\text{plasma}} = \alpha\lambda T^2$, where α is a numerical constant of order unity. At finite temperatures, the effective mass of the scalar field around the classical solution $\langle\phi\rangle = 0$ becomes

$$m_T^2 = -\lambda\sigma^2 + m^2_{\text{plasma}} \,. \tag{1.125}$$

For temperatures where $m_T^2 < 0$, the point $\langle\phi\rangle = 0$ is unstable, signaling the onset of SSB. Conversely, for temperatures where $m_T^2 \geq 0$, the effective mass is real, and $\langle\phi\rangle = 0$ becomes a stable classical minimum of the potential. There exists a critical temperature $T_c \simeq \sigma/\alpha^{1/2}$ at which $m_T^2 = 0$. For temperatures above T_c, the vacuum $\langle\phi\rangle = 0$ becomes a stable minimum, and the symmetry is restored.

We can estimate this phenomenon by focusing on the specific example of domain walls, which arise from the SSB of the discrete symmetry $\mathbb{Z}_2$, representing parity. Following the phase transition, different regions of the Universe adopt one of the vacua $\langle\varphi\rangle = +\sigma$ or $\langle\varphi\rangle = -\sigma$. Since φ must vary smoothly between $+\sigma$ and $-\sigma$, there will be intermediate zones where the field resides in the false vacuum, resulting in the formation of imperfections known as domain walls. For simplicity, let us assume that $\langle\varphi\rangle = +\sigma$ in the upper half of $\mathbb{R}^3$ and $\langle\varphi\rangle = -\sigma$ in the lower half. In this configuration, domain walls are localized near the plane $z = 0$. With these boundary conditions, the equations of motion derived from the potential in eq. (1.124) admit the solution

$$\varphi(z) = \sigma \tanh\left(\frac{z}{\Delta}\right) \,, \tag{1.126}$$

where Δ represents the "thickness" of the domain wall. The thickness Δ is determined by balancing contributions from the surface energy, $\Delta(\partial_i\varphi)^2 \simeq \sigma^2/\Delta$, and the potential energy, $\Delta V(\varphi) \simeq \Delta\lambda\sigma^4$. On one hand, the gradient term is minimized by increasing the thickness of the domain wall; on the other hand, the volume term is minimized by reducing it. The equilibrium thickness that optimizes this balance is given by

$$\Delta^2 \simeq \lambda^{-1/2}\sigma^{-2} \,. \tag{1.127}$$

We now define ξ as the typical scale over which $\varphi \simeq$ const., corresponding to the characteristic distance where a single domain wall is expected to be found. The number density of these relics can be estimated as $n_X \simeq \xi^{-3}$. However, as noted earlier, φ is constant at most within the particle horizon, leading to the constraint $n_X > d_{\text{H}}^{-3}(t)$. Since most theories involving the

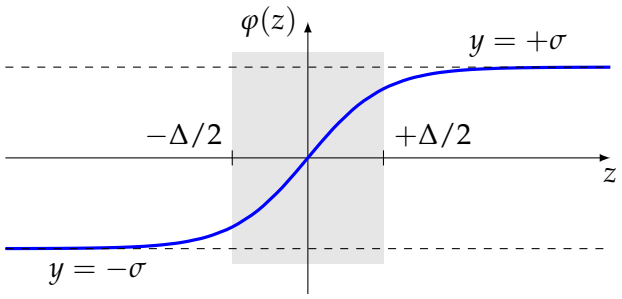

Figure 1.6: Domain wall solution, eq. (1.126).

production of these objects are formulated in the context of the primordial Universe, we can safely assume radiation domination. In this regime, the horizon can be approximated as

$$d_H(T) \simeq H^{-1}(T) \simeq 0.6\, g_*^{-1/2}(T) \frac{m_{\rm pl}}{T^2} \,, \tag{1.128}$$

where g_* represents the effective number of relativistic degrees of freedom, and $m_{\rm pl}$ is the Planck mass. Unless exotic scenarios are considered, topological defects are generally non–interacting. Their number density therefore evolves via free–streaming, similar to photons. For typical temperatures associated with GUT SSB transitions ($T_{\rm GUT} \simeq 10^{14} \div 10^{16}$ GeV), the present–day number density can be estimated as

$$\frac{n_X(T_0)}{n_\gamma(T_0)} = \frac{n_X(T_{\rm GUT})}{n_\gamma(T_{\rm GUT})} > \left[\frac{g_*^{1/2}(T_{\rm GUT})}{0.6} \frac{T_{\rm GUT}}{m_{\rm pl}}\right]^3 \simeq 10^{-9} \div 10^{-10} \simeq \eta_{\rm B} \,, \tag{1.129}$$

which is comparable to the present–day baryon–to–photon ratio $\eta_{\rm B}$. Finally, we estimate the density parameter of topological defects as

$$\Omega_{X0} = \frac{n_{X0} m_X}{\rho_{0,\rm crit}} > \frac{n_{X0} m_p}{\rho_{0,\rm crit}} \frac{m_X}{m_p} = \Omega_{b0} \left(\frac{m_X}{m_p}\right) \simeq 10^{14} \div 10^{15} \,, \tag{1.130}$$

where m_X and m_p denote the masses of the defects and protons, respectively, and $\rho_{0,\rm crit}$ is the critical density of the Universe. From observations, we know that $\Omega_{\rm tot} \simeq 1$, which poses a significant consistency issue for the Hot Big Bang model. Once again, the solution is provided by the inflationary paradigm. Topological defects, being produced at very early times, are subject to the effects of exponential expansion during inflation. Unlike standard particles, which are generated after inflation ends, the number density of these relics evolves as $n_X(t) \propto e^{-3Ht}$, diluting them to practically negligible densities.

1.4.2 Interlude: Conditions for Inflation

Previously, we examined inflation as a potential solution to several challenges inherent in the ΛCDM model. Before delving into the physical mechanisms that could generate such a phase in the early Universe, let us summarize the key conditions that define and uniquely characterize the inflationary epoch.

From the definition of the Hubble parameter, one can derive the following relation

$$\ddot{a} = a\left(H^2 + \dot{H}\right) , \tag{1.131}$$

which indicates that, for a constant Hubble parameter, inflation corresponds to a phase of accelerated expansion

$$\ddot{a} > 0 . \tag{1.132}$$

This relationship explains why inflation is often described as a period of accelerated expansion in the Universe. Furthermore, from eq. (1.8), it follows that inflation requires $w = P/\rho < -1/3$, meaning that it must be driven by the energy density of a component with negative pressure.

In a perfect inflationary phase, the spacetime evolves into a de Sitter space. However, for inflation to end and transition into the Hot Big Bang model, it cannot correspond to an exact de Sitter solution. Instead, during the rapid expansion phase, the de Sitter solution serves as an excellent approximation, which is why inflation is often described as a quasi–de Sitter period. Deviations from this regime can be characterized using effective parameters known as the *slow–roll parameters*. As an example, let us rewrite eq. (1.131) in the following form

$$\ddot{a} = aH^2(1-\varepsilon) , \qquad \text{where} \qquad \varepsilon \equiv -\frac{\dot{H}}{H^2} , \tag{1.133}$$

where ε, the first slow–roll parameter, quantifies how gradually the Hubble parameter is changing. Inflation occurs if and only if $\varepsilon < 1$.

For inflation to resolve the issues discussed in the preceding sections, it must persist for a sufficiently long period. This condition is quantified by the second slow–roll parameter

$$\eta \equiv \frac{d\ln\varepsilon}{dN} = \frac{\dot{\varepsilon}}{H\varepsilon} , \tag{1.134}$$

where N is the number of e–folds. When $|\eta| < 1$, the fractional change of ε per Hubble time is small, ensuring that inflation continues uninterrupted.

1.4.3 Single Field Slow–Roll Inflation

To illustrate inflation, we consider a simple toy model involving a scalar field called the *inflaton*, denoted by $\phi(t, \mathbf{x})$. This field can depend on both time t and spatial position $\mathbf{x}$. The potential energy density associated with the inflaton is described by a function $V(\phi)$ (see fig. 1.7). In addition to potential energy, the dynamic evolution of the inflaton field contributes to kinetic energy density. If the stress–energy tensor of the scalar field dominates the Universe's total energy content, it governs the evolution of the FRW background. The objective

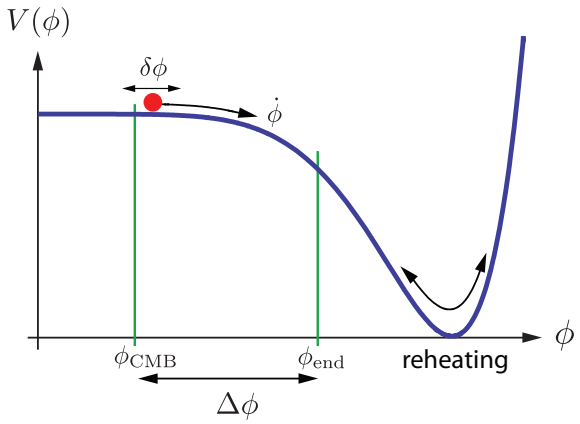

Figure 1.7: The Universe undergoes accelerated expansion when the potential energy of the inflaton field exceeds its kinetic energy (flat part). Inflation ends at $\phi_{\rm end}$, where the kinetic energy becomes comparable to the potential energy. Figure taken from Baumann (2011).

is to determine the conditions under which such a configuration results in accelerated expansion.

The dynamics of a scalar field minimally coupled to gravity is described by the action

$$S = S_{\rm EH} + S_\phi = \int d^4x\sqrt{-g}\left[\frac{M_{\rm Pl}^2}{2}R - \frac{1}{2}g^{\mu\nu}\partial_\mu\phi\partial_\nu\phi - V(\phi)\right] , \quad (1.135)$$

where $M_{\rm Pl} \equiv (8\pi G)^{-1/2}$ is the reduced Planck mass, $g = \det(g_{\mu\nu})$ represents the determinant of the metric tensor, and $V(\phi)$ is the potential of the scalar field. The first term corresponds to the Einstein–Hilbert action, while the second term describes the scalar field coupled to gravity through the metric $g_{\mu\nu}$.

Varying this action with respect to ϕ yields the Klein–Gordon equation, which, in an FRW universe, is given by

$$\ddot{\phi} + 3H\dot{\phi} - \frac{\nabla^2\phi}{a^2} + V'(\phi) = 0 , \quad (1.136)$$

where $V'(\phi) = \partial V/\partial\phi$. The stress–energy tensor for the scalar field can be derived as

$$T_{\mu\nu} \equiv -\frac{2}{\sqrt{-g}}\frac{\delta S}{\delta g^{\mu\nu}} = \partial_\mu\phi\partial_\nu\phi - g_{\mu\nu}\left(\frac{1}{2}g^{\alpha\beta}\partial_\alpha\phi\partial_\beta\phi + V(\phi)\right) . \quad (1.137)$$

The inflaton field can be expressed as

$$\phi(x,t) = \phi_0(t) + \delta\phi(x,t) , \quad (1.138)$$

where $\phi_0(t)$ denotes the "classical" field, representing the vacuum expectation value in a homogeneous and isotropic background, $\phi_0(t) = \langle\phi(x,t)\rangle$, and

$\delta\phi(x,t)$ represents the quantum fluctuations around this value. For now, we focus on the dynamics of the homogeneous classical field. Due to the symmetry of the FRW spacetime, the background inflaton depends only on time, $\phi = \phi(t)$. From the time–time component of the stress–energy tensor, $T^0_0 = \rho_\phi$, the energy density of the inflaton is

$$\rho_\phi = \frac{1}{2}\dot{\phi}^2 + V(\phi) \,. \tag{1.139}$$

Thus, the total energy density ρ_ϕ is the sum of the kinetic energy density, $1/2\,\dot{\phi}^2$, and the potential energy density, $V(\phi)$. Similarly, the space–space components, $T^i_j = -P_\phi \delta^i_j$, yield the pressure

$$P_\phi = \frac{1}{2}\dot{\phi}^2 - V(\phi) \,. \tag{1.140}$$

Inflation occurs if the condition $P_\phi < -1/3\,\rho_\phi$ is met, which requires the potential energy of the inflaton to dominate over its kinetic energy.

By substituting ρ_ϕ and P_ϕ into the second Friedmann equation, eq. (1.8), we obtain

$$\dot{H} = -\frac{\dot{\phi}^2}{2M_{\rm Pl}^2} \,. \tag{1.141}$$

Further substituting eq. (1.141) into the definition of the first slow–roll parameter, ε, gives

$$\varepsilon = \frac{\dot{\phi}^2}{2M_{\rm Pl}^2 H^2} \,. \tag{1.142}$$

Inflation thus occurs when the kinetic energy, $1/2\,\dot{\phi}^2$, contributes only a small fraction to the total energy density, $\rho_\phi = 3M_{\rm Pl}^2 H^2$, a regime referred to as *slow–roll inflation*. To sustain this regime, the acceleration of the inflaton field must also remain small. This can be quantified using the dimensionless parameter describing acceleration per Hubble time

$$\delta \equiv -\frac{\ddot{\phi}}{H\dot{\phi}} \,. \tag{1.143}$$

Taking the time derivative of eq. (1.133) and comparing it to the second slow–roll parameter, η, leads to

$$\eta = 2\left(\varepsilon - \frac{\ddot{\phi}}{H\dot{\phi}}\right) \,. \tag{1.144}$$

Thus, the conditions $\{\varepsilon, |\delta|\} \ll 1$ imply $\{\varepsilon, |\eta|\} \ll 1$, ensuring the slow–roll regime is maintained.

At this stage, no approximations have been introduced. It is simply observed that inflation begins and persists when $\{\varepsilon, |\delta|\} \ll 1$. Using these conditions, the equations of motion can be simplified under what is referred

to as the slow–roll approximation. The condition $\varepsilon \ll 1$ implies $\dot{\phi}^2 \ll V(\phi)$, allowing the Friedmann equation to be approximated as

$$H^2 \simeq \frac{V(\phi)}{3M_{\rm Pl}^2} \,. \tag{1.145}$$

In this regime, the Hubble expansion is dominated by the potential energy of the inflaton. Similarly, the condition $|\delta| \ll 1$ simplifies the Klein–Gordon equation to

$$3H\dot{\phi} \simeq -V'(\phi) \,. \tag{1.146}$$

These approximations establish a direct link between the gradient of the potential and the velocity of the inflaton field. By substituting eq. (1.145) and eq. (1.146) into the expression for ε, the first slow–roll parameter can be written in terms of the potential as

$$\varepsilon_V \equiv \frac{M_{\rm Pl}^2}{2}\left(\frac{V'(\phi)}{V(\phi)}\right)^2 \,. \tag{1.147}$$

Additionally, differentiating the simplified Klein–Gordon equation with respect to time leads to the second slow–roll parameter

$$|\eta_V| \equiv M_{\rm Pl}^2 \frac{|V''(\phi)|}{V(\phi)} \,. \tag{1.148}$$

To assess whether a given potential $V(\phi)$ supports slow–roll inflation, one evaluates the slow–roll parameters ε_V and $|\eta_V|$. Inflation is successful when these parameters satisfy the condition $\{\varepsilon_V, |\eta_V|\} \ll 1$.

The duration of inflation is characterized by the total number of "e–folds" of accelerated expansion, defined as

$$N_{\rm tot} \equiv \int_{a_I}^{a_E} d\ln a = \int_{t_I}^{t_E} H(t)\, dt \,, \tag{1.149}$$

where t_I and t_E denote the times at which $\varepsilon(t_I) = \varepsilon(t_E) \equiv 1$. Under the slow–roll approximation, the total number of e–folds can be expressed as an integral over the inflaton field:

$$N_{\rm tot} = \int_{\phi_I}^{\phi_E} \frac{1}{\sqrt{2\varepsilon_V}} \frac{|d\phi|}{M_{\rm Pl}} \,, \tag{1.150}$$

where ϕ_I and ϕ_E are the field values at the onset and conclusion of inflation, determined by the condition $\varepsilon_V < 1$.

The largest observable scales in the CMB correspond to approximately 60 e–folds before the end of inflation. This can be quantified as

$$N_{\rm CMB} = \int_{\phi_{\rm E}}^{\phi_{\rm CMB}} \frac{1}{\sqrt{2\varepsilon_V}} \frac{|d\phi|}{M_{\rm Pl}} \simeq 60 \,. \tag{1.151}$$

To successfully resolve the horizon problem, the total number of e–folds must satisfy $N_{\rm tot} > N_{\rm CMB}$.

Introducing an inflationary phase in the early Universe resolves several shortcomings of the standard cosmological model. However, it soon became evident that inflation provides much more than a solution to these issues. One of its most profound implications is the natural mechanism it offers for generating primordial density perturbations. These perturbations act as the seeds for the formation of LSS and appear as temperature and polarization anisotropies in the CMB. This process is driven by quantum fluctuations in the inflaton field, which are stretched to super–horizon scales due to the rapid expansion during inflation. Once these fluctuations cross the horizon, they become "frozen", as no causal processes can act on them. The fluctuations in the scalar field translate into energy density and curvature perturbations. As these perturbations re-enter the horizon during the radiation– or matter–dominated era, they evolve into matter density and temperature fluctuations, as described by the Poisson equation.

To leading order in the slow–roll parameters, the dimensionless power spectrum of scalar perturbations is expressed as

$$\Delta_\zeta(k) = A_s(k_*)\left(\frac{k}{k_*}\right)^{n_s-1}, \tag{1.152}$$

where

$$A_s(k_*) = \frac{H_*^2}{8\pi^2 M_{\rm Pl}^2 \varepsilon_*} \tag{1.153}$$

represents the amplitude of scalar fluctuations at the pivot scale k_*, and n_s is the scalar spectral index. The scalar spectral index is connected to the slow–roll parameters by the relation

$$n_s - 1 = 2\eta - 6\varepsilon\,. \tag{1.154}$$

Slow–roll inflation predicts a spectrum that is slightly red–tilted ($n_s < 1$), indicating a small deviation from exact scale invariance. This corresponds to a situation where the longest–wavelength modes, which exit the horizon earlier, exhibit slightly larger amplitudes compared to shorter–wavelength modes. This phenomenon arises because the Hubble parameter decreases gradually during inflation. By contrast, an exact de Sitter phase with a constant Hubble parameter would produce a perfectly scale–invariant *Harrison–Zel'dovich spectrum*.

Inflation predicts the existence of a stochastic background of Primordial Gravitational Waves (PGWs), which are transverse, traceless tensor perturbations of the metric. These gravitational waves are often described as the "smoking gun" of inflation because they are a universal prediction of inflationary models and are not typically anticipated in most alternative scenarios. Their detection would provide compelling evidence supporting the inflationary framework. The dimensionless power spectrum of tensor perturbations is given by

$$\Delta_T(k) = A_T(k_*)\left(\frac{k}{k_*}\right)^{n_T}, \tag{1.155}$$

where

$$A_T(k_*) = \frac{2H_*^2}{\pi^2 M_{\rm Pl}^2} \,, \tag{1.156}$$

and the tensor spectral index is

$$n_T = -2\varepsilon \,. \tag{1.157}$$

This implies that slow–roll inflationary models predict a nearly scale–invariant, red–tilted spectrum ($n_T < 0$) for PGWs, similar to the case of scalar perturbations. Importantly, the amplitude of tensor perturbations is directly tied to the Hubble parameter during inflation, which, in turn, reflects the energy scale of inflation. From eq. (1.156) and eq. (1.145), it follows that

$$A_T(k_*) \propto H_*^2 \propto V_* \,, \tag{1.158}$$

where V_* denotes the value of the inflationary potential when the pivot scale crosses the horizon.

The tensor–to–scalar ratio is defined as

$$r(k_*) \equiv \frac{A_T(k_*)}{A_s(k_*)} \,, \tag{1.159}$$

which quantifies the relative amplitude of tensor perturbations compared to scalar perturbations at the pivot scale k_*. This ratio is directly connected to the slow–roll parameter ε through the relation

$$r = 16\varepsilon \,. \tag{1.160}$$

This expression indicates that single–field slow–roll inflation predicts gravitational waves with amplitudes significantly smaller than those of scalar perturbations. When combined with the tensor spectral index, $n_T = -2\varepsilon$, it leads to the so–called *consistency relation*

$$r = -8n_T \,, \tag{1.161}$$

which establishes a direct link between the amplitude of tensor perturbations and their spectral tilt.

Observations of CMB anisotropies and Baryon Acoustic Oscillations (BAO) provide stringent constraints on inflationary models. The most recent Planck data release places the scalar spectral index at $n_s = 0.9649 \pm 0.0042$ (68% confidence level) [Akrami et al., 2020], excluding a scale–invariant (Harrison–Zel'dovich) spectrum while remaining consistent with slow–roll inflationary predictions. The strongest constraint on the tensor–to–scalar ratio comes from the combination of Planck data with BICEP/Keck 2018 and BAO, yielding $r_{0.05} < 0.036$ at 95% CL [Ade et al., 2021].

1.4.4 Reheating

During inflation, the energy density of the universe is predominantly stored in the inflaton potential, $V(\phi)$. Inflation concludes when the potential steepens, leading to a significant increase in the kinetic energy of the inflaton field. Following this, the energy within the inflaton sector must be transferred to Standard Model particles through a process known as *reheating*. This phase marks the transition to the Hot Big Bang era. Below, we outline the key features of the reheating process.

After inflation, the inflaton field ϕ begins oscillating around the minimum of its potential $V(\phi)$ (see fig. 1.7). Assuming that the potential is approximately quadratic near its minimum, where the amplitude of ϕ is small, the inflaton remains spatially homogeneous, $\phi = \phi(t)$. The equation governing its motion is given by

$$\ddot{\phi} + 3H\dot{\phi} = -m^2\phi \, . \tag{1.162}$$

As the universe continues to expand, the Hubble time scale eventually becomes much longer than the oscillation period, $H^{-1} \gg m^{-1}$. In this regime, the friction term becomes negligible, and the field oscillates with a frequency determined by m.

The energy continuity equation for the inflaton field is expressed as

$$\dot{\rho}_\phi + 3H\rho_\phi = -3H\left(m^2\phi^2 - \dot{\phi}^2\right) \, . \tag{1.163}$$

The term on the right–hand side averages to zero over a single oscillation period. Consequently, the oscillating inflaton field behaves like pressureless matter, with $\rho_\phi \propto a^{-3}$. This energy density decay corresponds to a gradual reduction in the oscillation amplitude.

To prevent the universe from becoming empty, the inflaton must interact with Standard Model fields, allowing the transfer of its energy into ordinary particles. If this decay process is slow—such as in the case of the inflaton decaying into fermions—the energy density of the inflaton evolves according to the equation

$$\dot{\rho}_\phi + 3H\rho_\phi = -\Gamma_\phi\rho_\phi \, , \tag{1.164}$$

where Γ_ϕ represents the inflaton decay rate. On the other hand, if the inflaton decays into bosons, the decay can occur rapidly through a mechanism known as parametric resonance, driven by Bose condensation effects. This fast decay process is referred to as preheating, as the bosons produced are not in thermal equilibrium.

The particles produced by the inflaton decay then interact with one another, leading to the generation of additional particles through various reactions. This "particle soup" eventually attains thermal equilibrium at a temperature T_{RH}. The process through which this gas of particles evolves into a thermal state can be intricate. In most cases, it is assumed that thermalization occurs

as the particles interact. However, some particles, such as gravitinos, may never achieve thermal equilibrium due to their extremely weak interactions. Nevertheless, as long as the particle momenta vastly exceed their masses, the energy density of the universe behaves like radiation, regardless of the specific momentum-space distribution. Once baryons, photons, and neutrinos reach thermal equilibrium, the standard Hot Big Bang era commences.

2 NEUTRINO PHYSICS

In this chapter we delve into the pivotal role of neutrinos in particle physics, highlighting their unique ability in pushing the request for physics BSM. In section 2.1, we trace the historical development of neutrino physics, from their theoretical prediction to their experimental discovery. Special attention is given to experimental anomalies, such as the solar neutrino problem and the atmospheric neutrino anomaly, which eventually culminated in the discovery of neutrino oscillations. In section 2.2, we explore the formalism of neutrino oscillations in both vacuum and matter. The mathematical framework presented here serves as a foundation for understanding the experimental data and their implications for neutrino masses and mixing parameters. section 2.3 transitions to the theoretical aspects of neutrinos within the Standard Model. It discusses the SM Lagrangian, the mechanisms of electroweak symmetry breaking, and the mass problem, emphasizing the need for extensions to the SM to accommodate the observed properties of neutrinos. Finally, in section 2.4, we address some prominent extensions of the neutrino sector of interest for the following discussion.

This chapter aims to provide a basilar understanding of neutrino physics within the context of particle physics, while also serving as a gateway to advanced discussions. For readers interested in more technical details and extended reviews, we recommend consulting works such as Giunti and Kim (2007), Lesgourgues et al. (2013), Mohapatra and Pal (1998), Roulet and Vissani (2022), and Valle and Romao (2015). Together with chapter 1, these chapter establish the groundwork for subsequent chapters, where the focus shifts to the role of neutrinos in the early Universe and their imprints on cosmological observables.

2.1 BRIEF NEUTRINO HISTORY

The history of weak interactions and the eventual discovery of the neutrino emerged from a series of experimental observations and theoretical puzzles in the early 20th century. The story begins with Becquerel's discovery of radioactivity in uranium in 1896. In the following years, Rutherford identified two distinct types of radiation: α and β rays, with γ rays being discovered subsequently. A crucial development occurred in 1914 when Chadwick made an unexpected observation: the β–spectrum exhibited a continuous energy distribution, in stark contrast to the discrete energy spectra of α and γ radiation. This finding, later confirmed by Ellis and Wooster in 1927, posed a fundamental challenge to the understanding of nuclear physics at the time.

Meitner's subsequent work ruled out the possibility that the missing energy could be attributed to neutral γ–rays, leading to a profound crisis in physics that prompted Bohr to even question whether energy conservation might hold only statistically in weak decays.

The situation was further complicated by the contemporary model of nuclear structure. In the 1920s, only three elementary particles were known: the electron (negatively charged), the proton (positively charged), and the photon (neutral). Within this framework, a nucleus with mass number A and atomic number Z was thought to consist of A protons and $A - Z$ electrons. This model faced three severe challenges that would eventually contribute to its downfall. First, the electron confinement paradox: if electrons were indeed present within the nucleus before β decay, the uncertainty principle would require their momentum (and hence kinetic energy) to be approximately 100 MeV, given the nuclear size of order femtometer. However, the observed maximum energies in β decays were consistently an order of magnitude smaller. Second, the β–decay spectrum puzzle: if the decay process followed the simple scheme

$$ {}^{A}_{Z}X \rightarrow {}^{A}_{Z+1}Y + e^{-} \, , \tag{2.1} $$

the electron energy should manifest as a discrete line at the mass difference $m(A, Z) - m(A, Z + 1)$. The observed continuous spectrum directly contradicted this prediction. Third, the nuclear spin statistics problem, demonstrated by Rasetti's experiments between 1928 and 1929 through measurements of Raman rotation spectra in homonuclear molecules. This revealed a particularly glaring contradiction in the case of ^{14}N. According to the proton–electron model, the nitrogen nucleus, comprising 14 protons and 7 electrons (totaling 21 fermions), should have exhibited half–integer spin. However, experimental measurements definitively showed that the ^{14}N nucleus possessed an integer spin of $I = 1$.

Pauli's Proposal of the Neutrino

The mounting experimental anomalies in nuclear physics called for a radical solution, which came from Wolfgang Pauli in a now-famous letter dated December 4, 1930. Addressed to the *Dear Radioactive Ladies and Gentlemen* attending a nuclear physics meeting in Tübingen, the letter proposed a *desperate remedy* to simultaneously resolve the β–decay spectrum and nuclear spin statistics puzzles. Pauli's revolutionary proposal postulated the existence of a new particle in atomic nuclei: an electrically neutral fermion with spin–1/2 that obeyed the exclusion principle. He initially called this particle a *neutron* specifying that its mass should be of the same order as the electron mass and, crucially, not exceeding 0.01 proton masses. This hypothetical particle was proposed to be emitted alongside the electron during β–decay, such that

Figure 2.1: Wolfgang Ernst Pauli (1900 – 1958).

$$ {}^{A}_{Z}X \rightarrow {}^{A}_{Z+1}Y + e^{-} + \text{`}n\text{'} \, , \tag{2.2} $$

where the quotation marks around 'n' distinguish Pauli's particle from what we now know as the neutron. This scheme elegantly explained the continuous

electron energy spectrum, as the total energy would be shared between the electron and the new particle. Under this paradigm, the troublesome case of ^{14}N could be resolved by a nuclear composition of $14p + 7e + 7'n'$, yielding the correct bosonic statistics. However, this model still faced one unresolved challenge: the electron confinement paradox was actually exacerbated, as it now applied to both the electron and Pauli's neutron.

A crucial experimental development occurred in 1932 when James Chadwick discovered what we now call the neutron – a neutral particle with mass comparable to the proton. While this particle could not be Pauli's lightweight neutral particle, it revolutionized our understanding of nuclear structure. The nitrogen nucleus could now be simply described as $^{14}\mathrm{N} = 7p + 7n$, naturally yielding the correct bosonic statistics without requiring the presence of electrons within the nucleus.

In light of Chadwick's discovery, Enrico Fermi introduced the term *neutrino* (little neutral one) to distinguish Pauli's particle from the newly discovered neutron. The first published reference to the neutrino appears in the Proceedings of the Solvay Conference of October 1933. During that same year, Fermi and Perrin independently reached a remarkable theoretical insight: the possibility that neutrinos might be massless particles. This hypothesis, though later proved incorrect, would significantly influence the development of weak interaction theory.

Fermi's theory of β–decay

Following Pauli's neutrino hypothesis, a revolutionary theoretical framework emerged through Enrico Fermi's seminal work in 1933–1934. In his paper "Tentativo di una teoria dell'emissione di raggi beta" (Attempt for a theory of beta rays emission), Fermi introduced a radically new perspective on β–decay. The genius of Fermi's approach lay in its departure from previous models: electrons and neutrinos were no longer considered pre–existing nuclear constituents but were instead created at the moment of decay. This paradigm shift immediately resolved the electron confinement paradox, as particles no longer needed to be confined within the nuclear volume before emission.

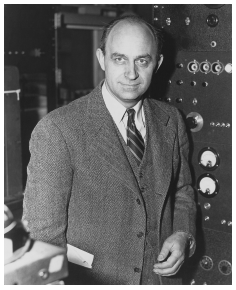

Figure 2.2: Enrico Fermi (1901 – 1955).

Drawing an analogy with Quantum ElectroDynamics (QED), Fermi proposed a fundamental interaction beyond gravity and electromagnetism. He assumed protons and neutrons to be two states of the same particle (following Heisenberg's proposal) and employed the mathematical formalism of second quantization developed by Dirac, Jordan, and Klein. The interaction Hamiltonian took the form of a contact interaction between vector currents

$$\mathcal{H}_F = G_\mathrm{F} \left[\bar{\psi}_p \gamma_\mu \psi_n\right] \left[\bar{\psi}_e \gamma^\mu \psi_\nu\right] + \mathrm{h.c.}\,, \tag{2.3}$$

where G_F is now known as the Fermi constant. From available data, Fermi estimated $G_\mathrm{F} \simeq 0.4 \times 10^{-63}\,\mathrm{Jm}^3$, remarkably close to the modern value of $1.4 \times 10^{-63}\,\mathrm{Jm}^3$ (known today with a relative uncertainty of 5.1×10^{-7}) [Navas et al., 2024].

In the same year, Bethe and Peierls published a crucial analysis in *Nature* comparing Pauli's original hypothesis (nuclei containing neutrinos) with

Fermi's model (neutrinos created at decay). They noted that Fermi's theory predicted the possibility of positive electron emission, consistent with the recent experiments by Curie and Joliot on artificial β^+–decay. More significantly, they introduced the concept of inverse β–decay

$$\nu + {}^{A}_{Z}\mathrm{N} \to e^{\mp} + {}^{A}_{Z\pm1}\mathrm{N}\,. \tag{2.4}$$

Their calculations yielded a startlingly small cross-section

$$\sigma \simeq 4\left(\frac{G_\mathrm{F}^2}{\pi}\right) p_e E_e \simeq 2.3\times10^{-44}\left(\frac{p_e E_e}{m_e^2}\right)\ \mathrm{cm}^2\,, \tag{2.5}$$

resulting in $\sigma < 10\times10^{-44}\,\mathrm{cm}^2$ at energies of a few MeV. For a typical neutrino energy of 2.5 MeV, this implied a mean free path in water of $\lambda \simeq 1\times10^{20}$ cm – eleven orders of magnitude larger than Earth's diameter and comparable to the Galaxy's thickness. This led them to their famous conclusion that it was "absolutely impossible to observe processes of this kind with the neutrinos created in nuclear transformations".

The theory evolved significantly in subsequent years. Gamow and Teller extended it in 1936 to include axial–vector currents, explaining the observed unit change in nuclear spin during some β–decays. The theoretical framework expanded to consider other possible couplings (scalar, pseudoscalar, and tensor), leading to what Konopinski's 1955 review described as a "state of extreme confusion" regarding the true nature of weak interactions.

A broader perspective on weak interactions emerged with the 1937 discovery of the muon by Street, Stevenson, Neddermeyer, and Anderson. This led to Pontecorvo's 1947 proposal of the universality of Fermi interactions for electrons and muons–a concept further developed by Puppi, Klein, Tiomno, Wheeler, Lee, Rosenbluth, and Yang. This universality would later evolve into the modern concept of particle *generations* or *families*.

The experimental discovery of the neutrino

The quest for direct neutrino detection gained momentum in the early 1950s, particularly driven by B. Pontecorvo's urging for experimental verification. However, this seemingly insurmountable challenge could be approached from a different perspective: with a sufficiently intense neutrino source, detection becomes feasible even with a relatively modest detector volume. Nuclear reactors, which became operational after the Second World War, provided exactly such intense sources. In a typical fission reaction of uranium, the neutron–rich fragments undergo beta decay, producing approximately six antineutrinos while liberating ~ 200 MeV of energy. The resulting isotropic antineutrino flux from a reactor can be expressed as

$$\frac{\mathrm{d}\Phi_\nu}{\mathrm{d}\Omega} \simeq \frac{2\times10^{20}}{4\pi}\frac{\mathrm{Power}}{\mathrm{GWatt}}\,\frac{\bar{\nu}}{\mathrm{s\,sr}}\,. \tag{2.6}$$

Several pioneering attempts to detect reactor neutrinos were made in the 1950s. A notable early effort was led by Ray Davis, who constructed a 4 t

detector using CCl_4 at the Brookhaven reactor, attempting to observe the reaction

$$\nu + {}^{37}\mathrm{Cl} \rightarrow {}^{37}\mathrm{Ar} + e^{-} \ . \tag{2.7}$$

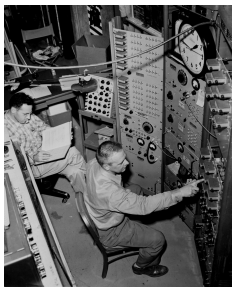

Figure 2.3: Frederick Reines (left) and Clyde Cowan, at the controls of the Savannah River experiment, 1956.

The experiment's negative results were later understood to be due to the fact that reactors produce antineutrinos rather than neutrinos, a distinction that was not fully appreciated at the time. This experimental approach, however, would later prove crucial in Davis's subsequent work on solar neutrinos.

The definitive detection of neutrinos was finally achieved in 1956 by Frederick Reines and Clyde Cowan at the Savannah River reactor. Their experimental design employed a detector consisting of Cd–doped water tanks sandwiched between liquid scintillator detectors viewed with photomultiplier tubes. The detection principle relied on observing the inverse beta decay process

$$\bar{\nu}_e + p \rightarrow n + e^{+} \ . \tag{2.8}$$

The experimental signature consisted of two distinct signals: a prompt signal from the positron annihilation producing two back–to–back 511 keV gamma rays, and a delayed signal from neutron capture on cadmium. This dual-signature technique provided powerful discrimination against backgrounds, a crucial aspect of the experiment. The successful detection was reported to Pauli via telegram on June 14, 1956, confirming a measured cross-section of approximately $6 \times 10^{-44}\,\mathrm{cm}^2$, in agreement with theoretical predictions.

This groundbreaking experiment marked the beginning of experimental neutrino physics and demonstrated the power of liquid scintillator technology, which would become a cornerstone of neutrino detection. Liquid scintillators offered the crucial advantages of scalability to large volumes and the capability for extreme purification from radioactive contaminants, while maintaining good transparency for photon detection via photomultipliers mounted on the detector walls. For his pivotal role in this discovery, Frederick Reines was awarded the Nobel Prize in Physics in 1995, four decades after the original experiment (Clyde Cowan had passed away in 1974).

2.1.1 The solar neutrino problem

In the early Universe, the only nuclei present in significant quantities were protons and helium. Consequently, stars such as the Sun, which formed billions of years ago, are predominantly composed of protons. Despite the immense gravitational forces acting on them, stars remain stable due to nuclear reactions occurring in their cores. These reactions produce radiation pressure that counterbalances the inward gravitational pull, maintaining a state of hydrostatic equilibrium. While this balance is essential to understanding stellar physics, its importance to neutrino studies lies in the byproducts of these nuclear processes. Neutrinos, produced in abundance in stellar cores, have an exceptionally long mean free path compared to the radius of a star.

Once created, they escape the stellar interior without significant interactions, carrying invaluable information about the inner workings of stars.

In the Sun, neutrinos are produced through specific nuclear reaction chains, referred to as the so–called *pp chain*. These reactions generate a characteristic energy spectrum, with most neutrinos having energies in the MeV range and a maximum kinematically allowed energy of approximately 18 MeV. The integrated solar neutrino flux reaching Earth is substantial, around $\phi_\nu \simeq 6.5 \times 10^{10}\,\mathrm{cm}^{-2}\,\mathrm{s}^{-1}$. However, despite this high flux, detecting neutrinos remains challenging due to their exceedingly small interaction cross section. Efforts to detect solar neutrinos began in the 1960s, using two primary techniques: absorption and scattering. These experiments uncovered a puzzling discrepancy between theoretical predictions and the observed neutrino fluxes, suggesting the presence of physics BSM.

ABSORPTION EXPERIMENTS The first significant effort to detect solar neutrinos was undertaken by Ray Davis in the 1960s. He designed an experiment to observe the reaction

$$\nu_e + {}^{37}\mathrm{Cl} \to e^- + {}^{37}\mathrm{Ar}\ . \tag{2.9}$$

This process has a relatively high energy threshold, making it sensitive to only a subset of solar neutrinos. Davis's experiment observed approximately one–third of the expected neutrino flux, marking the first evidence of the *solar neutrino deficit*.

In the 1990s, subsequent absorption experiments employed gallium as the target nucleus:

$$\nu_e + {}^{71}\mathrm{Ga} \to e^- + {}^{71}\mathrm{Ge}\ . \tag{2.10}$$

This reaction, with a lower energy threshold, allowed sensitivity to a broader portion of the solar neutrino spectrum. Two prominent experiments, GALLEX at Italy's Gran Sasso Laboratory and SAGE in Russia, utilized this approach. Despite the enhanced sensitivity, these experiments also detected a deficit, observing only about half of the theoretically predicted neutrino flux.

SCATTERING EXPERIMENTS A different class of experiments focused on neutrino scattering, exemplified by the Kamiokande experiment, which utilized a large, water–filled tank situated deep underground. This experiment aimed to detect neutrinos through their elastic scattering with electrons:

$$\nu_e + e^- \to \nu_e + e^-\ . \tag{2.11}$$

Recoil electrons from this interaction emit Cherenkov radiation, which can be observed using photomultiplier tubes. Although this method has a high energy threshold and is primarily sensitive to the high–energy tail of the solar neutrino spectrum, it offers unique advantages. The directional information of the scattered electrons confirms the solar origin of the neutrinos,

and the elastic scattering process is sensitive to neutral current interactions, enabling detection of ν_μ and ν_τ neutrinos, albeit with reduced sensitivity. The Kamiokande experiment, along with its larger successor, Super–Kamiokande, predominantly detected elastic scattering events involving electron neutrinos, where charged current interactions dominate. Both experiments confirmed the solar neutrino deficit, consistently observing only about half of the expected neutrino flux.

In summary, early experiments designed to detect solar neutrinos consistently uncovered a persistent and intriguing discrepancy between theoretical predictions and observational data. The magnitude of the deficit varied across experiments, influenced by their respective energy thresholds, but the recurring observation of fewer neutrinos than anticipated pointed to a profound issue. This puzzle became one of the earliest indications of new physics BSM.

2.1.2 The Atmospheric Neutrino Anomaly

In the 1980s, a new inconsistency in neutrino data emerged, this time involving atmospheric neutrinos. When highly energetic protons from cosmic rays collide with nuclei in the Earth's atmosphere, they initiate a cascade of hadrons. Among these, pions are produced in significant quantities through interactions such as

$$p + X \to \pi + \pi + \pi + \dots \,. \tag{2.12}$$

This process generates both neutral and charged pions. While neutral pions decay into photons, charged pions predominantly decay via weak interactions. Almost all charged pions decay into muons and muon neutrinos, with an extremely small branching ratio ($\sim 10^{-4}$) for decay channels involving electrons or positrons

$$\pi^\pm \to \mu^\pm + \nu_\mu \,. \tag{2.13}$$

Subsequently, the muons decay into electrons or positrons, accompanied by the emission of two neutrinos

$$\mu^\pm \to e^\pm + \nu_\mu + \nu_e \,. \tag{2.14}$$

The type of neutrino or antineutrino produced depends on the charge of the initial particle, ensuring conservation of lepton number. The timescales for these decay processes are well established

$$\tau_{\pi^\pm} = 2.6 \times 10^{-8}\,\mathrm{s}\,, \quad \tau_{\mu^\pm} = 2.2 \times 10^{-6}\,\mathrm{s}\,. \tag{2.15}$$

Predicting the atmospheric neutrino flux is more challenging than for solar neutrinos due to the less precise knowledge of both the atmospheric composition and the flux of incoming cosmic protons. However, these uncertainties

largely cancel out when focusing on the ratio of muon neutrinos to electron neutrinos

$$R_\nu = \frac{N(\nu_\mu + \bar{\nu}_\mu)}{N(\nu_e + \bar{\nu}_e)} \,. \tag{2.16}$$

Based on the decay chains described above, a naive expectation would be $R_\nu = 2$ under idealized conditions. However, this simplistic picture is complicated by the finite thickness of the atmosphere and relativistic effects. The lifetimes of pions and muons are extended due to Lorentz dilation, increasing their decay lengths, $L = \beta\gamma\tau$. For highly energetic pions and muons, the elongated decay lengths mean that some particles may not decay fully before reaching the detector. At lower energies, R_ν approaches the expected value of 2, but at higher energies, the reduced number of muon decays leads to $R_\nu > 2$. Theoretical models incorporate these effects to provide more accurate predictions for R_ν as a function of neutrino energy. Observations, however, revealed a significant discrepancy. Experimental measurements consistently found

$$R_\nu^{\text{observed}} \simeq 0.5\, R_\nu^{\text{expected}} \,. \tag{2.17}$$

This result implied either an unexpectedly large flux of electron neutrinos or a significantly reduced flux of muon neutrinos. The latter explanation ultimately provided groundbreaking insights into the phenomenon of neutrino oscillations.

2.1.3 Solution to the Neutrino Puzzle

By the 1990s, two significant anomalies in neutrino data were firmly established. First, experiments measuring solar neutrinos consistently observed only about half of the predicted flux reaching Earth. Second, the ratio of atmospheric muon neutrinos to electron neutrinos was found to be significantly lower than expected. These discrepancies puzzled physicists, leading to the proposal of various theories to explain them. While many of these ideas were speculative or implausible, one explanation ultimately emerged as correct: neutrinos undergo flavor transformations as they propagate, a phenomenon known as neutrino oscillation. This discovery implied that neutrinos possess non–zero masses, as will be discussed in the next section.

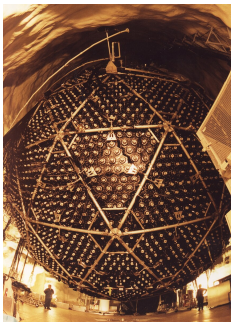

Figure 2.4: Outside view of the Sudbury Neutrino Observatory detector.

The solar neutrino deficit was resolved by the Sudbury Neutrino Observatory (SNO), which employed heavy water, D_2O, as a detection medium. The experiment observed three distinct neutrino interaction processes. The first was a Charged–Current (CC) reaction, where electron neutrinos interacted with deuterium nuclei to produce two protons and an electron. This process was sensitive exclusively to ν_e and allowed a direct measurement of their flux

$$\nu_e + {}^2\mathrm{H} \to \mathrm{p} + \mathrm{p} + e^- \,. \tag{2.18}$$

The second process involved elastic scattering, where neutrinos interacted with electrons. This reaction was primarily sensitive to ν_e, but it also included contributions from ν_μ and ν_τ through Neutral–Current (NC) interactions

$$\nu_i + e^- \rightarrow \nu_i + e^- \ . \tag{2.19}$$

The third and most critical process was the NC interaction, in which neutrinos of any flavor interacted with deuterium nuclei, producing a neutron and a proton. This process was equally sensitive to all neutrino flavors, enabling the measurement of the total neutrino flux irrespective of flavor

$$\nu_i + {}^2\mathrm{H} \rightarrow \nu_i + \mathrm{p} + \mathrm{n} \ . \tag{2.20}$$

The ability to measure NC interactions was SNO's key innovation. Earlier experiments focused on CC and elastic scattering reactions, which measured only the flux of ν_e. SNO demonstrated that although the flux of solar ν_e was indeed lower than predicted, the total flux, including ν_μ and ν_τ, was consistent with theoretical expectations based on solar models. This provided compelling evidence that electron neutrinos produced in the Sun were transforming into other flavors as they traveled to Earth.

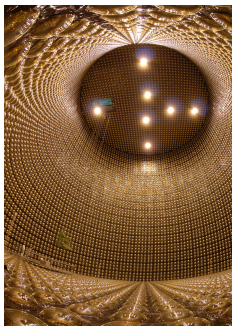

Figure 2.5: Inside view of the Super-Kamiokande detector with nearly full PMTs.

The atmospheric neutrino anomaly was resolved by the Super–Kamiokande experiment, which confirmed that the observed deficit in ν_μ flux was caused by neutrino oscillations. Observations revealed that the flux of ν_e was consistent with theoretical predictions, while the flux of ν_μ was significantly reduced. This depletion was particularly evident for upward–going neutrinos, which traveled a longer path through the Earth before detection. The observed reduction in ν_μ flux was consistent with the oscillation $\nu_\mu \rightarrow \nu_\tau$. Upward–going neutrinos had more time to oscillate during their extended journey.

The resulting ν_τ neutrinos could not be detected directly, as the CC interaction required,

$$\nu_\tau + X \rightarrow \tau + Y \ , \tag{2.21}$$

has a kinematic threshold that atmospheric neutrinos cannot surpass. Together, the results from SNO and Super–Kamiokande provided definitive evidence for neutrino oscillations, resolving the long–standing solar and atmospheric neutrino anomalies.

2.2 NEUTRINO OSCILLATIONS

2.2.1 Neutrino Oscillations in Vacuum

In the standard framework of neutrino oscillations [Bilenky and Pontecorvo, 1976a; b; 1978; Eliezer and Swift, 1976; Fritzsch and Minkowski, 1976], a

neutrino of flavor α with momentum $\mathbf{p}$, produced via a CC weak interaction either in association with a charged lepton ℓ_α^- or a charged antilepton ℓ_α^+, is described by a flavor eigenstate. By definition, this state is not a physical particle but rather a superposition of the physical states ν_i with distinct masses m_i

$$|\nu_\alpha\rangle = \sum_i U_{\alpha i}^* |\nu_i\rangle \qquad (\alpha = e, \mu, \tau) \,, \tag{2.22}$$

where U represents the unitary matrix that governs the mixing of neutrino states. To simplify the analysis of the propagation of this state, it is assumed that the components of the beam share the same 3–momentum $\mathbf{p}$. However, due to differences in their masses, the energies of these components differ. For each component ν_i, the energy is determined by the relativistic energy–momentum relation

$$E_i = \sqrt{p^2c^2 + m_i^2c^4} \,, \tag{2.23}$$

where E_i is the energy of the component, m_i its mass, and c the speed of light.

The neutrino mass states $|\nu_i\rangle$ are eigenstates of the Hamiltonian

$$\mathcal{H} |\nu_i\rangle = E_i |\nu_i\rangle \,. \tag{2.24}$$

These mass states propagate in time according to the Schrödinger equation

$$i\frac{\mathrm{d}}{\mathrm{d}t} |\nu_i(t)\rangle = \mathcal{H} |\nu_i(t)\rangle \,, \tag{2.25}$$

which implies that after a time t, the evolution of the initial state given in eq. (2.22) is

$$|\nu_\alpha(t)\rangle = \sum_i e^{-iE_it} U_{\alpha i}^* |\nu_i\rangle \,. \tag{2.26}$$

It is important to note that this treatment assumes neutrinos are stable particles. If neutrinos are unstable, the description of vacuum oscillations changes significantly. A detailed discussion of this scenario lies beyond the scope of this work but can be found in Sec. 5.4 of Mohapatra and Pal (1998). Since the energies E_i differ for states with unequal masses, eq. (2.26) represents a superposition of physical eigenstates ν_i that differs from the initial state in eq. (2.22). As a result, the state exhibits characteristics not only of ν_α but also of other flavor states.

Precisely because flavor states are not eigenstates of the Hamiltonian during propagation, the evolution of a neutrino produced as $|\nu_\alpha\rangle$ can also be expressed in terms of a different flavor state $|\nu_\beta\rangle$:

$$|\nu_\alpha(t)\rangle = \sum_i e^{-iE_it} U_{\alpha i}^* U_{\beta i} |\nu_\beta\rangle \,. \tag{2.27}$$

From this, the transition amplitude of finding a ν_β in an initially ν_α beam can be computed as

$$\mathcal{A}_{\nu_\alpha \to \nu_\beta}(t) \equiv \langle \nu_\beta | \nu_\alpha(t) \rangle = \sum_i e^{-iE_it} U_{\alpha i}^* U_{\beta i} \,, \tag{2.28}$$

using the orthonormality of the mass eigenstates, $\langle \nu_j | \nu_i \rangle = \delta_{ji}$. At $t = 0$, as expected, the amplitude simplifies to $\delta_{\alpha\beta}$, which follows from the unitarity of the matrix U. At any time t, the probability of observing a ν_β in a beam originally composed of ν_α is given by

$$\begin{aligned} P_{\nu_\alpha \nu_\beta}(t) &= \left| \mathcal{A}_{\nu_\alpha \to \nu_\beta}(t) \right|^2 \\ &= \sum_{i,j} \left| U^*_{\alpha i} U_{\beta i} U_{\alpha j} U^*_{\beta j} \right| \cos\left[(E_i - E_j)t - \varphi_{\alpha\beta ij} \right] , \end{aligned} \tag{2.29}$$

where

$$\varphi_{\alpha\beta ij} = \arg\left(U^*_{\alpha i} U_{\beta i} U_{\alpha j} U^*_{\beta j} \right) . \tag{2.30}$$

In practical scenarios, neutrinos are highly relativistic, allowing us to approximate the mass–shell relation as

$$E_i \simeq |\mathbf{p}| + \frac{m_i^2}{2|\mathbf{p}|} , \tag{2.31}$$

and replace the time t with the distance x traveled by the neutrino beam. The transition probability then becomes

$$P_{\nu_\alpha \to \nu_\beta}(x) = \sum_{i,j} \left| U^*_{\alpha i} U_{\beta i} U_{\alpha j} U^*_{\beta j} \right| \cos\left(\frac{2\pi x}{L_{ij}} - \varphi_{\alpha\beta ij} \right) , \tag{2.32}$$

where, for brevity, we write $|\mathbf{p}| = E$, and define

$$L_{ij} \equiv \frac{4\pi E}{\Delta m^2_{ij}} , \tag{2.33}$$

with

$$\Delta m^2_{ij} \equiv m_i^2 - m_j^2 . \tag{2.34}$$

The quantities L_{ij} are known as *oscillation lengths*, which characterize the distance over which oscillation effects become significant. In eq. (2.32), it is evident that if the distance x is an integral multiple of all L_{ij}, the transition probability reduces to $P_{\nu_\alpha \nu_\beta} = \delta_{\alpha\beta}$, corresponding to the original beam. However, for distances where this condition is not met, nontrivial oscillation effects arise, which are precisely the phenomena explored in experiments.

A PROPEDEUTICAL CASE: TWO–FLAVOURS APPROXIMATION In the two–flavor approximation, we consider only two neutrino mass eigenstates, denoted $|\nu_1\rangle$ and $|\nu_2\rangle$, and their corresponding flavor eigenstates, $|\nu_e\rangle$ and $|\nu_\mu\rangle$. The Pontecorvo–Maki–Nakagawa–Sakata (PMNS) mixing matrix in this scenario is a 2×2 unitary matrix, which can be expressed as a rotation matrix

$$U = \begin{pmatrix} \cos\theta & \sin\theta \\ -\sin\theta & \cos\theta \end{pmatrix} , \tag{2.35}$$

where θ is the mixing angle. In this case, the matrix contains only real terms, as it lacks any complex phase. Consequently, there is no source of CP violation in two–flavor neutrino oscillations, since CP violation requires the presence of a complex phase that cannot be removed by rephasing the states.

The oscillation probability for a transition from ν_e to ν_μ is given by

$$P_{\nu_e \to \nu_\mu}(L, E) = \sin^2(2\theta) \sin^2\left(\frac{\Delta m^2 L}{4E}\right) , \tag{2.36}$$

while $P_{\nu_e \to \nu_e}(L, E)$ is simply $1 - P_{\nu_e \to \nu_\mu}(L, E)$ in this two-flavour case. Here, $\Delta m^2 = m_2^2 - m_1^2$ represents the mass–squared difference, E is the neutrino energy, and L is the distance traveled. Probabilities describing transitions between different flavors ($\alpha \neq \beta$) are commonly referred to as *conversion probabilities*, while probabilities for remaining in the same flavor ($\alpha = \beta$) are termed *survival probabilities*.

Finally, for two generations of Majorana neutrinos, the most general form of the mixing matrix is

$$U = \begin{pmatrix} \cos\theta & \sin\theta\, e^{-i\rho} \\ -\sin\theta\, e^{i\rho} & \cos\theta \end{pmatrix} . \tag{2.37}$$

It can be shown that the phase ρ does not affect oscillation probabilities. As a result, the probabilities remain identical to those given by eq. (2.36).

In the real world, there are three neutrinos, making the two–generation approximation strictly valid only in specific limiting cases, such as when one neutrino does not mix with the other two. For the general case where all three neutrinos mix, starting from eq. (2.32) and separating the $i = j$ terms from the rest, the oscillation probability can be expressed as

$$\begin{aligned} P_{\nu_\alpha \to \nu_\beta}(x) = \sum_i |U_{\alpha i}|^2 |U_{\beta i}|^2 + 2 \sum_{i>j} \mathrm{Re}\left[U_{\alpha i}^* U_{\beta i} U_{\alpha j} U_{\beta j}^*\right] \cos\left(\frac{\Delta m_{ij}^2 x}{2E}\right) \\ + 2 \sum_{i>j} \mathrm{Im}\left[U_{\alpha i}^* U_{\beta i} U_{\alpha j} U_{\beta j}^*\right] \sin\left(\frac{\Delta m_{ij}^2 x}{2E}\right) . \end{aligned} \tag{2.38}$$

Using the relationship

$$\sum_i |U_{\alpha i}|^2 |U_{\beta i}|^2 = \delta_{\alpha\beta} - 2 \sum_{i>j} \mathrm{Re}\left[U_{\alpha i}^* U_{\beta i} U_{\alpha j} U_{\beta j}^*\right] , \tag{2.39}$$

the oscillation probability simplifies to the well–known expression

$$\begin{aligned} P_{\nu_\alpha \to \nu_\beta}(x) = \delta_{\alpha\beta} - 4 \sum_{i>j} \mathrm{Re}\left[U_{\alpha i}^* U_{\beta i} U_{\alpha j} U_{\beta j}^*\right] \sin^2\left(\frac{\Delta m_{ij}^2 x}{2E}\right) \\ + 2 \sum_{i>j} \mathrm{Im}\left[U_{\alpha i}^* U_{\beta i} U_{\alpha j} U_{\beta j}^*\right] \sin\left(\frac{\Delta m_{ij}^2 x}{2E}\right) . \end{aligned} \tag{2.40}$$

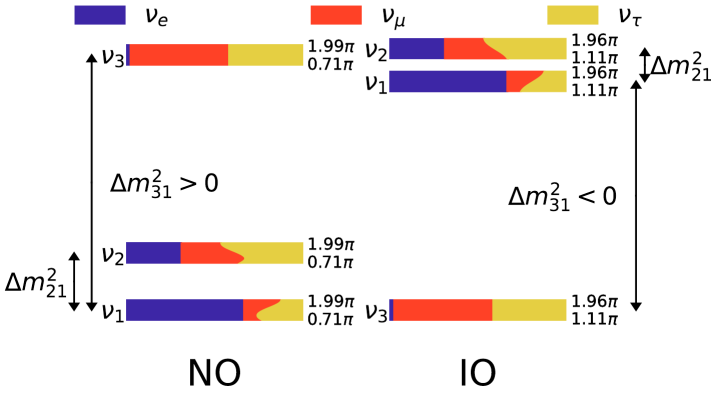

Figure 2.6: The two possible orderings of neutrino mass eigenstates, normal and inverted (denoted as NO and IO, respectively), are illustrated. The flavor composition of the three mass eigenstates is presented, highlighting the dependence on δ_{CP}. Figure taken from Salas et al. (2021).

For Dirac neutrinos, the lepton mixing matrix U can be parameterized using $n(n-1)/2$ angles and $(n-1)(n-2)/2$ phases, with n being the number of neutrino flavors. In the case of Majorana neutrinos, an additional $n-1$ phases are required.

In the context of three active neutrino mixing, the phenomenon of oscillation is characterized by three mixing angles and a single CP–violating phase, δ_{CP}. This parametrization applies regardless of whether neutrinos are Dirac or Majorana particles [Rodejohann and Valle, 2011]. Additionally, the oscillation framework depends on two mass–squared differences, Δm^2_{21} and Δm^2_{31}. By convention, Δm^2_{21} is always taken as positive, while the sign of Δm^2_{31} must be determined experimentally. Currently, the uncertainty in the sign of Δm^2_{31} leads to two possible configurations for the neutrino mass spectrum. If $\Delta m^2_{31} > 0$, the mass ordering is referred to as *Normal Ordering (NO)*, indicating that the lightest neutrino state contributes most significantly to the electron neutrino flavor eigenstate. Conversely, if $\Delta m^2_{31} < 0$, the mass ordering is known as *Inverted Ordering (IO)*. These two possible mass hierarchies, along with the flavor composition of the mass eigenstates, are depicted in fig. 2.6. This visualization summarizes our current understanding of oscillation parameters and the associated uncertainties.

2.2.2 Neutrino Oscillations in Matter

Wolfenstein [Wolfenstein, 1978] was the first to observe that neutrino oscillation patterns can be significantly modified when neutrinos propagate through a material medium rather than a vacuum. The underlying reason is straightforward: ordinary matter contains electrons but lacks muons and tau leptons. As a result, an electron neutrino, ν_e, traveling through matter interacts with electrons via both CC and NC interactions, whereas muon and

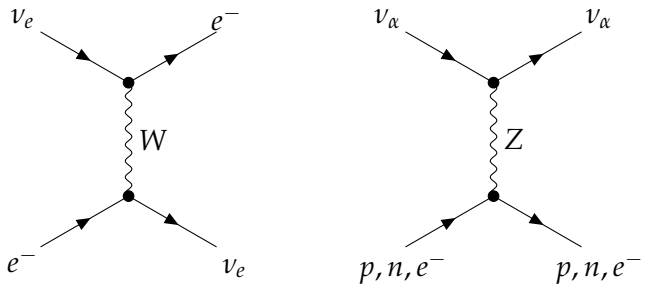

Figure 2.7: Standard Model diagrams for neutrino interactions with matter fields. The left panel shows CC interactions, and the right panel shows NC interactions, both of which contribute to the effective potentials in eqs. (2.43) and (2.46).

tau neutrinos, ν_μ and ν_τ, experience only NC interactions. This disparity in interaction types causes ν_e to exhibit a distinct interaction strength compared to ν_μ and ν_τ.

These interactions modify the effective mass of a neutrino propagating through a medium. Since ν_e interacts differently from other neutrino flavors, its effective mass is uniquely affected. This distinction can have profound consequences when neutrinos are mixed in a vacuum. In such scenarios, a physical eigenstate comprises components of ν_e, ν_μ, ν_τ, and potentially other states. As this eigenstate propagates through a medium, the modulation of its ν_e component differs from its behavior in vacuum, leading to changes in oscillation probabilities compared to their vacuum values.

In the following, we compute this effect for CC interactions between an electron neutrino and a homogeneous, isotropic medium of unpolarized electrons. The four–fermion weak Hamiltonian for a $\nu_e - e^-$ CC interaction is given by

$$\mathcal{H}_{\text{eff}}^{\text{CC}} = \frac{G_\text{F}}{\sqrt{2}} \left[\bar{e}\gamma^\mu(1-\gamma^5)\nu_e\right] \left[\bar{\nu}_e\gamma_\mu(1-\gamma^5)e\right] \ . \tag{2.41}$$

To determine the effective potential experienced by a neutrino propagating through an isotropic and unpolarized medium of non–relativistic electrons with number density n_e and statistical distribution function $f(E_e)$, we average the Hamiltonian in eq. (2.41) over the background, obtaining

$$\overline{\mathcal{H}_{\text{eff}}^{\text{CC}}} = \sqrt{2} G_\text{F} n_e (\bar{\nu}_{eL}\gamma_0\nu_{eL}) \ , \tag{2.42}$$

where L denotes the left-chiral components of the fields. It is then straightforward to associate an effective potential with this Hamiltonian, given by

$$V_{\text{CC}} = \sqrt{2} G_\text{F} n_e \ . \tag{2.43}$$

The same method can be applied to the weak NC interaction term. The four–fermion weak Hamiltonian corresponding to the right diagram in fig. 2.7 is

$$\mathcal{H}_{\text{eff}}^{\text{NC}} = \frac{G_\text{F}}{\sqrt{2}} \sum_{\alpha=e,\mu,\tau} \left[\bar{\nu}_\alpha\gamma^\mu(1-\gamma_5)\nu_\alpha\right] \sum_f \left[\bar{f}\gamma_\mu\left(g_V^f - g_A^f\gamma_5\right)f\right] \ , \tag{2.44}$$

where f represents any fermion species. In this context, the effective potential experienced by a neutrino of flavor α in a background of unpolarized fermions f is

$$V_{\mathrm{NC}}^{f} = \sqrt{2} G_{\mathrm{F}} n_f g_V^f \,, \tag{2.45}$$

where n_f is the number density of fermions f. In typical astrophysical environments, such as the Sun, the only relevant fermions are electrons, protons, and neutrons. The total neutral current effective potential, assuming background neutrality, can be written as

$$V_{\mathrm{NC}} = \sum_{f=p,n,e} V_{\mathrm{NC}}^{f} = -\frac{1}{2} G_{\mathrm{F}} n_n \,. \tag{2.46}$$

For antineutrinos, the sign of the potentials changes.

To address the problem of matter oscillations, note that by recalling the form of the mixing matrix U, eq. (2.25) for the evolution of mass eigenstates can be rewritten as

$$i \frac{\mathrm{d}}{\mathrm{d}t} |\nu_\alpha(t)\rangle = \mathcal{H}_{\mathrm{F}} |\nu_\alpha(t)\rangle \,, \tag{2.47}$$

where $\mathcal{H}_{\mathrm{F}} \equiv U \mathcal{H} U^\dagger$ is the Hamiltonian in the flavor basis. In our case, the total Hamiltonian can be divided into a vacuum term,

$$\mathcal{H}_0 \equiv U \mathrm{diag}(E_1, \ldots, E_{n_{\mathrm{F}}}) U^\dagger \,, \tag{2.48}$$

where E_i is given by eq. (2.23), and an interaction term

$$\mathcal{H}_I |\nu_\alpha\rangle = \sqrt{2} G_{\mathrm{F}} \left(n_e \delta_{\alpha e} - \frac{n_n}{2} \right) |\nu_\alpha\rangle \equiv V_\alpha |\nu_\alpha\rangle \,. \tag{2.49}$$

Following the same reasoning as for vacuum oscillations, we can derive the evolution of the transition amplitude from eq. (2.47), resulting in

$$i \frac{\mathrm{d}}{\mathrm{d}t} \mathcal{A}_{\nu_\alpha \to \nu_\beta}(t) = \sum_\lambda \left(\sum_k U_{\beta k} \frac{\Delta m_{k1}^2}{2E} U_{\lambda k}^* + \delta_{\lambda e} \delta_{\beta e} V_{\mathrm{CC}} \right) \mathcal{A}_{\nu_\alpha \to \nu_\lambda}(t) \,, \tag{2.50}$$

which shows that neutrino oscillations in matter, like those in vacuum, depend on the differences of squared neutrino masses and not on their absolute values.

Finally, eq. (2.50) can be equivalently expressed in matrix form as

$$i \frac{\mathrm{d}}{\mathrm{d}x} \Psi_\alpha = \mathbb{H}_{\mathrm{F}} \Psi_\alpha \,, \tag{2.51}$$

where for ultra–relativistic neutrinos $t = x$. Here, the Hamiltonian is written as $\mathbb{H} = \frac{1}{2E} \left(U \mathbb{M}^2 U^\dagger + \mathbb{A} \right)$. In the case of three–neutrino mixing, we have

$$\Psi_\alpha = \begin{pmatrix} \mathcal{A}_{\nu_\alpha \to \nu_e} \\ \mathcal{A}_{\nu_\alpha \to \nu_\mu} \\ \mathcal{A}_{\nu_\alpha \to \nu_\tau} \end{pmatrix} \,, \quad \mathbb{M}^2 = \begin{pmatrix} 0 & 0 & 0 \\ 0 & \Delta m_{21}^2 & 0 \\ 0 & 0 & \Delta m_{31}^2 \end{pmatrix} \,, \quad \mathbb{A} = \begin{pmatrix} A_{\mathrm{CC}} & 0 & 0 \\ 0 & 0 & 0 \\ 0 & 0 & 0 \end{pmatrix} \,,$$

(2.52)

where $A_{CC} \equiv 2EV_{CC}$.

Here we conclude the observation initiated in the previous section. From the evolution equation eq. (2.50), it can be demonstrated that the Majorana phases in the mixing matrix have no impact on neutrino oscillations, both in vacuum [Bilenky et al., 1980; Doi et al., 1981] and in matter [Langacker et al., 1987]. This is because the diagonal matrix of Majorana phases on the right side of the mixing matrix cancels out in the product $U\mathbb{M}^2U^\dagger$. Consequently, neutrino oscillations cannot distinguish between the Dirac or Majorana nature of neutrinos.

THE MIKHEEV–SMIRNOV–WOLFENSTEIN EFFECT To illustrate the main features of matter effects, it is useful to consider the simpler case of two–flavor oscillations, analogous to the vacuum oscillation case. Let us examine a two–component model involving ν_e and ν_μ, with corresponding mass eigenstates ν_1 and ν_2. This scenario is similar to the ν_e–ν_τ case, as ν_μ and ν_τ experience the same matter potential. The Hamiltonian in the flavor basis reduces to

$$\mathbb{H}_{\rm F} = \frac{1}{4E}\begin{pmatrix} -\Delta m^2\cos 2\theta + A_{CC} & \Delta m^2 \sin 2\theta \\ \Delta m^2 \sin 2\theta & \Delta m^2 \cos 2\theta - A_{CC} \end{pmatrix} , \tag{2.53}$$

where $\Delta m^2 \equiv m_2^2 - m_1^2$, and θ is the mixing angle defined in eq. (2.35). As a general property, this matrix can be diagonalized by an orthogonal transformation, $U_M \in O(2)$, such that

$$U_M^T \mathbb{H}_{\rm F} U_M = \mathbb{H}_{\rm M} , \tag{2.54}$$

resulting in

$$\mathbb{H}_{\rm M} = \frac{1}{4E}{\rm diag}\left(-\Delta m_M^2, \Delta m_M^2\right) , \tag{2.55}$$

where the effective squared–mass difference is

$$\Delta m_M^2 \equiv \sqrt{(\Delta m^2\cos 2\theta - A_{CC})^2 + (\Delta m^2 \sin 2\theta)^2} . \tag{2.56}$$

The unitary matrix diagonalizing the Hamiltonian can be interpreted as an effective mixing matrix, with the mixing angle given by

$$\tan 2\theta_M \equiv \tan 2\theta \left(1 - \frac{A_{CC}}{\Delta m^2 \cos 2\theta}\right)^{-1} . \tag{2.57}$$

The remarkable phenomenon, first described by Mikheev and Smirnov in 1985 [Mikheev and Smirnov, 1986; Mikheyev and Smirnov, 1985] and explained clearly in Bethe (1986), is characterized by the occurrence of a resonance when the term A_{CC} satisfies

$$A_{CC} = \Delta m^2 \cos 2\theta , \tag{2.58}$$

which corresponds to an electron number density of

$$n_e^{\text{res}} = \frac{\Delta m^2 \cos 2\theta}{2\sqrt{2} E G_{\text{F}}} \,. \tag{2.59}$$

At this resonance, the effective mixing angle reaches $\pi/4$, indicating maximal mixing. This results in the potential for complete flavor transitions between the two neutrino flavors, provided the resonance region is sufficiently broad. This phenomenon is known as the *Micheev–Smirnov–Wolfenstein (MSW) effect*.

2.3 NEUTRINOS IN THE STANDARD MODEL

The fundamental interactions in modern particle physics find their theoretical foundation in gauge symmetry, which has become an essential principle in their description. The comprehensive framework known as the SM of particle physics is based on a relativistic quantum field theory governed by the gauge group

$$\mathcal{G}_{\text{SM}} = \text{SU}(3)_C \times \text{SU}(2)_L \times \text{U}(1)_Y \,. \tag{2.60}$$

In this notation, the subscripts represent physical properties: C denotes *colour*, L indicates *left–handed chirality*, and Y corresponds to *weak hypercharge*. This theoretical framework, developed through the seminal contributions of multiple physicists [Fritzsch et al., 1973; Glashow, 1961; Gross and Wilczek, 1973; Politzer, 1973; Salam, 1968; Weinberg, 1967], has demonstrated remarkable predictive power.

In examining the symmetry structure of the SM, distinct behaviors emerge in different sectors. The strong interaction, governed by $\text{SU}(3)_C$ symmetry, remains exact across all energy scales. In contrast, the electroweak sector exhibits more intricate behavior, undergoing spontaneous symmetry breaking via the Higgs mechanism. This breaking transforms the initial $\text{SU}(2)_L \times \text{U}(1)_Y$ symmetry into $\text{U}(1)_Q$, where Q represents the electromagnetic charge. For our analysis of neutrino physics, after a brief general discussion, we focus on the electroweak sector, as leptons, including neutrinos, do not participate in strong interactions due to their lack of colour charge.

The principle of gauge invariance imposes strict constraints on the theoretical framework, definitively determining both the interaction forms and the gauge boson content. However, significant freedom remains in assigning fermions and the Higgs scalar boson to Irreducible Representations (IRs) of the gauge group. The primary theoretical constraint arises from the requirement to cancel chiral anomalies, a condition essential for preserving gauge symmetry at the quantum level. The fermionic content of the SM consists of spin–1/2 particles, organized into three distinct generations of *quarks* and *leptons* (see Fig. 2.8). The electroweak properties of each generation are characterized by specific IRs of the gauge group, along with their associated charges.

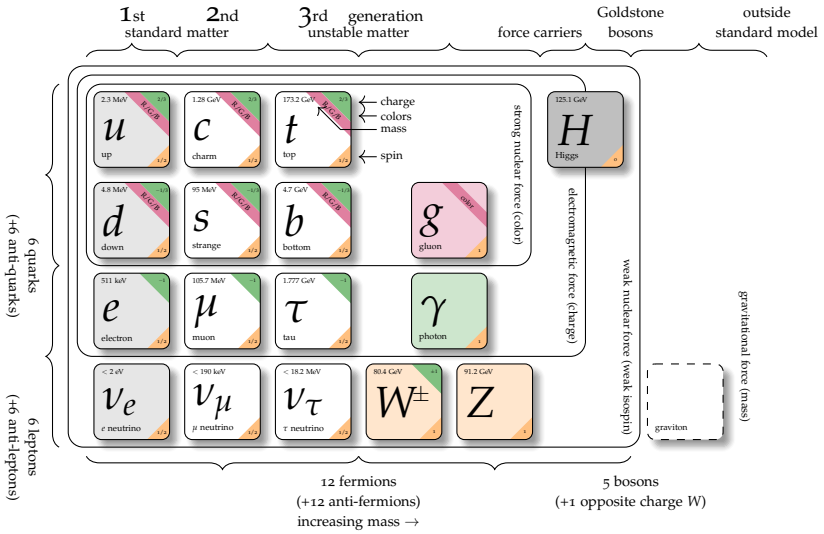

Figure 2.8: Particle content of the SM. Figure adapted from `https://texample.net/tikz/examples/model-physics/`.

Within this framework, the quantum numbers label different representations. For the electroweak sector, the key quantities include the weak isospin, denoted by I, which takes the value $1/2$ for particles in $\mathrm{SU}(2)_L$ doublets and vanishes for singlets. Its third component, I_3, relates to the electric charge Q through the Gell-Mann–Nishijima formula

$$Q = I_3 + \frac{Y}{2} \,. \tag{2.61}$$

2.3.1 The Standard Model Lagrangian

The complex structure outlined in the previous paragraph can be schematically encoded in the Lagrangian

$$\mathcal{L}_{\mathrm{SM}} = \mathcal{L}_{\mathrm{YM}} + \mathcal{L}_{\mathrm{fermions}} + \mathcal{L}_{\mathrm{Higgs}} + \mathcal{L}_{\mathrm{Yukawa}} \,, \tag{2.62}$$

where each term corresponds to a fundamental sector of the theory: the gauge field dynamics, fermion fields, the Higgs field, and the Yukawa couplings. We now examine each term in detail.

The Yang–Mills Lagrangian, $\mathcal{L}_{\mathrm{YM}}$, describes the kinetic and interaction terms of the gauge bosons associated with the Standard Model gauge symmetry,

$$\mathcal{L}_{\mathrm{YM}} = -\frac{1}{4} G^A_{\mu\nu} G^{A\,\mu\nu} - \frac{1}{4} W^I_{\mu\nu} W^{I\,\mu\nu} - \frac{1}{4} B_{\mu\nu} B^{\mu\nu} \,. \tag{2.63}$$

Here, $G^A_{\mu\nu}$, $W^I_{\mu\nu}$, and $B_{\mu\nu}$ represent the field strength tensors for the $SU(3)_C$, $SU(2)_L$, and $U(1)_Y$ gauge groups, respectively. The indices $A = 1, \ldots, 8$ and $I = 1, 2, 3$ label the generators of $SU(3)_C$ and $SU(2)_L$ in their adjoint

representations. Each field strength tensor is defined by the gauge–covariant structure

$$G^A_{\mu\nu} = \partial_\mu G^A_\nu - \partial_\nu G^A_\mu + g_s f^{ABC} G^B_\mu G^C_\nu \,, \tag{2.64}$$

$$W^I_{\mu\nu} = \partial_\mu W^I_\nu - \partial_\nu W^I_\mu + g\, \epsilon^{IJK} W^J_\mu W^K_\nu \,, \tag{2.65}$$

$$B_{\mu\nu} = \partial_\mu B_\nu - \partial_\nu B_\mu \,. \tag{2.66}$$

These gauge field strengths encapsulate both the gauge boson kinetic terms and their self–interactions, with f^{ABC} and ϵ^{IJK} denoting the structure constants of $SU(3)_C$ and $SU(2)_L$, respectively.

To ensure gauge invariance of the fermionic and Higgs sectors in the presence of gauge interactions, we construct a covariant derivative defined as

$$D_\mu = \partial_\mu - i g_s \frac{\lambda^A}{2} G^A_\mu - i g \frac{\sigma^I}{2} W^I_\mu - i g' Y B_\mu \,, \tag{2.67}$$

where the Gell–Mann matrices, λ^A, act on color indices, the Pauli matrices, σ^I, act on weak isospin indices, and Y represents the hypercharge assignment for each field. The couplings g_s, g, and g' correspond to the strengths of the $SU(3)_C$, $SU(2)_L$, and $U(1)_Y$ interactions, respectively.

The fermionic Lagrangian introduces the kinetic terms for the matter fields, organized by generation

$$\mathcal{L}_{\text{fermions}} = \sum_{i=1}^{3} \left(\overline{Q}^i_L i \not{D} Q^i_L + \bar{u}^i_R i \not{D} u^i_R + \bar{d}^i_R i \not{D} d^i_R + \bar{L}^i_L i \not{D} L^i_L + \bar{e}^i_R i \not{D} e^i_R \right) \,. \tag{2.68}$$

Each fermion family includes left–handed quark doublets Q_L, right–handed up–type quarks u_R, right–handed down–type quarks d_R, left–handed lepton doublets L_L, and right–handed charged leptons e_R. Each term is gauge–invariant under $\mathcal{G}_{\text{SM}}$, owing to the covariant derivative structure and the specific hypercharge assignments.

The Higgs sector introduces a scalar field responsible for electroweak symmetry breaking. The Higgs Lagrangian is given by

$$\mathcal{L}_{\text{Higgs}} = \left| D_\mu H \right|^2 - V(H) \,, \tag{2.69}$$

where H is the Higgs doublet field with hypercharge $Y = 1/2$. The Higgs potential is chosen to undergo spontaneous symmetry breaking and is defined by

$$V(H) = -\mu^2 H^\dagger H + \lambda (H^\dagger H)^2 \,. \tag{2.70}$$

The parameter $\mu^2 > 0$ induces a non–zero vacuum expectation value (vev) for the Higgs field, breaking $SU(2)_L \times U(1)_Y$ down to $U(1)_Q$ and thereby giving masses to the gauge bosons and fermions through the Higgs mechanism.

Finally, the Yukawa interactions couple the fermions to the Higgs doublet, generating fermion masses after electroweak symmetry breaking. The Yukawa Lagrangian is written as

$$\mathcal{L}_{\text{Yukawa}} = -\sum_{i=1}^{3} \left(\lambda_{u^{(i)}} \overline{Q}_L^i \tilde{H} u_R^i + \lambda_{d^{(i)}} \overline{Q}_L^i H d_R^i + \lambda_{e^{(i)}} \overline{L}_L^i H e_R^i \right) + \text{h.c.} \,, \quad (2.71)$$

where the Yukawa couplings $\lambda_{u^{(i)}}$, $\lambda_{d^{(i)}}$, and $\lambda_{e^{(i)}}$ are assumed to be diagonal for simplicity, neglecting flavor–changing effects. To ensure gauge invariance, we define the conjugate Higgs doublet

$$\tilde{H} = \epsilon H^* \,, \quad (2.72)$$

where ϵ is the antisymmetric tensor, ensuring that $\tilde{H}$ transforms like H under $SU(2)_L$ but with opposite hypercharge. The Yukawa terms thus combine doublets in a gauge–invariant way.

2.3.2 Electroweak Symmetry Breaking

In the SM, mass terms for both fermions and gauge bosons are prohibited by gauge invariance. For fermions, a direct mass term would require coupling left– and right–handed components, which would explicitly break $SU(2)_L$ and $U(1)_Y$ gauge invariance, as left– and right–handed fields transform differently under these symmetries. Similarly, a mass term for any gauge boson would not remain invariant under gauge transformations, thereby violating gauge symmetry.

The solution lies in the concept of spontaneous symmetry breaking. While the full electroweak gauge symmetry, $SU(2)_L \times U(1)_Y$, is respected by the Lagrangian, it is not preserved in the vacuum state of the theory. To analyze this in a quantitative framework, we turn to the Higgs potential in eq. (2.70). The behavior of the potential depends critically on the sign of μ^2. If $\mu^2 < 0$, the configuration of lowest energy corresponds to a vanishing Higgs field, preserving the symmetry. However, if $\mu^2 > 0$, the minimum energy configuration instead favors a non–zero vev of the Higgs field, which is the case in our Universe. Fermion and gauge boson masses arise once we expand around the ElectroWeak Simmetry Breaking (EWSB) vacuum state, parameterized as

$$\langle H \rangle = \frac{1}{\sqrt{2}} \begin{pmatrix} 0 \\ v_H \end{pmatrix}, \quad \text{where} \quad v_H = \sqrt{\frac{\mu^2}{\lambda}} \simeq 246 \text{ GeV} \,. \quad (2.73)$$

It is important to align the vev with the neutral component of the Higgs field to ensure that the resulting vacuum state is electrically neutral. This alignment preserves the gauge invariance of electromagnetism, leaving the photon massless, as confirmed experimentally. This vev explicitly breaks $SU(2)_L \times U(1)_Y$ down to $U(1)_Q$.

GAUGE BOSON MASSES Mass terms for the electroweak gauge bosons originate from the kinetic term of the Higgs field. The covariant derivatives of the Higgs field are explicitly written as

$$D_\mu H = \partial_\mu H - igW_\mu^I \frac{\sigma^I}{2} H - i\frac{g'}{2} B_\mu H \,. \tag{2.74}$$

After substituting the Higgs vev from eq. (2.73) and expanding all terms, we obtain

$$D_\mu \langle H \rangle = -\frac{i}{\sqrt{2}} \frac{v_H}{2} \begin{pmatrix} g\left(W_\mu^1 - iW_\mu^2\right) \\ -gW_\mu^3 + g' B_\mu \end{pmatrix} \,. \tag{2.75}$$

Squaring this expression yields the gauge boson mass terms

$$\mathcal{L}_{\text{mass}}^{\text{(gauge bosons)}} = \frac{v_H^2}{8} \left[g^2 \left| W_\mu^1 - iW_\mu^2 \right|^2 + \left| -gW_\mu^3 + g' B_\mu \right|^2 \right] , \tag{2.76}$$

from which it is evident that there are two separate contributions corresponding to charged and neutral bosons. In both cases, the resulting mass matrix is not diagonal, requiring field redefinitions to determine the physical basis and corresponding masses.

For the charged bosons, the transformation straightforwardly follows from eq. (2.76). Specifically, by defining

$$W_\mu^\pm \equiv \frac{W_\mu^1 \pm W_\mu^2}{\sqrt{2}} \,, \tag{2.77}$$

the first term in eq. (2.76) becomes the mass term of a complex vector field with mass

$$M_W = \frac{1}{2} g v_H \simeq 80.4\,\text{GeV} \,. \tag{2.78}$$

These particles are referred to as charged bosons because they interact with matter via electromagnetic interactions. A more explicit demonstration of this would involve expanding the interactions encoded in the SM Lagrangian around the Higgs vev, but this analysis is beyond the scope of this section.

The case of neutral gauge bosons is similar; however, it is not immediately clear how to define the physical fields, and we need to diagonalize the mass matrix. It is straightforward to show that the second element of eq. (2.76) can be written in matrix form as

$$\left| D_\mu H \right| \Big|_{\text{neutral}} = \frac{1}{2} \begin{pmatrix} W_\mu^3 & B_\mu \end{pmatrix} \begin{pmatrix} \frac{g^2 v^2}{4} & -\frac{g g' v^2}{4} \\ -\frac{g g' v^2}{4} & \frac{g'^2 v^2}{4} \end{pmatrix} \begin{pmatrix} W_\mu^3 \\ B_\mu \end{pmatrix} \,, \tag{2.79}$$

and the mass matrix for the neutral bosons W^3 and B is therefore

$$\mathcal{M}_{\text{neutral}}^2 = \frac{v_H^2}{4} \begin{pmatrix} g^2 & -gg' \\ -gg' & g'^2 \end{pmatrix} \,. \tag{2.80}$$

This matrix is symmetric and can be diagonalized by an orthogonal transformation, specifically a rotation by the Weinberg angle

$$\tan\theta_W \equiv \frac{g}{g'} \,. \tag{2.81}$$

This transformation allows us to identify the mass eigenstates of the neutral bosons as

$$Z_\mu = \cos\theta_W W^3_\mu - \sin\theta_W B_\mu \,, \tag{2.82}$$
$$A_\mu = \sin\theta_W W^3_\mu + \cos\theta_W B_\mu \,. \tag{2.83}$$

These states represent the Z boson, with a mass

$$M_Z = \frac{v_H}{2}\sqrt{g^2 + g'^2} \simeq 91.2\,\text{GeV} \,, \tag{2.84}$$

and the photon, which remains massless, respectively.

FERMION MASSES Similarly, fermion masses arise from the Yukawa sector of the SM Lagrangian. Substituting the Higgs vev from eq. (2.73) into eq. (2.71), we find

$$\mathcal{L}_{\text{Yukawa}} = -\frac{1}{\sqrt{2}}\sum_{i=1}^{3}\left(\lambda_{u^{(i)}} v_H \bar{u}^i_L u^i_R + \lambda_{d^{(i)}} v_H \bar{d}^i_L d^i_R + \lambda_{e^{(i)}} v_H \bar{e}^i_L e^i_R\right) + \text{h.c.} \,. \tag{2.85}$$

This equation clearly contains mass terms, from which the mass of the fermions is

$$m_f \equiv \frac{\lambda_f v_H}{\sqrt{2}} \,. \tag{2.86}$$

In a generic fermion basis, the Yukawa matrices, and thus the fermion mass matrices, are not diagonal. They can be diagonalized by performing a bi-unitary rotation on the fields, meaning left– and right–handed fermions are rotated separately using unitary matrices. For charged leptons, this process is

$$e_{L_i} \to V^{(e_L)}_{ij}\, e_{L_j} \,, \tag{2.87}$$
$$e_{R_i} \to V^{(e_R)}_{ij}\, e_{R_j} \,, \tag{2.88}$$

for left– and right–handed leptons, respectively. In the new basis, the mass matrix becomes diagonal, yielding the mass eigenvalues

$$V^{(e_L)} m^{(e)} V^{(e_R)} = \hat{m}^{(e)} = \{m_e, m_\mu, m_\tau\} \,. \tag{2.89}$$

The experimentally measured mass eigenvalues for charged leptons are approximately

$$\{m_e, m_\mu, m_\tau\} \simeq \{0.511\,\text{MeV}, 105.66\,\text{MeV}, 1.777\,\text{GeV}\} \,. \tag{2.90}$$

The case of charged leptons is particularly simple. In the SM, neutrinos are massless. This means that the diagonalization of charged lepton fields does not leave any observable effect, as it is always possible to absorb it into a redefinition of the neutrino fields. The issue typically arises in CC interactions, but in the massless neutrino case, we always have the freedom to choose

$$V_{ij}^{(\nu_L)} = V_{ij}^{(e_L)} \ , \tag{2.91}$$

without changing any physical observable (since we lack a neutrino mass term). This ensures that the CC interactions remain invariant

$$\begin{aligned} \mathcal{L}_{\text{CC}}^{\text{leptons}} &= -\frac{g}{\sqrt{2}} \bar{\nu}_L^i \gamma^\mu \left(V^{(\nu_L)\dagger} V^{(e_L)} \right)_{ij} e_L^j W_\mu^\dagger + \text{h.c.} \\ &\overset{(2.91)}{=} -\frac{g}{\sqrt{2}} \bar{\nu}_L^i \gamma^\mu e_L^j W_\mu^\dagger + \text{h.c.} \ . \end{aligned} \tag{2.92}$$

The case of quarks is different. Both up– and down–type quarks have mass terms and thus require the diagonalization of their mass matrices. Following the same procedure as in the charged lepton case, it is straightforward to show that diagonal mass matrices can be obtained through biunitary transformations

$$V^{(u_L)\dagger} \, m^{(u)} \, V^{(u_R)} = \hat{m}^{(u)} = \{m_u, m_c, m_t\} \ , \tag{2.93}$$

$$V^{(d_L)\dagger} \, m^{(d)} \, V^{(d_R)} = \hat{m}^{(d)} = \{m_d, m_s, m_b\} \ . \tag{2.94}$$

The measured quark masses are

$$\{m_u, m_c, m_t\} \simeq \{2.3\,\text{MeV}, 1.3\,\text{GeV}, 173\,\text{GeV}\} \ , \tag{2.95}$$

$$\{m_d, m_s, m_b\} \simeq \{4.8\,\text{MeV}, 95\,\text{MeV}, 4.2\,\text{GeV}\} \ . \tag{2.96}$$

However, the situation in CC interactions is different. These interactions are flavor–diagonal but involve couplings between up–type and down–type fields within the same generation. As shown by the transformations above, the up–type and down–type fields are rotated differently. The net effect is the generation of off–diagonal couplings with the charged ElectroWeak (EW) boson, described by the Cabibbo–Kobayashi–Maskawa (CKM) matrix

$$\mathcal{L}_{\text{CC}}^{\text{quarks}} = -\frac{g}{\sqrt{2}} \bar{u}_L^i \gamma^\mu \underbrace{\left(V^{(u_L)\dagger} V^{(d_L)} \right)_{ij}}_{\equiv (V_{\text{CKM}})_{ij}} d_L^j W_\mu^\dagger + \text{h.c.} \ , \tag{2.97}$$

which is a unitary matrix.

2.3.3 The Mass Problem in the Standard Model

As we have seen in the previous section, the simplest way to give masses to neutrinos is to mimic the mechanism used for other fermions after the

spontaneous symmetry breaking in the Yukawa sector of the Lagrangian. Mass terms generated by this mechanism are referred to as *Dirac mass terms* from now on. In particular, for a generic fermion ψ, it is possible to express it as a four–component object composed of two two–component objects, known as Weyl spinors

$$\psi = \begin{pmatrix} \chi_L \\ \chi_R \end{pmatrix} . \tag{2.98}$$

Here, χ_L and χ_R can be defined using chiral projectors as

$$\psi_L \equiv P_L \psi = \psi \begin{pmatrix} \chi_L \\ 0 \end{pmatrix} , \quad \psi_R \equiv P_R \psi = \psi \begin{pmatrix} 0 \\ \chi_R \end{pmatrix} . \tag{2.99}$$

The Dirac mass term for this fermion can then be written as

$$\mathcal{L}_{\text{mass}}^{(\text{Dirac})} = -m\left(\chi_L^\dagger \chi_R + \chi_R^\dagger \chi_L\right) . \tag{2.100}$$

The issue with the original formulation of the SM is now evident. Any hypothetical Right–Handed (RH) neutrinos would be SU(2) singlets with zero hypercharge. This implies they would have no electric charge, no color charge, and would not interact via the weak force. In other words, they would be completely non–interacting, or *sterile*, within the SM framework. Since RH neutrinos do not participate in any of the SM's interactions, they are not required by the gauge structure of the theory. Historically, RH neutrinos were also unnecessary to explain known particle interactions and experimental observations. Consequently, the SM was constructed without them, focusing solely on particles that interact through the known fundamental forces.

We might be tempted to explain neutrino masses by simply introducing RH neutrinos. However, for a Dirac mass to account for the tiny observed neutrino masses, the Yukawa coupling λ_ν would need to be extremely small, significantly smaller than the Yukawa couplings of other fermions. This is theoretically unsatisfactory.

A possible alternative is to construct a mass term using only Left–Handed (LH) Weyl spinors. This is feasible through the introduction of the so–called Majorana spinor

$$\psi_M \equiv \begin{pmatrix} \chi_L \\ i\sigma^2 (\chi_L^\dagger)^T \end{pmatrix} . \tag{2.101}$$

The key insight here is that, given any LH Weyl spinor, we can construct a RH Weyl spinor via charge conjugation, and vice versa. The resulting object resembles a proper Dirac field, with four components divided into left and right helicity components. However, a crucial distinction is that the two components are not independent, resulting in half the degrees of freedom compared to a Dirac spinor.

It is possible to construct a mass term for Majorana fields as

$$\mathcal{L}_{\text{mass}}^{(\text{Majorana})} = -\frac{1}{2} m \bar{\psi}_M \psi_M = -\frac{1}{2} m \left[\chi_L^T (-i\sigma^2) \chi_L + \chi_L^\dagger (i\sigma^2) \chi_L^{\dagger T} \right] , \quad (2.102)$$

where in the second equality the chiral components are explicitly displayed.

Despite the elegance of this construction, Majorana mass terms cannot explain neutrino masses within the SM. While this approach would be the most economical-—avoiding the introduction of additional degrees of freedom by relying solely on the left–handed neutrinos already present in the SM–it violates electroweak symmetry. Specifically, it breaks hypercharge invariance, as it is not invariant under phase rotations and it spoils weak isospin symmetry, since these rotations mix neutrinos with charged leptons. Consequently, we must extend the SM and introduce new degrees of freedom to accommodate neutrino masses.

2.4 BEYOND THE STANDARD MODEL: NEUTRINO SECTOR EXTENSIONS

Majorana mass terms behave as isospin triplets, rather than singlets, as required by SM gauge invariance. Consequently, Majorana neutrino masses are absent in the SM due to the particle content and the requirement of renormalizability. However, if the SM is interpreted as an Effective Field Theory (EFT) valid at the electroweak scale, new higher–dimensional effective operators beyond the renormalizable interactions included in $\mathcal{L}_{\text{SM}}$ should be considered, suppressed by high-energy scales. The lowest–order effective operator leading to neutrino masses and compatible with SM symmetries is the so–called Weinberg operator [Weinberg, 1979]

$$\mathcal{L}_5 = \frac{g}{\mathcal{M}} \bar{L}_L^c \tilde{H} \tilde{H}^\dagger L_L + \text{h.c.} , \quad (2.103)$$

where g is a dimensionless coupling coefficient, and $\mathcal{M}$ is a mass scale. As a result of electroweak symmetry breaking (see section 2.3.2), $\mathcal{L}_5$ generates the Majorana mass term for ν_L

$$\mathcal{L}_{\text{mass}}^M = \frac{1}{2} \frac{g v^2}{\mathcal{M}} \bar{\nu}_L^c \nu_L + \text{h.c.} , \quad (2.104)$$

which, by comparison with eq. (2.102), corresponds to the Majorana mass $m = g v^2 / \mathcal{M}$.

It can be shown that this dimension–five operator is unique in the sense that one must go beyond dimension five to find other lepton number–violating effective operators. This observation by Weinberg suggests that lepton number conservation appears to be accidental, as non–renormalizable operators like the one in eq. (2.102) violate it. In fact, the Weinberg operator provides an effective description for most high-energy models. The specific mechanism generating this dimension–five operator may vary significantly, and, as we will demonstrate below, several realizations are possible.

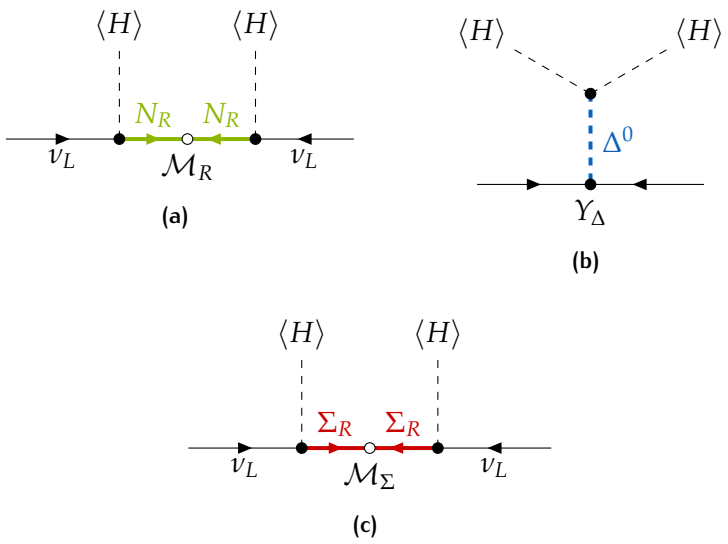

Figure 2.9: Feynman diagrams of the processes responsible for neutrino mass generation in seesaw mechanisms of type I (a), type II (b) and type III (c).

2.4.1 The seesaw mechanism

To introduce the concept of Dirac and Majorana neutrinos further, we now examine the well–known *seesaw mechanism* [Minkowski, 1977; Mohapatra and Senjanovic, 1980; Schechter and Valle, 1980]. This mechanism is widely regarded as the most natural explanation for the remarkably small masses of neutrinos compared to charged fermions. There are three primary variants of the seesaw mechanism, all of which rely on the exchange of a heavy particle. However, these models differ in the specific properties and interactions of the particles involved.

TYPE I: $SU(3)_C \times SU(2)_L \times U(1)_Y$ SINGLET FERMIONS In the electroweak SM, the only active neutrino components are $\nu_{\alpha L}$, which are, indeed, the only neutrinos we can directly detect. As discussed in the previous section, with the introduction of n_s right–handed singlets, N_R^s, a Dirac mass term becomes feasible and can be explicitly written as

$$\mathcal{L}^{\rm D}_{\rm mass} = -\sum_{\alpha=1}^{3}\sum_{s=1}^{n_s}\left[\mathcal{M}^{\rm D}_{\alpha s}\bar{\nu}^{\alpha}_{L}N^{s}_{R} + \text{h.c.}\right], \tag{2.105}$$

where $\mathcal{M}^{\rm D}$ is a $3 \times n_s$ matrix.

Since ν_R is a gauge singlet, we can also introduce a Majorana mass term for it, avoiding the gauge invariance issues discussed in the previous section. Explicitly

$$\mathcal{L}^{M}_{\rm mass} = -\frac{1}{2}\sum_{s=1}^{n_s}\sum_{s'=1}^{n_s}\left[\mathcal{M}^{M}_{ss'}\overline{N}^{s\,c}_{R}N^{s'}_{R} + \text{h.c.}\right], \tag{2.106}$$

where $\mathcal{M}^{\rm M}$ is an $n_s \times n_s$ matrix.

In general, when both Majorana and Dirac mass terms are included, the neutrino mass matrix becomes a $(3+n_s)\times(3+n_s)$ complex symmetric matrix

$$\mathcal{M}^{\text{tot}} \equiv \begin{pmatrix} \mathcal{M}^L & \mathcal{M}^D \\ \mathcal{M}^{D\,T} & \mathcal{M}^R \end{pmatrix} = \begin{pmatrix} \mathbb{O}_3 & \lambda v_H/\sqrt{2} \\ \lambda^T v_H/\sqrt{2} & \mathcal{M}^R \end{pmatrix} . \tag{2.107}$$

Here, for generality, we included $\mathcal{M}^L$, a possible Majorana mass term for LH neutrinos. However, in the SM, this term is forbidden by gauge symmetry, and the mass matrix reduces to the form shown in the second equality. Defining the $3+n_s$ dimensional row vector of neutrino fields as

$$\Psi_\nu^T \equiv \left(\nu_{eL}^c \quad \nu_{\mu L}^c \quad \nu_{\tau L}^c \quad | \quad \overline{N}_{1R}^c \quad \cdots \quad \overline{N}_{n_s R}^c\right) = \left(\Psi_{\nu L}^T \quad | \quad \Psi_{NR}^T\right) , \tag{2.108}$$

and its corresponding charge-conjugated field, the full Lagrangian can be expressed compactly as

$$\mathcal{L}_{\text{mass}}^\nu = -\frac{1}{2}\overline{\Psi}_\nu^{c\,T}\mathcal{M}^{\text{tot}}\Psi_\nu + \text{h.c.} . \tag{2.109}$$

This matrix is symmetric. In the most general case, it is not diagonal and can be diagonalized via a suitable unitary transformation of the neutrino fields. It is helpful to consider some limiting cases. When $\mathcal{M}^R = 0$, the diagonalization is straightforward: the neutrino masses arise purely from Dirac mass terms. However, this scenario requires unrealistically small Yukawa couplings to explain the tiny observed neutrino masses.

On the other hand, when $\mathcal{M}_R \neq 0$, the mass matrix contains two well–defined mass scales: the Higgs vev, $v_H = 246\,\text{GeV}$, and the Majorana mass, M (where M represents the typical entries of the Majorana mass matrix $\mathcal{M}_R$). We focus on the limit where $M \gg v_H$. In this regime, it is standard practice to diagonalize the full mass matrix by treating the Dirac mass terms as a perturbation. In this case, eq. (2.109) can be expressed as

$$\mathcal{L}_{\text{mass}}^\nu = -\frac{1}{2}\overline{\Psi}_{N_R}^{c\,T} M \Psi_{N_R} - \frac{v_H^2}{4}\overline{\Psi}_{\nu_L}^{c\,T}\left(\lambda^T \frac{1}{M}\lambda\right)\Psi_{\nu_L} + \text{h.c.} . \tag{2.110}$$

The mass spectrum described by this Lagrangian consists of n_R heavy states with masses around the scale M and three light neutrino states with masses

$$m_\nu \simeq \frac{\lambda^2 v_H^2}{M^2} , \tag{2.111}$$

where λ and M denote the typical entries of the Yukawa matrix and Majorana mass matrix, respectively. This mechanism is more attractive from a theoretical perspective compared to the Dirac mass scenario, as tiny neutrino masses naturally emerge from the hierarchy between the two mass scales without requiring fine–tuning. This is what is known as the *seesaw mechanism*.

TYPE II: $SU(2)_L$ TRIPLET SCALARS The seesaw mechanism is not limited to the singlet fermion realization. Another possibility is to generate neutrino masses via the exchange of an $SU(2)_L$ triplet scalar, Δ [Lazarides et al., 1981; Magg and Wetterich, 1980; Mohapatra and Senjanovic, 1981; Schechter and Valle, 1980; Wetterich, 1981]. This triplet must be a color singlet and carry a hypercharge of $Y = +1$ (using the normalization where the lepton doublets have $Y = -1/2$). In the simplest version of the model, there is a single scalar field, represented in $SU(2)_L$ space as a 2×2 matrix [Davidson et al., 2008]

$$\Delta = \begin{pmatrix} \Delta^+/\sqrt{2} & \Delta^{++} \\ \Delta^0 & -\Delta^+/\sqrt{2} \end{pmatrix} . \tag{2.112}$$

The terms in the Lagrangian density involving Δ are

$$\begin{aligned} \mathcal{L}_\Delta = \mathrm{Tr}\left[\left(D_\mu \Delta\right)^\dagger \left(D^\mu \Delta\right) \right] - M_\Delta^2 \, \mathrm{Tr}\left[\Delta^\dagger \Delta\right] + \\ + \frac{1}{2} \sum_{\alpha,\beta=e,\mu,\tau} \left(\lambda_L^{\alpha\beta} \bar{L}^c_{L\alpha} i\sigma_2 \Delta L_{L\beta} + M_\Delta \lambda_H H^T i\sigma_2 \Delta^\dagger H + \mathrm{h.c.} \right) , \end{aligned} \tag{2.113}$$

where M_Δ is a real mass parameter, λ_L is a symmetric 3×3 matrix of complex Yukawa couplings, and λ_H is a dimensionless complex coupling. The first term of eq. (2.113) is the kinetic term, the second is the mass term, and the third corresponds to the potential. It is worth noting that this expression omits the self-interaction potential of Δ and interaction terms of the form $H^\dagger H \Delta^\dagger \Delta$. While such terms could be included (see Schmidt (2007) for a detailed discussion), they are not relevant for generating a neutrino mass term.

Through the exchange of scalar triplets, an effective dimension–5 operator $LL\tilde{H}\tilde{H}/M_\Delta$ is created, resulting in a Majorana mass

$$(m_{\mathrm{II}})_{\alpha\beta} = \frac{\lambda_L^{\alpha\beta} v^2}{M_\Delta} . \tag{2.114}$$

The simultaneous presence of λ_L and λ_H violates lepton number conservation, as it precludes a consistent assignment of lepton charge to Δ.

TYPE III: $SU(2)_L$ TRIPLET FERMIONS An alternative class of models that generates effective dimension–5 operators $LLHH$ involves the tree–level exchange of $SU(2)_L$–triplet right–handed fermions Σ^a_{Ri} [Foot et al., 1989; Ma, 1998; Ma and Roy, 2002]. Here, the index i represents the heavy mass eigenstates, while a denotes an $SU(2)_L$ index. These fields, Σ^a_{Ri}, are color singlets and have a vanishing hypercharge. Their representation in $SU(2)_L$ space is given by

$$\Sigma_{Ri} = \begin{pmatrix} \Sigma^0_{Ri}/\sqrt{2} & \Sigma^+_{Ri} \\ \Sigma^-_{Ri} & -\Sigma^0_{Ri}/\sqrt{2} \end{pmatrix} . \tag{2.115}$$

The corresponding Lagrangian terms are structured similarly to those in the singlet–fermion case but involve distinct $\mathrm{SU}(2)_\mathrm{L}$ index contractions. Following the conventions used by Davidson et al. (2008) and Ma and Roy (2002), the Yukawa term associated with the triplet can be expressed as

$$\mathcal{L}_\Sigma = \bar{L}_{\alpha L}\lambda^{\Sigma}_{\alpha i}\Sigma_{Ri} i\sigma_2 \phi^* - \frac{1}{2}\sum_i M_i \mathrm{Tr}\left(\Sigma^T_{Ri} C^\dagger \Sigma_{Ri}\right) + \mathrm{h.c.}\,. \tag{2.116}$$

In this expression, M_i are real mass parameters, and λ^Σ is a 3×3 matrix composed of dimensionless, complex Yukawa couplings. The exchange of fermion triplets leads to the generation of an effective dimension–5 operator, which provides the neutrino mass term

$$(m_{\mathrm{III}})_{\alpha\beta} = \sum_k \lambda^\Sigma_{\alpha k}\frac{v^2}{M_k}\lambda^\Sigma_{\beta k}\,. \tag{2.117}$$

Part II

NON–STANDARD NEUTRINO PHYSICS IN THE EARLY UNIVERSE

In this part, we carry out a detailed exploration of non–standard neutrino physics in the Early Universe. Specifically, we study the production of non–thermal neutrinos in very low reheating scenarios, exploiting current data to update constraints on post–inflationary physics. Additionally, we investigate models with neutrino featuring NSIs. In particular, we study their optical activity, showing how these interactions can leave interesting signatures on cosmological observables such as the CMB polarization, and carry out a comprehensive data analysis on the most cutting–edge cosmological data.

3 NEUTRINOS IN VERY LOW REHEATING SCENARIOS

The discussion in this chapter focuses on the role of neutrinos in cosmological models with very low reheating temperatures, and it is based on the results reported in Barbieri et al. (2025b). In section 3.1, we develop the tools necessary to an exact description of neutrino decoupling. This discussion sets the stage for understanding the modifications introduced by models with low reheating temperatures of which a benchmark case is studied in section 3.2. Then, in section 3.3, we present numerical results about the production of neutrinos in very low reheating scenarios, quantifying deviations from the standard equilibrium distributions. These deviations are found to play a significant role in shaping the evolution of the Universe and its observable features. Specifically, in section 3.4 we assess the impact of low reheating temperatures on BBN, deriving constraints on the reheating temperature based on the predicted abundances of light elements. Finally, in section 3.5, we extend the analysis to the CMB, examining how non–thermal neutrinos affect key cosmological parameters. This section incorporates also the results of advanced statistical analyses and compares them with observational data.

3.1 EXACT DESCRIPTION OF NEUTRINO DECOUPLING

To accurately study neutrino decoupling in the early Universe in the presence of flavor oscillations, the neutrino ensemble is described using generalized occupation numbers. Specifically, we represent the ensemble by 3×3 density matrices for neutrinos and anti–neutrinos, following the formalism outlined in [McKellar and Thomson, 1994; Sigl and Raffelt, 1993]. The density matrix for neutrinos of a given momentum mode p is expressed as

$$\varrho(p,t) = \begin{pmatrix} \varrho_{ee} & \varrho_{e\mu} & \varrho_{e\tau} \\ \varrho_{\mu e} & \varrho_{\mu\mu} & \varrho_{\mu\tau} \\ \varrho_{\tau e} & \varrho_{\tau\mu} & \varrho_{\tau\tau} \end{pmatrix} . \tag{3.1}$$

The diagonal elements, $\varrho_{\alpha\alpha}$, correspond to the occupation numbers of the neutrino flavors ν_α ($\alpha = e, \mu, \tau$), while the off–diagonal elements, $\varrho_{\alpha\beta}$ with $\alpha \neq \beta$, encode coherence and are non–zero in the presence of neutrino mixing. A similar equation applies to the antineutrino density matrix, $\bar{\varrho}$; however, in the absence of a neutrino asymmetry, antineutrinos evolve identically to neutrinos. Therefore, $\bar{\varrho}$ is not required for the analysis presented in the following.

The equation of motion for the density matrices, in the most general case, can be expressed as[1] [McKellar and Thomson, 1994]:

$$i\frac{d\rho}{dt} = \left[\Omega_p^0, \rho_p\right] + \left[\Omega_p^{\rm int}, \rho_p\right] + \mathbb{C}\left[\rho_p, \bar{\rho}_p\right] \ , \tag{3.2}$$

with a similar expression for the antineutrino density matrices $\bar{\rho}_p$. The first two terms on the right–hand side represent the effective potential experienced by neutrinos. The first term governs vacuum oscillations and is given by

$$\Omega_p^0 = \pm\frac{\mathbb{M}_{\rm F}^2}{2p} \ , \tag{3.3}$$

where $\mathbb{M}_{\rm F}^2$ denotes the mass–squared matrix in the flavor basis. The signs above and below correspond to the neutrino and antineutrino density matrices, respectively. The flavor–basis mass–squared matrix is related to the diagonal matrix in the mass basis, diag $\left(m_1^2, m_2^2, m_3^2\right)$, via the neutrino mixing matrix

$$\mathbb{M}_{\rm F}^2 = U_{\rm PMNS}\,{\rm diag}\left(m_1^2, m_2^2, m_3^2\right) U_{\rm PMNS}^\dagger \ , \tag{3.4}$$

where the PMNS matrix is parameterized as

$$U_{\rm PNMS} = \begin{pmatrix} c_{12}c_{13} & s_{12}c_{13} & s_{13} \\ -s_{12}c_{23} - c_{12}s_{23}s_{13} & c_{12}c_{23} - s_{12}s_{23}s_{13} & s_{23}c_{13} \\ s_{12}s_{23} - c_{12}c_{23}s_{13} & -c_{12}s_{23} - s_{12}c_{23}s_{13} & c_{23}c_{13} \end{pmatrix} . \tag{3.5}$$

Here, $c_{ij} = \cos\theta_{ij}$ and $s_{ij} = \sin\theta_{ij}$, where $ij = 12,\ 23,$ or 13. Assuming CP conservation, the system is characterized by five oscillation parameters: $\Delta m_{21}^2 = m_2^2 - m_1^2$, $\Delta m_{31}^2 = m_3^2 - m_1^2$, θ_{12}, θ_{23}, and θ_{13}. These parameters are well–determined from global analyses of experimental data on flavor neutrino oscillations. Using the best–fit values from Salas et al. (2021) for the NO case, we have

$$\left(\frac{\Delta m_{21}^2}{10^{-5}\ {\rm eV}^2}, \frac{\Delta m_{31}^2}{10^{-3}\ {\rm eV}^2}, \frac{s_{12}^2}{10^{-1}}, \frac{s_{23}^2}{10^{-1}}, \frac{s_{13}^2}{10^{-3}}\right)_{\rm NO} = \\ = (7.50,\ 2.55,\ 3.18,\ 5.74,\ 2.200) \ . \tag{3.6}$$

Neutrino decoupling occurs at temperatures on the order of the MeV, during which neutrinos experience both collisions and refractive effects from the surrounding medium. The second term in eq. (3.2) represents the matter potential, given by [Mangano et al., 2002; Mirizzi et al., 2012; Salas and Pastor, 2016; Saviano et al., 2013]

$$\Omega_p^{\rm int} = \sqrt{2}G_{\rm F}\left[\mathbb{L} \mp \frac{2p}{M_W^2}(\mathbb{E} + \mathbb{P})\right] + \sqrt{2}G_{\rm F}\left[\rho - \bar{\rho} \mp \frac{8p}{3M_Z^2}\left(\mathbb{U} + \bar{\mathbb{U}}\right)\right] \ , \tag{3.7}$$

1 Similar to the Boltzmann equation, in the early Universe this expression implicitly includes the derivative term $\left(\partial_t - Hp\partial_p\right)\rho$ and can be reformulated in terms of the dimensionless variables x and y.

with the same sign convention as in eq. (3.2).

The first two terms in eq. (3.7) represent the matter potential experienced by neutrinos due to a background of charged leptons. These terms are diagonal in the flavor basis and are proportional to either the difference, $\mathbb{L}$, of number densities or the sum of energy densities, $\mathbb{E}$, and pressures, $\mathbb{P}$, of charged leptons and anti–leptons. At temperatures around 1 MeV, the energy density term dominates[2], particularly in an almost charge–symmetric Universe. In this context, only the contributions of electrons and positrons are relevant, with the sole non–zero component being $\mathbb{E}_{11} = \rho_{e^-} + \rho_{e^+}$. Note that the $\mathbb{E} + \mathbb{P}$ term in eq. (3.7) differs from its usual presentation found in, e.g., eq. (2.2) of Berryman (2019), which has $\mathbb{E} + \mathbb{P}$ replaced with $(4/3)\mathbb{E}$. First reported in Ichikawa et al. (2005), the former is in fact the more general result, while $(4/3)\mathbb{E}$ applies strictly only when the charged leptons are ultra–relativistic. In practice, however, using the incorrect expression incurs an error no larger than 10^{-5} in $N_{\rm eff}$.

The last two terms in eq. (3.7) account for the refractive effects of background neutrinos, arising from neutrino self–interactions. These terms are defined as

$$\rho = \int \frac{d^3p}{(2\pi)^3}\rho_p \,, \qquad \mathbb{U} = \int \frac{d^3p}{(2\pi)^3} p\rho_p \,, \tag{3.8}$$

with analogous definitions for antineutrinos. These terms may include non–diagonal elements in the flavor basis, which can lead to unexpected behaviors in neutrino transitions in high–density environments. However, they are subdominant compared to the energy density term. Furthermore, assuming a vanishing lepton asymmetry, the first of this term, along with the term proportional to $\mathbb{L}$, vanish completely, leaving only the energy density contribution.

Finally, the collision integral $\mathbb{C}\left[\rho_p, \bar{\rho}_p\right]$ in eq. (3.2) accounts for all possible neutrino interaction processes, proportional to $G_{\rm F}^2$. Its most general form, for each interaction involving one or more neutrinos, is a matrix of collision integrals for each component of ρ_p. This means that, for each neutrino appearing in a given process, a matrix element replaces the distribution functions in eq. (1.88) [Sigl and Raffelt, 1993].

To simplify computations, it is common to approximate the off–diagonal terms of the density matrix as $\mathbb{C}\left[\rho_{\alpha\beta}\left(p\right)\right] = -D_p\rho_{\alpha\beta}\left(p\right)$, effectively treating collisions with a simple damping prescription . For the diagonal terms, however, the exact collision integral must be used to accurately describe

2 A detailed discussion of the effective matter potential in the primordial plasma, can be found in chapters 4 and 1 of Lesgourgues et al. (2013), respectively.

the neutrino heating process. For instance, in the case of a two–body weak interaction of the type $\nu_\alpha\,(1) + 2 \to 3 + 4$, the collision integral is given by

$$\mathbb{C}_{\nu_\alpha}\left[\rho_p, f\right] = \frac{1}{2E_1}\sum_{2,3,4}\iiint \frac{d^3\mathbf{p_2}}{2E_2\,(2\pi)^3}\frac{d^3\mathbf{p_3}}{2E_3\,(2\pi)^3}\frac{d^3\mathbf{p_4}}{2E_4\,(2\pi)^3} \times (2\pi)^4\,\delta\left(p_1 + p_2 - p_3 - p_4\right)\Lambda_{\alpha\alpha}\left[\rho_{p_1}, f_2, f_3, f_4\right] S\,|\mathcal{M}|^2_{12\to 34}\ , \tag{3.9}$$

where the phase space factor $\Lambda_{\alpha\alpha}$ includes Pauli blocking of the final states

$$\Lambda_{\alpha\alpha}\left[\rho_{p_1}, f_2, f_3, f_4\right] = = f_3 f_4\left(1 - \rho_{\alpha\alpha}\left(p_1\right)\right)\left(1 - f_2\right) - \rho_{\alpha\alpha}\left(p_1\right) f_2\left(1 - f_3\right)\left(1 - f_4\right)\ . \tag{3.10}$$

In this expression, S is the symmetrization factor, equal to $1/2!$ for each pair of identical particles in the initial or final states, and $|\mathcal{M}|^2_{12\to 34}$ is the spin–summed and averaged squared matrix element. The summation is performed over all possible configurations of particles labeled as 2, 3, and 4, with 1 reserved for the neutrino. Explicit forms of the matrix elements for all relevant processes can be found in tables 1 and 2 of Dolgov et al. (1997).

The kinetic equations governing the neutrino density matrix are supplemented by the continuity equation for the total energy density, $\rho_{\rm tot}$,

$$\frac{d\rho_{\rm tot}}{dt} = -3H(\rho_{\rm tot} + P_{\rm tot})\ , \tag{3.11}$$

where $P_{\rm tot}$ represents the total pressure of the relativistic plasma, which includes contributions from the three neutrino states as well as the electromagnetic components γ, $e^\pm$, and $\mu^\pm$. The electromagnetic components are assumed to be in thermodynamic equilibrium at a common photon temperature T_γ. This equation determines the evolution of T_γ. Finite–temperature QED corrections to the electromagnetic plasma modify the equations of state for $e^\pm$ and γ. These corrections are incorporated as described in Bennett et al. (2021) (see also Drewes et al. (2024) and Jackson and Laine (2024) for a deeper discussion on QED corrections also at the level of neutrino–neutrino interaction rate). For the physical system under consideration, the total energy density and pressure are defined as

$$\rho_{\rm tot} \equiv \rho_{\rm QED} + \rho_\nu\ , \tag{3.12}$$

$$P_{\rm tot} \equiv P_{\rm QED} + P_\nu\ , \tag{3.13}$$

where the QED and neutrino sectors contribute independently[3]. The QED sector is assumed to be in thermodynamic equilibrium at all times, ensuring that $\rho_{\rm QED}$ and $P_{\rm QED}$ are related by the standard thermodynamic relation

$$\rho_{\rm QED} = -P_{\rm QED} + T\left(\frac{\partial}{\partial T}\right)P_{\rm QED}\ . \tag{3.14}$$

3 We neglect the small universal matter–antimatter asymmetry of $\mathcal{O}(10^{-10})$, treating each particle name as representing both the particle and its antiparticle.

Our set of equations, eq. (3.2) and eq. (3.11), can be simplified by introducing the following dimensionless variables to replace time, neutrino momenta, and photon temperature

$$x \equiv ma\,, \quad y \equiv pa\,, \quad z \equiv T_\gamma a\,, \tag{3.15}$$

where m is an arbitrary mass scale, chosen here to be the electron mass, and a is the scale factor of the Universe (normalized so that $a \propto 1/T_\gamma$ at high temperatures). For further details and explicit expressions of the terms appearing in the equations, we refer the reader to the appendix of Dolgov et al. (2002), noting that in that work, the mass scale m was chosen to be 1 MeV. The kinetic equations in eq. (3.2) are integro–differential in nature due to the presence of collision terms, such as those in eq. (3.9). In previous analyses of neutrino decoulping, the system was solved either by discretizing the equations on a grid of dimensionless momenta [Dolgov et al., 1997; 1999; Gnedin and Gnedin, 1998; Grohs et al., 2016; Hannestad and Madsen, 1995; Mangano et al., 2005; Salas and Pastor, 2016], or by expanding the non–thermal distortions in terms of moments [Birrell et al., 2014; Esposito et al., 2000; Mangano et al., 2002].

3.2 A DEEPER LOOK INTO REHEATING DYNAMICS

We now want to discuss in some detail the dynamics of the final phase of inflation, reheating, introduced in section 1.4.4. This phase is fundamental for recovering the predictions of the Hot Big Bang model at the end of inflation, namely, an era dominated by radiation. However, this is not a trivial requirement because, as we know, due to rapid expansion, there is significant supercooling ($T \propto e^{-Ht}$ during inflation), which brings the temperature to extremely low values. To sustain radiation dominance and the thermalization of the primordial plasma, a mechanism is needed to heat the Universe immediately after inflation and just before the radiation era.

To end inflation, the curvature of the potential must no longer be negligible compared to the Hubble rate. The inflaton will then fall into the potential minimum, where it begins to oscillate with a frequency $\omega^2 \propto V''(\sigma) \gg H^2$. Additionally, since reheating also requires entropy production, we must modify the scalar field's equation of motion, eq. (1.162), by adding a viscous damping term $\Gamma_\phi \dot{\phi}$ that accounts for the energy lost by the inflaton through its decays. The equation of motion during reheating thus becomes

$$\ddot{\phi} + \left(3H + \Gamma_\phi\right)\dot{\phi} + V'(\phi) = 0\,, \tag{3.16}$$

which describes a damped harmonic oscillator influenced by the expansion of the Universe and decays. Taking the time derivative of eq. (3.16), and

recalling that the inflaton's energy density can be expressed as in eq. (3.27), the equation of motion can be rewritten as

$$\dot{\rho}_\phi + \dot{\phi}^2\left(3H + \Gamma_\phi\right) = 0\,. \tag{3.17}$$

Since during reheating $\omega^2 \gg H^2$, we can safely average over oscillation periods, obtaining

$$\frac{1}{2}\left\langle \dot{\phi}^2 \right\rangle = \langle V(\phi) \rangle\ , \tag{3.18}$$

which immediately leads to $\rho_\phi = \left\langle \dot{\phi}^2 \right\rangle$, a reformulation of the virial theorem. Thus, eq. (3.17) can finally be rewritten as

$$\dot{\rho}_\phi = \rho_\phi\left(3H + \Gamma_\phi\right) = 0\,, \tag{3.19}$$

whose solution[4] is

$$\rho_\phi = \rho_\phi^{\rm osc}\left(\frac{a_{\rm osc}}{a}\right)^3 e^{-(t-t_{\rm osc})\Gamma_\phi}\ . \tag{3.20}$$

We thus see that a rapidly oscillating scalar field around the potential minimum behaves like *pressureless matter*.

The situation is that immediately after slow–roll, decays are not very effective, so the inflaton energy density scales as a^{-3} and continues to dominate the Universe. Then, at $t \simeq \Gamma_\phi^{-1}$, decays become active, and the energy density begins to decrease significantly, even though it still dominates (at this point, radiation begins to be quantitatively produced). Eventually, radiation takes over.

The presence of inflaton decays modifies the continuity equation for radiation as follows

$$\dot{\rho}_r + 4H\rho_r = \Gamma_\phi \rho_\phi\ . \tag{3.21}$$

Since from $t_{\rm osc} \simeq H^{-1=3M_{\rm pl}}/M^2$ to $t_{\rm decay} \simeq$ decays are not yet active, radiation follows its usual scaling $\rho_r \propto a^{-4}$, while the Universe is dominated by the matter-like field, generating $H = 2/3t$, so we can write the radiation continuity equation as

$$\dot{\rho}_r + \frac{8}{3t}\rho_r = \frac{3\Gamma_\phi M_{\rm pl}^2}{t^2}\ , \tag{3.22}$$

which, taking $\rho_r(t_{\rm osc}) = 0$ as the initial condition and looking for solutions of the form $\rho(t) \propto t^\alpha$, gives the solution

$$\rho_r = \frac{9}{5}\Gamma_\phi M_{\rm pl} M^2 \left(\frac{a}{a_{\rm osc}}\right)^{-3/2}\left[1 - \left(\frac{a}{a_{\rm osc}}\right)^{-5/2}\right]\ . \tag{3.23}$$

During the oscillation phase, radiation density grows due to decay contributions until it reaches a maximum, after which it starts decreasing as

4 As an initial condition, one can use, for instance, $\rho_{\rm osc} \simeq M^4$, the energy scale of inflation.

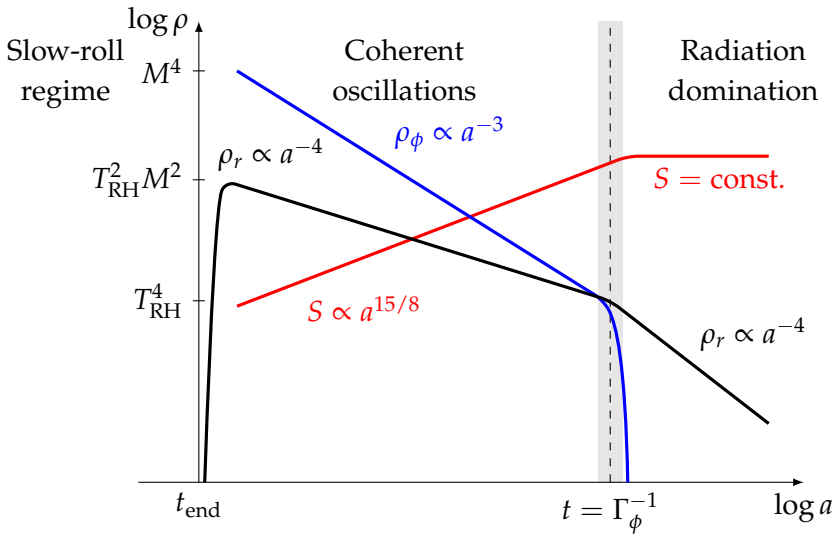

Figure 3.1: Dynamics of energy density and entropy in single-field slow-roll models reheating.

$\rho_r \propto a^{-3/2}$. Note that this decreases more slowly than the usual $\rho_r \propto a^{-4}$ due to the constant decay rate partially offsetting the expansion effect. When decays cease to be effective, the usual behavior is recovered. It can be shown that the maximum radiation density achieved is

$$\rho_r^{\max} \simeq \Gamma_\phi M_{\rm pl} M^2 \,, \tag{3.24}$$

which corresponds to a maximum temperature of

$$T_{\max} \simeq g_*^{-1/4} M_{\rm pl}^{1/4} \Gamma_\phi^{1/4} M^{1/2} \,, \tag{3.25}$$

indicating that, after a rapid initial transient, the temperature decreases during reheating.

It is also interesting to study what happens to entropy during reheating due to this behavior. In general, the entropy per comoving volume can be written as in eq. (1.43). In a standard radiation–dominated Universe, it is conserved; however, during reheating, we have[5]

$$S \propto T^3 a^3 \propto \rho_r^{3/4} a^3 \propto a^{15/8} \,. \tag{3.26}$$

Thus, after the maximum temperature is reached, entropy increases until decays cease to be effective, bringing us back to standard radiation dominance. All these considerations are summarized graphically in fig. 3.1.

5 We have implicitly assumed $g_* \sim g_{*s}$ even though they are certainly not equivalent during this phase. Nevertheless, considering average values, this behavior is found to be a good approximation.

3.3 PRODUCTION OF NEUTRINOS IN VERY LOW–REHEATING SCENARIOS

The inflationary paradigm provides a natural framework for studying reheating processes. The accelerated expansion characteristic of the inflationary epoch leads to a significant super–cooling of the plasma, making the efficient thermalization of SM particles challenging. A commonly adopted solution to this problem, ensuring the onset of a radiation–dominated phase, involves allowing the massive scalar particle that dominates the energy density during inflation to decay into SM degrees of freedom. This decay process reheats the primordial plasma and transitions the Universe into the standard Hot Big Bang scenario.

To analyze low–reheating scenarios, we model the reheating phase inspired by the mechanism that concludes the inflationary epoch. Let us denote the massive scalar field by ϕ, referred to as the *inflaton*, which decays into SM particles with a decay rate Γ_ϕ. The evolution of the energy density of the scalar field is described by the equation governing a decaying non–relativistic species in an expanding Universe

$$\frac{d\rho_\phi}{dt} + \left(3H + \Gamma_\phi\right)\rho_\phi = 0\,, \tag{3.27}$$

where inverse decay processes are neglected. Here, H represents the Hubble parameter, which depends on the total energy density of the Universe.

In the previous section, we established that reheating is not an instantaneous process. However, as is commonly done in analogous phenomena, it is practical to adopt a prescription for defining a reheating temperature, $T_{\rm RH}$, at which we can approximate that reheating has effectively concluded. There is no universal consensus in the literature on the precise definition of this temperature. In line with our prior analysis [Salas et al., 2015], we define the reheating temperature through the relation

$$\Gamma_\phi \equiv 3H(T_{\rm RH})\,, \tag{3.28}$$

which corresponds to the moment when the depletion of energy density due to decays overtakes the effects of cosmological redshift (see eq. (3.27)). At this point, it is reasonable to assume that the Universe has transitioned into a radiation–dominated phase.

If all relativistic particles are assumed to be the standard ones, the Hubble parameter can be expressed as

$$H(T_{\rm RH}) = \sqrt{\frac{\rho_{\rm rad}(T_{\rm RH})}{3M_{\rm pl}^2}} = \sqrt{\frac{\pi^2}{90}g_*(T_{\rm RH})}\frac{T_{\rm RH}^2}{M_{\rm pl}}\,, \tag{3.29}$$

where $M_{\rm pl} \equiv m_{\rm pl}/\sqrt{8\pi} = 2.4 \times 10^{18}\,\text{GeV}$ is the reduced Planck mass, and $g_*(T)$ represents the number of relativistic degrees of freedom at the temperature T. In the standard scenario, $g_*(T)$ is 10.75 for the range of temperatures

relevant to our discussion, and within our model, we use this value for the definition of $T_{\rm RH}$, despite the fact that neutrinos might be far from being in equilibrium with the electromagnetic plasma.

It becomes evident from this that $T_{\rm RH}$ provides an alternative prescription for expressing the decay rate of the massive particle. Using eq. (3.28) and eq. (3.29), we find the following relation between the reheating temperature and the decay rate

$$T_{\rm RH} \simeq 0.70 \left(\frac{\Gamma_\phi}{\rm s^{-1}}\right)^{1/2} \text{MeV} \,. \tag{3.30}$$

Alternative definitions of $T_{\rm RH}$ exist in the literature. For instance, Giudice et al. (2001) propose $\Gamma_\phi = H(T_{\rm RH})$, while Kolb and Turner (2019) suggest $\Gamma_\phi = 2H(T_{\rm RH})$, summarizing several studies on the out–of–equilibrium decay of massive particles. Let us focus on the first of these alternative definitions, as it deviates most significantly from our prescription. Under this assumption, the reheating temperature would instead be

$$T_{\rm RH} \simeq 1.21 \left(\frac{\Gamma_\phi}{\rm s^{-1}}\right)^{1/2} \text{MeV} \,, \tag{3.31}$$

which yields systematically higher temperatures for the same decay rate. In our analysis, we adopt the convention in eq. (3.28), as it provides the loosest bound on $T_{\rm RH}$. This ambiguity in the definition of the reheating temperature underscores its nature as an effective parameter, with its exact definition being somewhat arbitrary.

In the remainder of this chapter, we focus on a simplified scenario of reheating that occurs at very low temperatures. Specifically, we refer to *very low reheating* scenarios as those in which the reheating temperature satisfies $T_{\rm RH} < 20\,\text{MeV}$. A key assumption in our model is that the massive particle decays at a rate Γ_ϕ into relativistic particles, excluding neutrinos, thereby reheating the Universe. Neutrinos, on the other hand, are produced through weak interactions with charged leptons and may reach thermal equilibrium with the rest of the plasma if the inflaton decay takes place sufficiently early. However, in very low reheating scenarios, if the decay occurs too late, the neutrino fluid cannot equilibrate with the other relativistic particles. As a result, the neutrino energy density is smaller than in the standard scenario, and the final value of $N_{\rm eff}$ is correspondingly reduced.

The evolution of the neutrino fluid in this context is still described by eq. (3.2), and the corresponding discussion remains as outlined in section 3.1. Additionally, the other equation required to complete the system derives from the continuity equation for the total energy–momentum in the expanding Universe. As mentioned earlier, since all particles coupled via electromagnetic interactions share a common temperature, T_γ, it suffices to compute the time evolution of T_γ. This can be derived from the continuity equation for the total

energy density in an expanding Universe. However, considering the existence of low–reheating scenarios, this equation must be modified as follows

$$\frac{dT_\gamma}{dt} = \frac{-\Gamma_\phi \rho_\phi + 4H(\rho_\gamma + \rho_\nu) + 3H(\rho_l + P_l) + d\rho_\nu/dt}{\partial\rho_\gamma/\partial T_\gamma + \partial\rho_l/\partial T_\gamma} \,, \tag{3.32}$$

where l represents the charged leptons. As previously noted, it is necessary to include finite temperature QED corrections to the electromagnetic plasma in this equation.

3.3.1 Numerical results

In low–reheating scenarios, solving the system of differential equations described by eq. (3.27), together with the neutrino kinetic equations (eq. (3.2)) and the continuity equation (eq. (3.11)), becomes essential. This task has been carried out using a modified version of the `FortEPiaNO` code [Bennett et al., 2021; Gariazzo et al., 2019], which has been specifically adapted to address the unique requirements of low–reheating scenarios.

The initial condition for the comoving ρ_ϕ is determined using

$$\rho_\phi^{\rm in} = \frac{3m_p^2}{8\pi}\left(\frac{2}{3t_{\rm in}}\right)^2 \frac{x_{\rm in}^3}{m_e^4} \,, \tag{3.33}$$

where the initial time is given by

$$t_{\rm in} = t_0 \left(\frac{x_{\rm in}}{x_0}\right)^{3/2} \,, \tag{3.34}$$

with $t_0 = 10^{-3}$ and $x_0 = 10^{-2}$. It is important to note that the initial condition $\rho_\phi^{\rm in}$ in eq. (3.33) becomes independent of $x_{\rm in}$ once $t_{\rm in}$ is substituted using eq. (3.34). However, the choice of $x_{\rm in}$ must be made carefully during numerical calculations because the energy density ρ_ϕ can decrease rapidly from its initial value $\rho_\phi^{\rm in}$. If $x_{\rm in}$ exceeds approximately $m_e/(10\,T_{\rm RH})$, the initial condition in eq. (3.33) is no longer valid due to the effects of inflaton decay, which may lead to inaccurate final results. Consequently, for all calculations, we always consider that $x_{\rm in} \lesssim m_e/(10\,T_{\rm RH})$.

A few examples of our numerical calculations are presented in fig. 3.2, which illustrates the time evolution of the ratio of energy densities ρ_ν/ρ_γ for five different values of $T_{\rm RH}$. This ratio is normalized in two distinct ways along the y–axis, such that it corresponds to the effective number of neutrinos before and after $e^\pm$ annihilations (equal to 3 in both cases under the assumption of instantaneous neutrino decoupling) [Pastor et al., 2009; Salas et al., 2015]. At late times, $N_{\rm eff}$ is specifically defined as

$$\frac{\rho_\nu}{\rho_\gamma} = 1 + \frac{7}{8}\left(\frac{4}{11}\right)^{4/3} N_{\rm eff} \,. \tag{3.35}$$

For reheating temperatures as high as 15 MeV, the evolution of ρ_ν/ρ_γ closely resembles the standard scenario, apart from the very initial phase. A rapid

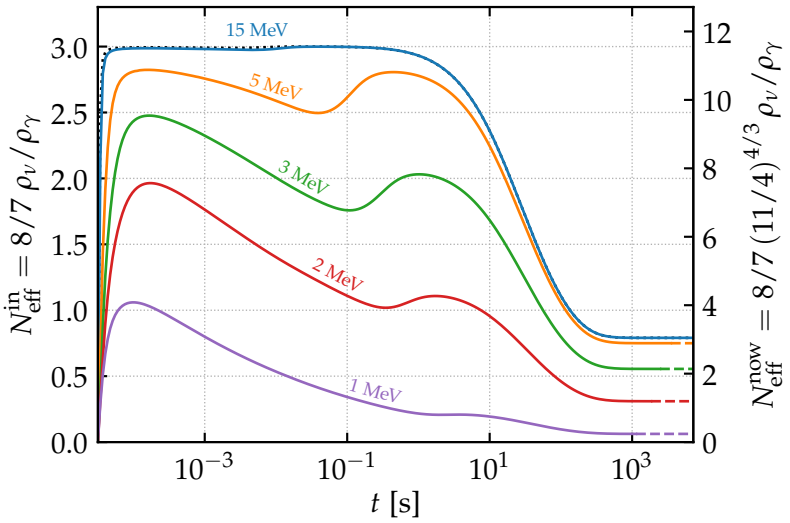

Figure 3.2: Temporal evolution of the ratio between neutrinos and photons energy densities for different reheating temperatures, normalized to correspond to $N_{\rm eff}$ before (left) and after (right) e^+e^- annihilation.

drop is observed at $t \sim 1\,\mathrm{s}$, attributed to photon heating during $e^\pm$ annihilations. In contrast, for smaller values of $T_{\rm RH}$, ρ_ν/ρ_γ decreases during the decay of ϕ, followed by a brief phase where the ratio slightly increases but never reaches the value expected in the standard case. This indicates that neutrinos fail to reach equilibrium, and the final value of $N_{\rm eff}$ falls below three. This behavior is more clearly demonstrated in fig. 3.3, which shows the differential energy spectrum of neutrinos at the end of the evolution for the same five values of $T_{\rm RH}$, compared to an equilibrium Fermi–Dirac spectrum. For $T_{\rm RH} = 15\,\mathrm{MeV}$, the energy distribution is very close to equilibrium, even slightly exceeding it at high momenta, as expected in the standard decoupling case that results in $N_{\rm eff} = 3.044$ [Bennett et al., 2021]. On the other hand, for smaller reheating temperatures, there is a significant suppression in neutrino production, particularly for $T_{\rm RH} = 1\,\mathrm{MeV}$.

The distortion of the neutrino spectra from equilibrium can be quantified using the parameter R_E, defined as [Kawasaki et al., 2000]:

$$R_E \equiv \frac{1}{3.151 T_{\nu,\rm eff}} \frac{\rho_\nu}{n_\nu}\,, \tag{3.36}$$

where the neutrino energy density ρ_ν, number density n_ν, and effective temperature $T_{\nu,\rm eff} = \left[2\pi^2 n_\nu/(3\zeta(3))\right]^{1/3}$ are obtained by integrating the spectrum. The parameter R_E represents the ratio of the mean neutrino energy to its equilibrium value. In fig. 3.4, R_E is shown for electron neutrinos as a function of $T_{\rm RH}$. A value close to unity indicates that the neutrino spectrum remains near equilibrium. By contrast, larger values of R_E signal significant distortions in the spectrum, as is observed for $T_{\rm RH} \lesssim 3\,\mathrm{MeV}$.

Finally, in fig. 3.5, we present the final contribution of neutrinos to the radiation energy density, expressed in terms of $N_{\rm eff}$. The value of $N_{\rm eff}$ falls

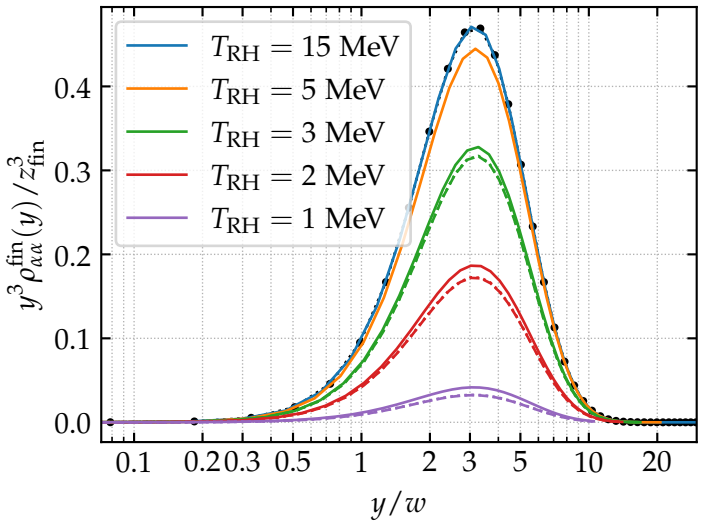

Figure 3.3: Final momentum distribution functions for the different neutrino flavor states as a function of the comoving momentum, $y = ap$. Coloured curves correspond to three different values of $T_{\rm RH}$, while solid, dashed and dotted lines correspond to ν_e, ν_μ, and ν_τ respectively. The solid black line with dots corresponds to an equilibrium spectrum (i.e. a Fermi-Dirac neutrino distribution).

below 3 for reheating temperatures $T_{\rm RH} \lesssim 7\,\text{MeV}$. Our findings are consistent with those reported in Salas et al. (2015), which, in turn, agree with earlier studies (see Hannestad (2004) and Ichikawa et al. (2007)).

3.4 BOUNDS FROM PRIMORDIAL NUCLEOSYNTHESIS

Neutrinos play a significant role in determining the primordial abundances of light elements during BBN. This influence arises through two primary mechanisms: first the comoving energy density of all neutrino flavors, which contributes to the Hubble expansion rate and the continuity equation for the radiation energy density (referred to as the RHO contribution in the plots), and second, the distribution of electron neutrinos, which directly affects the charged current weak rates that govern the neutron–proton chemical equilibrium (labeled as the WR contribution in the plots).

To use BBN as a tool for constraining low–reheating scenarios, we have modified the latest version of the `PArthENoPE` code [Gariazzo et al., 2022a]. Specifically, in the following analysis, we employ the neutron lifetime $\tau_n = (879.4 \pm 0.6)\,\text{s}$ [Workman et al., 2022]. It is worth noting that in our earlier analysis of low–reheating scenarios [Salas et al., 2015], a simplified modification of the weak rates was implemented in `PArthENoPE` . For each value of $T_{\rm RH}$, corrections to D/H and Y_p were computed by applying the modified ν_e momentum distribution to the weak Born rates in the BBN code. A global correction was then applied to account for radiative effects on the weak rates.

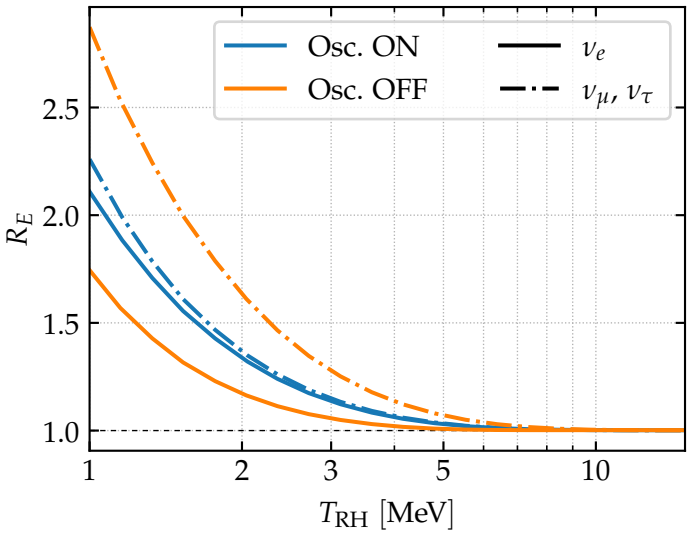

Figure 3.4: Distortion of neutrino spectra parameterized as R_E, eq. (3.36), as a function of $T_{\rm RH}$. A value $R_E > 1$ dindicates a significant deviation from the equilibrium spectrum. Solid curves are for electron neutrinos, while dashed dotted for μ and τ neutrinos. They are grouped together because they are essentially indistinguishable. Both the case with and without flavor oscillations are shown.

While this approach was justified as a second–order correction, we have now refined the procedure by including radiative corrections to the modified Born rates throughout the entire BBN evolution.

In fig. 3.6 we present the D/H and Y_p abundances as functions of the reheating temperature. In addition to the total final abundances (shown by the blue solid line), we separately show the individual contributions: RHO (orange lines) and WR (green lines).

For the RHO contribution, both deuterium and helium abundances increase with $T_{\rm RH}$. At lower reheating temperatures, the production of neutrinos becomes less efficient, reducing the expansion rate and leaving fewer neutrons available for the synthesis of light elements. Conversely, at low reheating temperatures, the WR contribution reflects changes in the electron neutrino distribution, leading to reduced weak rates and an earlier decoupling of processes interconverting protons and neutrons. This results in a higher freeze-out value of the neutron–to–proton (n/p) ratio, which in turn increases the final helium abundance (Y_p) and, to a lesser extent, the deuterium abundance (D/H). This explains the observed rise in Y_p at low reheating temperatures.

We have carried out a BBN likelihood analysis by varying the input parameters of our model, $T_{\rm RH}$ and the present value of the baryon density $\Omega_{\rm b}h^2$, where the present–day Hubble parameter is $H_0 = 100h\,{\rm km\,s^{-1}\,Mpc^{-1}}$. We consider the most recent astrophysical measurements of primordial abundances from Workman et al. (2022):

$$^2{\rm H/H} = (2.547 \pm 0.025) \times 10^{-5} \tag{3.37}$$

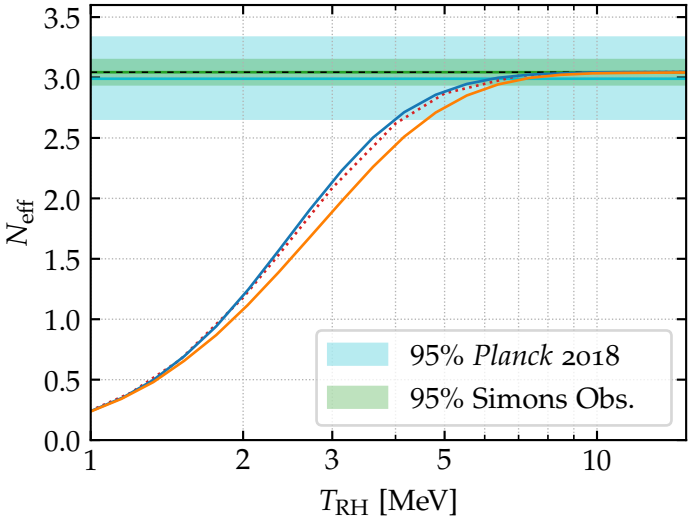

Figure 3.5: Final neutrino energy density expressed in terms of $N_{\rm eff}$, as a function of the reheating temperature. The horizontal line indicates the standard value, $N_{\rm eff} = 3.044$. Solid line represent our new simulations (with oscillations, blue, and without oscilations, orange), while dotted lines are the points used in the analysis of Salas et al. (2015)

for deuterium, and

$$Y_p = 0.245 \pm 0.003 \tag{3.38}$$

for helium.

In fig. 3.7 we display the contour lines of the likelihood function in the $T_{\rm RH} - \Omega_b h^2$ plane. As expected, the likelihood asymptotically approaches a constant value for large reheating temperatures, which are indistinguishable from the BBN perspective. Conversely, the likelihood drops to zero for $T_{\rm RH} \sim 3\,\text{MeV}$. Additionally, including a prior on the value of $\Omega_b h^2$ based on Planck results primarily affects the likelihood by constraining the left and right tails.

Additionaly, fig. 3.7 further illustrates that BBN data alone cannot constrain the highest reheating temperatures, as the likelihood function plateaus at high values of $T_{\rm RH}$ for nearly all choices of the mixing parameters considered in our analysis.

3.5 BOUNDS FROM CMB OBSERVATIONS

In this section, we complete the discussion on probes of $T_{\rm RH}$ by incorporating information from cosmological surveys. To compute the CMB angular power spectrum in models with a low reheating temperature, we modified the Boltzmann solver `CLASS` and the Markov Chain Monte Carlo (MCMC) sampler `MontePython` to allow for arbitrary forms of the neutrino distribution function (potentially distinct for each neutrino mass eigenstate). Unlike in our previous

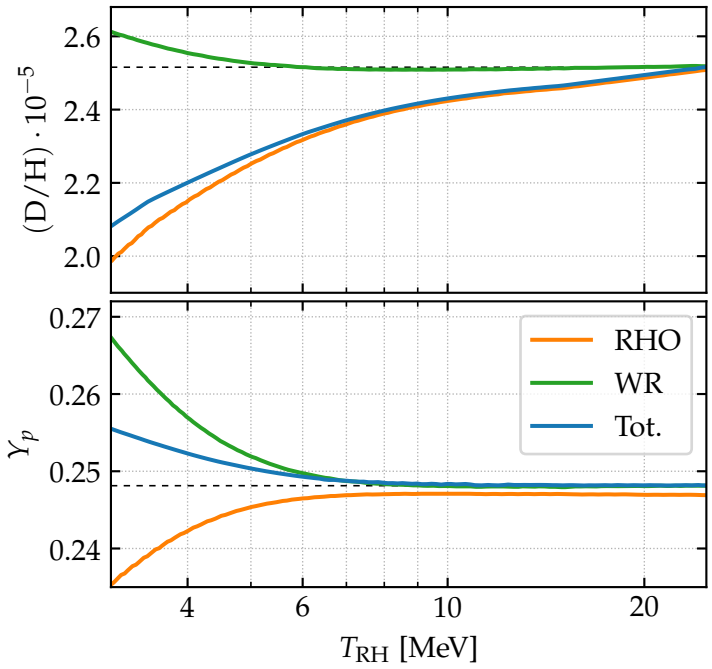

Figure 3.6: Deuterium (top) and Helium (bottom) abundances as a function of the reheating temperature for $\Omega_b h^2 = 0.02242$. Blue solid lines represent the total final abundances, while with orange and green solid lines we separately show RHO and WR contributions (see the text). Black dashed lines indicates the theoretical values computed in the standard cosmological model without the low reheating effects.

analysis, we transitioned from using `CAMB` to `CLASS` for the Boltzmann solver due to the latter's more efficient and flexible implementation of Non–Cold Dark Matter (NCDM) relics.

Indeed, Dark Matter (DM) candidates, of a given mass M_X, can be classified depending on their decoupling temperature[6], T_d. If this temperature is much smaller than the mass of the DM particle, these particles decouple being non–relativistic. In this case DM is *cold*. In the opposite case, $T_d \gtrsim M_X$, there are two possibilities, $M_X \lesssim 1\,\text{eV}$ and $M_X \gtrsim 1\,\text{eV}$. The former corresponds to *hot* DM: its particles remain relativistic at matter–radiation equality (recall that equality occurs at $T_{eq} \sim 1\,\text{eV}$, see section 1.2.2); this is the case, e.g., for neutrinos. In the latter case DM is called *warm*: it is non–relativistic by equality epoch. Density perturbations grow differently at radiation domination and matter domination, and that this growth strongly depends on whether DM is relativistic or not at equality. This is the reason for distinguishing hot and warm DM [Rubakov and Gorbunov, 2017].

Incorporating NCDM relics into a Boltzmann code is a complex task, as it requires tracking perturbations in the distribution function across a momentum grid. Standard Boltzmann codes typically sample distributions

6 Making the rather natural assumption that dark matter particles X were in kinetic equilibrium with conventional matter in the early Universe.

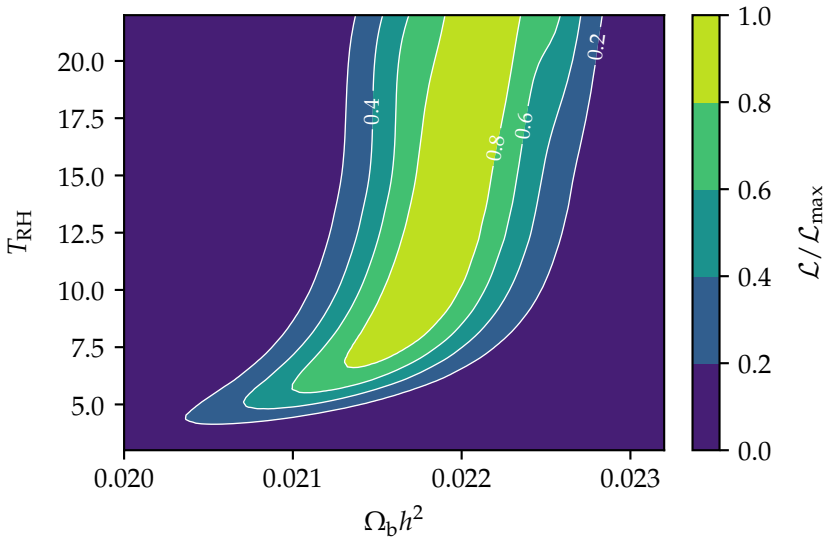

Figure 3.7: Contour plots for the pure BBN likelihood function (normalized to the maximum) in the $T_{\rm RH} - \Omega_{\rm b}h^2$ plane.

uniformly, employing a fixed step size and a predetermined maximum momentum, which are optimized for the case of a Fermi–Dirac distribution function, $f_{\rm FD}(y)$. Furthermore, the analytic form of $f_{\rm FD}(y)$ is often hard–coded within these codes and implicitly assumed in various contexts, such as in the relationship between mass and density. This rigid framework poses significant challenges for studying alternative models, including neutrinos with chemical potentials and flavor oscillations, neutrinos with non–thermal corrections, sterile neutrino species, or various warm dark matter candidates [Lesgourgues and Tram, 2011].

For these reasons, the NCDM implementation in `CLASS` provides an optimal platform for modeling non–thermal neutrinos. Our approach uses the flavor neutrino spectra calculated in section 3.3 as input to `CLASS`, corresponding to a given reheating temperature, $T_{\rm RH}$. For intermediate temperatures not explicitly computed with `FortEPiaNO`, we employ interpolation. The modifications to the Boltzmann solver were implemented at the interface level, enabling the dynamic passing and interpolation of distribution functions directly from the MCMC sampler. Unlike the standard version of `CLASS`, where distribution functions are typically provided via files, our approach ensures seamless communication between the two codes by passing these functions as lists.

Let us note that, within the redshift window relevant to our analysis—ranging from the last scattering surface ($z_{\rm rec} \simeq 1100$) for the computation of CMB anisotropies to essentially the present day for late–time observables—neutrinos can be approximated as completely free–streaming. By this time, they are well past their decoupling epoch, and their distribution functions evolve self–similarly, being simply redshifted by the expansion of the Uni-

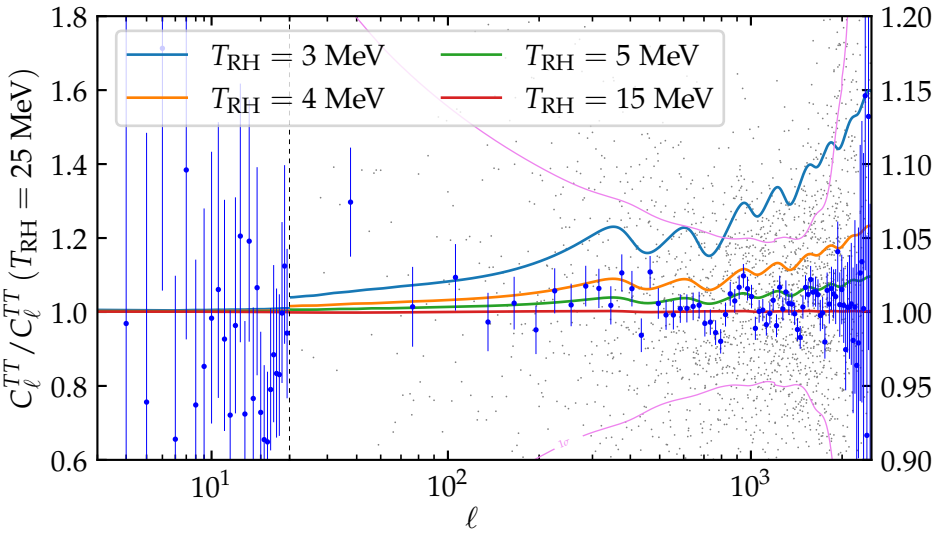

Figure 3.8: Plot of the difference between TT power spectrum of our benchmark model (ΛCDM + $T_{\rm RH} = 25$ MeV) and models with varying reheating temperature. To have an idea of the experimental constraining power we have superimposed residuals of the TT power spectrum (with respect to the benchmark model) as reported by the Planck collaboration [Aghanim et al., 2020b]. At $\ell = 30$, where the horizontal axis switches from logarithmic to linear, the vertical scale changes from the left to the right axis. The blue points are Planck 2018 data, unbinned in the $\ell < 30$ region and binned elsewhere. The 1σ violet region corresponds to the errors of the unbinned data points (which are in grey).

verse. As a result, only the final step of the time evolution described in section 3.3 is relevant for this purpose.

In section 3.3, we expressed the neutrino density matrix in terms of flavor eigenstates. This choice is customary in the study of neutrino decoupling, as interactions with the plasma are naturally described in the flavor basis, and the corresponding collision integrals are written in this form. However, once neutrinos decouple, they propagate through the Universe in their physical states, which correspond to the mass eigenstates. Consequently, in cosmological perturbation theory, it is preferable to write the Boltzmann equation in the mass basis. This approach is advantageous because it establishes a direct relationship between the mass and the energy density of each eigenstate and their respective effects on the large–scale structure of the Universe and its expansion rate. Specifically, the neutrino distribution functions in the mass basis, $f_{\nu_i}(y)$ ($i = 1, 2, 3$), and in the flavor basis, $f_{\nu_\alpha}(y)$ ($\alpha = e, \mu, \tau$), are related by:

$$f_{\nu_i}(y) = \sum_{\alpha=e,\mu,\tau} |U_{\alpha i}|^2 \, f_{\nu_\alpha}(y) \,, \tag{3.39}$$

where U denotes the PMNS matrix. The matrix elements are set to the best–fit values for the normal mass hierarchy, as determined by the global analysis of oscillation data in Salas et al. (2021).

To analyze the cosmological phenomenology of models with a very low reheating temperature, it is crucial to recognize that, using the results from section 3.3, a direct relationship can be established between $T_{\rm RH}$ and the effective number of relativistic species, $N_{\rm eff}$. Specifically, $N_{\rm eff}$ is not an independent parameter; it is determined solely by the neutrino energy density and, consequently, by their distribution functions. As shown in fig. 3.3, these distribution functions are suppressed as the reheating temperature decreases, leading to a one–to–one mapping between $T_{\rm RH}$ and $N_{\rm eff}$. This relationship is clearly illustrated in fig. 3.5.

Boltzmann solvers, such as `CLASS`, can automatically compute the correct value of $N_{\rm eff}$ for non–thermal neutrinos, provided the distribution functions are supplied. This is achieved through an internal integration of the distribution functions to compute their energy density. However, this introduces a small complication in our methodology. Due to differences in the integration algorithms, the values of $N_{\rm eff}$ obtained from `CLASS` and `FortEPiaNO` slightly differ. For clarity, we refer to the value computed by `CLASS` as $N_{\rm eff}$ and the value computed by `FortEPiaNO` as $N_{\rm eff}^{FP}$. This discrepancy presents an issue only when sampling extended models that directly involve $N_{\rm eff}$ as a parameter. In a standard ΛCDM cosmology, this is not a concern, as $N_{\rm eff}$ does not appear explicitly in the evolution equations; instead, the distribution function is consistently integrated, ensuring coherence. However, when $N_{\rm eff}$ is explicitly sampled, we adopt $N_{\rm eff}^{FP}$ as the prescription for the effective number of relativistic species to maintain consistency when translating it into a reheating temperature using the relationship in fig. 3.5. Note that this relationship is always expressed in terms of $N_{\rm eff}^{FP}$.

3.5.1 Theoretical background

The primary expected phenomenology of this model closely aligns with that of an extended cosmological model featuring a modified $N_{\rm eff}$. This topic has been extensively studied in dedicated works [Bashinsky and Seljak, 2004; Hou et al., 2013], and here we provide a brief summary of the main consequences.

The most intuitive approach to comparing models with varying relativistic neutrino energy densities is to assume that all other cosmological parameters remain fixed. Under this assumption, an increased neutrino energy density corresponds to a higher total radiation energy density, which delays the radiation–to–matter equality. Consequently, at the time of recombination, the Universe is more radiation–dominated compared to the standard cosmological model. This results in a gravitational potential that continues to decrease, acting as a driving force on the oscillations of the photon–baryon fluid and thereby enhancing the height of the acoustic peaks in the CMB power spectrum. Higher values of $N_{\rm eff}$ also lead to a faster expansion rate prior to photon decoupling. This reduces the size of the sound horizon at recombination, shifting the angular scale of the acoustic peaks towards smaller scales, or

equivalently, to higher multipole moments, ℓ. Similarly, variations in N_{eff} introduce minor changes to the diffusion damping scale. However, the damping scale is primarily sensitive to changes in the expansion history occurring just before recombination, making its dependence on N_{eff} significantly less pronounced than that of the sound horizon.

These effects are not uniquely attributable to variations in the neutrino energy density. Instead, due to degeneracies between cosmological parameters, they can be mimicked by various other transformations. This necessitates a more robust approach to isolate and characterize the specific impact of N_{eff}. Following the methodology outlined in Bashinsky and Seljak (2004) and summarized in Hou et al. (2013) and Lesgourgues et al. (2013), we assess the effects of different reheating temperatures-—and consequently variations in N_{eff}—-on CMB spectra by proportionally enhancing or diluting the energy densities of radiation, matter, and dark energy.

By increasing the matter density, we ensure that the redshift of matter–radiation equality remains fixed. Specifically, when this is done while keeping the baryon fraction constant (by adjusting the amount of Cold Dark Matter (CDM)), the balance between gravity and pressure in the tightly coupled photon–baryon fluid remains unaffected. This approach prevents any artificial alterations to the contrast between odd and even peaks, which could otherwise arise as a side effect of our transformation. This adjustment also modifies the expansion history after recombination, including the angular diameter distance to recombination. However, the latter changes by the same factor as the sound horizon, ensuring that the positions of the acoustic peaks in the CMB power spectrum remain unchanged.

Finally, the effect on the damping scale, which cannot be compensated by adjusting other parameters, emerges as a distinctive characteristic of our models. Together with perturbation effects, this provides a clear signature of variations in N_{eff}. This behavior is illustrated in fig. 3.8, where the colored curves represent the spectra of models with lowered reheating temperatures normalized to the standard ΛCDM spectrum. In this ratio, a step–like enhancement with superimposed oscillations is evident, along with a sharp increase for $\ell > 800$. The latter is primarily attributed to the shift of the diffusion damping scale towards higher multipoles.

It is worth noting that all other parameters are unrelated to the specific effects described above and can therefore be held fixed during this transformation.

In particular, a comparison between models with low T_{RH} and those with correspondingly reduced N_{eff} reveals that the differences, attributable to features in the distribution functions specific to low reheating scenarios, are at most around 1% in the C_ℓ coefficients. These observations are consistent with the findings of Alvey et al. (2022), which demonstrate that current and next–generation cosmological data are unlikely to detect specific features in the neutrino distribution functions. Instead, such data are primarily sen-

sitive to integrated properties, such as $N_{\rm eff}$ or $\rho^{\rm NR}_{\nu,0}$. Nevertheless, despite these qualitative considerations, our analysis employs the full form of the neutrino distribution function to capture all associated phenomenology with the highest possible accuracy.

3.5.2 Methodology and datasets

We conducted a MCMC analysis to sample posterior distributions for the parameters of our model and compute the corresponding Bayesian confidence intervals. For this, we employed the Metropolis–Hastings algorithm as implemented in our modified version of the MCMC sampler `MontePython` [Audren et al., 2013; Brinckmann and Lesgourgues, 2019], which is interfaced with our customized version of the Boltzmann solver `CLASS` [Blas et al., 2011; Lesgourgues and Tram, 2011] to generate theoretical predictions for the power spectra. Posterior distributions were analyzed and visualized using the `GetDist` package [Lewis, 2019].

Building on the discussion in the previous section, low–reheating models can be viewed as a simple extension of the standard cosmological model (or ΛCDM model) with one additional parameter: the reheating temperature, $T_{\rm RH}$. The 7–dimensional parameter space of our model is represented as

$$\Theta_{T_{\rm RH}} = \left\{\omega_{\rm b}, \omega_{\rm c}, 100\theta_{\rm s}, \log\left(10^{10} A_{\rm s}\right), n_{\rm s}, \tau_{\rm reio}, T_{\rm RH}\right\}, \tag{3.40}$$

where $\omega_{\rm b} \equiv \Omega_{\rm b} h^2$ and $\omega_{\rm c} \equiv \Omega_{\rm c} h^2$ are the present–day density parameters of baryons and cold dark matter, respectively. Here, $\theta_{\rm s}$ denotes the angular size of the sound horizon at recombination, $A_{\rm s}$ is the initial super–horizon amplitude of curvature perturbations (evaluated at a pivot scale of $k_* = 0.05\,{\rm Mpc}^{-1}$), $n_{\rm s}$ is the primordial scalar spectral index, and $\tau_{\rm reio}$ represents the optical depth to reionization. We assume a flat Universe with purely adiabatic scalar primordial perturbations following a power–law spectrum.

All baseline ΛCDM parameters were sampled using flat prior distributions. For $T_{\rm RH}$, we adopted a flat prior in the range $T_{\rm RH} \in [3\,{\rm MeV}, 10\,{\rm MeV}]$ when sampled directly. Alternatively, when sampling over $N^{FP}_{\rm eff}$, a non–linear prior was used, the precise shape of which is illustrated in fig. 3.12. The effective prior in the case of $N^{FP}_{\rm eff}$ sampling will be discussed further in the text.

We also conducted a series of runs, referred to as $\Lambda{\rm CDM} + T_{\rm RH} + m_\nu$, exploring the parameter space

$$\Theta_{T_{\rm RH}+m_\nu} = \left\{\omega_{\rm b}, \omega_{\rm c}, 100\theta_{\rm s}, \log\left(10^{10} A_{\rm s}\right), n_{\rm s}, \tau_{\rm reio}, T_{\rm RH}, m_\nu\right\}, \tag{3.41}$$

where the sum of neutrino masses was allowed to vary along with the other cosmological parameters. We assumed all neutrino mass eigenstates to be degenerate, with the individual mass m_ν drawn from a uniform prior distribution, $m_\nu \geq 0$.

To test the robustness of cosmological constraints on the sum of neutrino masses in extreme low–reheating scenarios, we additionally imposed tighter priors on the reheating temperature

$$3\,\mathrm{MeV} \leq T_{\mathrm{RH}} \leq 7\,\mathrm{MeV}\,, \tag{3.42}$$

$$3\,\mathrm{MeV} \leq T_{\mathrm{RH}} \leq 6\,\mathrm{MeV}\,, \tag{3.43}$$

$$3\,\mathrm{MeV} \leq T_{\mathrm{RH}} \leq 5\,\mathrm{MeV}\,. \tag{3.44}$$

As described earlier, for each parameter set corresponding to a step in the Markov chain and a single realization of our model, interpolation tables were used to compute the helium abundance Y_p and assign the corresponding neutrino distribution function. This distribution function was then passed to the Boltzmann solver along with the other parameters. When sampling on N_{eff}^{FP}, we drew values from a uniform prior distribution

$$N_{\mathrm{eff}}^{FP} \in [2.14, 3.044], \tag{3.45}$$

where the lower limit corresponds to a reheating temperature of 3 MeV and the upper limit represents the theoretical prediction of the standard cosmological model. We restricted N_{eff}^{FP} to this range, as higher values are excluded by our model. When applying reduced priors to test the robustness of constraints on the sum of neutrino masses, the priors were adjusted accordingly.

To compute our parameter constraints, we utilized the most recent data on CMB temperature and polarization anisotropies, publicly released by the Planck collaboration in 2018, including information from lensing reconstruction [Aghanim et al., 2020b; c; d]. In addition to CMB data, we incorporated geometric information from BAO scale measurements obtained from various surveys: low–redshift galaxy samples from 6dFGS [Beutler et al., 2011] and SDSS–MGS [Ross et al., 2015], intermediate–redshift emission line galaxies from eBOSS DR16 [Mattia et al., 2021; Tamone et al., 2020], high–redshift quasars [Bautista et al., 2020; Gil-Marin et al., 2020; Hou et al., 2020; Neveux et al., 2020], and Lyman-α measurements and their correlations [Bourboux et al., 2020], combining data from BOSS DR12 [Alam et al., 2017] and eBOSS DR16 [Alam et al., 2021]. Throughout the following, we will refer to this combined data set as "Planck+lensing+BAO", which will serve as the primary data set for our analysis.

Given the increasing interest in recent results from the DESI collaboration, we also consider comparisons using the "Planck+lensing+DESI" data set, where the BAO measurements from BOSS/eBOSS are replaced by those from DESI. Additionally, we performed a global analysis by combining cosmological surveys with measurements of light element abundances. In this case, we refer to the combined data sets as "Planck+lensing+BAO+BBN" and "Planck+lensing+DESI+BBN," where BAO data are drawn from BOSS/eBOSS and DESI, respectively.

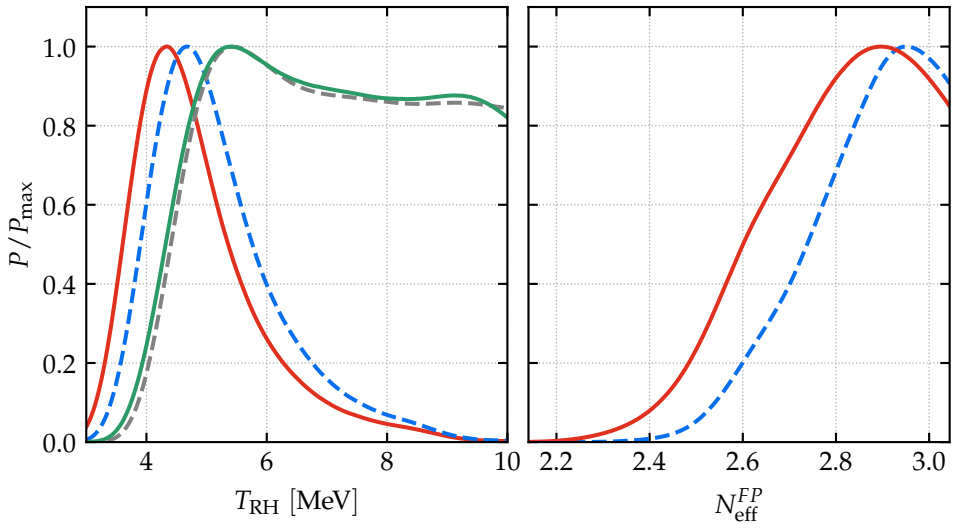

Figure 3.9: Posterior distributions for $T_{\rm RH}$ in the two sampling strategies adopted in the analysis with and without the implementation of the BBN consistency. In the case of $N_{\rm eff}^{FP}$ sampling also the original $N_{\rm eff}^{FP}$ posterior distributions are shown. Red an blue lines represent posteriors obtained with the $N_{\rm eff}^{FP}$ sampling, while green and gray lines those obtained with the $T_{\rm RH}$ sampling. Solid lines includes the effect of BBN consistency while dashed lines do not.

The likelihood functions for the CMB data sets mentioned above were evaluated and combined using the likelihood code distributed by the Planck collaboration [Aghanim et al., 2020b], which is publicly available through the Planck Legacy Archive (`https://pla.esac.esa.int/`). Furthermore, several "nuisance" parameters, accounting for unresolved foreground components, instrumental systematics, and other effects, were marginalized over during the analysis. All BOSS and eBOSS likelihoods were taken from the standard distribution of `MontePython` [Alvi et al., 2022; Audren et al., 2013; Brinckmann and Lesgourgues, 2019]. Finally, the DESI and BBN likelihoods were implemented as χ^2 functions, with tracers analogous to those of BOSS/eBOSS for the DESI Y1 results [Adame et al., 2024b] and light element abundances from PDG 2022 [Workman et al., 2022] (see section 3.4).

3.5.3 Results and discussion

As an initial step to test our setup, we performed a run with $T_{\rm RH}$ fixed to 25 MeV. As discussed in section 3.3, for $T_{\rm RH} > 15$ MeV, reheating occurs early enough to ensure that all neutrinos reach thermal equilibrium, effectively recovering a standard ΛCDM scenario. The results of this preliminary run, compared to the Planck collaboration results for the analogous data set, revealed that all differences were below 10% of σ for the relevant parameters, indicating full compatibility.

We then proceeded with Monte Carlo runs for the extended $\Lambda\text{CDM} + T_{\text{RH}}$ cosmological model. Unlike previous analyses (including our own past work and others in the literature), we conducted the runs using two parallel approaches: direct sampling on T_{RH} and sampling on N_{eff}^{FP}. While T_{RH} is the parameter with the most direct physical interpretation within our model, its highly non–linear relationship with N_{eff} poses a challenge. Direct sampling on T_{RH} tends to concentrate the sampling time on models close to the standard scenario ($N_{\text{eff}} \simeq 3$), thereby reducing the statistical weight for scenarios with significant out–of–equilibrium neutrino production. Conversely, sampling on N_{eff}^{FP} allows us to directly control the statistical weight of these scenarios. By applying a linear prior on N_{eff}^{FP}, we ensure that very out–of–equilibrium scenarios are sampled with the same probability as those close to equilibrium, enabling a more comprehensive exploration of the parameter space.

From these analyses, we derived the following 95% lower limits on the reheating temperature

$$T_{\text{RH}} > 4.47\,\text{MeV} \quad \text{(Planck+lensing+BAO)}\,, \tag{3.46}$$

based on the T_{RH} sampling, and

$$T_{\text{RH}} > 3.86\,\text{MeV} \quad \text{(Planck+lensing+BAO)}\,, \tag{3.47}$$

from the N_{eff}^{FP} sampling. The corresponding posterior distributions for T_{RH} and N_{eff}^{FP} are displayed in fig. 3.9.

The posterior distributions reveal that, when sampling on N_{eff}^{FP}, we do not directly obtain a lower limit on the reheating temperature but rather a full constraint. However, this result is evidently non–physical. Upon investigation, we determined that this artifact arises from the derivative of the coordinate transformation between N_{eff}^{FP} and T_{RH} when converting the posterior of N_{eff}^{FP} into a posterior for T_{RH}. This phenomenon is a known artifact in Bayesian statistics. To address this issue, we argue that the most reliable method to derive a lower limit on T_{RH} from N_{eff}^{FP} is to transform only the lower limit of N_{eff}^{FP}, rather than the entire posterior distribution. This approach was used to compute the limit presented in eq. (3.47).

The limit in eq. (3.46) is directly comparable to that obtained in our previous analysis [Salas et al., 2015]. According to the results of the Planck collaboration, the new and old data sets yield similar values for N_{eff}, with the newer data sets featuring slightly smaller error bars. Therefore, at first glance, one would therefore expect a tighter lower limit on T_{RH} compared to the previous analysis. However, the limits derived here are nearly identical to the earlier ones. We traced this behavior to the updates in the code used for the computation of neutrino distribution functions. The new physics incorporated into `FortEPiaNO` systematically shifts N_{eff} to lower values, as noted in section 3.3. This shift counterbalances the impact of reduced error bars on N_{eff}, thereby preventing a significant tightening of the lower limit on T_{RH}.

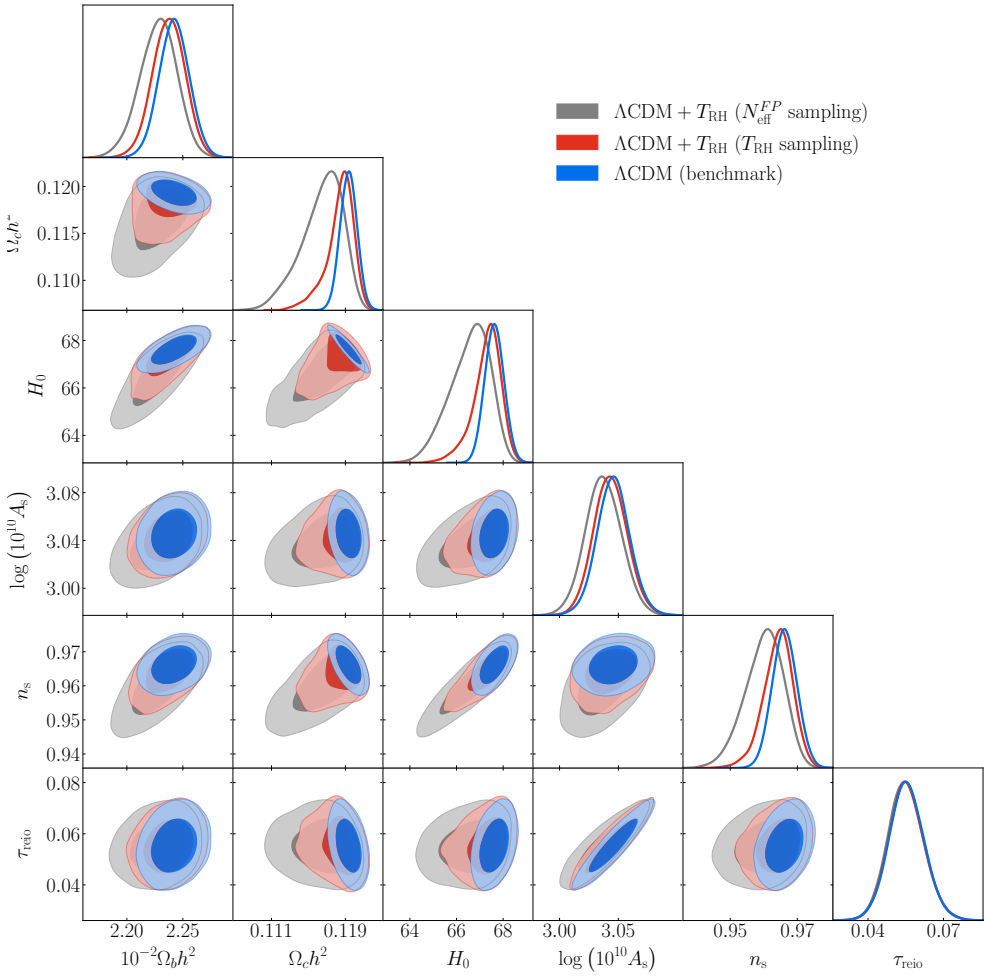

Figure 3.10: Triangle plot including one–dimensional posteriors and two-dimensional 68% and 95% credible regions for six cosmological parameters of the ΛCDM + T_{RH} model (plus the standard ΛCDM model shown as a benchmark reference) obtained from runs on the Planck+lensing+BAO data set. Note in particular the impact of the different sampling strategies on the posteriors of the various parameters. Numerical results with error bars are shown in Tab. 3.1.

It is worth noting that the limit derived from the N_{eff}^{FP} sampling runs is lower than the one obtained from direct T_{RH} sampling. We attribute this to the improved exploration of the low–reheating–temperature region of the parameter space when sampling on N_{eff}^{FP}. This approach assigns greater statistical weight to these scenarios, thereby shifting the limit to lower values. This effect is further corroborated by the behavior of the posterior distributions for all other parameters of the ΛCDM model, as shown in fig. 3.10.

When enabling BBN consistency-—i.e., a consistent computation of the helium fraction based on the baryon density and reheating temperature, using the BBN evolution computed with `PArthENoPE` as described in section 3.4—-the posterior distributions of cosmological parameters change as shown in fig. 3.11. This figure also includes the posterior distributions from runs

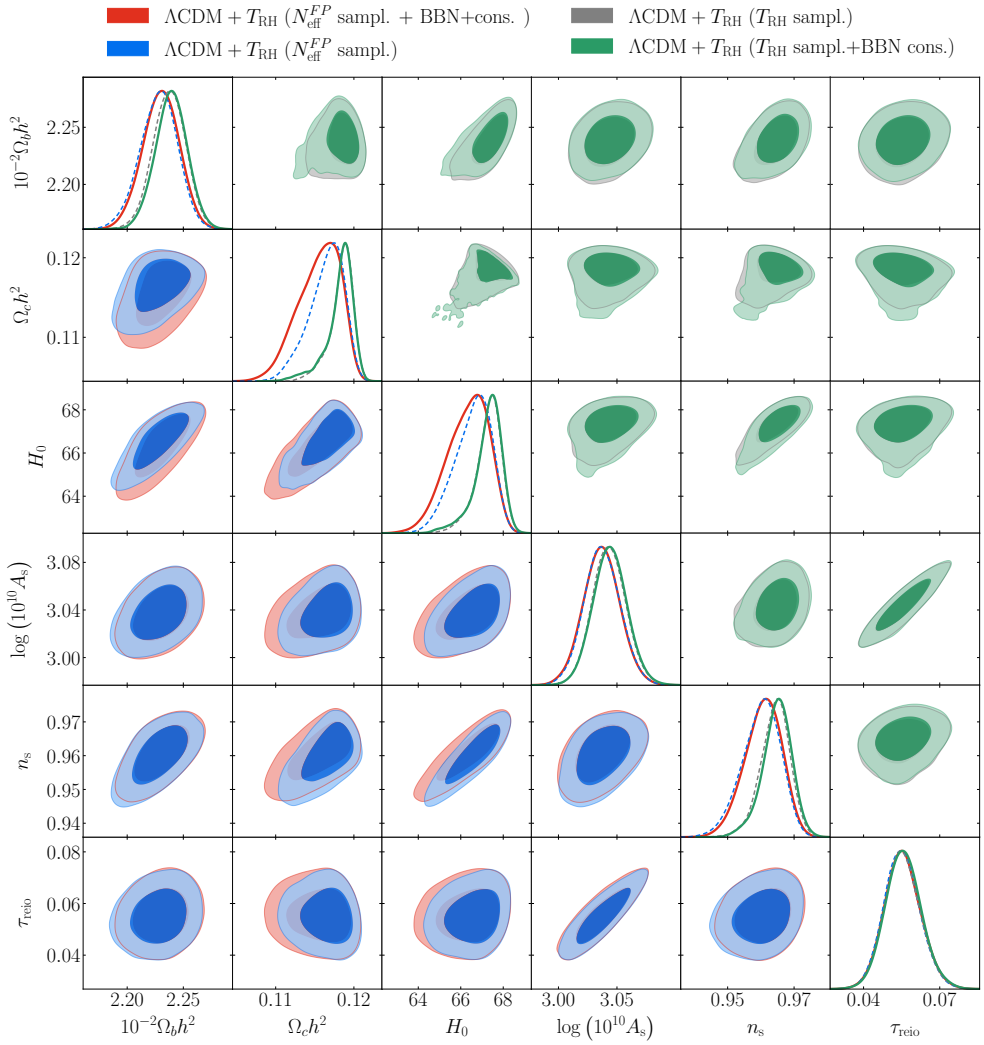

Figure 3.11: Double triangle plot including one–dimensional posteriors and two-dimensional 68% and 95% credible regions for six cosmological parameters of the ΛCDM + $T_{\rm RH}$ model (plus the standard ΛCDM model shown as a benchmark reference) obtained from runs on the Planck+lensing+BAO data set. Note in particular the impact of the different sampling strategies and of the addition of the BBN consistency on the posteriors of the various parameters. Numerical results with error bars are shown in Tab. 3.2.

Parameter	ΛCDM + T_{RH} (N_{eff}^{FP} sampling)	ΛCDM + T_{RH} (T_{RH} sampling)	ΛCDM
$10^{-2}\Omega_b h^2$	$2.228^{+0.031}_{-0.034}$	$2.237^{+0.028}_{-0.030}$	2.242 ± 0.026
$\Omega_c h^2$	$0.1164^{+0.0039}_{-0.0047}$	$0.1183^{+0.0027}_{-0.0035}$	0.1193 ± 0.0018
$\log(10^{10} A_s)$	$3.037^{+0.031}_{-0.030}$	$3.043^{+0.029}_{-0.028}$	3.046 ± 0.028
n_s	$0.960^{+0.011}_{-0.012}$	$0.9640^{+0.0090}_{-0.0095}$	$0.9662^{+0.0073}_{-0.0071}$
τ_{reio}	0.055 ± 0.014	0.055 ± 0.014	0.055 ± 0.014
H_0	$66.6^{+1.5}_{-1.8}$	$67.3^{+1.2}_{-1.4}$	$67.62^{+0.81}_{-0.80}$

Table 3.1: 95% Bayesian credible intervals for the basic six cosmological parameters of the ΛCDM + T_{RH} model obtained from runs on the Planck+lensing+BAO data set. Different columns refers to different sampling strategies, as indicated in the table, plus the standard ΛCDM model shown as a benchmark reference.

Parameter	ΛCDM + T_{RH} (N_{eff}^{FP} sampl+BBN cons.)	ΛCDM + T_{RH} (T_{RH} sampl.+BBN cons.)	ΛCDM
$10^{-2}\Omega_b h^2$	$2.230^{+0.031}_{-0.033}$	2.239 ± 0.028	2.242 ± 0.026
$\Omega_c h^2$	$0.1155^{+0.0046}_{-0.0053}$	$0.1182^{+0.0030}_{-0.0041}$	0.1193 ± 0.0018
$\log(10^{10} A_s)$	3.037 ± 0.031	$3.044^{+0.029}_{-0.028}$	3.046 ± 0.028
n_s	$0.961^{+0.010}_{-0.011}$	$0.9648^{+0.0087}_{-0.0094}$	$0.9662^{+0.0073}_{-0.0071}$
τ_{reio}	$0.055^{+0.015}_{-0.014}$	$0.056^{+0.015}_{-0.014}$	0.055 ± 0.014
H_0	$66.3^{+1.7}_{-1.9}$	$67.3^{+1.2}_{-1.5}$	$67.62^{+0.81}_{-0.80}$

Table 3.2: 95% Bayesian credible intervals for the basic six cosmological parameters of the ΛCDM + T_{RH} model obtained from runs on the Planck+lensing+BAO data set implementating BBN consistency. Different columns refers to different sampling strategies, as indicated in the table, plus the standard ΛCDM model shown as a benchmark reference.

without BBN consistency for reference. The posteriors of T_{RH} are presented again in fig. 3.9, providing the following 95% lower limits

$$T_{RH} > 4.47\,\text{MeV} \quad \text{(Planck+lensing+BAO)}\,, \tag{3.48}$$

from the T_{RH} sampling runs, and

$$T_{RH} > 3.62\,\text{MeV} \quad \text{(Planck+lensing+BAO)}\,, \tag{3.49}$$

from the N_{eff}^{FP} sampling runs.

It is evident that corrections due to BBN consistency have a greater impact when sampling on N_{eff}^{FP} than on T_{RH}, although the magnitude of these corrections remains small in both cases. This behavior can again be attributed to the more efficient sampling of the low–temperature region of the parameter space achieved with the N_{eff}^{FP} strategy. When sampling on T_{RH}, the MCMC chains spend most of their time in a temperature range corresponding to very small deviations of N_{eff} from its standard value. As a result, the helium

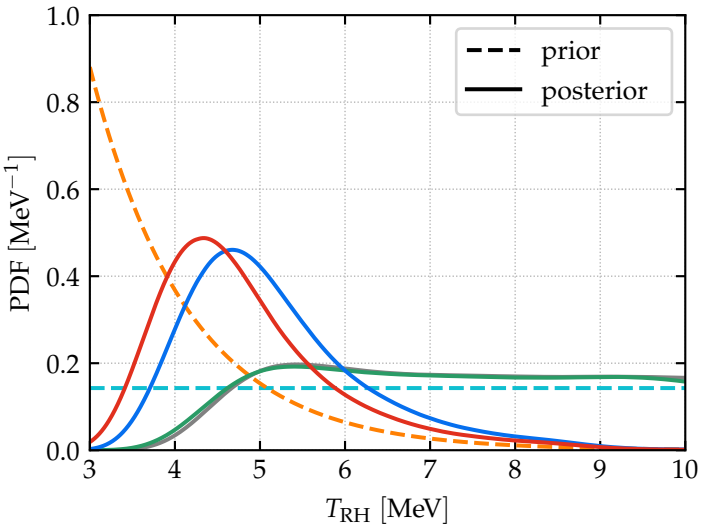

Figure 3.12: Comparison between prior and posterior distributions for $T_{\rm RH}$ in the two sampling strategies adopted in the analysis, with and without the implementation of the BBN consistency. Red (green) an blue (gray) lines represent posteriors obtained with the $N_{\rm eff}^{FP}$ sampling ($T_{\rm RH}$ sampling) with and without the implementation of BBN consistency respectively. Cyan and orange dashed lines represent the prior distributions for $T_{\rm RH}$ and $N_{\rm eff}^{FP}$ sampling strategies respectively.

abundance does not vary significantly, as illustrated in fig. 3.6, leading to cosmologies that are nearly identical with or without BBN consistency. In such cases, the differences are comparable to Monte Carlo noise.

Conversely, with $N_{\rm eff}^{FP}$ sampling, the low–temperature region is better explored, granting greater statistical weight to models with more significant corrections to the helium abundance. The helium abundance has an effect on the CMB damping tail opposite to that of $N_{\rm eff}$. A higher helium fraction, as observed at low reheating temperatures due to earlier recombination relative to hydrogen, results in fewer free electrons. This reduction in free electrons increases the photon mean free path, reducing the efficiency of diffusion and causing a greater loss of power at smaller scales (higher ℓ). Consequently, when enabling BBN consistency, disfavored models—-such as those with very low $N_{\rm eff}$-—become more favorable due to the increased helium fraction, which partially counterbalances the effects of $N_{\rm eff}$. This is reflected in the more pronounced left tail of the reheating temperature posterior distribution shown in fig. 3.9.

The sampling challenges inherent to low reheating models, as discussed above, necessitated the use of two complementary sampling strategies in our analysis. The $T_{\rm RH}$ sampling is the most physically motivated, as it directly represents the physical meaning of the model and avoids issues related to coordinate transformations. However, it exhibits clear sampling difficulties, particularly in its normalization, due to the very flat shape of the posterior. On the other hand, the $N_{\rm eff}^{FP}$ sampling enables better coverage of the farthest–

from–equilibrium region of the low reheating parameter space, ensuring a uniform exploration of all relevant regions at the cost of introducing a non–linear prior on the reheating temperature.

To assess the impact of these two different prior choices, we employed the Kullback–Leibler (KL) divergence. From a Bayesian perspective, this quantity is defined as

$$D_{\rm KL}(\mathcal{P}(\theta \mid D) \parallel \Pi(\theta)) = \int d\theta\, \mathcal{P}(\theta \mid D) \log\left[\frac{\mathcal{P}(\theta \mid D)}{\Pi(\theta)}\right], \tag{3.50}$$

where θ represents the parameter vector and D denotes the data. The KL divergence measures the information gain provided by the data in updating the prior distribution, Π, to the posterior, $\mathcal{P}$. A larger divergence indicates that the data contribute more significantly to the posterior compared to the prior. For readers interested in further details about the KL divergence and its applications, we refer to appendix A.

In fig. 3.12, we present all the distributions required to compute the KL divergence. Notably, we highlight the non–linear prior used in the $N_{\rm eff}^{FP}$ sampling strategy. This prior was obtained by transforming the flat prior on $N_{\rm eff}^{FP}$ using a mapping that preserves probability. Specifically, it was not sufficient to apply the inverse transformation of fig. 3.5; the derivative of the coordinate transformation was also accounted for to properly adjust the measure of the probability integrals. In contrast, the prior for the $N_{\rm eff}^{FP}$ sampling strategy is simply a uniform distribution.

The posteriors shown in fig. 3.12 were derived from runs on the Planck+lensing+BAO data set, both with and without the inclusion of BBN consistency. All distributions in fig. 3.12 were normalized to have a unit integral over their support, ensuring they are properly defined as Probability Density Function (PDF)s.

From the computation of the KL divergence, we obtain

$$D_{\rm KL}\left(\mathcal{P}^{T_{\rm RH}}_{T_{\rm RH}} \parallel \Pi^{T_{\rm RH}}_{T_{\rm RH}}\right) = 0.64\,, \tag{3.51}$$

$$D_{\rm KL}\left(\mathcal{P}^{N_{\rm eff}^{FP}}_{T_{\rm RH}} \parallel \Pi^{N_{\rm eff}^{FP}}_{T_{\rm RH}}\right) = 0.15\,, \tag{3.52}$$

$$D_{\rm KL}\left(\mathcal{P}^{T_{\rm RH}+Y_p}_{T_{\rm RH}} \parallel \Pi^{T_{\rm RH}+Y_p}_{T_{\rm RH}}\right) = 0.40\,, \tag{3.53}$$

$$D_{\rm KL}\left(\mathcal{P}^{N_{\rm eff}^{FP}+Y_p}_{T_{\rm RH}} \parallel \Pi^{N_{\rm eff}^{FP}+Y_p}_{T_{\rm RH}}\right) = 0.10\,. \tag{3.54}$$

From these values, it is evident that a slight preference exists for the $N_{\rm eff}^{FP}$ sampling strategy, which remains mildly reduced but stable when BBN consistency is included. The minor reduction in preference when BBN consistency is considered likely stems from the decreased constraining power in this case, due to the partial counterbalance provided by the consistent computation of the helium fraction, as explained in the previous paragraph. Thus, the use of a non–linear prior on $T_{\rm RH}$ does not introduce fictitious information, as might initially be expected. Instead, it allows us to extract more information from the data by enabling a more thorough exploration of the parameter space.

Different methods were tested for computing the derivative of the coordinate transformation between $N_{\rm eff}^{FP}$ and $T_{\rm RH}$ to ensure robustness in the KL divergence calculations. As described previously, this mapping was constructed using the points obtained from the `FortEPiaNO` runs shown in fig. 3.5. Due to the computational expense of these runs, a moderate density of points was used. Consequently, when directly differentiating the interpolation function, a step–like structure appeared in the computed derivative. To verify that this artifact did not significantly affect the KL divergence results, we tested two alternative approaches: smoothing the derivative after computation and analytically interpolating the coordinate transformation prior to differentiation. Both tests confirmed that the KL divergence is essentially insensitive to the specific parameterization of the coordinate transformation. Therefore, in our final analysis, we use the results derived directly from the computation using the true `FortEPiaNO` points.

As anticipated in section 3.5.2, we reproduced all runs using the BAO measurements from the DESI collaboration instead of those from BOSS/eBOSS, as used in our main dataset. The qualitative discussion remains identical to that presented earlier, with no significant differences observed. Therefore, we simply report the 95% lower limits on the reheating temperature derived from these runs

$$T_{\rm RH} > 4.49\,{\rm MeV} \quad \text{(Planck+lensing+DESI)}\,, \tag{3.55}$$

based on the $T_{\rm RH}$ sampling strategy, and

$$T_{\rm RH} > 3.78\,{\rm MeV} \quad \text{(Planck+lensing+DESI)}\,, \tag{3.56}$$

from the $N_{\rm eff}^{FP}$ sampling strategy. It is worth noting that, in both cases, these results show only a slight tightening of the lower limits compared to those obtained from the Planck+lensing+BAO dataset.

Building on our previous analysis, we investigated the behavior of the limits on the sum of neutrino masses, $\sum m_\nu$, within low reheating scenarios. For this purpose, we performed runs using both $T_{\rm RH}$ and $N_{\rm eff}^{FP}$ sampling strategies, applying progressively tighter priors to force the MCMC chains to explore regions of the parameter space beyond those that essentially reproduce the standard $\Lambda{\rm CDM} + \sum m_\nu$ scenario.

Unlike our earlier findings, we found no evidence for a relaxation of the limits on the sum of neutrino masses when using the complete data set. To better understand this discrepancy, we repeated the runs using only Planck 2018 data and Planck data combined with lensing data, excluding the BAO measurements from the full data set. The results obtained using Planck data alone, which replicate the conditions of our previous analysis, exhibit a relaxation of the neutrino mass bounds at lower reheating temperatures for both the $T_{\rm RH}$ and $N_{\rm eff}^{FP}$ sampling strategies. However, this effect diminishes progressively with the inclusion of lensing and BAO data. We interpret this behavior as follows: the additional constraining power provided by the

lensing and BAO data sets restricts the parameter space, effectively ruling out regions where the neutrino mass bounds were allowed to have freedom. Consequently, the limits on $\sum m_\nu$ become consistent across the low–reheating parameter space when the full data set is employed. The results from these runs, obtained using the $N_{\rm eff}^{FP}$ sampling strategy, are illustrated in fig. 3.13. This figure highlights the progressive tightening of the mass bounds as additional data sets are incorporated.

As a final task, we performed a series of runs on a joint data set that includes both CMB data and BBN measurements. These runs were conducted using our main data set, Planck+lensing+BAO, and additionally with Planck+lensing+DESI to provide a comparison incorporating more recent BAO measurements. The trends observed are consistent across all cases: the inclusion of BBN measurements significantly enhances the constraining power of the data sets. This effect is particularly pronounced when sampling on $N_{\rm eff}^{FP}$. Due to the flat behavior of the mapping between $N_{\rm eff}^{FP}$ and $T_{\rm RH}$ in the high reheating temperature region of the parameter space (see fig. 3.5), this sampling strategy becomes less effective in this regime. This is reflected in the extremely narrow shapes of the posteriors obtained in these cases, indicating reduced exploration of the parameter space at higher reheating temperatures.

The final 95% lower limits on the reheating temperature, using the most accurate implementation of the model, are

$$T_{\rm RH} > 6.69\,{\rm MeV} \quad \text{(Planck+lensing+BAO)}\,, \tag{3.57}$$

$$T_{\rm RH} > 6.75\,{\rm MeV} \quad \text{(Planck+lensing+DESI)}\,, \tag{3.58}$$

from the runs with the $T_{\rm RH}$ sampling strategy, and:

$$T_{\rm RH} > 5.56\,{\rm MeV} \quad \text{(Planck+lensing+BAO)}\,, \tag{3.59}$$

$$T_{\rm RH} > 5.85\,{\rm MeV} \quad \text{(Planck+lensing+DESI)}\,, \tag{3.60}$$

from the runs with the $N_{\rm eff}^{FP}$ sampling strategy. These results mirror the qualitative behavior observed in earlier stages of the analysis. The $N_{\rm eff}^{FP}$ sampling strategy yields slightly lower limits on $T_{\rm RH}$ due to its enhanced exploration of the low–reheating–temperature region of the parameter space. Additionally, for a given sampling strategy, replacing BOSS/eBOSS BAO measurements with those from DESI leads to slightly tighter limits, reflecting the improved precision of the DESI data.

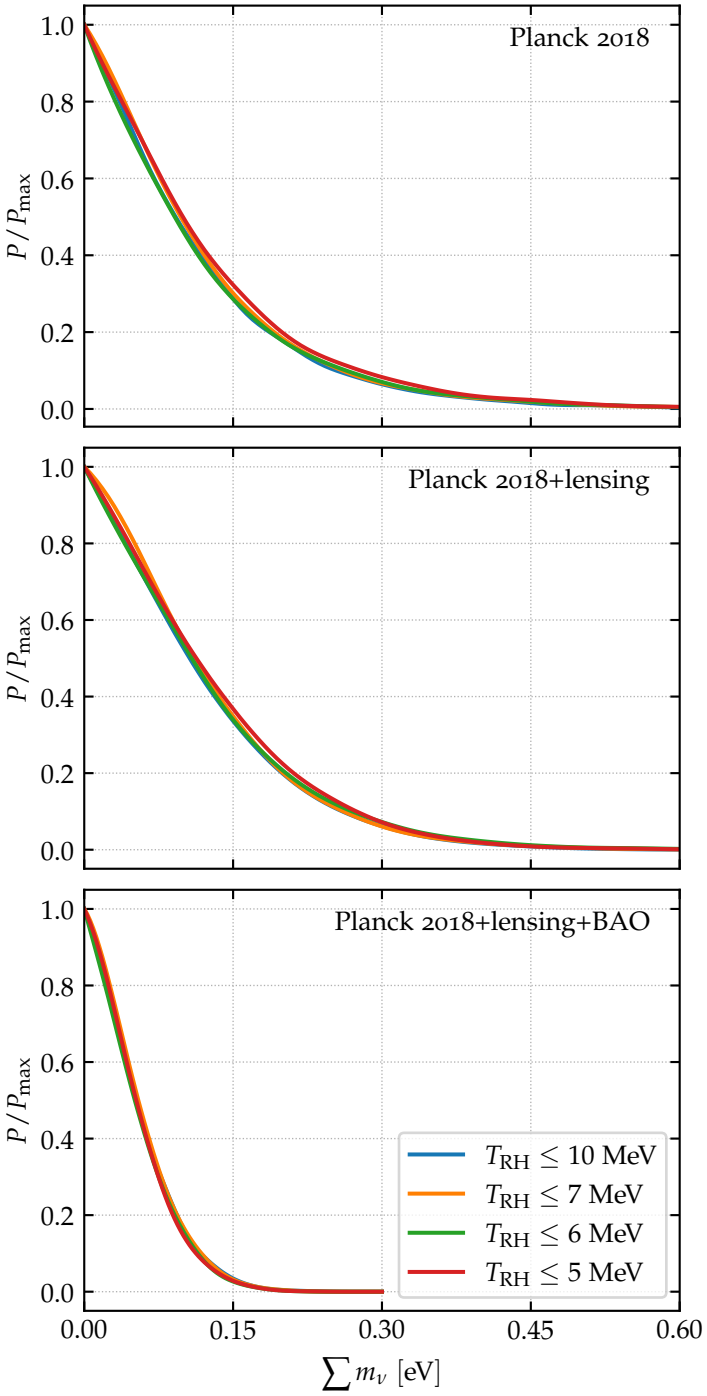

Figure 3.13: Comparison between posteriors on the sum of neutrino masses, $\sum m_\nu$, for different combinations of the data sets included in the full one considered in the main analysis. In each plot we asses the effect of a lowered reheating temperature, $T_{\rm RH}$, by means of ever narrower priors.

4 OPTICAL ACTIVITY OF NON–STANDARD NEUTRINO INTERACTIONS

The discussion in this chapter is focused on the optical activity induced by neutrino NSI in the early Universe, exploring how such effects can leave imprints on CMB polarization, and it is based on the results reported in Barbieri et al. (2025a).

We start in section 4.1 outlining the basic aspects of the formalism of Quantum Boltzmann Equation (QBE)s emphasizing its application to the study of photon propagation in the early Universe, and contextualizing the choice of our phenomenological scenario. In section 4.2 we carried out the calculations for the forward scattering considering both at tree–level and 1–loop corrections to neutrino photon scattering in our model. We then move to the evaluation of the collision term for the tree–level process in section 4.3 presenting the full reduction of collision integral. Finally we write the evolution equations and discuss the main oberservation consequences in section 4.4.

4.1 METHODOLOGY

Our object of interest will be the expectation value of bilinears of creation/annihilation operators. In this formalism the evolution of each momentum mode will be described by a square matrix whose size is determined by the number of discrete degrees of freedom. Conventional number densities will be given by the diagonal entries and coherences naturally as the off–diagonal ones. The kinetic equation that pertains to this matrix is usually referred to as the *density matrix equation* or the QBE. Notice however that the described object is actually a matrix of number densities that is fundamentally different from what it is usually referred to as a density matrix, which instead is a quantum mechanical operator which we will refer to as the *density operator*.

The derivation presented here applies techniques previously developed in the context of neutrino mixing in an interacting medium [Raffelt et al., 1993; Sigl and Raffelt, 1993]. For earlier works in this direction is useful to see [Barbieri and Dolgov, 1991; Dolgov, 1981]. As discrete quantum number, additionnaly to the flavor, also the helicity can be taken into account thanks to this formalism. Some good examples of this alternative possiblity can be found in [Rudzsky, 1990; Serreau and Volpe, 2014; Vlasenko et al., 2014]. In particular, after a first general discussion, we will focus our attention exactly

on the helicity to study the case of the CMB photons [Bartolo et al., 2019; 2018; Hoseinpour et al., 2020; Zarei et al., 2021].

4.1.1 Formalism: the QBE

This methodology can be fully understood starting working in the Heisenberg picture in which the states are time–independent (see appendix C). To follow the historical development of the formalism we start considering the case of a fermion field (at the end fo the derivation we will briefly show how the results can be adapted to the case of bosons, and then we will go on in that scenario), but we include just the helicity as discrete degree of freedom in the view of our subsequent application. The associated quantum field is decomposed as [Schwartz, 2014]

$$\psi(x) = \sum_s \int \frac{d^3\mathbf{p}}{(2\pi)^3 2E_\mathbf{p}} \left[\hat{a}_s(\mathbf{p}, t_0) u_s(p) e^{-ip\cdot x} + \hat{b}_s^\dagger(\mathbf{p}, t_0) v_s(p) e^{ip\cdot x}\right] . \quad (4.1)$$

In this expression, the creation and annihilation operators for particles and antiparticles satisfy the equal–time anticommutation rules

$$\left\{\hat{a}_r(\mathbf{p}, t), \hat{a}_s^\dagger(\mathbf{q}, t)\right\} = \left\{\hat{b}_r(\mathbf{p}, t), \hat{b}_s^\dagger(\mathbf{q}, t)\right\} = (2\pi)^3 2E_\mathbf{p} \delta_{rs} \delta^{(3)}(\mathbf{p} - \mathbf{q}) , \quad (4.2)$$

and all other anti–commutators vanish. Furthermore, $u_s(p)$ and $v_s(p)$ spinors are the plane–wave solution to the Dirac equation

$$(i\partial\!\!\!/ - m)\,\psi = 0 . \quad (4.3)$$

We are now able to define the main object of our formalism, the density matrix ρ for our fermionic particle and $\hat{\rho}$ for its antiparticle counterpart[1]

$$\left\langle \hat{a}_j^\dagger(\mathbf{p}, t)\, \hat{a}_i(\mathbf{q}, t) \right\rangle \equiv (2\pi)^3 2E_\mathbf{p} \delta^{(3)}(\mathbf{p} - \mathbf{q})\, \rho_{ij}(\mathbf{p}, t) , \quad (4.4)$$

$$\left\langle \hat{b}_i^\dagger(\mathbf{p}, t)\, \hat{b}_j(\mathbf{q}, t) \right\rangle \equiv (2\pi)^3 2E_\mathbf{p} \delta^{(3)}(\mathbf{p} - \mathbf{q})\, \bar{\rho}_{ij}(\mathbf{p}, t) . \quad (4.5)$$

To study the time evolution of density matrices is useful to lead back these bilinears to the definition of a quantum number operator

$$\hat{\mathcal{N}}_{ij}(\mathbf{p}, t) = \hat{a}_i^\dagger(\mathbf{p}, t)\, \hat{a}_j(\mathbf{p}, t) , \quad (4.6)$$

while an analogous definition can be made in case of antiparticles. From now on we focus our attention to the case of particles, a generalization to antiparticles case can be obtained with a few straightforward adaptations. According to eq. (4.4) the expectation value of $\hat{\mathcal{N}}_{ij}(\mathbf{p}, t)$ diverges because it involves a factor $(2\pi)^3 \delta^{(3)}(0)$ which is related to the infinite quantization volume necessary for our continuous momentum variables. However, the divergent factor cancels out of all physical results [Sigl and Raffelt, 1993].

1 The reversed order of the indices guarantees both matrices to transform in the same way under a unitary transformation $\psi' = U\psi$.

This operator follow the Heisenberg equation of motion (see eq. (C.6)). Splitting the Hamiltonian into the free field piece plus an interaction term

$$\hat{H}(t) = \hat{H}_0(t) + \hat{H}_{\rm int}(t) \ , \tag{4.7}$$

we obtain

$$\frac{\mathrm{d}}{\mathrm{d}t}\hat{\mathcal{N}}_{ij}(\mathbf{p},t) = i\left[\hat{H}_0(t), \hat{\mathcal{N}}_{ij}(\mathbf{p},t)\right] + i\left[\hat{H}_{\rm int}(t), \hat{\mathcal{N}}_{ij}(\mathbf{p},t)\right] \ . \tag{4.8}$$

In particular, taking into account just the helicity as discrete quantum number, the first term in eq. (4.8) is vanishing since $\left[\hat{H}_0(t), \hat{\mathcal{N}}_{ij}(\mathbf{p},t)\right] = 0$. This is nothing more than a way to express the helicity conservation in the absence of collision in our system. Then, taking the expectation value on both sides of the evolution equation one gets

$$(2\pi)^3 \delta^{(3)}(0)\, 2E_{\mathbf{p}} \frac{\mathrm{d}}{\mathrm{d}t}\rho_{ij}(\mathbf{p},t) = i\left\langle\left[\hat{H}_{\rm int}(t), \hat{\mathcal{N}}_{ij}(\mathbf{p},t)\right]\right\rangle \ . \tag{4.9}$$

We recall that here the number operator is in the Heisenberg picture and so it depends on creation and annihilation operators of the interacting theory, which in general are very hard to evaluate or even not possible to be introduced. A general approach to overcome this problem makes use of a perturbation series of the Heisenberg fields. For weak interactions it is possible to approximate the time evolution of Heisenberg operators as closed integration if we restrict ourselves to a given order in the interaction Hamiltonian. In particular, in our case for the number operator we get [Sigl and Raffelt, 1993]

$$\hat{\mathcal{N}}_{ij}(\mathbf{p},t) = \hat{\mathcal{N}}^I_{ij}(\mathbf{p},t) + i\int_{t_0}^{t} dt' \left[\hat{H}^I_{\rm int}(t-t'), \hat{\mathcal{N}}^I_{ij}(\mathbf{p},t)\right] \ , \tag{4.10}$$

where all the operators with the label I are intended to be in the interaction picture, and so can be expressed as functions of the free fields. The interpretation of this equation is that at the time $t = t_0$ the system starts to interact, but as the background does not yet contain any correlations between the interacting species we can still evaluate the collisions using the 0-th order number operator. This first order solution describes forward scatterings and we need to go to second order to find the first non–forward interactions.

We can now insert the first order solution (eq. (4.10)) into the second term on the r.h.s of eq. (4.8) and find the second order solution

$$\begin{aligned}\frac{\mathrm{d}}{\mathrm{d}t}\hat{\mathcal{N}}_{ij}(\mathbf{p},t) &= i\left[\hat{H}_{\rm int}(t), \hat{\mathcal{N}}_{ij}(\mathbf{p},t)\right] \\ &\simeq i\left[\hat{H}^I_{\rm int}(t), \hat{\mathcal{N}}^I_{ij}(\mathbf{p},t)\right] - \int_{t_0}^{t} dt' \left[\hat{H}^I_{\rm int}(t), \left[\hat{H}^I_{\rm int}(t-t'), \hat{\mathcal{N}}^I_{ij}(\mathbf{p},t)\right]\right] \ .\end{aligned} \tag{4.11}$$

The integral on the r.h.s of the above equation can be cast in a more practical form by making the following physical assumption: the duration of each collision (the time interval over which the interaction Hamiltonian is

non–negligible, which can be estimated as the inverse of the typical energy transfer) in small compared to the time scale for variation of the density matrix (which is on the order of the inverse collision frequency). We identify these two quantities as *microscopic* and *mesoscopic* time scale respectively, so that our assumption can be formulated as $t_{\rm mic} \ll t_{\rm mes}$. In particular, since we are taking the time derivative of the number operator with respect to the time t we may indentify the mesoscopic time as $t_{\rm mes} = t$. Expressed in this parameters we can rewrite eq. (4.11) as

$$\frac{\mathrm{d}}{\mathrm{d}t_{\rm mes}}\hat{\mathcal{N}}_{ij}(\mathbf{p},t) = i\left[\hat{H}^I_{\rm int}(t_{\rm mes}),\hat{\mathcal{N}}^I_{ij}(\mathbf{p},t_{\rm mes})\right] - \int_{t_0}^{t_{\rm mes}} dt_{\rm mic}\left[\hat{H}^I_{\rm int}(t_{\rm mes}),\left[\hat{H}^I_{\rm int}(t_{\rm mes}-t_{\rm mic}),\hat{\mathcal{N}}^I_{ij}(\mathbf{p},t_{\rm mes})\right]\right]. \tag{4.12}$$

Furthermore, we will always assume that the medium is not changed substantially by the interactions with the system ensemble, allowing us to neglect evolution equations for the medium variables which can thus be taken to be externally prescribed by their initial coniditions. If the medium is not stationary it is assumed that the time scale of variation is large compared to the typical duration of the interactions. Now, after extending the upper limit of the integral involving $t_{\rm mes}$ to the infinity and taking the expectation value of both sides of eq. (4.12), we find the final form of the QBE as [Fidler and Pitrou, 2017; Pitrou, 2021; Zarei et al., 2021]

$$(2\pi)^3\delta^{(3)}(0)\,2E_{\mathbf{p}}\frac{\mathrm{d}}{\mathrm{d}t_{\rm mes}}\rho_{ij}(\mathbf{x},\mathbf{p},t_{\rm mes}) = i\left\langle\left[\hat{H}^I_{\rm int}(t_{\rm mes}),\hat{\mathcal{N}}^I_{ij}(\mathbf{p},t_{\rm mes})\right]\right\rangle - \int_0^{\infty} dt_{\rm mic}\left\langle\left[\hat{H}^I_{\rm int}(t_{\rm mes}),\left[\hat{H}^I_{\rm int}(-t_{\rm mic}),\hat{\mathcal{N}}^I_{ij}(\mathbf{p},t_{\rm mes})\right]\right]\right\rangle. \tag{4.13}$$

As in the classical case, another typical assumption is the time–reversal symmetry for the process of interest. When this is the case, we have $H^I_{\rm int}(-t_{\rm mic}) = H^I_{\rm int}(t_{\rm mic})$, under which the quantum Boltzmann equation transform in the following form [Kosowsky, 1996; Zarei et al., 2021]

$$(2\pi)^3\delta^{(3)}(0)\,2E_{\mathbf{p}}\frac{\mathrm{d}}{\mathrm{d}t_{\rm mes}}\rho_{ij}(\mathbf{x},\mathbf{p},t_{\rm mes}) = i\left\langle\left[\hat{H}^I_{\rm int}(t_{\rm mes}),\hat{\mathcal{N}}^I_{ij}(\mathbf{p},t_{\rm mes})\right]\right\rangle - \frac{1}{2}\int_{-\infty}^{\infty} dt_{\rm mic}\left\langle\left[\hat{H}^I_{\rm int}(t_{\rm mes}),\left[\hat{H}^I_{\rm int}(t_{\rm mic}),\hat{\mathcal{N}}^I_{ij}(\mathbf{p},t_{\rm mes})\right]\right]\right\rangle. \tag{4.14}$$

Practically, thanks to the assumptions made on the time scales involved in the problem, the QBE can be evaluated at $t_{\rm mes} = 0$. This is not a problem in all those cases in which we can assume the Markov hypothesis, i.e. no memory of past interactions. Under such condition indeed the QBE evaluated at $t_{\rm mes} = 0$ is valid for all the times. In the following we always assume to work in this framework, a discussion on deviations from this regime can be found, e.g. in Zarei et al. (2021).

A SYSTEM OF PHOTONS Our final aim is to describe the evolution of the polarization state of a population of photons, that in our context will

be the CMB photons, during their propagation in an interacting medium. Now we want to define an effective way to describe the polarization of an electromagnetic wave from a quantum–mechanical point of view. In particular, we want to generalize the description of polarized light based on the Stokes parameters. These parameters, labeled by I, Q, U and V, are a particular convenient choice in view of experimental tests based on polarization measurements, since they allow to completely determine the polarization state of a wave through intensity measurements only.

The quantum behaviour of light is described in terms of a population of photons. The latter, being massless particles, can assume just two independent helicity states. The polarization state space is thus spanned by a pair of basis vectors, which we take to be the orthogonal linear polarizations $|\varepsilon_1\rangle$ and $|\varepsilon_2\rangle$. An arbitrary polarization state is given by

$$|\varepsilon\rangle = a_1 e^{i\theta_1} |\varepsilon_1\rangle + a_2 e^{i\theta_2} |\varepsilon_2\rangle \ , \tag{4.15}$$

where a_1 and a_2 can be in general function of time and corresponds to the amplitude of different components, while θ_1 and θ_2 are just phase factors. We can define four quantum mechanical operators which, in the linear basis corresponding to each Stokes parameter, are given by

$$\hat{I} \equiv |\varepsilon_1\rangle \langle\varepsilon_1| + |\varepsilon_2\rangle \langle\varepsilon_2| \ , \tag{4.16a}$$
$$\hat{Q} \equiv |\varepsilon_1\rangle \langle\varepsilon_1| - |\varepsilon_2\rangle \langle\varepsilon_2| \ , \tag{4.16b}$$
$$\hat{U} \equiv |\varepsilon_1\rangle \langle\varepsilon_2| + |\varepsilon_2\rangle \langle\varepsilon_1| \ , \tag{4.16c}$$
$$\hat{V} \equiv i\left(|\varepsilon_2\rangle \langle\varepsilon_1| - |\varepsilon_1\rangle \langle\varepsilon_2|\right) \ . \tag{4.16d}$$

It is easy to notice that the single–particle state expectation values of these operators reproduce the classical definitions. Taking the operator $\hat{I}$ as example, we have

$$\begin{aligned} \langle \hat{I} \rangle \equiv \langle\varepsilon| \hat{I} |\varepsilon\rangle &= \left(a_1 e^{-i\theta_1} \langle\varepsilon_1| + a_2 e^{-i\theta_2} \langle\varepsilon_2|\right) \\ &\quad \times \left(|\varepsilon_1\rangle \langle\varepsilon_1| + |\varepsilon_2\rangle \langle\varepsilon_2|\right) \left(a_1 e^{i\theta_1} |\varepsilon_1\rangle + a_2 e^{i\theta_2} |\varepsilon_2\rangle\right) \\ &= a_1^2 + a_2^2 \ , \end{aligned} \tag{4.17}$$

which exactly matches the intuitive definition of total intensity of a linear polarized wave[2].

In a similar way, for photons in a general mixed state defined by a density matrix ρ, the expectation value for the $\hat{I}$ Stokes parameter operator is given by

$$I = \langle \hat{I} \rangle = \mathrm{Tr}\left[\rho \hat{I}\right] = \mathrm{Tr}\left[\begin{pmatrix} \rho_{11} & \rho_{12} \\ \rho_{21} & \rho_{22} \end{pmatrix} \begin{pmatrix} 1 & 0 \\ 0 & 1 \end{pmatrix}\right] = \rho_{11} + \rho_{22} \ , \tag{4.18}$$

2 If one assumes to work with normalizated states it is easy to see that eq. (4.17) is identically equal to 1. This is not a problem, indeed the intensity of an electromagnetic radiation, roughly speaking, correspond to the number of photons. So this result just reflects the fact that with this quantum mechanical description we are just looking at the single photon.

and similarly for all the other three parameters. These relations thus allow us to define the density matrix in the linear polarization basis in terms of the Stokes parameters as

$$\rho = \frac{1}{2}\begin{pmatrix} I+Q & U-iV \\ U+iV & I-Q \end{pmatrix} = \frac{1}{2}\left(I\mathbb{I} + Q\sigma_3 + U\sigma_1 + V\sigma_2\right) \,, \tag{4.19}$$

where $\mathbb{I}$ is the identity matrix and σ_i are the Pauli matrices. Thus, the density matrix for a system of photons contains the same information as the four Stokes parameters, and the time evolution of the density matrix gives the time evolution of the system's polarization. In particular, by adopting the second-quantized formalism as in the derivation of the QBE in section 4.1.1, we can introduce creation and annihilation operators for photons satisfying the canonical commutation relationship

$$\left[\hat{a}_r\left(\mathbf{p},t\right), \hat{a}_s^\dagger\left(\mathbf{q},t\right)\right] = \left(2\pi\right)^3 2E_{\mathbf{p}}\delta^{(3)}\left(\mathbf{p}-\mathbf{q}\right)\delta_{rs} \,, \tag{4.20}$$

where r and s label the photon polarization. It is then possibile to define a density operator describing the full system of photon as [Kosowsky, 1996]

$$\hat{\rho} = \int \frac{d^3\mathbf{p}}{\left(2\pi\right)^3 2E_{\mathbf{p}}} \rho_{ij}\left(\mathbf{p}\right)\hat{\mathcal{N}}_{ij}\left(\mathbf{p},t\right) \,, \tag{4.21}$$

where we introduced the photon number operator $\hat{\mathcal{N}}_{ij}\left(\mathbf{p},t\right) \equiv \hat{a}_i^\dagger\left(\mathbf{p},t\right)\hat{a}_j\left(\mathbf{p},t\right)$. Now, by taking the expectation value of the number operator on the system described by the density operator introduced in eq. (4.21), we find that

$$\begin{aligned} \left\langle \hat{\mathcal{N}}_{ij}\left(\mathbf{p},t\right)\right\rangle &= \mathrm{Tr}\left[\hat{\rho}\hat{\mathcal{N}}_{ij}\left(\mathbf{p},t\right)\right] \equiv \sum_k \int \frac{d^3\mathbf{q}}{\left(2\pi\right)^3 2E_{\mathbf{q}}} \left\langle \mathbf{q}_k\right| \hat{\rho}\hat{\mathcal{N}}_{ij}\left(\mathbf{p},t\right)\left|\mathbf{q}_k\right\rangle \\ &= \left(2\pi\right)^3 2E_{\mathbf{p}}\delta^{(3)}\left(\mathbf{p}-\mathbf{q}\right)\rho_{ji}\left(\mathbf{p},t\right) \,, \end{aligned} \tag{4.22}$$

which perfectly matches the defintitions introduced at the beginning of Section 4.1.1. This fact proves that we have correctly defined the density operator of our system, which can then be used to determine the polarization evolution through the QBE formalism.

4.1.2 Phenomenological picture

In this work we want to study phenomenological consequences of neutrino–photon scattering, in particular at the level of CMB polarization. Neutrino counplings to scalar and pseudoscalar scalar particles are well motivated from a theoretical point of view thanks to models aimed to explain neutrino mass generation. As an example, we can cite the so-called Majoron models [Chikashige et al., 1981; Gelmini and Roncadelli, 1981; Schechter and Valle, 1982; Valle and Romao, 2015]. The basic idea is that lepton number L, which is necessarily violated if neutrinos are Majorana particles, is spontaneously

broken globally. The Majoron is the massless Goldstone boson that appears in the theory once the L symmetry is broken. In this framework, a dynamical realization of the see-saw mechanism is achieved, since the vacuum expectation value (vev) of the parent field σ of the Majoron, v_σ, generates the "large" Majorana term in the neutrino mass matrix. Once the mass matrix is diagonalized, two massive Majorana neutrinos emerge (per each generation), with masses $m_{\text{light}} \approx v_\Phi^2/v_\sigma$ and $m_{\text{heavy}} \approx v_\sigma$, where $v_\Phi \ll v_\sigma$ is the vev of the Standard Model Higgs doublet. Diagonalization of the mass matrix also yields Majoron-neutrino Yukawa interactions, which might be responsible for neutrino-neutrino scatterings like those considered in this work.

Coupling with photons is not usually included in simplest majoron models. However, there are some some recent explorations relying on the basic idea of unifying the role of the majoron (to generate neutrino masses) with the QCD axion (to solve the strong CP problem) which motivate, also from a theoreical side this choice [Ballesteros et al., 2017; 2019; Barenboim et al., 2024a; b; Ringwald, 2024]. From a phenomenological point of view, we thus decide to consider neutrinos and photons interacting with a light pseudoscalar boson ϕ, by means of the following extension of the SM Lagrangian

$$\mathcal{L}_{\text{BSM}} = \mathcal{L}_{\nu\phi} + \mathcal{L}_{\gamma\phi} \equiv -ig_{\nu\nu\phi}(\bar{\psi}_\nu \gamma_5 \psi_\nu)\phi + \frac{1}{4} g_{\gamma\gamma\phi} F_{\mu\nu}\tilde{F}^{\mu\nu}\phi \,, \tag{4.23}$$

where $F_{\mu\nu} \equiv \partial_\mu a_\nu - \partial_\nu A_\mu$, and $\tilde{F}_{\mu\nu} \equiv (1/2)\varepsilon_{\mu\nu\rho\sigma}F^{\rho\sigma}$ are the electromagnetic stress tensor and its dual, respectively. The electromagnetic free gauge field, $A_\mu(x)$ can be written in terms of plane wave solutions in the Coulomb gauge as

$$A^\mu(x) = \int \frac{d^3\mathbf{k}}{(2\pi)^3 2k^0} \sum_{\lambda=1}^{2} \left[\hat{a}_\lambda(\mathbf{k})\varepsilon_\lambda^\mu(\mathbf{k})e^{-ik\cdot x} + \hat{a}_\lambda^\dagger(\mathbf{k})\varepsilon_\lambda^{*\mu}(\mathbf{k})e^{ik\cdot x}\right] , \tag{4.24}$$

where $\varepsilon^\mu_{(\lambda)}(k)$ are the polarization four-vectors with forum k and dispersion relation $k^0 = \mathbf{k}$. The index $\lambda = 1, 2$ runs over the two transverse polarization of a free photon. The creation and annihilation operators, $\hat{a}_\lambda^\dagger(\mathbf{k})$ and $\hat{a}_\lambda(\mathbf{k})$ respectively, satisfy the canonical commutation rules

$$\left[\hat{a}_i(\mathbf{p}), \hat{a}_j^\dagger(\mathbf{q})\right] = (2\pi)^3 2E_\mathbf{p}\delta_{ij}\delta^{(3)}(\mathbf{p}-\mathbf{q}) \,. \tag{4.25}$$

In a similar way the free fermion field, $\psi(x)$, is represented as

$$\psi(x) = \int \frac{d^3\mathbf{p}}{(2\pi)^3 2E_\mathbf{p}} \sum_{r=1}^{2} \left[u_r(\mathbf{p})\hat{b}_r(\mathbf{p})e^{-ip\cdot x} + v_r(\mathbf{p})\hat{d}_r^\dagger(\mathbf{p})e^{ip\cdot x}\right] , \tag{4.26}$$

where $u_r(\mathbf{p})$ and $v_r(\mathbf{p})$ are Dirac spinors. The creation and annihilation operators for fermion (antifermions), $\hat{b}_r(\mathbf{p})$ ($\hat{d}_r(\mathbf{p})$) and $\hat{b}_r^\dagger(\mathbf{p})$ ($\hat{d}_r^\dagger(\mathbf{p})$) respectively, satisfy the canonical anticommutation rules

$$\left\{\hat{b}_r(\mathbf{p}), \hat{b}_s^\dagger(\mathbf{q})\right\} = \left\{\hat{d}_r(\mathbf{p}), \hat{d}_s^\dagger(\mathbf{q})\right\} = (2\pi)^3 2E_\mathbf{p}\delta_{rs}\delta^{(3)}(\mathbf{p}-\mathbf{q}) \,. \tag{4.27}$$

The scattering matrix describing all scattering processes in our theory is given in terms of the interaction Hamiltonian by

$$S = \sum_{n=0}^{\infty} S^{(n)} \equiv \sum_{n=0}^{\infty} \frac{(-i)^n}{n!} \int d^4x_1 \cdots d^4x_n \, \mathcal{T}\left\{\mathcal{H}_{\rm BSM}(x_1) \cdots \mathcal{H}_{\rm BSM}(x_n)\right\} \ , \tag{4.28}$$

where $\mathcal{T}\{.\}$ is the time ordered product. The n-th term in the series represents all scattering processes with n interaction vertices. Neutrino-photon scattering mediated by a scalar particle arises in the $n = 2$ term of the scattering matrix at tree level. To built the object needed in the QBE we recall that the interaction Hamiltonian is the density integrated over all the space

$$H(t) = \int d^3\mathbf{x} \, \mathcal{H}(x) \ . \tag{4.29}$$

Comparing now the $n = 2$ term with the $n = 1$ term of eq. (4.28) gives the interaction hamiltonian for second-order scattering processes

$$\begin{aligned} S^{(2)} &= -\frac{1}{2} \int_{-\infty}^{\infty} dt \int_{-\infty}^{\infty} dt' \, \mathcal{T}\left\{H_{\nu\phi}(t), H_{\gamma\phi}(t')\right\} \\ &\equiv -i \int_{-\infty}^{\infty} dt \, H^{(2)}_{\nu\gamma\to\nu\gamma}(t) \ . \end{aligned} \tag{4.30}$$

4.2 FORWARD SCATTERING TERM

We now proceed to evaluate on the l.h.s. of eq. (4.14). First we diplay here the expectation values of operators needed in the following subsections. As shown in Section 4.1, through the expansion in creation and annihilation operators of the photon field is possible to define a density operator where the polarization density matrix for a system of photons is defined as (see Section 4.1.1)

$$\rho^{(\gamma)}(\mathbf{x}, \mathbf{q}, t) \equiv \frac{1}{2} \begin{pmatrix} I(\mathbf{x}, \mathbf{q}, t) + Q(\mathbf{x}, \mathbf{q}, t) & U(\mathbf{x}, \mathbf{q}, t) - iV(\mathbf{x}, \mathbf{q}, t) \\ U(\mathbf{x}, \mathbf{q}, t) + iV(\mathbf{x}, \mathbf{q}, t) & I(\mathbf{x}, \mathbf{q}, t) - Q(\mathbf{x}, \mathbf{q}, t) \end{pmatrix} \ . \tag{4.31}$$

Then, we can easily compute the expectation value of the number operator, finding

$$\left\langle \hat{a}_i^\dagger \left(\mathbf{q}, t\right) \hat{a}_j \left(\mathbf{q}', t\right) \right\rangle = 2E_{\mathbf{q}} \left(2\pi\right)^3 \delta^{(3)} \left(\mathbf{q} - \mathbf{q}'\right) \rho_{ji}^{(\gamma)} \left(\mathbf{x}, \mathbf{q}, t\right) \ . \tag{4.32}$$

Under the molecular chaos assumption, the expectation values of larger products of creation and annihilation operators can be computed through a generalization of the Wick's theorem [Danielewicz, 1984]

$$\left\langle \hat{\alpha}_i \hat{\alpha}_j \cdots \hat{\alpha}_k \hat{\alpha}_l \right\rangle = \sum_{\text{pairs}} \left\langle \hat{\alpha}_i \hat{\alpha}_j \right\rangle \cdots \left\langle \hat{\alpha}_k \hat{\alpha}_l \right\rangle \ , \tag{4.33}$$

where $\hat{\alpha}_i$ is a shorthand notation that stands for both $\hat{a}_i$ and $\hat{a}_i^\dagger$. This approximation plays the analogous role that statistically independency of n-particle functions plays in the derivation of the Bogoljubov–Born–Green–Kirkwood–Yvon (BBGKY) hierarchy [Volpe, 2015]. In our case also the 4–points expectation values will be needed, so in the case of photons we have[3]

$$\begin{aligned}
&\left\langle \hat{a}^\dagger_{\lambda_1'}(\mathbf{q}_1')\hat{a}_{\lambda_1}(\mathbf{q}_1)\hat{a}^\dagger_{\lambda_2'}(\mathbf{q}_2')\hat{a}_{\lambda_2}(\mathbf{q}_2)\right\rangle = \\
&\quad = \left\langle \hat{a}^\dagger_{\lambda_1'}(\mathbf{q}_1')\hat{a}_{\lambda_1}(\mathbf{q}_1)\right\rangle \left\langle \hat{a}^\dagger_{\lambda_2'}(\mathbf{q}_2')\hat{a}_{\lambda_2}(\mathbf{q}_2)\right\rangle + \\
&\qquad + \left\langle \hat{a}^\dagger_{\lambda_1'}(\mathbf{q}_1')\hat{a}_{\lambda_2}(\mathbf{q}_2)\right\rangle \left\langle \hat{a}_{\lambda_1}(\mathbf{q}_1)\hat{a}^\dagger_{\lambda_2'}(\mathbf{q}_2')\right\rangle \\
&\quad = 4E_{\mathbf{q}_1}E_{\mathbf{q}_2}(2\pi)^6 \Big\{ \delta^{(3)}(\mathbf{q}_1-\mathbf{q}_1')\delta^{(3)}(\mathbf{q}_2-\mathbf{q}_2')\rho^{(\gamma)}_{\lambda_1\lambda_1'}(\mathbf{q}_1)\rho^{(\gamma)}_{\lambda_2\lambda_2'}(\mathbf{q}_2) \\
&\qquad + \delta^{(3)}(\mathbf{q}_1-\mathbf{q}_2')\delta^{(3)}(\mathbf{q}_2-\mathbf{q}_1')\rho^{(\gamma)}_{\lambda_1'\lambda_2}(\mathbf{q}_2)\left[\delta_{\lambda_1\lambda_2'}+\rho^{(\gamma)}_{\lambda_1\lambda_2'}(\mathbf{q}_1)\right]\Big\} \,.
\end{aligned} \tag{4.35}$$

The same procedure can be applied to the case of neutrinos. In particular, we can define an analogous density operator as

$$\hat{\rho}^{(\nu)}(\mathbf{x},t) \equiv \int \frac{d^3\mathbf{p}}{(2\pi)^3 2E_{\mathbf{p}}} \rho^{(\nu)}_{ij}(\mathbf{x},\mathbf{p},t)\,\hat{b}_i^\dagger(\mathbf{p},t)\,\hat{b}_j(\mathbf{p},t) \,, \tag{4.36}$$

where for a system composed of unpolarized fermions, $\rho^{(\nu)}_{ij}$ is given by[4]

$$\rho^{(\nu)}(\mathbf{x},\mathbf{p},t) \equiv \frac{1}{2}\begin{pmatrix} f_\nu(\mathbf{x},\mathbf{p},t) & 0 \\ 0 & f_\nu(\mathbf{x},\mathbf{p},t)\end{pmatrix} \,, \tag{4.37}$$

where f_ν denotes the distribution function of neutrinos. We can then compute the related 2–points and 4–points expectation values for the product of creation and annihilation operators, obtaining respectively

$$\left\langle \hat{b}_i^\dagger(\mathbf{p},t)\hat{b}_j(\mathbf{p}',t)\right\rangle = 2E_{\mathbf{p}}(2\pi)^3\delta^{(3)}(\mathbf{p}-\mathbf{p}')\delta_{ij}\frac{1}{2}f_\nu(\mathbf{x},\mathbf{p},t) \,, \tag{4.38}$$

and

$$\begin{aligned}
&\left\langle \hat{b}^\dagger_{r_1'}(\mathbf{p}_1')\hat{b}_{r_1}(\mathbf{p}_1)\hat{b}^\dagger_{r_2'}(\mathbf{q}_2')\hat{b}_{r_2}(\mathbf{p}_2)\right\rangle = \\
&\quad = 4E_{\mathbf{p}_1}E_{\mathbf{p}_2}(2\pi)^6 \Big\{ \delta^{(3)}(\mathbf{p}_1-\mathbf{p}_1')\delta^{(3)}(\mathbf{p}_2-\mathbf{p}_2')\frac{1}{4}\delta_{r_1r_1'}\delta_{r_2r_2'}f_\nu(\mathbf{p}_1)f_\nu(\mathbf{p}_2) \\
&\qquad + \delta^{(3)}(\mathbf{p}_1-\mathbf{p}_2')\delta^{(3)}(\mathbf{p}_2-\mathbf{p}_1')\frac{1}{2}\delta_{r_1'r_2}\delta_{r_1r_2'}f_\nu(\mathbf{p}_2)\left[1+\frac{1}{2}f_\nu(\mathbf{p}_1)\right]\Big\} \,.
\end{aligned} \tag{4.39}$$

3 We notice that we have just two terms in the sum, even if there are three possible combinations, because the expectation values of the same kind of operators are vanishing. Namely

$$\langle \hat{a}_{\lambda_1}(\mathbf{q}_1)\,\hat{a}_{\lambda_2}(\mathbf{q}_2)\rangle = \left\langle \hat{a}^\dagger_{\lambda_1'}(\mathbf{q}_1')\,\hat{a}^\dagger_{\lambda_2'}(\mathbf{q}_2')\right\rangle = 0 \,. \tag{4.34}$$

4 Different flavor states are not taken into account when writing the density matrix since, in all the time frame of interest for CMB computation, oscillations have already ceased to be effective and neutrinos are only described in terms of mass eigenstates.

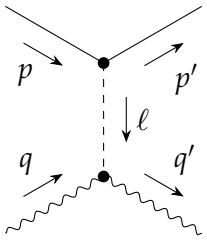

Figure 4.1: Feynman diagram of the tree–level contribution to the neutrino–photon scattering, $\nu\gamma \to \nu\gamma$, mediated by a pseudoscalar particle. Solid lines represent neutrinos, the dashed line the pseudoscalar particle and wavy lines the photons.

4.2.1 Tree-level

We want to begin our evaluation of the forward scattering terms considering the tree–level contribution to the neutrino–photon scattering, whose Feynman diagram can be found in fig. 4.1. From eq. (4.30) we see that the Hamiltonian describing this process can be simply determined from the integration over the spatial coordinates of the S–matrix term generating the considered diagram, which can be written as

$$S^{(2)}_{\nu\gamma} = 2 \cdot \frac{i}{2} g_{\nu\nu\phi} g_{\gamma\gamma\phi} \varepsilon^{\mu\alpha\nu\beta} \int d^4x_1 \int d^4x_2 \, D_{\mathrm{F}}(x_1 - x_2) \times \mathrm{N}\left[\left(\bar{\nu}_- \gamma^5 \nu_+\right)_{x_1} \left(\partial_\alpha A^+_\mu \partial_\beta A^-_\nu\right)_{x_2} \right] , \tag{4.40}$$

where $D_{\mathrm{F}}(x_1 - x_2)$ is the propagator associated to the pseudoscalar particle in coordinates space. The factor 2 is given by symmetry, corresponding to all the permutations of possible contractions between states and fields appearing during the bra–ket operation of the S–matrix operator between initial and final states. Then, going to momentum space, and taking integrations over spatial coordinates, is possible to write

$$\hat{H}_{\nu\gamma}(t) = \int d\Pi_{\mathbf{p}} d\Pi_{\mathbf{q}} d\Pi_{\mathbf{p}'} d\Pi_{\mathbf{q}'} (2\pi)^3 \, \delta^{(3)}(\mathbf{p}' + \mathbf{q}' - \mathbf{p} - \mathbf{q}) e^{i(p'+q'-p-q)t} \times \mathcal{M}_{\nu\gamma\to\nu\gamma}(pr, q\lambda, p'r', q'\lambda') \hat{b}^\dagger_{r'}(\mathbf{p}_3) \hat{a}^\dagger_{\lambda'}(\mathbf{p}_4) \hat{a}_\lambda(\mathbf{p}_2) \hat{b}_r(\mathbf{p}_1) , \tag{4.41}$$

where

$$\mathcal{M}_{\nu\gamma\to\nu\gamma} \equiv i g_{\nu\nu\phi} g_{\gamma\gamma\phi} \left(\bar{u}_{r'}(\mathbf{p}') \gamma^5 u_r(\mathbf{p})\right) \tilde{D}_{\mathrm{F}}(q - q') \varepsilon^{\mu\alpha\nu\beta} q_\alpha q'_\beta \varepsilon^\lambda_\mu(\mathbf{q}) \varepsilon^{\lambda'}_\nu(\mathbf{q}') \tag{4.42}$$

is the scattering amplitude.

Now, using the definitions of eqs. (4.6) and (4.41), and the commutation relations of the ladder operators, the commutator in the forward scattering term becomes

$$\begin{aligned}
&\left[\hat{H}_{\nu\gamma}(0), \hat{\mathcal{N}}_{ij}(\mathbf{k})\right] = \\
&\quad = \int d\Pi_{\mathbf{p}} d\Pi_{\mathbf{q}} d\Pi_{\mathbf{p}'} d\Pi_{\mathbf{q}'} (2\pi)^3 \, \delta^{(3)}(\mathbf{p}' + \mathbf{q}' - \mathbf{p} - \mathbf{q}) \mathcal{M}_{\nu\gamma\to\nu\gamma} \\
&\qquad \times \Big[(2\pi)^3 2E_{\mathbf{q}} \delta_{\lambda i} \delta^{(3)}(\mathbf{q} - \mathbf{k}) \hat{b}^\dagger_{r'}(\mathbf{p}') \hat{a}^\dagger_{\lambda'}(\mathbf{q}') \hat{a}_j(\mathbf{k}) \hat{b}_r(\mathbf{p}) \\
&\qquad\quad - (2\pi)^3 2E_{\mathbf{q}'} \delta_{\lambda' j} \delta^{(3)}(\mathbf{q}' - \mathbf{k}) \hat{b}^\dagger_{r'}(\mathbf{p}') \hat{a}^\dagger_i(\mathbf{k}) \hat{a}_\lambda(\mathbf{q}) \hat{b}_r(\mathbf{p}) \Big] \, .
\end{aligned} \tag{4.43}$$

Then, taking the expectation value and multiplicating by the imaginary unit to recover the right hand side of the quantum Boltzmann equation, one finds

$$\begin{aligned}
&i \left\langle \left[\hat{H}_{\nu\gamma}(0), \hat{\mathcal{N}}_{ij}(\mathbf{k})\right] \right\rangle = \\
&\quad = i \int d\Pi_{\mathbf{p}} d\Pi_{\mathbf{q}} d\Pi_{\mathbf{p}'} d\Pi_{\mathbf{q}'} (2\pi)^3 \, \delta^{(3)}(\mathbf{p}' + \mathbf{q}' - \mathbf{p} - \mathbf{q}) \\
&\qquad \times i g_{\nu\nu\phi} g_{\gamma\gamma\phi} \left[\bar{u}_{r'}(\mathbf{p}') \gamma^5 u_r(\mathbf{p})\right] \tilde{D}_{\mathrm{F}}(q - q') \varepsilon^{\mu\alpha\nu\beta} q_\alpha q'_\beta \varepsilon^\lambda_\mu(\mathbf{q}) \varepsilon^{\lambda'}_\nu(\mathbf{q}') \\
&\qquad \times \left\langle \hat{b}^\dagger_{r'}(\mathbf{p}') \hat{b}_r(\mathbf{p}) \right\rangle \Big[(2\pi)^3 2E_{\mathbf{q}} \delta_{\lambda i} \delta^{(3)}(\mathbf{q} - \mathbf{k}) \left\langle \hat{a}^\dagger_{\lambda'}(\mathbf{q}') \hat{a}_j(\mathbf{k}) \right\rangle \\
&\qquad\quad - (2\pi)^3 2E_{\mathbf{q}'} \delta_{\lambda' j} \delta^{(3)}(\mathbf{q}' - \mathbf{k}) \left\langle \hat{a}^\dagger_i(\mathbf{k}) \hat{a}_\lambda(\mathbf{q}) \right\rangle \Big] \, .
\end{aligned} \tag{4.44}$$

Finally, by substituting explicit expressions for the expectation values of the creation and annihilation operators (eqs. (4.32) and (4.38)), and taking the integrations over $\mathbf{q}$, $\mathbf{p}'$ and $\mathbf{q}'$, we reduce to

$$\begin{aligned}
&i \left\langle \left[\hat{H}_{\nu\gamma}(0), \hat{\mathcal{N}}_{ij}(\mathbf{k})\right] \right\rangle = i g_{\nu\nu\phi} g_{\gamma\gamma\phi} (2\pi)^3 \delta^{(3)}(0) \varepsilon^{\mu\nu\alpha\beta} k_\alpha k_\beta \varepsilon^\lambda_\mu(\mathbf{q}) \varepsilon^{\lambda'}_\nu(\mathbf{q}') \\
&\qquad \times \left[\delta_{\lambda i} \rho_{j\lambda'}(\mathbf{k}) - \delta_{\lambda' j} \rho_{\lambda i}(\mathbf{k})\right] \frac{1}{2M^2} \int d\Pi_{\mathbf{p}} f_\nu(\mathbf{p}) \left[\bar{u}_r(\mathbf{p}) \gamma^5 u_r(\mathbf{p})\right] \\
&\quad = 0 \, ,
\end{aligned} \tag{4.45}$$

which is identically vanishing due to the presence of the contraction between a symmetric and an antisymmetric tensor. Here M is the mass of the scalar particle ϕ, appearing from the explicit expression of the Feynman propagator in momentum space $\tilde{D}_{\mathrm{D}}(q) = i/(q^2 - M^2)$.

4.2.2 1-loop corrections

Given the vanishing result found for the forward scattering term of the tree–level diagram in the previous section, we have to move our attention to higher order effects in the QBE. Looking at eq. (4.14) one immediately sees that the forward scattering term is of order $\mathcal{O}(g^2)$, while the collision term is of order $\mathcal{O}(g^4)$. However, in our theory effects of this order can be obtained also computing the forward scattering term related to 1–loop corrections of the neutrino–photon scattering. This kind of contributions are provided both by the SM Lagrangian [Mohammadi, 2014] and by the BSM sector introduced

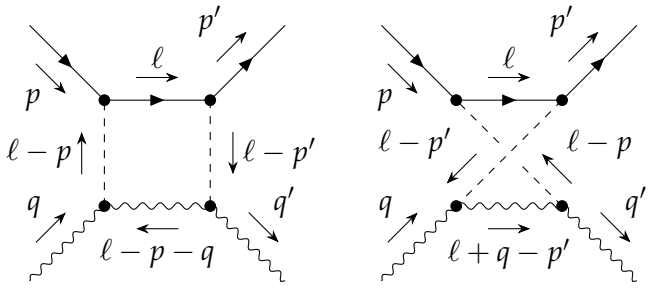

(a) t-channel **(b)** u-channel

Figure 4.2: Feynman diagrams of the 1–loop corrections to the neutrino–photon scattering, $\nu\gamma \to \nu\gamma$, assuming the BSM Lagrangian defined in eq. (4.23). Solid lines represent neutrinos, dashed lines the pseudoscalar particle and wavy lines the photons.

in eq. (4.23). For the moment we restrict our discussion to the latter, which provides the two box diagrams depicted in Figure 4.2.

Since the external structure of the process is the same of the one considered in the previous section, the Hamiltonian can still be written as in eq. (4.41). The only change needed is to account for the 1–loop correction in the computation of the scattering amplitude. First of all, we notice that both these diagrams share the common fermion line

$$\bar{u}_{r'}\left(\mathbf{p}'\right)\gamma_5\left(\not{\ell}+m\right)\gamma_5 u_r\left(\mathbf{p}\right)\ , \tag{4.46}$$

which making use of the anti-commutation rules $\left\{\gamma^5,\gamma^\mu\right\}=0$, can be easily reduced to

$$\bar{u}_{r'}\left(\mathbf{p}'\right)\left(m-\not{\ell}\right)u_r\left(\mathbf{p}\right)\ . \tag{4.47}$$

The full amplitude then can be be written as

$$\mathcal{M}^{\text{1-loop}}_{\text{tot}} \equiv \mathcal{M}^{\text{1-loop}}_{1} + \mathcal{M}^{\text{1-loop}}_{2}\ , \tag{4.48}$$

where

$$\begin{aligned}
&\mathcal{M}^{\text{1-loop}}_{1}(pr,q\lambda,p'r',q'\lambda') = \\
&\quad = \left(g_{\nu\nu\phi}g_{\gamma\gamma\phi}\right)^2\left(\varepsilon^{\mu\rho\alpha\gamma}\varepsilon^{\nu\sigma\beta\delta}\eta_{\alpha\beta}\right)\varepsilon^{\lambda}_{\mu}(\mathbf{q})\varepsilon^{\lambda'}_{\nu}\left(\mathbf{q}'\right)q_\rho q'_\sigma \\
&\qquad \times\int\frac{d^4\ell}{(2\pi)^4}\frac{(\ell_\gamma-p_\gamma-q_\gamma)(\ell_\delta-p_\delta-q_\delta)[\bar{u}_{r'}(\mathbf{p}')(m-\not{\ell})u_r(\mathbf{p})]}{(\ell^2-m^2)[(\ell-p)^2-M^2][(\ell-p')^2-M^2](\ell-p-q)^2} \\
&\quad \equiv \left(g_{\nu\nu\phi}g_{\gamma\gamma\phi}\right)^2\left(\varepsilon^{\mu\rho\alpha\gamma}\varepsilon^{\nu\sigma\beta\delta}\eta_{\alpha\beta}\right)\varepsilon^{\lambda}_{\mu}(\mathbf{q})\varepsilon^{\lambda'}_{\nu}\left(\mathbf{q}'\right)q_\rho q'_\sigma \\
&\qquad \times\bar{u}_{r'}\left(\mathbf{p}'\right)\Xi^{(t)}_{\gamma\delta}(p,q,p';m,M)u_r(\mathbf{p})\ ,
\end{aligned} \tag{4.49}$$

and

$$\begin{aligned}
\mathcal{M}_2^{\text{1-loop}}(pr,q\lambda,p'r',q'\lambda') &= \\
&= (g_{\nu\nu\phi}g_{\gamma\gamma\phi})^2\Big(\varepsilon^{\mu\rho\alpha\gamma}\varepsilon^{\nu\sigma\beta\delta}\eta_{\alpha\beta}\Big)\varepsilon_\mu^\lambda(\mathbf{q})\varepsilon_\nu^{\lambda'}(\mathbf{q}')q_\rho q'_\sigma \\
&\quad\times\int\frac{d^4\ell}{(2\pi)^4}\frac{(\ell_\gamma+q_\gamma-p'_\gamma)(\ell_\delta+q_\delta-p'_\delta)[\bar u_{r'}(\mathbf{p}')(m-\ell\!\!\!/)u_r(\mathbf{p})]}{(\ell^2-m^2)[(\ell-p)^2-M^2][(\ell-p')^2-M^2](\ell+q-p')^2} \\
&\equiv (g_{\nu\nu\phi}g_{\gamma\gamma\phi})^2\Big(\varepsilon^{\mu\rho\alpha\gamma}\varepsilon^{\nu\sigma\beta\delta}\eta_{\alpha\beta}\Big)\varepsilon_\mu^\lambda(\mathbf{q})\varepsilon_\nu^{\lambda'}(\mathbf{q}')q_\rho q'_\sigma \\
&\quad\times\bar u_{r'}(\mathbf{p}')\Xi^{(u)}_{\gamma\delta}(p,q,p';m,M)u_r(\mathbf{p})\,. \qquad (4.50)
\end{aligned}$$

Finally, we can write the original amplitude as

$$\begin{aligned}
\mathcal{M}_{\text{tot}}^{\text{1-loop}}(pr,q\lambda,p'r',q'\lambda') &\equiv (g_{\nu\nu\phi}g_{\gamma\gamma\phi})^2\Big(\varepsilon^{\mu\rho\alpha\gamma}\varepsilon^{\nu\sigma\beta\delta}\eta_{\alpha\beta}\Big)\varepsilon_\mu^\lambda(\mathbf{q})\varepsilon_\nu^{\lambda'}(\mathbf{q}') \\
&\quad\times q_\rho {q'}_\sigma\bar u_{r'}(\mathbf{p}')\Big[\Xi^{(t)}_{\gamma\delta}(p,q,p';m,M)+\Xi^{(u)}_{\gamma\delta}(p,q,p';m,M)\Big]u_r(\mathbf{p})\,. \qquad (4.51)
\end{aligned}$$

Using again the Hamiltonian in eq. (4.41), we compute the commutator in eq. (4.43), and finally we take the expectation value to obtain the forward scattering term of the QBE, which now is equal to

$$\begin{aligned}
i\left\langle\left[\hat H_{\nu\gamma}(0),\hat{\mathcal{N}}_{ij}(\mathbf{k})\right]\right\rangle &= \int d\Pi_{\mathbf{p}}d\Pi_{\mathbf{q}}d\Pi_{\mathbf{p}'}d\Pi_{\mathbf{q}'}(2\pi)^3\,\delta^{(3)}(\mathbf{p}'+\mathbf{q}'-\mathbf{p}-\mathbf{q}) \\
&\quad\times i(g_{\nu\nu\phi}g_{\gamma\gamma\phi})^2\Big(\varepsilon^{\mu\rho\alpha\gamma}\varepsilon^{\nu\sigma\beta\delta}\eta_{\alpha\beta}\Big)\varepsilon_\mu^\lambda(\mathbf{q})\varepsilon_\nu^{\lambda'}q_\rho q'_\sigma(\mathbf{q}') \\
&\quad\times\bar u_{r'}(\mathbf{p}')\Big[\Xi^{(t)}_{\gamma\delta}(p,q,p')+\Xi^{(u)}_{\gamma\delta}(p,q,p')\Big]u_r(\mathbf{p})\left\langle\hat b^\dagger_{r'}(\mathbf{p}')\hat b_r(\mathbf{p})\right\rangle \\
&\quad\times\Big[(2\pi)^3 2E_{\mathbf{q}}\delta_{\lambda i}\delta^{(3)}(\mathbf{q}-\mathbf{k})\left\langle\hat a^\dagger_{\lambda'}(\mathbf{q}')\hat a_j(\mathbf{k})\right\rangle \\
&\quad-(2\pi)^3 2E_{\mathbf{q}'}\delta_{\lambda' j}\delta^{(3)}(\mathbf{q}'-\mathbf{k})\left\langle\hat a^\dagger_i(\mathbf{k})\hat a_\lambda(\mathbf{q})\right\rangle\Big]\,. \qquad (4.52)
\end{aligned}$$

Again, using eqs. (4.32) and (4.38), and taking the integrations over $\mathbf{q}$, $\mathbf{p}'$ and $\mathbf{q}'$, we reduce to

$$\begin{aligned}
i\left\langle\left[\hat H_{\nu\gamma}(0),\hat{\mathcal{N}}_{ij}(\mathbf{k})\right]\right\rangle &= (2\pi)^3\delta^{(3)}(0)(g_{\nu\nu\phi}g_{\gamma\gamma\phi})^2\Big(\varepsilon^{\mu\rho\alpha\gamma}\varepsilon^{\nu\sigma\beta\delta}\eta_{\alpha\beta}\Big)\frac{i}{2} \\
&\quad\times\varepsilon_\mu^{(\lambda)}(\mathbf{k})\varepsilon_\nu^{(\lambda')}(\mathbf{k})k_\rho k_\sigma\left[\delta_{\lambda i}\rho_{j\lambda'}(\mathbf{k})-\delta_{\lambda' j}\rho_{\lambda i}(\mathbf{k})\right] \\
&\quad\times\int d\Pi_{\mathbf{p}}f_\nu(\mathbf{p})\bar u_r(\mathbf{p})\Big[\Xi^{(t)}_{\gamma\delta}(p,k,p;m,M)+\Xi^{(u)}_{\gamma\delta}(p,k,p;m,M)\Big]u_r(\mathbf{p})\,. \qquad (4.53)
\end{aligned}$$

In order to make now some simplifications in the expression of eq. (4.53) we notice that

$$\begin{aligned}
\varepsilon^{\mu\rho\alpha\gamma}\varepsilon^{\nu\sigma\beta\delta}\eta_{\alpha\beta} &= \eta_{\gamma\sigma}\eta_{\delta\rho}\eta_{\mu\nu}-\eta_{\gamma\delta}\eta_{\mu\nu}\eta_{\rho\sigma}-\eta_{\gamma\nu}\eta_{\delta\rho}\eta_{\mu\sigma} \\
&\quad-\eta_{\gamma\sigma}\eta_{\delta\mu}\eta_{\nu\rho}+\eta_{\gamma\delta}\eta_{\mu\sigma}\eta_{\nu\rho}+\eta_{\gamma\nu}\eta_{\delta\mu}\eta_{\rho\sigma}\,, \qquad (4.54)
\end{aligned}$$

so that the factor contracted in front of the integral turns out to be (recalling that the mass–shell condition for photons implies $k^2=0$)

$$\varepsilon^{\mu\rho\alpha\gamma}\varepsilon^{\nu\sigma\beta\delta}\varepsilon_\mu^\lambda(\mathbf{k})\varepsilon_\nu^{\lambda'}(\mathbf{k})k_\rho k_\sigma\eta_{\alpha\beta}=k^\gamma k^\delta\Big[\varepsilon^\lambda(\mathbf{k})\cdot\varepsilon^{\lambda'}(\mathbf{k})\Big]=k^\gamma k^\delta\delta_{\lambda\lambda'}\,, \qquad (4.55)$$

where a lot of terms vanishes because of the transversality condition $k \cdot \varepsilon^{(\lambda)}(\mathbf{k}) = 0$ of polarization vectors. However, this last factor multiplied by the difference of density matrices in the second line of eq. (4.53), leaves us again with a vanishing forward scattering term

$$i \left\langle \left[\hat{H}_{\nu\gamma}(0), \hat{\mathcal{N}}_{ij}(\mathbf{k}) \right] \right\rangle \propto$$
$$\propto k^{\gamma} k^{\delta} \delta_{\lambda\lambda'} \left[\delta_{\lambda i} \rho_{j\lambda'}(\mathbf{k}) - \delta_{\lambda' j} \rho_{\lambda i}(\mathbf{k}) \right] = \rho_{ji}(\mathbf{k}) - \rho_{ji}(\mathbf{k}) = 0 \,. \tag{4.56}$$

4.3 COLLISION TERM

Given the results of the previous sections, we now write the QBE, eq. (4.14) with a vanishing forward scattering term which reads[5]

$$(2\pi)^3 \delta^{(3)}(0) 2|\mathbf{k}| \frac{d}{dt} \rho_{ij}(\mathbf{x}, \mathbf{k}) = -\frac{1}{2} \int_{-\infty}^{\infty} dt' \, \left\langle \left[\hat{H}^I_{\text{int}}(t'), \left[\hat{H}^I_{\text{int}}(0), \hat{\mathcal{N}}_{ij}(\mathbf{k}) \right] \right] \right\rangle \,, \tag{4.57}$$

And so, our QBE finally reads

$$\begin{aligned} \frac{d}{dt} \rho_{ij}(\mathbf{x}, \mathbf{k}) = & -\frac{1}{8|\mathbf{k}|} \int d\Pi_{\mathbf{p}_1} d\Pi_{\mathbf{p}_2} d\Pi_{\mathbf{q}_2} \; (2\pi)^4 \delta^{(4)} \left(p_1 + k - p_2 - q_2 \right) \\ & \times \sum_{r_1, r_2} \sum_{\lambda_1, \lambda_2} \mathcal{M}_{\nu\gamma} \left(p_1 r_1, k\lambda_1, p_2 r_2, q_2 \lambda_1' \right) \mathcal{M}_{\nu\gamma} \left(p_2 r_2, q_2 \lambda_2, p_1 r_1, k \lambda_2' \right) \\ & \times \Big\{ f_{\nu}(\mathbf{x}, \mathbf{p}_1) \, \delta_{\lambda_2 \lambda_1'} \left[\delta_{\lambda_1 i} \rho_{j\lambda_2'}(\mathbf{x}, \mathbf{k}) + \delta_{j\lambda_2'} \rho_{\lambda_1 i}(\mathbf{x}, \mathbf{k}) \right] \\ & - 2 f_{\nu}(\mathbf{x}, \mathbf{p}_2) \, \delta_{j\lambda_2'} \delta_{\lambda_1 i} \rho_{\lambda_2 \lambda_1'}(\mathbf{x}, \mathbf{q}_2) \Big\} \,. \end{aligned} \tag{4.58}$$

Using now the expression for the amplitude, eq. (4.42) inside the QBE, we obtain

$$\begin{aligned} & \frac{d}{dt} \rho_{ij}(\mathbf{x}, \mathbf{k}) = \\ & = -\frac{\left(g_{\phi\nu\nu} g_{\phi\gamma\gamma} \right)^2}{4|\mathbf{k}|} \Bigg\{ \int d\Pi_{\mathbf{p}_1} d\Pi_{\mathbf{p}_2} d\Pi_{\mathbf{q}_2} \; (2\pi)^4 \delta^{(4)}(p_1 + k - p_2 - q_2) f_{\nu}(\mathbf{x}, \mathbf{p}_1) \frac{t}{(t - M^2)^2} \\ & \quad \times \Big[\left(\varepsilon^{\mu_1 \nu_1 \rho_1 \sigma_1} k_{\mu_1} \varepsilon^{i}_{\nu_1}(\mathbf{k}) q_{2\rho_1} \varepsilon^{\lambda_2}_{\sigma_1}(\mathbf{q}_2) \right) \left(\varepsilon^{\mu_2 \nu_2 \rho_2 \sigma_2} q_{2\mu_2} \varepsilon^{\lambda_2}_{\nu_2}(\mathbf{q}_2) k_{\rho_2} \varepsilon^{\lambda_2'}_{\sigma_2}(\mathbf{k}) \right) \rho_{j\lambda_2'}(\mathbf{x}, \mathbf{k}) \\ & \qquad + \left(\varepsilon^{\mu_1 \nu_1 \rho_1 \sigma_1} k_{\mu_1} \varepsilon^{\lambda_1}_{\nu_1}(\mathbf{k}) q_{2\rho_1} \varepsilon^{\lambda_2}_{\sigma_1}(\mathbf{q}_2) \right) \left(\varepsilon^{\mu_2 \nu_2 \rho_2 \sigma_2} q_{2\mu_2} \varepsilon^{\lambda_2}_{\nu_2}(\mathbf{q}_2) k_{\rho_2} \varepsilon^{j}_{\sigma_2}(\mathbf{k}) \right) \rho_{\lambda_1 i}(\mathbf{x}, \mathbf{k}) \Big] \\ & \quad - 2 \int d\Pi_{\mathbf{p}_1} d\Pi_{\mathbf{p}_2} d\Pi_{\mathbf{q}_2} \; (2\pi)^4 \delta^{(4)}(p_1 + k - p_2 - q_2) f_{\nu}(\mathbf{x}, \mathbf{p}_2) \frac{t}{(t - M^2)^2} \\ & \qquad \times \left(\varepsilon^{\mu_1 \nu_1 \rho_1 \sigma_1} k_{\mu_1} \varepsilon^{i}_{\nu_1}(\mathbf{k}) q_{2\rho_1} \varepsilon^{\lambda_1'}_{\sigma_1}(\mathbf{q}_2) \right) \left(\varepsilon^{\mu_2 \nu_2 \rho_2 \sigma_2} q_{2\mu_2} \varepsilon^{\lambda_2}_{\nu_2}(\mathbf{q}_2) k_{\rho_2} \varepsilon^{j}_{\sigma_2}(\mathbf{k}) \right) \rho_{\lambda_2 \lambda_1'}(\mathbf{x}, \mathbf{q}_2) \Bigg\} \end{aligned} \tag{4.59}$$

The task now is to carry out the sums over polarization vectors. Let's start from the first two factors. Employing the following parameterization for the 3-momenta

5 Let us recall that the Hamiltonian evaluated at $t = 0$ can be safely moved in the inner commutation because of the commutativity of two copies of the same Hamiltonian evaluated of two different instants in time.

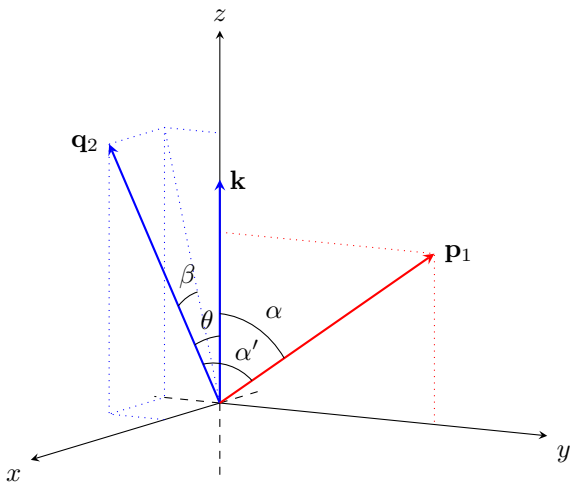

Figure 4.3: Parametrization of momenta in eqs. (4.60a) to (4.60c). Here $\mathbf{k}$ is the momentum of the incoming photon. While $\mathbf{q}_2$ and $\mathbf{p}_1$ are the momenta of the outcoming photon and neutrino respectively.

$$\mathbf{k} = k(0,0,1)\ , \tag{4.60a}$$
$$\mathbf{p}_1 = p_1(0,\sin\alpha,\cos\alpha)\ , \tag{4.60b}$$
$$\mathbf{q}_2 = q_2(\sin\beta\sin\theta,\cos\beta\sin\theta,\cos\theta)\ , \tag{4.60c}$$

we have inside the amplitude

$$\frac{t}{(t-M^2)^2} = -\frac{2}{q_2 k}\frac{(1-\cos\theta)}{\left[2(1-\cos\theta)+\Lambda\right]^2}\ , \tag{4.61}$$

where we defined the parameter

$$\Lambda \equiv \frac{M^2}{q_2 k}\ . \tag{4.62}$$

In the same way, the sums over the Levi-Civita tensors become

$$\left(\varepsilon^{\mu_1\nu_1\rho_1\sigma_1} k_{\mu_1}\varepsilon^{i}_{\nu_1}(\mathbf{k})\, q_{2\rho_1}\varepsilon^{\lambda_2}_{\sigma_1}(\mathbf{q}_2)\right)\left(\varepsilon^{\mu_2\nu_2\rho_2\sigma_2} q_{2\mu_2}\varepsilon^{\lambda_2}_{\nu_2}(\mathbf{q}_2)\, k_{\rho_2}\varepsilon^{\lambda_2'}_{\sigma_2}(\mathbf{k})\right)\rho_{j\lambda_2'}(\mathbf{x},\mathbf{k}) =$$
$$= \left(\varepsilon^{\mu_1\nu_1\rho_1\sigma_1} k_{\mu_1}\varepsilon^{\lambda_1}_{\nu_1}(\mathbf{k})\, q_{2\rho_1}\varepsilon^{\lambda_2}_{\sigma_1}(\mathbf{q}_2)\right)\left(\varepsilon^{\mu_2\nu_2\rho_2\sigma_2} q_{2\mu_2}\varepsilon^{\lambda_2}_{\nu_2}(\mathbf{q}_2)\, k_{\rho_2}\varepsilon^{j}_{\sigma_2}(\mathbf{k})\right)\rho_{\lambda_1 i}(\mathbf{x},\mathbf{k}) \tag{4.63}$$
$$= k^2 q_2^2(1-\cos\theta)^2\left[\delta_{i1}\rho_{j1}(\mathbf{x},\mathbf{k}) + \delta_{i2}\rho_{j2}(\mathbf{x},\mathbf{k})\right]\ . \tag{4.64}$$

Concering the first factor instead, we can employ the following parametrization for the 3-momenta

$$\mathbf{k} = |\mathbf{k}|(0,0,1)\ , \tag{4.65a}$$
$$\mathbf{q}_2 = |\mathbf{q}_2|(0,\sin\theta,\cos\theta)\ , \tag{4.65b}$$
$$\mathbf{p}_2 = |\mathbf{p}_2|(\sin\beta'\sin\alpha',\cos\beta'\sin\alpha',\cos\alpha')\ . \tag{4.65c}$$

We have thus that the factor in eq. (4.61) stays unaltered, while the sum involving Levi-Civita tensors is now

$$\left(\varepsilon^{\mu_1\nu_1\rho_1\sigma_1}k_{\mu_1}\varepsilon^{i}_{\nu_1}(\mathbf{k})\,q_{2\rho_1}\varepsilon^{\lambda_1'}_{\sigma_1}(\mathbf{q}_2)\right)\left(\varepsilon^{\mu_2\nu_2\rho_2\sigma_2}q_{2\mu_2}\varepsilon^{\lambda_2}_{\nu_2}(\mathbf{q}_2)\,k_{\rho_2}\varepsilon^{j}_{\sigma_2}(\mathbf{k})\right)\rho_{\lambda_2\lambda_1'}(\mathbf{x},\mathbf{q}_2) = \\ = k^2q_2^2(1-\cos\theta)^2\left[\delta_{i1}\delta_{j1}\rho_{22}(\mathbf{x},\mathbf{q}_2)+\delta_{i2}\delta_{j2}\rho_{11}(\mathbf{x},\mathbf{q}_2)+\delta_{i1}\delta_{j2}\rho_{12}(\mathbf{x},\mathbf{q}_2)+\delta_{i2}\delta_{j1}\rho_{21}(\mathbf{x},\mathbf{q}_2)\right. \tag{4.66}$$

Now we can rewrite everything in terms of Stokes parameters thanks to the relations

$$I(\mathbf{x},\mathbf{k}) \equiv \frac{1}{2}\left[\rho_{11}(\mathbf{x},\mathbf{k})+\rho_{22}(\mathbf{x},\mathbf{k})\right]\,, \tag{4.67a}$$

$$Q(\mathbf{x},\mathbf{k}) \equiv \frac{1}{2}\left[\rho_{11}(\mathbf{x},\mathbf{k})-\rho_{22}(\mathbf{x},\mathbf{k})\right]\,, \tag{4.67b}$$

$$U(\mathbf{x},\mathbf{k}) \equiv \frac{1}{2}\left[\rho_{12}(\mathbf{x},\mathbf{k})+\rho_{21}(\mathbf{x},\mathbf{k})\right]\,, \tag{4.67c}$$

$$V(\mathbf{x},\mathbf{k}) \equiv \frac{i}{2}\left[\rho_{11}(\mathbf{x},\mathbf{k})-\rho_{21}(\mathbf{x},\mathbf{k})\right]\,. \tag{4.67d}$$

All the equations obtained have the same structure, as an example we show the one for the Q parameter

$$\frac{d}{dt}Q(\mathbf{x},\mathbf{k}) = \left(g_{\phi\nu\nu}g_{\phi\gamma\gamma}\right)^2\int d\Pi_{\mathbf{p}_1}d\Pi_{\mathbf{p}_2}d\Pi_{\mathbf{q}_2}\,(2\pi)^4\,\delta^{(4)}\left(p_1+k-p_2-q_2\right) \\ \times\frac{q_2(1-\cos\theta)^3}{\left[2(1-\cos\theta)+\Lambda\right]^2}\left[Q(\mathbf{x},\mathbf{k})f_\nu(\mathbf{x},\mathbf{p}_1)+f_\nu(\mathbf{x},\mathbf{p}_2)Q(\mathbf{x},\mathbf{q}_2)\right]\,. \tag{4.68}$$

4.3.1 Perturbation theory

Now we want to apply cosmological perturbations theory to our Botlzmann equations. We can perform the following perturbative expansion on the photon density matrix

$$\rho_{ij}(\mathbf{x},\mathbf{k}) = \rho^{(0)}_{ij}(k)+\rho^{(1)}_{ij}(\mathbf{x},\mathbf{k})+\cdots\,, \tag{4.69}$$

where the unperturbed density matrix is

$$\rho^{(0)}_{ij}(k) = \frac{1}{2}\begin{pmatrix} I_0(k) & 0 \\ 0 & I_0(k)\end{pmatrix}\,, \tag{4.70}$$

while the perturbations are defined as

$$\rho^{(1)}_{ij}(\mathbf{x},\mathbf{k}) = \frac{k}{2}\frac{\partial I_0(k)}{\partial k}\begin{pmatrix}\Delta_I(\mathbf{x},\mathbf{k})+\Delta_Q(\mathbf{x},\mathbf{k}) & \Delta_U(\mathbf{x},\mathbf{k})-i\Delta_V(\mathbf{x},\mathbf{k}) \\ \Delta_U(\mathbf{x},\mathbf{k})+i\Delta_V(\mathbf{x},\mathbf{k}) & \Delta_I(\mathbf{x},\mathbf{k})-\Delta_Q(\mathbf{x},\mathbf{k})\end{pmatrix}\,. \tag{4.71}$$

Here $\mathbf{k}_c = a\mathbf{k}$ is the comoving wave number of photons, with $a(\eta)$ denoting the scale factor as a function of conformal time $d\eta = dt/a(t)$, and

$I_0(k) = [\exp(k/T) - 1]^{-1}$ is the Bose-Einstein distribution function describing the homogeneous (unperturbed) distribution of the CMB photons. Given the linearity of the perturbative expansion, and the linearity of the transformations relating the density matrix elements to the Stokes parameters (see eqs. (4.67b)-(4.67d)), we find that also the parameters inherit a perturbative expansion as

$$I(\mathbf{x}, \mathbf{k}) = I^{(0)}(k) + I^{(1)}(\mathbf{x}, \mathbf{k}) + \cdots , \tag{4.72}$$

where

$$I^{(1)}(\mathbf{x}, \mathbf{k}) \equiv k \frac{\partial I_0(k)}{\partial k} \Delta_I(\mathbf{x}, \mathbf{k}) \tag{4.73}$$

In an analogous way, we can write the neutrino distribution function as

$$f_\nu(\mathbf{x}, \mathbf{p}) = f_\nu^{(0)}(p) + f_\nu^{(1)}(\mathbf{x}, \mathbf{p}) + \cdots , \tag{4.74}$$

where the unperturbed distribution function is a standard Fermi-Dirac distribution

$$f_\nu^{(0)}(p) = \left[\exp\left(\frac{p}{T_\nu}\right) + 1\right]^{-1} . \tag{4.75}$$

After the substitution of these two expansions, we find at 0-th order

$$\begin{aligned} \frac{d}{dt} I_0(k) = & \\ = & \left(g_{\phi\nu\nu} g_{\phi\gamma\gamma}\right)^2 \int d\Pi_{\mathbf{p}_1} d\Pi_{\mathbf{p}_2} d\Pi_{\mathbf{q}_2} (2\pi)^4 \delta^{(4)}(p_1 + k - p_2 - q_2) \\ & \times \frac{q_2 (1 - \cos\theta)^3}{\left[2(1 - \cos\theta) + \Lambda\right]^2} \left[I_0(k) f_\nu^{(0)}(p_1) - f_\nu^{(0)}(p_2) I_0(q_2) \right] . \end{aligned} \tag{4.76}$$

while at 1-st order we have, for the Stokes parameters related to linear polarization

$$\begin{aligned} \frac{d}{dt} Q^{(1)}(\mathbf{x}, \mathbf{k}) = & \\ = & \left(g_{\phi\nu\nu} g_{\phi\gamma\gamma}\right)^2 \int d\Pi_{\mathbf{p}_1} d\Pi_{\mathbf{p}_2} d\Pi_{\mathbf{q}_2} (2\pi)^4 \delta^{(4)}(p_1 + k - p_2 - q_2) \\ & \times \frac{q_2 (1 - \cos\theta)^3}{\left[2(1 - \cos\theta) + \Lambda\right]^2} \left[Q^{(1)}(\mathbf{x}, \mathbf{k}) f_\nu^{(0)}(p_1) + f_\nu^{(0)}(p_2) Q^{(1)}(\mathbf{x}, \mathbf{q}_2) \right] , \end{aligned} \tag{4.77}$$

and

$$\begin{aligned} \frac{d}{dt} U^{(1)}(\mathbf{x}, \mathbf{k}) = & \\ = & \left(g_{\phi\nu\nu} g_{\phi\gamma\gamma}\right)^2 \int d\Pi_{\mathbf{p}_1} d\Pi_{\mathbf{p}_2} d\Pi_{\mathbf{q}_2} (2\pi)^4 \delta^{(4)}(p_1 + k - p_2 - q_2) \\ & \times \frac{q_2 (1 - \cos\theta)^3}{\left[2(1 - \cos\theta) + \Lambda\right]^2} \left[U^{(1)}(\mathbf{x}, \mathbf{k}) f_\nu^{(0)}(p_1) - f_\nu^{(0)}(p_2) U^{(1)}(\mathbf{x}, \mathbf{q}_2) \right] . \end{aligned} \tag{4.78}$$

While for circular polarization we have

$$\frac{d}{dt}V^{(1)}(\mathbf{x},\mathbf{k}) = \\ = -\left(g_{\phi\nu\nu}g_{\phi\gamma\gamma}\right)^2 \int d\Pi_{\mathbf{p}_1} d\Pi_{\mathbf{p}_2} d\Pi_{\mathbf{q}_2} \left(2\pi\right)^4 \delta^{(4)}\left(p_1 + k - p_2 - q_2\right) \\ \times \frac{q_2(1-\cos\theta)^3}{\left[2(1-\cos\theta)+\Lambda\right]^2}\left[V^{(1)}(\mathbf{x},\mathbf{k}) f_\nu^{(0)}(p_1) + f_\nu^{(0)}(p_2) V^{(1)}(\mathbf{x},\mathbf{q}_2)\right] . \tag{4.79}$$

4.3.2 Reduction of $\mathbb{C}_1\left[Q, f_\nu\right]$

We have that

$$\mathbb{C}_1\left[Q, f_\nu\right] \equiv \left(g_{\phi\nu\nu}g_{\phi\gamma\gamma}\right)^2 Q^{(1)}(\mathbf{x},\mathbf{k}) \int d\Pi_{\mathbf{p}_1} d\Pi_{\mathbf{p}_2} d\Pi_{\mathbf{q}_2} \ \left(2\pi\right)^4 \\ \times \delta^{(4)}\left(p_1 + k - p_2 - q_2\right) \frac{|\mathbf{q_2}|(1-\cos\theta)^3}{\left[2(1-\cos\theta)+\Lambda\right]^2} f_\nu^{(0)}(|\mathbf{p_1}|) . \tag{4.80}$$

Thanks to the parametrization in eqs. (4.60a)-(4.60c), we can expand the three integrals in the collision term obtaining

$$\mathbb{C}_1\left[Q, f_\nu\right] = \frac{\left(g_{\phi\nu\nu}g_{\phi\gamma\gamma}\right)^2}{4\left(2\pi\right)^4} Q^{(1)}(\mathbf{x},\mathbf{k}) \int_0^\infty d|\mathbf{p}_1| \ |\mathbf{p}_1| f_\nu^{(0)}(|\mathbf{p}_1|) \int_{-1}^1 d\cos\alpha \\ \times \int_0^\infty d|\mathbf{q}_2| \ |\mathbf{q}_2|^2 \int_{-1}^1 d\cos\theta \frac{(1-\cos\theta)^3}{\left[2(1-\cos\theta)+\Lambda\right]^2} \\ \times \int_0^{2\pi} d\beta \int \frac{d^3\mathbf{p}_2}{2|\mathbf{p}_2|} \ \delta^{(4)}(p_1 + k - p_2 - q_2) , \tag{4.81}$$

where we have used $d^3\mathbf{p}_1 = 2\pi|\mathbf{p}_1|^2 d|\mathbf{p}_1|^2 d\cos\alpha$ and $d^3\mathbf{q}_2 = |\mathbf{q}_2|^2 d|\mathbf{q}_2|^2 d\cos\theta d\beta$. Since the only dependence here is in the Dirac delta, we first integrate over $d^3\mathbf{p}_2$ to get

$$\int \frac{d^3\mathbf{p}_2}{2|\mathbf{p}_2|}\delta^{(4)}\left(p_1 + k - p_2 - q_2\right) = \\ = \delta\left(\left[|\mathbf{p}_1| + |\mathbf{k}| - |\mathbf{q}_2|\right]^2 - |\mathbf{p}_1 + \mathbf{k} - \mathbf{q}_2|^2\right)\Theta\left(|\mathbf{p}_1| + |\mathbf{k}| - |\mathbf{q}_2|\right) , \tag{4.82}$$

and again, thanks to the parametrization in Eqs. (4.60a)-(4.60c), this relation can be equivalently expressed as

$$\int \frac{d^3\mathbf{p}_2}{2|\mathbf{p}_2|}\delta^{(4)}\left(p_1 + k - p_2 - q_2\right) = \\ = \delta(g_1(|\mathbf{k}|,|\mathbf{p}_1|,|\mathbf{q}_2|,\alpha,\beta,\theta))\Theta\left(|\mathbf{p}_1| + |\mathbf{k}| - |\mathbf{q}_2|\right) , \tag{4.83}$$

where

$$g_1\left(|\mathbf{p}_1|,|\mathbf{k}|,|\mathbf{q}_2|,\alpha,\beta,\theta\right) \equiv 2\left[|\mathbf{p}_1||\mathbf{k}|(1-\cos\alpha) - |\mathbf{k}||\mathbf{q}_2|\left(1-\cos\theta\right)\right. \\ \left. -|\mathbf{p}_1||\mathbf{q}_2|\left(1-\sin\alpha\sin\theta\cos\beta-\cos\alpha\cos\theta\right)\right] , \tag{4.84}$$

which turn eq. (4.81) as

$$\mathbb{C}_1[Q, f_\nu] = \frac{\left(g_{\phi\nu\nu} g_{\phi\gamma\gamma}\right)^2}{4\,(2\pi)^4} Q^{(1)}(\mathbf{x}, \mathbf{k}) \int_0^\infty d|\mathbf{p}_1|\; |\mathbf{p}_1| f_\nu^{(0)}(|\mathbf{p}_1|) \int_{-1}^1 d\cos\alpha$$
$$\times \int_0^\infty d|\mathbf{q}_2|\; |\mathbf{q}_2|^2 \int_{-1}^1 d\cos\theta \frac{(1-\cos\theta)^3}{[2(1-\cos\theta)+\Lambda]^2}$$
$$\times \int_0^{2\pi} d\beta\; \delta(g_1(|\mathbf{k}|, |\mathbf{p}_1|, |\mathbf{q}_2|, \alpha, \beta, \theta)) \Theta\left(|\mathbf{p}_1| + |\mathbf{k}| - |\mathbf{q}_2|\right) , \tag{4.85}$$

For the β integral, we use the well–known identity of the Dirac's delta

$$\int_0^{2\pi} d\beta\; \delta\left(g_1(\ldots, \beta, \ldots)\right) = \int_0^{2\pi} \sum_i \left|\frac{\partial g_1}{\partial \beta}\right|_{\beta_i}^{-1} \delta\left(\beta - \beta_i\right) , \tag{4.86}$$

where β_i are the simple roots of the real–valued function $g(\ldots, \beta, \ldots)$. In our case, we have

$$\cos\beta_i = \frac{|\mathbf{k}||\mathbf{q}_2|(1-\cos\theta) - |\mathbf{p}_1||\mathbf{k}|(1-\cos\alpha) + |\mathbf{p}_1||\mathbf{q}_2|(1-\cos\alpha\cos\theta)}{|\mathbf{p}_1||\mathbf{q}_2|\sin\alpha\sin\theta} , \tag{4.87}$$

and

$$\frac{\partial g_1}{\partial \beta} = -2|\mathbf{p}_1||\mathbf{q}_2|\sin\alpha\sin\theta\sin\beta . \tag{4.88}$$

Because $\cos\beta_i = \cos(-\beta_i)$, eq. (4.87) has one solution for β_i in $[0, \pi]$ and one in $[\pi, 2\pi]$. So, eq. (4.86) can be trivially rewritten as

$$\int_0^{2\pi} d\beta\; \delta\left(g_1(\beta, \ldots)\right) = 2\int_0^{\pi} d\beta \left|\frac{\partial g_1}{\partial \beta}\right|_{\beta_i}^{-1} \delta\left(\beta - \beta_i\right) = 2\left|\frac{\partial g_1}{\partial \beta}\right|_{\beta_i}^{-1} , \tag{4.89}$$

provided any further dependence of the collision integrand on β is a function of $\cos\beta$. Moreover, we remember that $\cos\beta_i$ must lie in $[-1, 1]$, or, equivalently, $\cos^2\beta_i \leq 1$. When applied to eq. (4.87), this condition effectively limits the values the outgoing parameters $|\mathbf{q}_2|$ and $\cos\theta$ can take in a physical process for a given combination of incoming parameters $|\mathbf{p}_1|$, $|\mathbf{k}|$ and $\cos\alpha$ (recall that eq. (4.87) originates from energy-momentum conservation). To ensure that this physical limitation is respected in subsequent integrations, we introduce in eq. (4.89) a step function

$$\Theta\left(1 - \cos^2\beta_i\right) = \Theta\left(\left|\frac{\partial g_1}{\partial \beta}\right|_{\beta_i}^2\right) = \Theta\left(a_1\cos^2\theta + b_1\cos\theta + c_1\right) , \tag{4.90}$$

where the first equality follows from the observation that the condition $\cos^2\beta_i \leq 1$ translates simply into $|\partial g/\partial\beta|^2_{\beta_i} = 4|\mathbf{p}_1|^2|\mathbf{q}_2|^2\sin^2\alpha\sin^2\theta\left(1-\cos^2\beta_i\right) \geq 0$ using equation eq. (4.88). Instead, in the second equality we have defined

$$a_1 \equiv -4|\mathbf{q}_2|^2\left(|\mathbf{p}_1|^2 + 2|\mathbf{p}_1||\mathbf{k}|\cos\alpha + |\mathbf{k}|^2\right) = -4|\mathbf{q}_2|^2|\mathbf{p}_1+\mathbf{k}|^2 \leq 0\,, \tag{4.91a}$$

$$b_1 \equiv 8|\mathbf{q}_2|(|\mathbf{k}| + |\mathbf{p}_1|\cos\alpha)\left[|\mathbf{q}_2|(|\mathbf{p}_1|+|\mathbf{k}|) - |\mathbf{k}||\mathbf{p}_1|(1-\cos\alpha)\right]\,, \tag{4.91b}$$

$$\begin{aligned} c_1 \equiv\ & 4|\mathbf{p}_1|^2|\mathbf{q}_2|^2(1-\cos^2\alpha) \\ & - 4\left[|\mathbf{p}_1||\mathbf{q}_2| + |\mathbf{k}||\mathbf{q}_2| - |\mathbf{p}_1||\mathbf{k}|(1-\cos\alpha)\right]^2\,, \end{aligned} \tag{4.91c}$$

nothing that a_1 is always negative. Now we want to substitute Eqs. (4.89) and (4.90) into eq. (4.85), keeping and mind that the computation of the β integral imply the substitution of every $\cos\beta$ factor with eq. (4.87) due to the presence of the Dirac's delta function. So that we arrive to

$$\begin{aligned} \mathbb{C}_1[Q, f_\nu] = & \frac{\left(g_{\phi\nu\nu}g_{\phi\gamma\gamma}\right)^2}{2\,(2\pi)^4} Q^{(1)}(\mathbf{x},k)\int_0^\infty d|\mathbf{p}_1|\ |\mathbf{p}_1| f_\nu^{(0)}(|\mathbf{p}_1|)\int_{-1}^1 d\cos\alpha \\ & \times \int_0^\infty d|\mathbf{q}_2|\ |\mathbf{q}_2|^2\Theta(|\mathbf{p}_1|+|\mathbf{k}|-|\mathbf{q}_2|) \\ & \times \int_{-1}^1 d\cos\theta\ \frac{(1-\cos\theta)^3}{\left[2(1-\cos\theta)+\Lambda\right]^2}\frac{\Theta\left(-|a_1|\cos^2\theta + b_1\cos\theta + c_1\right)}{\sqrt{-|a_1|\cos^2\theta + b_1\cos\theta + c_1}} \end{aligned} \tag{4.92}$$

Let's consider now the $\cos\theta$-integral in the second line of eq. (4.92). Since a_1 is always negative, the argument of the step function is a downward parabola. So, to ensure the integrand to be real we have to restrict our integration domain between parabola's roots,

$$x_\pm = \frac{b_1}{2|a_1|} \pm \sqrt{\left(\frac{b_1}{2|a_1|}\right)^2 + \frac{c_1}{|a_1|}}\,, \tag{4.93}$$

with $x_+ > x_-$. We require $b_1^2 - 4a_1c_1 > 0$, through a new Heaviside's step function, in order to have a non-vanishing region of integration. We can then rewrite the integral in eq. (4.92) as

$$\begin{aligned} & \frac{1}{\sqrt{|a_1|}}\int_{x_-}^{x_+} dx\ \frac{(1-\cos\theta)^3}{\left[2(1-x)+\Lambda\right]^2}\frac{\Theta\left(b_1^2-4a_1c_1\right)}{\sqrt{(x-x_-)(x_+-x)}} = \\ & = \Theta\left(b_1^2-4a_1c_1\right)\frac{\pi}{8\sqrt{|a_1|}} \\ & \quad \times \begin{cases} 2 - x_- - x_+ - 2\Lambda + \dfrac{\Lambda^2}{2}\dfrac{3}{\sqrt{(1-x_-)(1-x_+)}} & \text{LML} \\ \dfrac{1}{2\Lambda^2}\left[16 - 24(x_-+x_+) + 12x_-x_+ + 18\left(x_-^2+x_+^2\right)\right. & \text{HML} \\ \qquad\qquad \left. -3x_-x_+(x_-+x_+) - 5\left(x_-^3+x_+^3\right)\right] & \end{cases} \end{aligned} \tag{4.94}$$

LIGHT MEDIATOR LIMIT In what follows for the light mediator limit we take only leading order contribution in Λ to carry out easier calculations. Under this approximation, out collision term becomes

$$\begin{aligned}\mathbb{C}_1^{\text{light}}[Q, f_\nu] = &\frac{\left(g_{\phi\nu\nu}g_{\phi\gamma\gamma}\right)^2}{64\,(2\pi)^3}Q^{(1)}(\mathbf{x},k)\int_0^\infty d|\mathbf{p}_1|\;|\mathbf{p}_1|f_\nu^{(0)}(|\mathbf{p}_1|)\\ &\times\int_{-1}^{1}d\cos\alpha\int_0^\infty d|\mathbf{q}_2|\;|\mathbf{q}_2|\Theta(|\mathbf{p}_1|+|\mathbf{k}|-|\mathbf{q}_2|)\\ &\times\frac{\Theta\left(b_1^2-4a_1c_1\right)}{\sqrt{|\mathbf{k}|^2+|\mathbf{p}_1|^2+2|\mathbf{k}||\mathbf{p}_1|\cos\alpha}}\left[2(1-\Lambda)-x_--x_+\right]\,. \end{aligned}\tag{4.95}$$

Looking now at the step function $\Theta\left(b_1^2-4a_1c_1\right)$, and evaluating its argument explicitly, using the definitions of Eqs. (4.91a)–(4.91c), we find

$$\begin{aligned}b_1^2-4a_1c_1 = &\,64|\mathbf{k}||\mathbf{p}_1|^3|\mathbf{q}_2|^2\sin^2\alpha(1-\cos\alpha)\\ &\times\left[-2|\mathbf{q}_2|^2+2|\mathbf{q}_2|(|\mathbf{p}_1|+|\mathbf{k}|)-|\mathbf{k}||\mathbf{p}_1|(1-\cos\alpha)\right]\,. \end{aligned}\tag{4.96}$$

We see immediately that it has four $|\mathbf{q}_2|$–roots at $\{0,0,R_1,R_2\}$, where

$$R_{1,2}\equiv\frac{1}{2}\left(|\mathbf{k}|+|\mathbf{p}_1|\pm\sqrt{|\mathbf{k}|^2+|\mathbf{p}_1|^2+2|\mathbf{k}||\mathbf{p}_1|\cos\alpha}\right)\,,\tag{4.97}$$

and $R_2\geq R_1\geq 0$ because of the triangular inequality. Given that the parabolic part of eq. (4.96) always opens downwards, the region enclosed by R_1 and R_2 is always positive. Thus, we can rewrite $\Theta\left(b_1^2-4a_1c_1\right)$ as

$$\Theta\left(b_1^2-4a_1c_1\right)=\Theta(|\mathbf{q}_2|-R_1)\Theta(R_2-|\mathbf{q}_2|)\,,\tag{4.98}$$

so that the $|\mathbf{q}_2|$-integral in eq. (4.95) evaluates to

$$\begin{aligned}&\int_{R1}^{R2}d|\mathbf{q}_2|\;|\mathbf{q}_2|\Theta(|\mathbf{p}_1|+|\mathbf{k}|-|\mathbf{q}_2|)\left[2(1-\Lambda)-x_--x_+\right]=\\ &\quad=2|\mathbf{p}_1||\mathbf{k}+\mathbf{p}_1|\left[\sin^2\left(\frac{\alpha}{2}\right)-\frac{M^2}{|\mathbf{k}||\mathbf{p}_1|}\right]\,,\end{aligned}\tag{4.99}$$

noting that the step function $\Theta(|\mathbf{p}_1|+|\mathbf{k}|-|\mathbf{q}_2|)$ has become redundant because $R_2\leq|\mathbf{k}|+|\mathbf{p}_1|$ from eq. (4.97).

Now, our collision term reduces to

$$\begin{aligned}\mathbb{C}_1^{\text{light}}[Q, f_\nu] = &\frac{\left(g_{\phi\nu\nu}g_{\phi\gamma\gamma}\right)^2}{32\,(2\pi)^3}Q^{(1)}(\mathbf{x},k)\int_0^\infty d|\mathbf{p}_1|\;|\mathbf{p}_1|^2f_\nu^{(0)}(|\mathbf{p}_1|)\\ &\int_{-1}^{1}d\cos\alpha\;\left[\sin^2\left(\frac{\alpha}{2}\right)-\frac{M^2}{|\mathbf{k}||\mathbf{p}_1|}\right]\\ =&\frac{1}{256}\left(\frac{g_{\nu\phi}g_{\gamma\phi}}{2\pi}\right)^2\left[3\zeta(3)T_\nu^3-\frac{\pi^2}{3|\mathbf{k}|}M^2T_\nu^2\right]Q^{(1)}(\mathbf{x},k)\end{aligned}\tag{4.100}$$

HEAVY MEDIATOR LIMIT On the opposite side, in the heavy mediator limit, our collision integral becomes

$$\begin{aligned}\mathbb{C}_1^{\text{heavy}}[Q, f_\nu] = &\frac{\left(g_{\phi\nu\nu}g_{\phi\gamma\gamma}\right)^2}{128\,(2\pi)^3}Q^{(1)}(\mathbf{x},k)\frac{|\mathbf{k}|^2}{M^4}\int_0^\infty d|\mathbf{p}_1|\;|\mathbf{p}_1|f_\nu^{(0)}(|\mathbf{p}_1|)\\ &\times\int_{-1}^{1}d\cos\alpha\int_0^\infty d|\mathbf{q}_2|\;|\mathbf{q}_2|^3\Theta(|\mathbf{p}_1|+|\mathbf{k}|-|\mathbf{q}_2|)\\ &\times\frac{\Theta\left(b_1^2-4a_1c_1\right)}{\sqrt{|\mathbf{k}|^2+|\mathbf{p}_1|^2+2|\mathbf{k}||\mathbf{p}_1|\cos\alpha}}\left[16-24(x_-+x_+)\right.\\ &\left.+12x_-x_+ +18\left(x_-^2+x_+^2\right)-3x_-x_+(x_-+x_+)-5\left(x_-^3+x_+^3\right)\right]\,.\end{aligned} \tag{4.101}$$

With a procedure analogous to what we have done for the light mediator limit, we can evaluate the $|\mathbf{q}_2|$-integral

$$\begin{aligned}&\int_{R1}^{R2}d|\mathbf{q}_2|\;|\mathbf{q}_2|^3\Theta(|\mathbf{p}_1|+|\mathbf{k}|-|\mathbf{q}_2|)\left[16-24(x_-+x_+)\right.\\ &\qquad\left.+12x_-x_+ +18\left(x_-^2+x_+^2\right)-3x_-x_+(x_-+x_+)-5\left(x_-^3+x_+^3\right)\right]\\ &=32|\mathbf{p}_1|^3|\mathbf{k}+\mathbf{p_1}|\sin^6\left(\frac{\alpha}{2}\right)\,,\end{aligned} \tag{4.102}$$

with our collision term reducing now to

$$\begin{aligned}\mathbb{C}_1^{\text{heavy}}[Q, f_\nu] &= \frac{\left(g_{\phi\nu\nu}g_{\phi\gamma\gamma}\right)^2}{4\,(2\pi)^3}Q^{(1)}(\mathbf{x},k)\frac{|\mathbf{k}|^2}{M^2}\int_0^\infty d|\mathbf{p}_1|\;|\mathbf{p}_1|^4f_\nu^{(0)}(|\mathbf{p}_1|)\\ &\qquad\times\int_{-1}^{1}d\cos\alpha\;\sin^6\left(\frac{\alpha}{2}\right)\\ &= \frac{225}{256}\left(\frac{g_{\nu\phi}g_{\gamma\phi}}{2\pi}\right)^2\frac{|\mathbf{k}|^2}{M^4}\zeta(5)T_\nu^5Q^{(1)}(\mathbf{x},k)\end{aligned} \tag{4.103}$$

4.3.3 Reduction of $\mathbb{C}_2[Q, f_\nu]$

We have that

$$\begin{aligned}\mathbb{C}_2[Q, f_\nu] \equiv &\left(g_{\phi\nu\nu}g_{\phi\gamma\gamma}\right)^2\int d\Pi_{\mathbf{p}_1}d\Pi_{\mathbf{p}_2}d\Pi_{\mathbf{q}_2}\;(2\pi)^4\\ &\times\delta^{(4)}\left(p_1+k-p_2-q_2\right)\frac{q_2(1-\cos\theta)^3}{\left[2(1-\cos\theta)+\Lambda\right]^2}f_\nu^{(0)}(p_2)Q^{(1)}(\mathbf{x},\mathbf{q}_2)\,.\end{aligned} \tag{4.104}$$

Since the integrand does not depend on $\mathbf{p}_1$, the Dirac's delta can be simplified to

$$\begin{aligned}&\int\frac{d^3\mathbf{p}_1}{2|\mathbf{p}_1|}\delta^{(4)}\left(p_1+k-p_2-q_2\right)=\\ &\quad=\delta\left(\left[|\mathbf{p}_2|+|\mathbf{q}_2|-|\mathbf{k}|\right]^2-|\mathbf{p}_2+\mathbf{q}_2-\mathbf{k}|^2\right)\Theta\left(|\mathbf{p}_2|+|\mathbf{q}_2|-|\mathbf{k}|\right)\,.\end{aligned} \tag{4.105}$$

Then, using the parametrization in Eqs. (4.65b)–(4.65c) and following the arguments of section 4.3.2, we find

$$\begin{aligned}\mathbb{C}_2\left[Q, f_\nu\right] = &\frac{\left(g_{\phi\nu}g_{\phi\gamma\gamma}\right)^2}{4\left(2\pi\right)^4}\int_0^\infty d|\mathbf{q}_2|\;|\mathbf{q}_2|^2 Q^{(1)}(\mathbf{x},\mathbf{q}_2)\int_{-1}^1 d\cos\theta\\ &\times\frac{(1-\cos\theta)^3}{\left[2(1-\cos\theta)+\Lambda\right]^2}\int_0^\infty d|\mathbf{p}_2|\;|\mathbf{p}_2| f_\nu^{(0)}(|\mathbf{p}_2|)\int_{-1}^1 d\cos\alpha'\\ &\times\int_0^{2\pi} d\beta'\;\delta\big(g_2(|\mathbf{k}|,|\mathbf{p}_2|,|\mathbf{q}_2|,\alpha',\beta',\theta)\big)\Theta\left(|\mathbf{p}_2|+|\mathbf{q}_2|-|\mathbf{k}|\right)\;,\end{aligned} \tag{4.106}$$

where

$$\begin{aligned}g_2\big(|\mathbf{k}|,|\mathbf{p}_2|,|\mathbf{q}_2|,\alpha',\beta',\theta\big) \equiv 2\big[&-|\mathbf{k}||\mathbf{q}_2|(1-\cos\theta)-|\mathbf{k}||\mathbf{p}_2|\big(1-\cos\alpha'\big)\\ &|\mathbf{p}_2||\mathbf{q}_2|\big(1-\cos\theta\cos\alpha'-\cos\beta'\sin\alpha'\sin\theta\big)\big]\end{aligned} \tag{4.107}$$

is the argument of the Dirac's delta distribution.

Again, because the Dirac's delta alone depends on β', we can rewrite the β'–integral as per equation eq. (4.89), where in this case the step function has arguments

$$\left|\frac{\partial g_2}{\partial\beta'}\right|^2_{\beta'_i} = a_2\cos^2\alpha' + b_2\cos\alpha' + c_2\;, \tag{4.108}$$

with

$$a_2 \equiv -4|\mathbf{p}_2|^2\left(|\mathbf{k}|^2-2|\mathbf{k}||\mathbf{q}_2|\cos\theta+|\mathbf{q}_2|^2\right) = -4|\mathbf{p}_2|^2|\mathbf{k}-\mathbf{q}_2|^2 \leq 0\;, \tag{4.109}$$

$$b_2 \equiv 8|\mathbf{p}_2|\left(|\mathbf{k}|-|\mathbf{q}_2|\cos\theta\right)\left[|\mathbf{p}_2|\left(|\mathbf{k}|-|\mathbf{q}_2|\right)+|\mathbf{k}||\mathbf{q}_2|(1-\cos\theta)\right]\;, \tag{4.110}$$

$$\begin{aligned}c_2 \equiv\;&4|\mathbf{q}_2|^2|\mathbf{p}_2|^2\left(1-\cos^2\theta\right)\\ &-4\left[|\mathbf{k}||\mathbf{p}_2|-|\mathbf{p}_2||\mathbf{q}_2|+|\mathbf{q}_2||\mathbf{k}|(1-\cos\theta)\right]^2\;,\end{aligned} \tag{4.111}$$

and a_2 is, again, always negative. Following the reasoning of section 4.3.2, eq. (4.106) can be recast as

$$\begin{aligned}\mathbb{C}_2\left[Q, f_\nu\right] = &\frac{\left(g_{\phi\nu}g_{\phi\gamma\gamma}\right)^2}{4(2\pi)^4}\int_0^\infty d|\mathbf{q}_2|\int_{-1}^1 d\cos\theta\, Q^{(1)}(\mathbf{x},\mathbf{q}_2)\\ &\times\frac{|\mathbf{q}_2|^2}{\sqrt{|\mathbf{k}|^2+|\mathbf{q}_2|^2-2|\mathbf{k}||\mathbf{q}_2|\cos\theta}}\frac{(1-\cos\theta)^3}{\left[2(1-\cos\theta)+\Lambda\right]^2}\int_0^\infty d|\mathbf{p}_2|\, f_\nu^{(0)}(|\mathbf{p}_2|)\\ &\times\int_{y_-}^{y_+} d\cos\alpha'\;\Theta\left(|\mathbf{p}_2|+|\mathbf{q}_2|-|\mathbf{k}|\right)\frac{\Theta\left(b_2^2-4a_2c_2\right)}{\sqrt{(y_+-\cos\alpha)(\cos\alpha-y_-)}}\end{aligned} \tag{4.112}$$

which, taking also the $\cos\alpha'$–integral becomes

$$\begin{aligned}\mathbb{C}_2\left[Q, f_\nu\right] = &\frac{\left(g_{\phi\nu\nu}g_{\phi\gamma\gamma}\right)^2}{8(2\pi)^3}\int_0^\infty d|\mathbf{q}_2|\int_{-1}^1 d\cos\theta\, Q^{(1)}(\mathbf{x},\mathbf{q}_2)\\ &\times\frac{|\mathbf{q}_2|^2}{\sqrt{|\mathbf{k}|^2+|\mathbf{q}_2|^2-2|\mathbf{k}||\mathbf{q}_2|\cos\theta}}\frac{(1-\cos\theta)^3}{\left[2(1-\cos\theta)+\Lambda\right]^2}\\ &\times\int_0^\infty d|\mathbf{p}_2|\, f_\nu^{(0)}(|\mathbf{p}_2|)\Theta\left(|\mathbf{p}_2|+|\mathbf{q}_2|-|\mathbf{k}|\right)\Theta\left(b_2^2-4a_2c_2\right)\end{aligned} \tag{4.113}$$

where $y_\pm$ are the real and non–degenerate roots of the quadratic in eq. (4.108).

Looking at the step function $\Theta\left(b_2^2-4a_2c_2\right)$, we see that

$$\begin{aligned}b_2^2-4a_2c_2 = &\,64|\mathbf{k}||\mathbf{q}_2|^3|\mathbf{p}_2|^2\sin^2\theta(1-\cos\theta)\\ &\times\left[2|\mathbf{p}_2|^2+2|\mathbf{p}_2|(|\mathbf{q}_2|-|\mathbf{k}|)-|\mathbf{k}||\mathbf{q}_2|(1-\cos\theta)\right]\end{aligned} \tag{4.114}$$

has four $|\mathbf{p}_2|$–roots at $\{0,0,R_3,R_4\}$, where

$$R_{3,4}\equiv\frac{1}{2}\left(|\mathbf{k}|-|\mathbf{q}_2|\pm\sqrt{|\mathbf{k}|^2+|\mathbf{q}_2|^2-2|\mathbf{k}||\mathbf{q}_2|\cos\theta}\right), \tag{4.115}$$

and $R_{3,4}\gtrless 0$ follows from the reverse triangular inequality. We discard the negative root R_4 because it is unphysical. For the remaining R_3, because the parabolic part of eq. (4.114) opens upwards, it serves as a lower limit on $|\mathbf{p}_2|$ integration, so that the step function is equivalently

$$\Theta\left(b_2^2-4a_2c_2\right)=\Theta(|\mathbf{p}_2|-R_3)\,. \tag{4.116}$$

Also, because $R_3\geq|\mathbf{k}|-|\mathbf{q}_2|$, the other step function $\Theta\left(|\mathbf{p}_2|+|\mathbf{q}_2|-|\mathbf{k}|\right)$ in the collision integral eq. (4.113) becomes redundant. Therefore, we find

$$\begin{aligned}\mathbb{C}_2\left[Q, f_\nu\right] = &\frac{\left(g_{\phi\nu\nu}g_{\phi\gamma\gamma}\right)^2}{8(2\pi)^3}\int_0^\infty d|\mathbf{q}_2||\mathbf{q}_2|^2\\ &\times\int_{-1}^1 d\cos\theta\, Q^{(1)}(\mathbf{x},\mathbf{q}_2)\mathcal{K}_2(|\mathbf{k}|,|\mathbf{q}_2|,\cos\theta,\eta)\,,\end{aligned} \tag{4.117}$$

with

$$\begin{aligned}\mathcal{K}_2(|\mathbf{k}|,|\mathbf{q}_2|,\cos\theta,\eta)\equiv &\frac{1}{\sqrt{|\mathbf{k}|^2+|\mathbf{q}_2|^2-2|\mathbf{k}||\mathbf{q}_2|\cos\theta}}\\ &\times\frac{(1-\cos\theta)^3}{\left[2(1-\cos\theta)+\Lambda\right]^2}\int_{R_3}^\infty d|\mathbf{p}_2|\, f_\nu^{(0)}(|\mathbf{p}_2|,\eta)\,,\end{aligned} \tag{4.118}$$

as integration kernel.

The last factor can be analytically computed and it correspond to

$$\begin{aligned}\mathcal{F}(|\mathbf{k}|,|\mathbf{q}_2|,\cos\theta)\equiv &\int_{R_3}^\infty d|\mathbf{p}_2|\, f_\nu^{(0)}(|\mathbf{p}_2|,\eta)\\ = &\,T_\nu\log\left[1+\exp\left(\frac{R_3(|\mathbf{k}|,|\mathbf{q}_2|,\cos\theta)}{T_\nu}\right)\right]-R_3(|\mathbf{k}|,|\mathbf{q}_2|,\cos\theta)\,.\end{aligned} \tag{4.119}$$

Instead, concerning the second factor, we find useful to expand it into the limit studied in the previous section in order to have and easier matching of these results. We write then

$$\mathcal{K}_2(|\mathbf{k}|,|\mathbf{q}_2|,\cos\theta,\eta) = \\ = \begin{cases} \frac{1}{4}\left[(1-\cos\theta) - \frac{M^2}{|\mathbf{k}||\mathbf{q}_2|}\right] \frac{\mathcal{F}(|\mathbf{k}|,|\mathbf{q}_2|,\cos\theta)}{\sqrt{|\mathbf{k}|^2+|\mathbf{q}_2|^2-2|\mathbf{k}||\mathbf{q}_2|\cos\theta}} & \text{LML} \\ \frac{|\mathbf{k}|^2|\mathbf{q}_2|^2}{M^4}(1-\cos\theta)^3 \frac{\mathcal{F}(|\mathbf{k}]|,|\mathbf{q}_2|,\cos\theta)}{\sqrt{|\mathbf{k}|^2+|\mathbf{q}_2|^2-2|\mathbf{k}||\mathbf{q}_2|\cos\theta}} & \text{HML} \end{cases} \tag{4.120}$$

To have an idea of the order of magnitude of these integral kernel we studied them through a numerical evalutaion. We expanded the angular dependence on a basis of Legendre polynomials[6]. From the analysis of the first multipoles it is possible to see that they are suppressed for increasing ℓ thus, when needed, as a first approximation we will consider only the monopole to approximate the kernel. A numerical evaulation of the monopole of the kernel in $\mathbb{C}_2$ integral is shown in fig. 4.4. Concering the momenta dependence it is possible to see that the most significant contribution comes from the left part of the plots, i.e. from the region $k_c/T_\nu \ll 1$. In such a limit, the kernel contributes at most as a $\mathcal{O}(1)$ factor in the Light Mediator Limit (LML), and a $\mathcal{O}(10)$ factor in the Heavy Mediator Limit (HML). These considerations, in first approximation, are true both for the light and heavy mediator limits of the integral kernels.

4.4 STOKES PARAMETERS EQUATIONS

Using now the definition of brightness perturbations (with analogous definitions for the other parameters)

$$Q^{(1)}(\mathbf{x},k_c) = k_c \frac{\partial I_0(k_c)}{\partial k_c} \Delta_Q(\mathbf{x},k_c)\,, \tag{4.121}$$

and moving to comoving momenta $k_c \equiv a(\eta)k$ and conformal time $dt \equiv a(\eta)d\eta$, we can rewrite the previous equation as

6 This step is actually needed if one plans to implement these equations in a Boltzmann solver like `CLASS` or `CAMB`

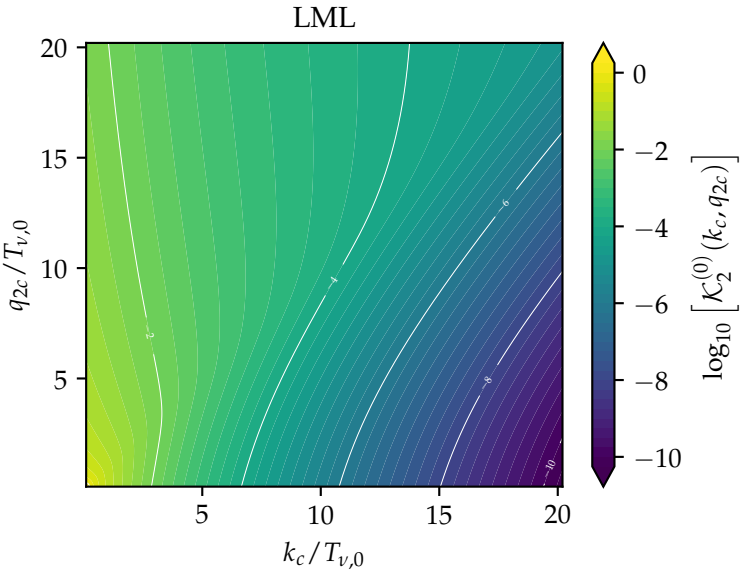

(a)

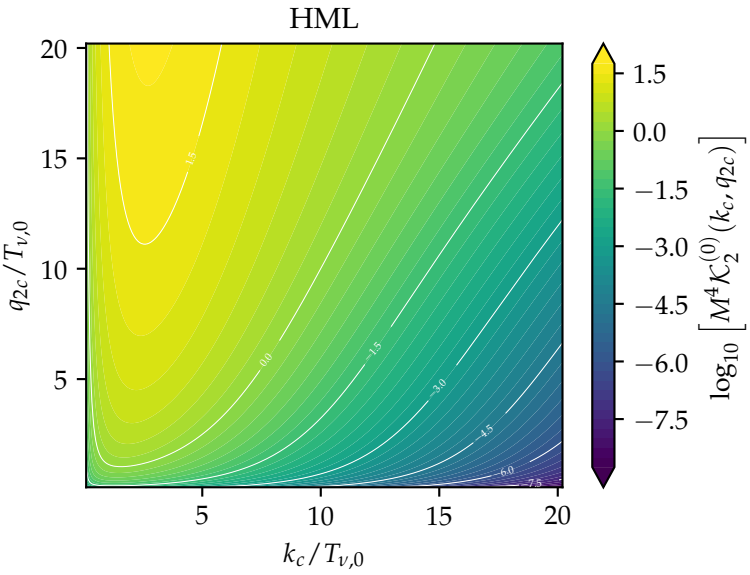

(b)

Figure 4.4: Monopole of the Legendre expansion of the integral kernel defined in eq. (4.120) in the light mediator limit (a) and in the heavy mediator limit (b). Values of momenta in the plot are given in units of $T_{\nu,0}$.

4.4.1 Light mediator limit

$$\frac{d}{d\eta}\Delta_{Q,U}(\mathbf{x},k_c) = \\ = \frac{1}{8a^2}\left(\frac{g_{\phi\nu\nu}g_{\phi\gamma\gamma}}{2\pi}\right)^2\left\{\frac{1}{32}\left[3\zeta(3)T_{\nu 0}^3 - \frac{\pi^2}{3k_c}a^2M^2T_{\nu 0}^2\right]\Delta_{Q,U}(\mathbf{x},k_c)\right. \\ \pm\frac{1}{2\pi k_c}\left[\frac{\partial I_0}{\partial k_c}\right]^{-1}\int_0^\infty dq_{2c}q_{2c}^3\frac{\partial I_0}{\partial q_{2c}} \\ \left.\times\int_{-1}^1 d\cos\theta\,\mathcal{K}_2(k_c,q_{2c},\theta,\eta)\Big|_{\substack{T_\nu=T_{\nu 0}\\M=aM}}\Delta_{Q,U}(\mathbf{x},\mathbf{q}_2)\right\}. \tag{4.122}$$

Then, adding standard CMB terms (due to Compton scattering contribution at recombination) and moving to Fourier space, we have

$$\frac{d}{d\eta}\Delta_{Q,U}(\mathbf{K},\mathbf{k}_c) = -\tau'\left[-\Delta_{Q,U}(\mathbf{K},k_c) + \frac{1}{2}(1-P_2(\mu))\widetilde{\Pi}_{Q,U}(\mathbf{K})\right] \\ + \frac{1}{8a^2}\left(\frac{g_{\phi\nu\nu}g_{\phi\gamma\gamma}}{2\pi}\right)^2\left\{\frac{1}{32}\left[3\zeta(3)T_{\nu 0}^3 - \frac{\pi^2}{3k_c}a^2M^2T_{\nu 0}^2\right]\Delta_{Q,U}(\mathbf{K},\mathbf{k}_c)\right. \\ \pm\frac{1}{2\pi k_c}\left[\frac{\partial I_0}{\partial k_c}\right]^{-1}\int_0^\infty dq_{2c}q_{2c}^3\frac{\partial I_0}{\partial q_{2c}} \\ \left.\times\int_{-1}^1 d\cos\theta\,\mathcal{K}_2(k_c,q_{2c},\theta,\eta)\Big|_{\substack{T_\nu=T_{\nu 0}\\M=aM}}\Delta_{Q,U}(\mathbf{K},\mathbf{q}_2)\right\}. \tag{4.123}$$

4.4.2 Heavy mediator limit

$$\frac{d}{d\eta}\Delta_{Q,U}(\mathbf{x},k_c) = \frac{1}{8a^2}\left(\frac{g_{\phi\nu\nu}g_{\phi\gamma\gamma}}{2\pi}\right)^2\left\{\frac{225}{32}\zeta(5)\frac{k_c^2T_{\nu 0}^5}{a^4M^4}\Delta_{Q,U}(\mathbf{x},k_c)\right. \\ \pm\frac{1}{2\pi k_c}\left[\frac{\partial I_0}{\partial k_c}\right]^{-1}\int_0^\infty dq_{2c}q_{2c}^3\frac{\partial I_0}{\partial q_{2c}} \\ \left.\times\int_{-1}^1 d\cos\theta\,\mathcal{K}_2(k_c,q_{2c},\theta,\eta)\Big|_{\substack{T_\nu=T_{\nu 0}\\M=aM}}\Delta_{Q,U}(\mathbf{x},\mathbf{q}_2)\right\}. \tag{4.124}$$

Then, adding standard CMB terms (due to Compton scattering contribution at recombination) and moving to Fourier space, we have

$$\frac{d}{d\eta}\Delta_{Q,U}(\mathbf{K},\mathbf{k}_c) = -\tau'\left[-\Delta_{Q,U}(\mathbf{K},k_c) + \frac{1}{2}(1-P_2(\mu))\widetilde{\Pi}_{Q,U}(\mathbf{K})\right] \\ + \frac{1}{8a^2}\left(\frac{g_{\phi\nu\nu}g_{\phi\gamma\gamma}}{2\pi}\right)^2\left\{\frac{225}{32}\zeta(5)\frac{k_c^2T_{\nu 0}^5}{a^4M^4}\Delta_{Q,U}(\mathbf{K},\mathbf{k}_c)\right. \\ \pm\frac{1}{2\pi k_c}\left[\frac{\partial I_0}{\partial k_c}\right]^{-1}\int_0^\infty dq_{2c}q_{2c}^3\frac{\partial I_0}{\partial q_{2c}} \\ \left.\times\int_{-1}^1 d\cos\theta\,\mathcal{K}_2(k_c,q_{2c},\theta,\eta)\Big|_{\substack{T_\nu=T_{\nu 0}\\M=aM}}\Delta_{Q,U}(\mathbf{K},\mathbf{q}_2)\right\}. \tag{4.125}$$

These equations represent the main result of this chapter. Given the complex structure of Stokes' parameter equations when considering the scenario studied in this work, we decided to study the cosmological phenomenology to a qualitative level, leaving a full analysis for future works. In the following we study separately the physical consequences of the two additional contributions to eqs. (4.123) and (4.125) turning them on one at a time. In principle, there is no hierarchical structure between the two additional terms in the equation, so the actual solution will be a mix of the two extremal behaviour that we are going to discuss.

4.4.3 Correction to photon's visibility function

At this point, we can rewrite everything in terms of the polarization tensor thanks to the definitions

$$\Delta_P^{\pm} \equiv \Delta_Q \pm i\Delta_U \,. \tag{4.126}$$

Then, adding standard CMB terms (due to Compton scattering contribution at recombination) and moving to Fourier space, we have

$$\begin{aligned}\frac{d}{d\eta}\Delta_P^{\pm}(\mathbf{K},k_c) + iK\mu\Delta_P^{\pm}(\mathbf{K},k_c) = \\ = -\tau'\left[-\Delta_P^{\pm}(\mathbf{K},k_c) + \frac{1}{2}(1-P_2(\mu))\Pi(\mathbf{K})\right] + A'_{\nu\gamma}\Delta_Q(\mathbf{x},k_c)\end{aligned} \tag{4.127}$$

where $\tau'(\eta)$ is the so-called "differential optical depth" of Thomson scattering, defined as

$$\tau(\eta) = \int_{\eta}^{\eta_0} d\eta'\; a(\eta')n_e x_e \sigma_T \,, \tag{4.128}$$

from which $\tau'(\eta) = -a(\eta)n_e x_e \sigma_T$. With n_e being the electron density, x_e the ionization fraction, and $\sigma_T = (8\pi/3)\alpha^2/m_e^2$ the Thomson cross section;

$$\mu \equiv \hat{\mathbf{K}}\cdot\hat{\mathbf{k}}_c \tag{4.129}$$

is the cosine of the angle between the observed CMB photons and the Fourier mode $\mathbf{K}$; and

$$A'_{\nu\gamma} = \frac{1}{256a^2}\left(\frac{g_{\phi\nu\nu}g_{\phi\gamma\gamma}}{2\pi}\right)^2 \begin{cases} 3\zeta(3)T_{\nu 0}^3 - \dfrac{\pi^2}{3k_c}a^2M^2T_{\nu 0}^2 \\ \\ 225\zeta(5)\dfrac{k_c^2T_{\nu 0}^5}{a^4M^4} \end{cases} , \tag{4.130}$$

$$\Pi = \Delta_{I2} + \Delta_{Q0} + \Delta_{Q2} \,, \tag{4.131}$$

where $\Delta_{I\ell}$ and $\Delta_{Q\ell}$ represent the ℓth-order terms in the Legendre polynomial expansion of the corresponding quantities and $T_{\nu,0}$ denotes the CNB temperature today.

In analogy with the standard CMB radiation transport solutions, the differential equations in eq. (4.127) admit the following integral solutions

$$\Delta_P^{\pm}(\mathbf{K}, k_c, \eta_0) = \\ = \int_0^{\eta_0} d\eta \left[\frac{3}{4}(1-\mu^2)\tau'\Pi(\mathbf{K},\eta)\right] e^{iK\mu(\eta-\eta_0)-\tau(\eta)+A_{\nu\gamma}(\eta_0)-A_{\nu\gamma}(\eta)} , \tag{4.132}$$

where η_0 denotes the conformal time today with the condition $e^{-\tau(\eta_0)} = 1$. We have also assumed $e^{-\tau(0)} \approx 0$ as a first approximation. The last terms as argument of the exponential correspond to the correction due to the neutrino-photon scattering. In particular, we have that

$$A_{\nu\gamma}(\eta_0) - A_{\nu\gamma}(\eta) \simeq \frac{3}{256}\zeta(3)T_{\nu,0}^3\left(\frac{g_{\phi\nu\nu}g_{\phi\gamma\gamma}}{2\pi}\right)^2\frac{\eta_0}{3}\left(\frac{\eta_0^3}{\eta^3}-1\right) \\ \simeq 1.29418\times 10^5\left(g_{\phi\nu\nu}g_{\phi\gamma\gamma}\right)^2 \mathrm{GeV}^2 \tag{4.133}$$

where we assumed to be in matter domination to integrate the time dependence of the scale factor.

Now we want to rephrase in terms of the most familiar notion of CMB E– and B– modes as [Zaldarriaga and Seljak, 1997]

$$\Delta_E \equiv -\frac{1}{2}\left[\bar{\eth}^2\Delta_P^+ + \eth^2\Delta_P^-\right] , \tag{4.134}$$

$$\Delta_B \equiv \frac{i}{2}\left[\bar{\eth}^2\Delta_P^+ - \eth^2\Delta_P^-\right] . \tag{4.135}$$

Then, using eq. (4.132), we get the following expression for E– and B– modes

$$E(\mathbf{K},\mu,\eta_0) = -\frac{3}{4}\int_0^{\eta_0} d\eta\, g(\eta)\Pi(\eta,\mathbf{K})\partial_\mu^2\left[(1-\mu^2)^2 e^{iK(\eta-\eta_0)\mu}\right] e^{A_{\nu\gamma}(\eta_0)-A_{\nu\gamma}(\eta)} \\ = \frac{3}{4}\int_0^{\eta_0} d\eta\, g(\eta)\Pi(\eta,\mathbf{K})(1-\partial_x^2)^2\left[x^2 e^{ix\mu}\right] e^{A_{\nu\gamma}(\eta_0)-A_{\nu\gamma}(\eta)} \tag{4.136}$$

$$B(\mathbf{K},\mu,\eta_0) = 0 , \tag{4.137}$$

where $x \equiv K(\eta-\eta_0)$.

Now, following, e.g. Seljak and Zaldarriaga (1996) and Zaldarriaga and Seljak (1997), in order to obtain the expected value of the E–mode polarization today in the $\hat{n}$ direction to the sky, we need to integrate over all the possible Fourier momenta as

$$\Delta_E(\mathbf{n}) = \int d^3\mathbf{K}\,\zeta(\mathbf{K})\Delta_E(\eta_0,\mathbf{K},\mu) , \tag{4.138}$$

where $\zeta(\mathbf{K})$ is a random function used to describe the initial amplitude of primordial scalar perturbations from inflation.[7] After computing eq. (4.138), we can define its harmonic sphere coefficients as

$$a_{\ell m}^E = \left[\frac{(\ell-2)!}{(\ell+2)!}\right]^{1/2}\int d\Omega_{\mathbf{n}}\, Y_{\ell m}^*(\mathbf{n})\Delta_E(\mathbf{n}) . \tag{4.139}$$

7 We remind that primordial tensor perturbations are neglected in our picture. In fact, they are observationally bound to have a much smaller amplitude, thus yielding a subdominant effect on the CMB polarization field.

Then, the E–mode angular power spectrum reads

$$C_\ell^{EE} = \frac{1}{2\ell+1}\sum_m \langle a_{\ell m}^{E*} a_{\ell m}^{E}\rangle \,. \tag{4.140}$$

Therefore, inserting eqs. (4.138) and (4.139), we get

$$\begin{aligned} a_{\ell m}^{E} = &\left[\frac{(\ell-2)!}{(\ell+2)!}\right]^{1/2} \int d\Omega_{\mathbf{n}}\, Y_{\ell m}^{*}(\mathbf{n}) \int d^3\mathbf{K}\, \zeta(\mathbf{K}) \\ &\times \left\{-\frac{3}{4}\int_0^{\eta_0} d\eta\; g(\eta)\Pi(\eta,\mathbf{K})(1-\partial_x^2)^2\left[x^2 e^{ix\mu}\right] e^{A_{\nu\gamma}(\eta_0)-A_{\nu\gamma}(\eta)}\right\} \end{aligned} \tag{4.141}$$

and thus the E–mode power spectrum reads

$$\begin{aligned} C_\ell^{EE} = &\frac{1}{2\ell+1}\left[\frac{(\ell-2)!}{(\ell+2)!}\right]^{1/2} \int d^3\mathbf{K}\, \mathcal{P}_\zeta(K) \\ &\times \sum_m \left| \int d\Omega_{\mathbf{n}} Y_{\ell m}^{*}(\mathbf{n}) \int_0^{\eta_0} d\eta\; g(\eta)\Pi(\eta,\mathbf{K})(1-\partial_x^2)^2\left[x^2 e^{ix\mu}\right] e^{A_{\nu\gamma}(\eta_0)-A_{\nu\gamma}(\eta)}\right|^2 \end{aligned} \tag{4.142}$$

where $\mathcal{P}_\zeta(K)$, is defined as

$$\langle \zeta(\mathbf{K}'), \zeta(\mathbf{K})\rangle \equiv \delta^{(3)}(\mathbf{K}'-\mathbf{K})\mathcal{P}_\zeta(K)\,. \tag{4.143}$$

Now, using that in the $\mathbf{k} \parallel \hat{\mathbf{z}}$ frame we have

$$\int d\Omega_{\mathbf{n}} Y_{\ell m}^{*}(\mathbf{n}) e^{ix\mu} = \sqrt{4\pi(2\ell+1)}\, i^\ell j_\ell(x)\delta_{m0}\,, \tag{4.144}$$

and the fact that spherical Bessel functions satisfy the following relation

$$j_\ell'' + \frac{2}{x}j_\ell' + \left[1 - \frac{\ell(\ell+1)}{x^2}\right] j_\ell = 0\,, \tag{4.145}$$

we find

$$\begin{aligned} C_\ell^{EE} = &\,4\pi\left(\ell^4+2\ell^3-\ell^2-2\ell\right)\int d^3\mathbf{K}\, \mathcal{P}_\zeta(K) \\ &\times \left|\frac{3}{4}\int_0^{\eta_0} d\eta\; g(\eta) e^{A_{\nu\gamma}(\eta_0)-A_{\nu\gamma}(\eta)}\Pi(\eta,\mathbf{K})\frac{j_\ell(x)}{x^2}\right|^2\,, \end{aligned} \tag{4.146}$$

which, thanks to the estimate of eq. (4.133) gives us

$$C_{\ell,\nu\gamma}^{EE} \simeq \exp\left[1.29\times 10^5 \left(g_{\phi\nu\nu} g_{\phi\gamma\gamma}\right)^2 \mathrm{GeV}^2\right] C_\ell^{EE}\,. \tag{4.147}$$

From this equation it is easy to see that taking typical values for the couplings allowed from complementary searches we obtain a variation of the polarization power spectrum below the sensitivity of current experiments.

4.4.4 Cosmic birefringence

The angle describing the linear polarization of an electromagnetic wave in terms of the Stokes parametrs can be written as

$$\alpha \equiv \frac{1}{2}\tan^{-1}\frac{U}{Q}\,. \tag{4.148}$$

Cosmic birefringence is defined as a rotation of the photons polarization direction during its propagation through space[8]. We thus expect the polarization angle to exhibit some time dependence. From eq. (4.148) we can find a general condition on the equation of motion for the Stokes parameters for this to be true, in particular we have

$$\frac{d}{dt}\tan(2\alpha) = \frac{1}{Q}\left[\frac{dU}{dt} - \tan(2\alpha)\frac{dQ}{dt}\right]\,, \tag{4.149}$$

being equal to zero only if the terms in the square brakets equal each other[9]. From this condition it is easy to see that when Q and U feature the same evolution equations we do not have variation of the polarization angle. The most general system satisfying this condition is the propedeutical case

$$\frac{d}{dt}Q(t) = Q_0 f'(t)\,, \tag{4.150a}$$
$$\frac{d}{dt}U(t) = U_0 f'(t)\,, \tag{4.150b}$$

where Q_0 and U_0 are the initial conditions (we can imagine them as the value of the Stokes' parameters in the physical frame at the recombination for the purpose of the study of birefringence generation) and $f'(t)$ is a function representing the generic temporal evolution of the Stokes parameters (here equal between them). It is easy to see that eqs. (4.150a) and (4.150b) give the solution

$$Q(t) = Q_0[1 + f(t)]\,, \tag{4.151a}$$
$$U(t) = U_0[1 + f(t)]\,. \tag{4.151b}$$

These, when inserted in eq. (4.148), show how the polarization angle stays fixed to the initial condition as time passes.

To study a more realistic case we recall that cosmic birefringence is usually introduced as Faraday rotation of linear polarization modes, i.e. Q and U

8 In optics the term birefringence is used to refer to a property where a medium splits a light wave into beams with different refractive indices. In the case of cosmic birefringence the space itself acts like such a medium, potentially due to some new physics BSM.

9 This argument can be safely rewritten in terms of the brightness function for the Stokes parameters being independent on time.

linear polarization parameters sourcing each other. This situation can be summarized with the following evolution equations

$$\frac{d}{d\eta}\Delta_Q(\eta) + iK\mu\Delta_Q(\eta) = 2\theta'(\eta)\, i\Delta_U \,, \tag{4.152a}$$

$$\frac{d}{d\eta}\Delta_U(\eta) + iK\mu\Delta_U(\eta) = -2\theta'(\eta)\Delta_Q \,, \tag{4.152b}$$

where $\theta(t)$ is a function determined by the microphysics responsible for the generation of the additional terms providing cosmic birefringence. This system can be easily solved finding

$$\begin{pmatrix}\Delta_Q(\eta)\\ \Delta_U(\eta)\end{pmatrix} = e^{-iK\mu}\begin{pmatrix}\cos 2\theta(\eta) & \sin 2\theta(\eta)\\ -\sin 2\theta(\eta) & \cos 2\theta(\eta)\end{pmatrix}\begin{pmatrix}\Delta^{\rm in}_Q(\eta)\\ \Delta^{\rm in}_U(\eta)\end{pmatrix} \,, \tag{4.153}$$

where $\Delta^{\rm in}_{Q,U}$ are the initial conditions. Taking now an initial polarization state aligned with the Q–mode, thanks to eq. (4.148) it is easy to see that after a time η it gets rotated by

$$\alpha(\eta) = \frac{1}{2}\tan^{-1}\frac{\Delta_U(\eta)}{\Delta_Q(\eta)} = -\theta(\eta) \,. \tag{4.154}$$

This was a concrete example of how a difference in the temporal evolution of different polarization mode induces a rotation angle on the linear polarization state of the CMB.

Let us come back now to our system with neutrino NSI. Given that we are interested only in the evaluation of cosmic birefringence again we can neglect all terms in common between the evolution equations of Δ_Q and Δ_U. This reduces us to study on equations with only $\mathbb{C}_2$ on their rhs. Before continuing, given that we are interested again in an order of magnitude estimate of this effect, we want to make some assumptions to simplify the collision integrals. After a numerical evaluation, we can approximate the integral kernels as a constant contribution (corresponding) to the monopole of their Legendre decomposition, times a factor pushing the integral towards the region with $k_c \ll 1$. Thus, noticing that

$$\left[\frac{\partial I_0}{\partial k_c}\right]^{-1} \sim_{k_c\to 0} -\frac{k_c^2}{T^2_{\gamma,0}} \,, \tag{4.155}$$

and in turn

$$\left[\frac{\partial I_0}{\partial k_c}\right]^{-1}\int_0^\infty dq_c\, q_c^3\frac{\partial I_0}{\partial q_c} = 6k_c^2\zeta(3) \,, \tag{4.156}$$

we can finally approximate the collision integral $\mathbb{C}_2$ as

$$\begin{aligned}\mathbb{C}_2^{\rm light}[Q/U, f_\nu] &\sim \pm\frac{1}{8a^2}\left(\frac{g_{\phi\nu\nu}g_{\phi\gamma\gamma}}{2\pi}\right)^2 3\frac{\zeta(3)}{\pi}k_c\Delta_{Q,U}(\mathbf{K},\mathbf{q}_2)\\ &\equiv \pm B'_{\nu\gamma}(\eta)\Delta_{Q,U}(k_c) \,.\end{aligned} \tag{4.157}$$

The HML kernel can be approximated in an analogous way. At the end one finds it to be

$$\mathbb{C}_2^{\text{heavy}}[Q/U, f_\nu] = \frac{1}{a^4 M^4}\,\mathbb{C}_2^{\text{light}}[Q/U, f_\nu]\,. \tag{4.158}$$

Thus, we end up with the following evolution equations

$$\frac{d}{d\eta}\Delta_Q(\eta) + iK\mu\Delta_Q(\eta) = B'_{\nu\gamma}(\eta)\Delta_Q\,, \tag{4.159a}$$

$$\frac{d}{d\eta}\Delta_U(\eta) + iK\mu\Delta_U(\eta) = -B'_{\nu\gamma}(\eta)\Delta_U\,, \tag{4.159b}$$

which are solved by

$$\Delta_Q(\eta) = \Delta_Q^{\text{in}}(\eta)e^{B_{\nu\gamma}(\eta)-B_{\nu\gamma}(\eta_{\text{in}})} \tag{4.160a}$$

$$\Delta_U(\eta) = \Delta_U^{\text{in}}(\eta)e^{-[B_{\nu\gamma}(\eta)-B_{\nu\gamma}(\eta_{\text{in}})]}\,. \tag{4.160b}$$

Which finally gives the final polarization angle

$$\tan[\alpha(\mathbf{K},\eta_0)] = \frac{\Delta_Q(\mathbf{K},\eta_0)}{\Delta_Q(\mathbf{K},\eta_0)} = \tan(2\phi_{\mathbf{K}})e^{-2[B_{\nu\gamma}(\eta_0)-B_{\nu\gamma}(\eta_{\text{in}})]}\,. \tag{4.161}$$

Where we restored the dependence on the momentum of the polarization $\mathbf{K}$. Here $\phi_{\mathbf{K}}$ is the initial polarization angle at recombination. One could argue that we can always choose a reference frame in which this is equal to zero. However this is true if we look to only one point at the sky. When looking at the whole sky we have to choose a reference frame independent on the direction we are looking at. In that case this map of initial polarization angles is different from zero and the angle in a specific point depend on $\mathbf{K}$. This is why in section 4.4 we carefully rotated Compton scattering terms before writing the final form for the polarization equations. Details on the rotation and the reference frame we are considering can be found in appendix D.

5 SELF–INTERACTING NEUTRINOS AT ACT

This chapter delves into the investigation of neutrino self–interactions within a cosmological framework. The content presented is derived from the findings reported in Calabrese et al. (2025) and contributes to the data analysis of ACT DR6 as part of the work done for the ACT collaboration[1]. The structure begins in section 5.1, where we review the fundamental properties of neutrinos in cosmology, their influence on cosmological observables, and the properties that can be constrained through cosmological measurements. Subsequently, in sections 5.2 and 5.3, we introduce the concept of neutrino NSI and analyze how these extended models modify the scenarios described in the earlier sections in some limiting cases. In section 5.4 we provide an overview of the ACT instrument and its data colletion activity, while section 5.5 presents the outcomes of our data analysis.

5.1 NEUTRINOS IN COSMOLOGY

Neutrino properties leave distinct and observable signatures in cosmological data, which can, in turn, be utilized to constrain their fundamental characteristics. This highlights the profound interconnection between nuclear physics, particle physics, astrophysics, and cosmology [Hannestad, 2010; Lattanzi and Gerbino, 2018; Lesgourgues and Pastor, 2006; Wong, 2011]. Current cosmological datasets already impose constraints on neutrino properties that are not only complementary to but also competitive with those from terrestrial experiments. Furthermore, upcoming cosmological observations hold the potential to provide critical insights that cannot be obtained through other means, such as a direct determination of the absolute neutrino mass scale.

Neutrinos are unique among known particles as they behave as radiation at early epochs (during the CMB acoustic oscillations) and as dark matter at later times (during the era of structure formation), influencing the background evolution. Neutrinos transition to a non–relativistic state well within the matter–dominated regime. This transition occurs when their mass equals their average momentum, which, for a Fermi–Dirac distributed particle, can be approximated as

$$z_i^{\rm NR} \simeq \frac{m_i}{0.53\ \text{meV}} - 1\,, \tag{5.1}$$

for each mass eigenstate m_i. For example, a neutrino with $m_i = 60\,\text{meV}$ would transition at approximately $z_i^{\rm NR} \simeq 110$. Before this transition, neutrinos

1 https://act.princeton.edu/people

propagate at the speed of light; after it, their velocity is reduced to a typical value given by

$$\left\langle \frac{v_i}{c} \right\rangle \simeq 0.53 \frac{(1+z)}{m_i} \text{ meV} , \tag{5.2}$$

which is orders of magnitude larger than the velocity of the dominant cold dark matter (or even warm dark matter) component. This difference results in a characteristic diffusion scale, known as the *free–streaming* length, given by

$$k_{\text{fs}} \simeq 0.018 \Omega_m^{1/2} \left(\frac{m}{1 \text{ eV}} \right)^{1/2} h \text{ Mpc}^{-1} , \tag{5.3}$$

which takes on cosmologically relevant values. The free–streaming scale impacts gravitational clustering and the growth of structures, as neutrinos cluster only on scales larger than k_{fs}, thereby suppressing structure formation on smaller scales.

On the other hand, while neutrinos remain relativistic, they contribute to an increased radiation density. This effect is quantified by the parameter N_{eff} and can be analyzed independently of the influence of their mass. An increase in N_{eff} affects the observable spectra of CMB anisotropies and matter fluctuations through its impact on both the background evolution and perturbations.

5.1.1 Effects on the Cosmic Microwave Background

Neutrinos constitute a significant fraction of the Universe's energy density, influencing the expansion rate $H(z)$ at any redshift as described by

$$H^2(z) = H_0^2 \left[(\Omega_c + \Omega_b)(1+z)^3 + \Omega_\gamma (1+z)^4 + \Omega_\Lambda + \frac{\rho_\nu(z)}{\rho_{c,0}} \right] , \tag{5.4}$$

where Ω_b and Ω_c represent the baryonic and cold dark matter density parameters, Ω_γ is the photon density parameter, and Ω_Λ corresponds to the dark energy density parameter modeled as a cosmological constant, all evaluated at the present epoch. The energy density of neutrinos, $\rho_\nu(z)$, evolves differently with redshift depending on whether they behave as radiation or matter.

We first consider the case of relativistic neutrinos, where the energy density is solely determined by N_{eff}. The background effects depend on which parameters are held constant when N_{eff} is varied or increased. If the densities of other species remain fixed, a higher N_{eff} leads to a reduced redshift of matter–radiation equality, z_{eq}, given by

$$1 + z_{\text{eq}} = \frac{\Omega_m}{\Omega_\gamma} = \frac{\Omega_m h^2}{\Omega_\gamma h^2} \frac{1}{1 + 0.0271 N_{\text{eff}}} . \tag{5.5}$$

This implies that at the time of recombination radiation is still a subdominant component and the gravitational potential is still slowly decreasing. The outcome is an enhancement of the early Integrated Sach–Wolfe (ISW) effect, which amplifies the CMB perturbation peaks around $\ell \sim 200$. Additionally, changes in $H(z)$ alter the angular scales associated with cosmological observables. For instance, the angle $\theta(z_{\rm rec}) \equiv d_s(z_{\rm rec})/d_A(z_{\rm rec})$ is affected. While the angular diameter distance $d_A(z_{\rm rec})$, which depends on the post-decoupling expansion history, remains unchanged, the sound horizon at decoupling, $d_s(z_{\rm rec})$, is influenced by the time of equality. A later equality corresponds to a reduced sound horizon, shifting all peaks to higher ℓ values.

These effects are not uniquely indicative of the neutrino density, as they can arise from variations in other parameters. To specifically characterize the impact of $N_{\rm eff}$, it is more insightful to increase the total radiation, matter, and Λ densities uniformly, keeping the redshifts of matter–radiation equality, $z_{\rm eq}$, and matter–Λ equality, z_Λ, fixed [Bashinsky and Seljak, 2004; Hou et al., 2013; Lesgourgues et al., 2013]. The primordial spectrum parameters, the baryon density $\omega_{\rm b} \equiv \Omega_{\rm b}h^2$, and the optical depth to reionization $\tau_{\rm reio}$ can also be held constant by simultaneously varying $N_{\rm eff}$ and the Hubble parameter h while maintaining fixed values for $\{\omega_b, \Omega_c, \Omega_\Lambda\}$. Under this transformation, the primary background effect of $N_{\rm eff}$ is an increase in the *diffusion scale* (or *Silk damping scale*) at decoupling [Hu, 1995],

$$r_d^2 = (2\pi)^2 \int_0^{a_*} \frac{da}{a^3 \sigma_T n_e H} \left[\frac{R^2 + 16/15\,(1+R)}{6\,(1+R^2)}\right], \tag{5.6}$$

where $R \equiv 3\rho_b/4\rho_\gamma$, σ_T is the Thomson cross section, and n_e is the electron number density. This larger diffusion scale reduces C_ℓ^{TT} at high ℓ values and induces smaller effects, including a slight increase in the redshift of photon decoupling.

At the level of perturbations, an increased $N_{\rm eff}$ implies that photons experience gravitational interactions with a denser neutrino component. Since neutrinos are more smoothly distributed compared to photons, this leads to a suppression of the acoustic peaks and a shift to larger scales (i.e., smaller multipoles). Neutrinos, traveling at the speed of light, propagate faster than the sound waves in the relativistic photon–baryon fluid, which move at $c_s = c/\sqrt{3}$. This supersonic propagation of neutrino perturbations introduces a characteristic phase shift in the sound waves of the primordial plasma. Because neutrinos travel faster than other perturbations, they generate metric perturbations ahead of the sound horizon r_s of the photon–baryon acoustic waves. As shown in [Bashinsky and Seljak, 2004], this results in a constant phase shift of the acoustic oscillations in the limit of large wave numbers.

The effect of increasing $N_{\rm eff}$ on the polarization spectrum is analogous to its effect on the temperature spectrum: increased Silk damping and shifts in the amplitude and location of the acoustic peaks. In the polarization spectrum, these shifts are even more evident, as the location of the acoustic peaks is not

additionally influenced by Doppler effects, unlike in the temperature spectrum. The combination of these effects uniquely characterizes the radiation density parameter N_{eff}, making it distinguishable from variations in other parameters and enabling precise measurement of N_{eff} from CMB data alone.

As indicated in (5.1), the non–relativistic transition of neutrinos occurs after photon decoupling. Thus, neutrinos contribute to the present non–relativistic matter density but not to the matter density at the time of recombination or matter–radiation equality. If the neutrino mass is increased while keeping the baryon and dark matter densities (ω_b and ω_c) fixed, the early cosmological evolution remains unaffected by the neutrino mass until the non–relativistic transition occurs. While one might expect the CMB temperature and polarization power spectra to remain unchanged in this case, this is not true.

Neutrinos enhance the total non–relativistic density at late times, $\omega_m = \omega_b + \omega_c + \omega_\nu$, where $\omega_\nu \equiv \Omega_\nu h^2$ is a function of the total mass $\sum m_\nu$ as given in (1.59). The late-time background evolution affects the CMB spectrum through its influence on the angular scales associated with the last scattering surface and through the late ISW effect. These depend, respectively, on the angular diameter distance to recombination, $d_A(z_{\text{rec}})$, and the redshift of matter–Λ equality. Increasing $\sum m_\nu$ alters these quantities, and while h and Ω_Λ can be adjusted to keep one of them constant, it is not possible to fix both simultaneously. Since CMB observations measure the angular scale of acoustic oscillations with high precision and are only weakly sensitive to the late ISW effect (due to cosmic variance), we choose to vary the Hubble parameter to maintain a fixed scale $d_A(z_{\text{rec}})$. In this setup, an increase in neutrino mass reduces the late ISW effect, leading to a suppression of the CMB spectrum at $\ell \leq 20$. The dependence of $d_A(z_{\text{rec}})$ on both $\sum m_\nu$ and h implies that neutrino mass measurements from CMB data are strongly correlated with the value of h [Lesgourgues et al., 2013].

The transition of neutrinos to a non–relativistic state also impacts the equation of state of the cosmic fluid and induces slight variations in metric fluctuations. If this transition occurs shortly after photon decoupling, these variations manifest through the early ISW effect, producing the dip observed in the CMB spectrum around $20 \leq \ell \leq 200$ [Lesgourgues and Pastor, 2006].

Finally, it is worth noting that a higher neutrino mass reduces the weak lensing effect on the CMB spectrum caused by large–scale structures at low redshift. This occurs because a higher neutrino mass suppresses the matter power spectrum, as will be discussed in the next section [Lesgourgues and Pastor, 2006; Navas et al., 2024].

5.1.2 Effects on the matter power spectrum

The clustering of matter serves as another powerful probe of cosmology. This property can be described through the two–point correlation function or, equivalently, by the power spectrum of matter density fluctuations:

$$\left\langle \delta_m\left(\mathbf{k}, z\right) \delta_m\left(\mathbf{k}', z\right)\right\rangle = P\left(k, z\right) \delta^{(3)}\left(\mathbf{k} - \mathbf{k}'\right) \ , \tag{5.7}$$

where $\delta_m\left(\mathbf{k}, z\right) \equiv \delta\rho_m / \bar{\rho}_m$[2] is the Fourier transform of the matter density perturbation at redshift z. Unlike the CMB, which is observed at a single redshift (recombination), the matter power spectrum can, in principle, be measured at various epochs in cosmic history, enabling tomographic analysis.

In the previous section, we explored the effect of increasing N_{eff} while keeping z_{eq} and ω_b fixed, as these quantities are tightly constrained by CMB data. This leads to an increase in $\omega_c \equiv \Omega_c h^2$ and a reduction in the baryon-to-dark matter ratio $\omega_b/\omega_c = \Omega_b/\Omega_c$, as given by

$$1 + 0.2271 N_{\text{eff}} = \frac{\omega_b}{\omega_\gamma} \frac{1 + \omega_c/\omega_b}{1 + z_{\text{eq}}} \ , \tag{5.9}$$

which is derived by rewriting $\omega_m = \omega_b + \omega_c = \omega_b\left(1 + \omega_c/\omega_b\right)$ using the inverse of (5.5). This altered baryon-to-dark matter ratio significantly affects the shape of the matter power spectrum. Prior to baryon decoupling, CDM undergoes gravitational collapse, while baryons remain smoothly distributed due to photon pressure and are affected by acoustic oscillations. A decrease in Ω_b/Ω_c gives more weight to the highly clustered dark matter component, leading to an enhancement of the small–scale matter power spectrum and a suppression of the amplitude of BAO. Additionally, the scale of BAOs experiences a slight shift due to the same neutrino dragging effects as observed in the CMB peaks.

The enhancement of the small–scale matter power spectrum also affects the CMB spectra: the last scattering surface becomes slightly more influenced by weak lensing caused by large–scale structures, which smooths out the maxima, minima, and damping scale of the CMB spectra [Lewis and Challinor, 2006].

After the non–relativistic transition, the main influence of neutrinos on the matter power spectrum is governed by their velocity dispersion. The key parameter here is the free–streaming length, given in (5.3), which approximately represents the distance neutrinos travel within a Hubble time[3]. Below this

2 For multiple fluids, such as CDM, baryons, and non–relativistic neutrinos, the total matter power spectrum can be expressed as

$$\delta_m = \frac{\sum_i \bar{\rho}_i \delta_i}{\sum_i \bar{\rho}_i} \ . \tag{5.8}$$

3 To be precise, the velocity of non–relativistic neutrinos decreases over time (or with redshift), so the free–streaming length is not constant. After the non–relativistic transition, the free–streaming length continuously grows. For practical purposes, its minimum value, given in (5.3) at the transition, suffices for our discussion [Lesgourgues and Pastor, 2006].

scale ($k \gg k_{\rm fs}$), neutrinos retain a high thermal velocity and do not contribute to structure formation, effectively erasing perturbations. Conversely, above this scale ($k \ll k_{\rm fs}$), neutrinos behave like matter and contribute to clustering.

Two primary consequences arise. First, the growth of matter perturbations is suppressed below $k_{\rm fs}$ because volumes on scales smaller than the free–streaming length resemble a mixed matter–radiation Universe, rather than a purely matter–dominated one. In a purely matter–dominated regime, perturbations δ evolve proportionally to the scale factor, so $\delta_m\,(k \ll k_{\rm fs}) \propto a$. In contrast, in a mixed regime, where neutrinos constitute a fraction f_ν of the total matter density, perturbations evolve more slowly, as $\delta_m\,(k \gg k_{\rm fs}) \propto a^{1-3/5f_\nu}$. Second, the clustering of structures becomes scale–dependent, with a reduction in power at smaller scales. This occurs because free–streaming neutrinos escape the potential wells that matter tends to cluster into. At large scales, however, neutrinos effectively behave like CDM [Gerbino, 2018; Lattanzi and Gerbino, 2018; Lesgourgues and Pastor, 2006].

5.2 WHY NON–STANDARD INTERACTIONS?

The observation of neutrino oscillations provides compelling evidence that at least two of the three neutrino mass states possess small but non–zero masses [Navas et al., 2024]. The global program for studying neutrino oscillations has entered a new phase, with mixing angles and mass-squared differences being measured to ever–increasing precision. Next–generation long–baseline experiments, such as Deep Underground Neutrino Experiment (DUNE)[4] [Acciarri et al., 2015], aim to probe subdominant effects in oscillation data, potentially uncovering the currently unknown parameters, including the Dirac CP phase, the sign of the atmospheric mass–squared difference, and the octant of the atmospheric mixing angle. These analyses are typically conducted within the 3×3 neutrino mixing framework, assuming that neutrinos interact with matter exclusively through weak interactions mediated by the SM W and Z bosons. However, the origin of neutrino mass itself indicates the necessity of physics beyond the Standard Model (BSM), which often brings additional NSIs in the neutrino sector.

Beyond the generation of neutrino masses, the SM faces several other challenges, such as explaining the existence of dark matter and the baryon asymmetry of the Universe. To address these issues, the SM must be extended by introducing new particles or interactions. Over the past decades, numerous models have been proposed and thoroughly investigated, including SUperSYmmetry (SUSY), Two–Higgs–Doublet Model (2HDM), and seesaw mechanisms. Unfortunately, experimental searches for such new physics have so far yielded null results, suggesting that if new physics exists, it may reside at energy scales beyond the reach of current experimental facilities. Conse-

4 https://www.dunescience.org/

quently, EFTs provide a promising framework for exploring new physics in a model–independent manner.

In the context of the SM EFT, higher–dimensional operators can introduce NSIs into processes predicted by the SM. Among these operators, neutrino NSIs have garnered considerable attention due to their relevance to neutrino oscillations. These interactions, first proposed in [Wolfenstein, 1978], can be categorized into two types: CC interactions and NC interactions, expressed as:

$$\mathcal{L}_{\text{EFT}}^{\text{NC}} = -2\sqrt{2}G_{\text{F}} \sum_{f,P,\alpha,\beta} \varepsilon_{\alpha\beta}^{f,P} \left(\bar{\nu}_\alpha \gamma^\mu P_L \nu_\beta\right) \left(\bar{f}\gamma_\mu P f\right) , \tag{5.10}$$

$$\mathcal{L}_{\text{EFT}}^{\text{CC}} = -2\sqrt{2}G_{\text{F}} \sum_{f,P,\alpha,\beta} \varepsilon_{\alpha\beta}^{f,P} \left(\bar{\nu}_\alpha \gamma^\mu P_L \ell_\beta\right) \left(\bar{f}\gamma_\mu P f'\right) . \tag{5.11}$$

Here, ε parameterizes the strength of the new interaction relative to the weak scale. The summation extends over matter fermions, typically $f, f' \in \{e, \mu, \tau\}$, and $P \in \{P_L, P_R\}$ represent the chirality projection operators.

Allowing for these NSI in neutrino production, propagation, and detection can, in principle, alter the entire framework and significantly impact the interpretation of experimental data in terms of the standard 3×3 oscillation parameters. Therefore, it is crucial to comprehensively understand all possible NSI effects and to determine the extent to which they can manifest while remaining consistent with existing theoretical and experimental constraints. Furthermore, the study of NSI provides an opportunity to use neutrino oscillations as a tool to investigate the origin of neutrino mass. In summary, NSI offers an additional pathway to explore new physics at energy scales below or near the electroweak scale, complementing various other low– and high–energy experimental approaches.

NSI interactions of the type shown in Eqs. (5.10) and (5.11) are mediated by either vector or charged scalar particles. These types of interactions were among the first to be proposed and have been extensively studied due to their resemblance to standard interactions of neutrinos with matter fields. However, neutrinos can also couple to neutral scalar fields, leading to terms such as [Ge and Parke, 2019]:

$$\mathcal{L}_{\text{EFT}}^{S} = \frac{y_f y_{\alpha\beta}}{m_\phi^2} \left(\bar{\nu}_\alpha \nu_\beta\right) \left(\bar{f} f\right) , \tag{5.12}$$

where y_f and $y_{\alpha\beta}$ denote the Yukawa couplings of the matter fermions and neutrinos to the scalar mediator ϕ, respectively. To some extent, neutrino coupling to scalar fields is considered even more natural than other interactions. A well–motivated mechanism for neutrinos to acquire mass is via coupling to a scalar field with a non–zero vacuum expectation value. Since left–handed neutrinos belong to $\text{SU}(2)_L$ doublets, a scalar coupling with neutrinos can also couple to charged leptons, for instance, through mixing with the neutral Higgs boson. Consequently, it is reasonable to expect matter effects arising from such scalar particles.

In the following sections, we will focus specifically on the study of these scalar NSI, which are often associated with Majoron–like models for neutrino mass generation.

5.3 NEUTRINO NSI IN COSMOLOGY

Neutrino self–interactions can emerge in a variety of BSM models. For instance, in scenarios where Majorana neutrinos interact with a (pseudo)scalar field, the Majoron, these interactions are associated with the breaking of lepton number symmetry [Chikashige et al., 1980; 1981; Schechter and Valle, 1982]. The coupling between neutrinos and the Majoron is instrumental in generating small neutrino masses through the see–saw mechanism, akin to how couplings with the Higgs boson produce masses for the charged fermions in the SM (see section 2.4). Additionally, these interactions can facilitate neutrino–neutrino scattering processes. Specifically, the neutrino–Majoron interaction Lagrangian includes the term:

$$\mathcal{L}_{\nu\phi} = \frac{ig}{2}\bar{\nu}\gamma^5\nu\phi, \tag{5.13}$$

where g is the coupling constant, γ^5 represents the fifth Dirac gamma matrix, ϕ denotes the Majoron field, and ν corresponds to a light neutrino mass eigenstate[5]. In many models, the coupling constant g is proportional to m_ν/v_L, where m_ν is the neutrino mass and v_L is the scale of the new physics responsible for lepton number violation.

The interaction described in eq. (5.13) can lead to neutrino–neutrino scattering processes, $\nu\nu \to \nu\nu$, mediated by a (virtual) Majoron. In this section, we explore the cosmological implications of such interactions and establish constraints on the neutrino self–scattering cross–section.

Although the Lagrangian in eq. (5.13) specifically describes neutrinos coupling to a new pseudoscalar, the cosmological effects of neutrino self–interactions remain qualitatively similar even if the mediator is a scalar or vector particle. For simplicity, we will use the symbol ϕ to denote a generic mediator, regardless of its spin or parity, unless a distinction is explicitly necessary.

We focus on interactions involving the three active (weakly–interacting) neutrinos[6]. These interactions include mixing between different mass eigenstates ν_i $(i = 1, 2, 3)$, with an eigenstate–dependent coupling strength, such

5 In these models, neutrinos are Majorana particles, such that $\nu = \nu^c \equiv \mathcal{C}\bar{\nu}^{\mathrm{T}}$, where $\mathcal{C}$ is the charge conjugation operator.

6 In Majoron models, the light mass eigenstates in eq. (5.13) are superpositions of active neutrinos and new sterile states. However, due to the small mixing angles, these eigenstates are predominantly active. The "mostly sterile" eigenstates resulting from mixing are highly massive and couple weakly to SM particles, rendering them irrelevant to the cosmological evolution at the epochs of interest.

that $\mathcal{L}_{\nu\phi} = (ig_{ij}/2)\bar{\nu}_i\gamma^5\nu_j\phi$. For simplicity, we consider the case of diagonal and universal couplings, $g_{ij} = g\delta_{ij}$.

Neutrino self–interactions impact the evolution of cosmological perturbations by causing neutrinos to behave as a collisional fluid instead of free–streaming particles. This collisional behavior allows for the development of acoustic oscillations in the neutrino fluid, which enhances photon fluctuations through gravitational coupling. Moreover, collisions erase the characteristic phase shift imprinted on photon and matter perturbations by neutrino free streaming. These effects are significant during the radiation–dominated era, when neutrinos contribute substantially to the total energy density, and are imprinted when perturbations enter the horizon. Consequently, the scales affected are those smaller than the horizon size at matter–radiation equality. The precise impact at a given angular scale depends on whether neutrinos were collisional or free–streaming at the time of horizon crossing, which, in turn, is determined by the strength of self–interactions and the energy dependence of the scattering rate.

To illustrate this, we consider two limiting cases for the mediator mass: a very light ("massless") or very heavy mediator. These scenarios simplify the energy dependence of the scattering rate and highlight the distinct cosmological signatures of neutrino self–interactions.

5.3.1 Massless mediator limit

In the case of a light mediator, i.e., with a mass much smaller than the average neutrino momentum, the production of ϕ particles via the annihilation process $\nu\nu \to \phi\phi$ becomes kinematically allowed during the relevant timeframe. This necessitates introducing a separate Boltzmann hierarchy for the scalar particles, in addition to the one for neutrinos.

Focusing on ϕ–mediated neutrino–neutrino scattering, the thermally averaged cross-section times velocity can be approximated as

$$\langle \sigma_{\nu\nu} v \rangle = \xi \frac{g^4}{T_\nu^2} \equiv \frac{g_{\rm eff}^4}{T_\nu^2} \,, \tag{5.14}$$

where the coefficient ξ depends on the details of the interaction, including the nature of the mediator. The scattering rate is then $\Gamma \sim g^4 T_\nu$. Given that the Universe's expansion rate decreases faster than T (with $H \propto T^2$ during the radiation–dominated era and $T^{3/2}$ during the matter–dominated era), neutrinos, which decoupled from the primordial plasma at $T \sim 1$ MeV, can become collisional again in the presence of a hidden interaction mediated by a light particle. The redshift $z_{\rm rec}$, at which this "recoupling"[7] occurs, depends on the strength of the interaction and can be determined by equating $\Gamma(z_{\rm rec}) \sim H(z_{\rm rec})$.

7 This term is somewhat misleading since neutrinos remain decoupled from the cosmological plasma. Instead, they transition from being collisionless to collisional.

In standard cosmological perturbation theory, developed well after weak decoupling, neutrinos are effectively treated as collisionless. This assumption holds in the ΛCDM model and most of its extensions. However, in this scenario, neutrino collisions become relevant again at $z \lesssim z_{\rm rec}$. These collisions affect the evolution of perturbations in the neutrino fluid, altering cosmological observables. This requires incorporating an appropriate collision term into the Boltzmann equation for the neutrino distribution function [Forastieri et al., 2019; Oldengott et al., 2015]. Neutrino self–collisions ($\nu\nu \to \nu\nu$) suppress higher moments of the distribution function, such as the quadrupole ($\ell = 2$, representing anisotropic stress), while enhancing the monopole and dipole moments ($\ell = 0, 1$, representing density and velocity perturbations). These changes propagate to the photon distribution through the gravitational potentials, affecting the CMB spectrum.

To understand the impact of altering the free–streaming nature of neutrinos on photon perturbations, consider the effects outlined by [Bashinsky and Seljak, 2004]. Neutrinos and photons interact only via gravitational potentials, which decay rapidly after a perturbation enters the horizon. Consequently, the impact of neutrino free streaming (or its absence) on photon perturbations is significant only at the time of horizon crossing. Free–streaming neutrinos cause a rapid decay of inhomogeneities and associated gravitational potentials, damping photon perturbations and suppressing the CMB acoustic peaks. Additionally, the higher velocity of neutrinos compared to the sound speed in the baryon–photon fluid induces a characteristic phase shift in the CMB acoustic oscillations, shifting the power spectrum toward larger scales.

Introducing neutrino interactions that counteract their collisionless nature undoes these effects. This manifests as a boost in the amplitude of fluctuations and a shift toward larger ℓ values (smaller scales) relative to the ΛCDM case. In this model, where neutrinos decouple at $T \sim 1$ MeV but become collisional again later, the impact is evident on scales smaller than the horizon at matter–radiation equality but larger than the horizon at recoupling. See fig. 5.1 for an illustration.

Once neutrinos recouple, a population of ϕ particles is rapidly generated through the annihilation process $\nu\nu \to \phi\phi$. This production is soon balanced by the inverse reaction $\phi\phi \to \nu\nu$, establishing chemical equilibrium. Similarly, $\nu\phi$ scatterings drive the system into kinetic equilibrium.

In the case of massive neutrinos, once they become non–relativistic, the inverse reaction $\phi\phi \to \nu\nu$ is suppressed, leading to a rapid depletion of neutrinos and resulting in a so–called neutrinoless Universe [Beacom et al., 2004]. Furthermore, for non–degenerate neutrino masses and non–zero flavor off–diagonal couplings (e.g., $g_{ij} \neq 0$ for $i \neq j$), the Lagrangian in eq. (5.13) also permits neutrino decay processes, such as $\nu_i \to \nu_j\phi$, in the light scalar limit. However, assuming diagonal couplings, as done previously, these decay channels can be neglected.

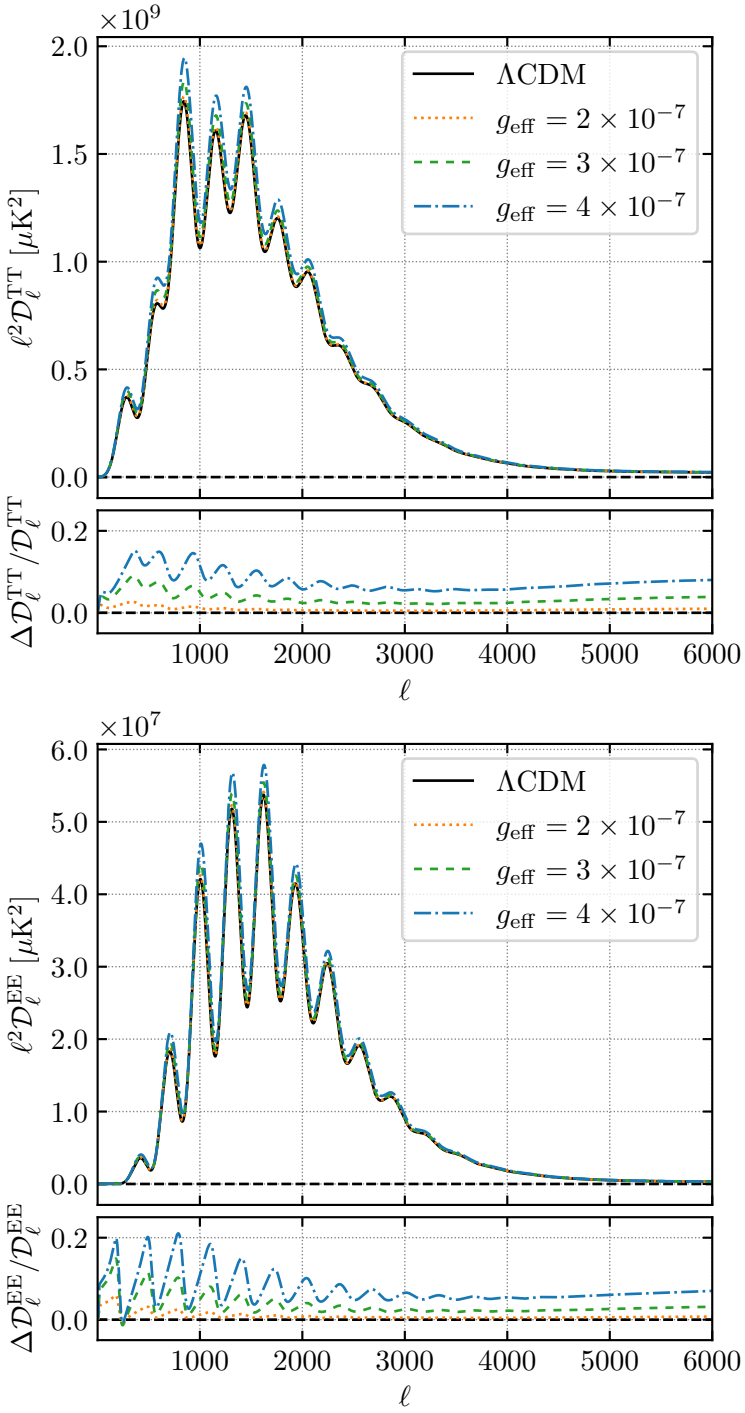

Figure 5.1: Theoretical temperature and polarization power spectra for the ΛCDM + $g_{\rm eff}$ model. The quantity $\ell^2\mathcal{D}_\ell = \ell^3\,(\ell+1)\,C_\ell/2\pi$ is plotted to emphasize variations at high multipoles. The upper panel displays the power spectrum for three values of the coupling constant, $g_{\rm eff} = \{2,3,4\} \times 10^{-7}$, represented by the orange dotted, the green dashed and the blue dashed–dotted curves, respectively. The black solid line corresponds to the ΛCDM benchmark model. The lower panel presents the differences relative to ΛCDM, while the bottom panel highlights the relative differences with respect to the benchmark model.

5.3.2 Heavy mediator limit

In the scenario where the mediator mass is much larger than the neutrino temperature, the mediator can be integrated out, and the interaction is effectively described by a four–fermion vertex with a dimensionful coupling constant

$$G_{\rm eff} \equiv \frac{g^2}{m_\phi^2} \, . \tag{5.15}$$

In this limit, the annihilation process $\nu\nu \to \phi\phi$ becomes kinematically suppressed, and any pre–existing ϕ population would have entirely annihilated or decayed into neutrinos long before the epochs of interest. Consequently, processes like $\nu\phi \to \nu\phi$ and $\phi\phi \to \nu\nu$ are also negligible. As a result, the analysis can focus solely on neutrino self–interactions and their effects on the neutrino Boltzmann hierarchy, treating the ϕ population as non–existent.

When neutrinos are relativistic, the thermally averaged cross–section times velocity scales as [Cyr-Racine and Sigurdson, 2014]:

$$\langle \sigma_{\nu\nu} v \rangle \propto G_{\rm eff}^2 T_\nu^2 \sim \left(\frac{G_{\rm eff}}{G_{\rm F}} \right)^2 \left\langle \sigma_{\nu\nu}^{\rm SM} v \right\rangle \, , \tag{5.16}$$

where T_ν is the temperature of the neutrino bath, $G_{\rm F}$ is the Fermi constant, v is the neutrino velocity, and $\sigma_{\nu\nu}^{\rm SM}$ represents the SM neutrino interaction cross-section for standard weak processes. The interaction rate can then be approximated as $\Gamma_{\nu\nu} \sim G_{\rm eff}^2 T_\nu^5$, which has the same temperature dependence as weak interactions. However, for $g^4/m_\phi^4 \gg G_{\rm F}^2$, neutrino self–interactions delay the epoch of neutrino decoupling.

In the early Universe, such self–interactions make the neutrino medium opaque, with an opacity given by $\dot{\tau}_\nu \equiv -a\xi G_{\rm eff}^2 T_\nu^5$, where ξ is an order-unity constant that depends on the specific neutrino interaction model and the thermal averaging process, and a is the scale factor of the Universe. Since $\dot{\tau}_\nu \propto \langle \sigma_{\nu\nu} v \rangle$, electroweak contributions to the neutrino opacity can be neglected when $G_{\rm eff} \gg G_{\rm F}$, allowing us to isolate the effects of neutrino self–interactions. The neutrino opacity implicitly defines a neutrino visibility function, $\tilde{g}_\nu(z) \equiv -\dot{\tau}_\nu e^{-\tau_\nu}$, which represents the probability density for the redshift at which neutrinos begin to free stream. In the presence of self–interactions, this visibility function peaks at lower redshifts compared to the standard case.

By preventing free–streaming, neutrino self–interactions suppress the growth of anisotropic stress, affecting the quadrupole and higher moments of the neutrino distribution function.

Free–streaming radiation induces gravitational potential perturbations that propagate beyond the sound horizon of the photon–baryon plasma, suppressing the amplitude and shifting the phase of photon density fluctuations [Bashinsky and Seljak, 2004; Hou et al., 2013]. If neutrino free–streaming is delayed until a redshift $z_\nu^{\rm fs}$, Fourier modes of photon fluctuations entering the

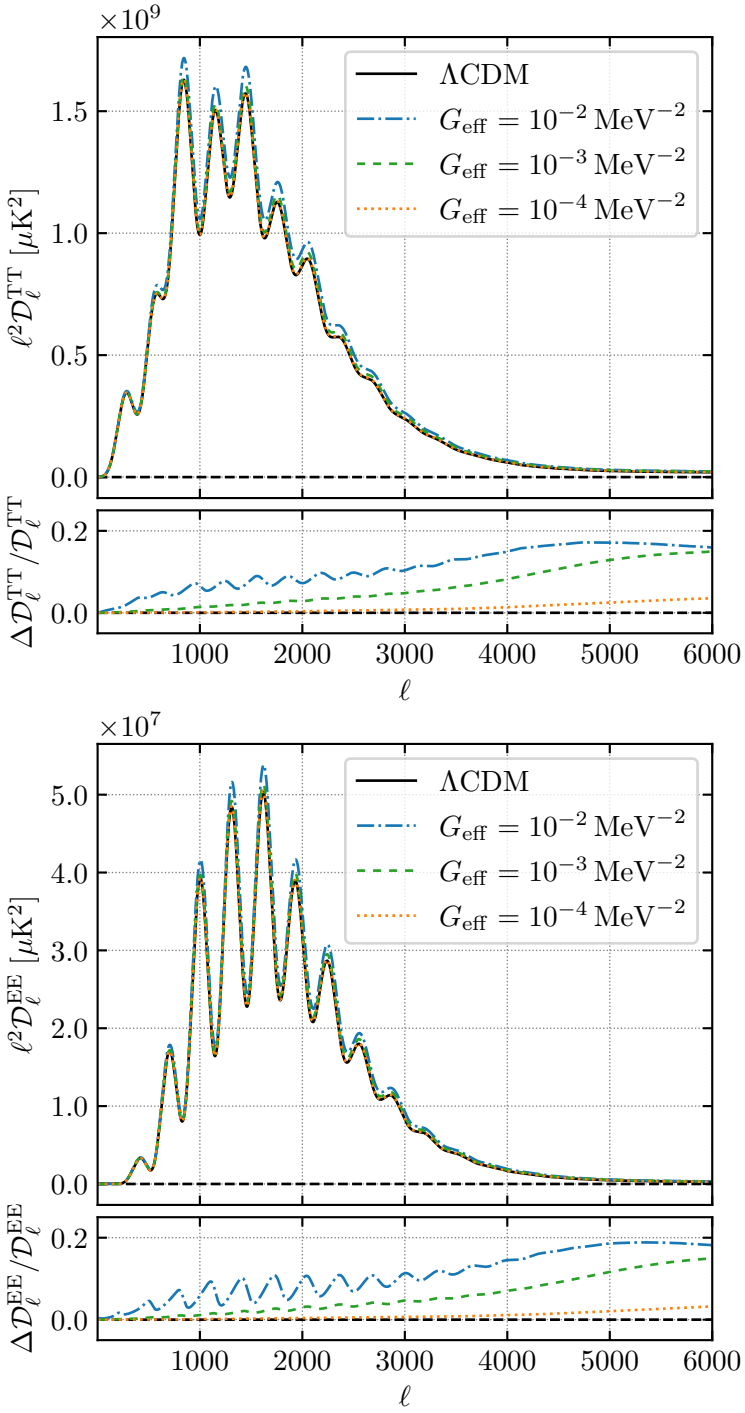

Figure 5.2: Theoretical temperature and polarization power spectra for the ΛCDM + $G_{\rm eff}$ model. The quantity $\ell^2\mathcal{D}_\ell = \ell^3\,(\ell+1)\,C_\ell/2\pi$ is plotted to emphasize variations at high multipoles. The upper panel displays the power spectrum for three values of the coupling constant, $g_{\rm eff} = \{10^{-2}, 10^{-3}, 10^{-4}\}\,\mathrm{MeV}^{-2}$, represented by the blue dashed–dotted, the green dashed and the orange dotted curves, respectively. The black solid line corresponds to the ΛCDM benchmark model. The lower panel presents the differences relative to ΛCDM, while the bottom panel highlights the relative differences with respect to the benchmark model.

horizon before z_ν^{fs} remain unaffected by the standard amplitude suppression and phase shift.

For photon fluctuations becoming sub–horizon at redshifts $z_{\mathrm{eq}} < z < z_\nu^{\mathrm{fs}}$, the amplitude is suppressed, and the phase is shifted toward larger scales (smaller ℓ). Thus, delayed neutrino free–streaming manifests in the CMB temperature and polarization power spectra as an ℓ-dependent shift in amplitude and phase. Multipoles $\ell_{\mathrm{eq}} < \ell < \ell_\nu^{\mathrm{fs}}$ are largely unaffected by neutrino self–interactions, while multipoles $\ell < \ell_\nu^{\mathrm{fs}}$ exhibit increased power and a phase shift toward smaller angular scales as ℓ increases. See fig. 5.2 for an illustration of these effects.

5.4 THE ATACAMA COSMOLOGY TELESCOPE

The Atacama Cosmology Telescope (ACT) (see fig. 5.3) was a 6 m off–axis aplanatic Gregorian telescope designed for millimeter–wavelength observations of the CMB at arcminute–scale resolution. Its primary objective was to produce high–resolution maps of the CMB temperature and polarization anisotropies, complementing the angular scales and sensitivities achieved by the WMAP and Planck satellites. Situated at an altitude of 5190 m on Cerro Toco in the Atacama Desert in northern Chile, ACT had access to over half the sky and ranked among the highest ground–based telescopes worldwide [Fowler et al., 2007]. The exceptional site conditions, with high altitude and low precipitable water vapor, provided excellent atmospheric transparency for millimeter and submillimeter observations.

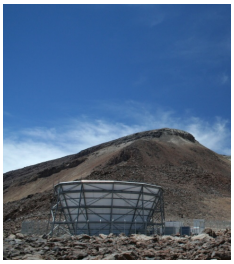

Figure 5.3: The Atacama Cosmology Telescope, with Cerro Toco in the background.

ACT operated by scanning in azimuth at fixed elevations as the sky drifted across its field of view, reducing systematic errors arising from variations in altitude. Observations were performed in both the eastern (rising sky) and western (setting sky) directions, enabling measurements at different parallactic angles. This crosslinking technique helped mitigate systematic effects caused by the scan direction during mapmaking and enhanced the ability to measure CMB modes aligned with the scan direction.

ACT featured three generations of receivers, each reflecting advancements in specialized detector technology optimized over time. These receivers utilized superconducting transition edge sensor arrays to achieve high sensitivity. The telescope was constructed in 2007 and saw first light in October 2007 with its initial receiver, the Millimeter Bolometric Array Camera (MBAC) [Swetz et al., 2011], which operated at frequencies of 150, 220, and 277 GHz.

Subsequent receiver upgrades enabled polarization-sensitive observations. The first such receiver, ACTPol [Niemack et al., 2010], operated between 2013 and 2016, observing at 98 and 150 GHz. This was followed by the Advanced ACTPol (AdvACT) receiver [Henderson et al., 2016], operational from 2017 to 2022. AdvACT featured detector arrays observing at 30, 40, 98, 150, and

220 GHz[8]. Compared to ACTPol, AdvACT expanded frequency coverage and increased the number of detectors, significantly improving the instrument's sensitivity. Observations with ACT concluded in mid–2022.

Figure 5.4: Location of the Atacama Cosmology Telescope.

5.4.1 Data releases

The ACT data releases[9] are categorized as follows:

- DR1: This release included data collected with the MBAC receiver in 2008, covering a southern sky region centered at RA = 60° and Dec = −52.7°[10] at 148 GHz [Dunkley et al., 2011; Dunner et al., 2013].
- DR2: Based on data from 2008 to 2010, this release extended coverage to include both the southern sky and the "SDSS Stripe 82" equatorial region. Observations included 148 GHz, 217 GHz, and 277 GHz frequencies [Das et al., 2011; Gralla et al., 2020; Sievers et al., 2013].
- DR3: Utilizing data from the ACTPol receiver, this release included both temperature and polarization data collected during 2013–2014. It focused on regions near the equator at 150 GHz [Louis et al., 2017; Naess et al., 2014].
- DR4: This release, also based on ACTPol data, covered seven regions of the sky spanning approximately 18 000 deg^2 from 2013 to 2016, with data at 98 GHz and 150 GHz [Aiola et al., 2020; Choi et al., 2020; Darwish et al., 2020; Han et al., 2021; Madhavacheril et al., 2020; Mallaby-Kay et al., 2021; Namikawa et al., 2020]. DR4 includes DR3 as a subset.
- DR5: This release combined previously published MBAC and ACTPol data with preliminary observations from AdvACT (2017–2018), including 230 GHz data. It provided high–resolution maps containing the largest collection of Sunyaev Zel'dovich (SZ) clusters and millimeter-wave sources to date. However, these maps were not suitable for precision cosmology due to their preliminary nature [Naess et al., 2020].
- DR6: The upcoming ACT data release will include power spectra and inferred cosmological parameters, similar to previous releases. The

8 The naming convention for ACT detector arrays can be inconsistent across publications due to variations in reported detector bandpasses. Each array is sensitive to a range of frequencies rather than a single frequency, making it challenging to define an effective central frequency. For example, ACTPol and AdvACT data frequently cite detectors at 98 GHz and 150 GHz, but in some cases, these may be referred to as 90 or 97 GHz and 148 or 149 GHz, respectively [Storer, 2023]

9 All ACT data releases are available on NASA's LAMBDA portal (https://lambda.gsfc.nasa.gov/product/act/index.html)

10 RA (right ascension) and Dec (declination) are sky coordinates analogous to longitude and latitude on Earth. RA measures east–west positions on the celestial sphere, while Dec measures north-south positions.

third-generation Advanced ACTPol receiver extended frequency coverage down to 20 GHz and has surveyed 40% of the sky since 2016.

The MBAC receiver from the first generation mapped CMB temperature anisotropies over an area of approximately 1000 $\deg^2$ with spectral bands centered at 148 GHz, 218 GHz, and 270 GHz, achieving an angular resolution of 1.4 arcminutes at 148 GHz. Key scientific achievements include the first measurement of the CMB lensing potential power spectrum [Das et al., 2011], evidence of dark energy using CMB data alone [Sherwin et al., 2011], the first statistical detection of the kinematic Sunyaev Zel'dovich effect [Hand et al., 2012], and measurements of primary and secondary CMB temperature anisotropy power over 600 $\deg^2$ [Sievers et al., 2013]. Other highlights include the detection of the tSZ effect in 10^{13} solar mass halos through stacking [Gralla et al., 2014] and the discovery of the extreme high–redshift merging galaxy cluster "El Gordo" [Menanteau et al., 2012].

The second-generation ACTPol receiver mapped 17 000 $\deg^2$ of the sky over four years (2013–2016), with the deepest 600 $\deg^2$ observed at noise levels below 10 μK − arcmin. It utilized multi–chroic polarization-sensitive detectors operating at 100 mK. DR3 highlights include measurements of the TE and EE power spectra [Naess et al., 2014], reconstruction of the CMB lensing potential using temperature and polarization data in cross–correlation with the cosmic infrared background [Engelen et al., 2015], and the first measurement of CMB lensing by DM halos [Madhavacheril et al., 2015]. DR4 provided maps, cosmological parameters [Aiola et al., 2020], and power spectra at 98 GHz and 150 GHz [Choi et al., 2020], along with a lensing mass map over 2100 $\deg^2$ of sky and its cross–correlation with BOSS–CMASS galaxies [Darwish et al., 2020], constraints on cosmic birefringence [Namikawa et al., 2020], component–separated CMB maps [Madhavacheril et al., 2020] and delensed power spectra measurements at 98 and 150 GHz and cosmological parameters [Han et al., 2021].

The third-generation Advanced ACTPol extended coverage down to 20 GHz and has surveyed 40% of the sky. Early results include a gravitational lensing mass map over 9400 $\deg^2$ with cosmological parameters and a measurement of the lensing power spectrum [Madhavacheril et al., 2024; Qu et al., 2024].

5.5 ACT DR6 DATA ANALYSIS

The ACT DR6 power spectra encompass five years of observations collected between 2017 and 2022. These observations utilize detector arrays sensitive to frequencies centered at 98, 150, and 220 GHz. The data set includes array–band combinations and multipole ranges that successfully passed a comprehensive suite of null tests, forming the nominal DR6 data set. This data set comprises temperature–temperature power spectra (TT), temperature–E-mode polarization power spectra (TE), and polarization–polarization power

spectra (EE). These spectra, along with their covariance matrices, serve as inputs to a multi–frequency likelihood framework.

5.5.1 Methodology and data sets

To fully exploit the multipole range accessible through CMB observations for cosmological analysis, ACT data are combined with satellite data. A minimal combination, employed in all analyses of the ACT primary CMB (referred to as ACT in this thesis), incorporates the Planck measurement of the optical depth using the low–multipole EE power spectrum ($\ell < 30$) `Sroll2` likelihood[11] [Pagano et al., 2020]. The baseline combination, labeled P-ACT, extends this data set further by including Planck observations on large–to–intermediate scales, specifically $\ell < 1000$ in TT and $\ell < 600$ in TE/EE. This approach maximizes the constraining power while minimizing overlap between the two experiments, allowing the cross–covariance between data sets to be safely neglected.

Adding CMB lensing data to the cosmological analysis provides complementary information to that derived from primary CMB power spectra. CMB lensing is a powerful probe of large–scale structure growth over a wide range of cosmic history, peaking at $z \sim 2$ with a tail extending to higher redshifts. ACT has been instrumental in advancing CMB lensing measurements. It was the first experiment to detect the four–point correlation function in CMB temperature maps caused by lensing [Das et al., 2011]. Furthermore, combining the lensing auto–spectrum measurement with the CMB power spectrum provided the first robust evidence of dark energy using CMB data alone [Sherwin et al., 2011]. The ACT DR6 CMB lensing release represents the most precise detection of lensing to date, achieving a 43σ [Madhavacheril et al., 2024; Qu et al., 2024] detection of the lensing power spectrum. The lensing signal is measured across multipoles $40 < \ell < 763$, with extensive testing confirming robustness against systematics and foreground contamination [MacCrann et al., 2024]. For the likelihood analysis, this baseline multipole range is used conservatively to minimize systematic effects.

The Planck PR4 data set offers a CMB lensing measurement with comparable signal–to–noise to ACT DR6, achieving an Signal–to–Noise Ratio (SNR) of 42 using reprocessed NPIPE maps over the multipole range $8 < \ell < 400$ [Carron et al., 2022]. Combining Planck and ACT DR6 produces a state–of–the–art lensing power spectrum, with ACT providing high–precision data at smaller scales ($\ell > 400$)[12]. This analysis adopts a Gaussian likelihood framework to combine ACT DR6 and Planck PR4 bandpowers, accounting for the small correlation between the two data sets [Madhavacheril et al., 2024]. Perturbative corrections are applied to account for the weak dependence of

11 https://web.fe.infn.it/~pagano/low_ell_datasets/sroll2/

12 The two data sets also differ in their instrumental noise characteristics and sky coverage.

Planck	$Planck^{TT/TE/EE}$ + `Sroll2`
ACT	$ACT^{TT/TE/EE}$ + `Sroll2`
P-ACT	$ACT^{TT/TE/EE}$ + $Planck^{TT/TE/EE}_{cut}$ + `Sroll2`
P-ACT-LB	when adding also CMB lensing and BAO

Table 5.1: Dictionary listing the main dataset combinations analyzed in this thesis. Here, CMB lensing always refers to ACT DR6+*Planck* NPIPE lensing; BAO refers to the DESI Year-1 release. All *Planck* results have been re-run to include an updated version of the `Sroll2` likelihood compared to Aghanim et al. (2020c).

these measurements on cosmological parameters, following methodologies outlined in Ade et al. (2016) and Madhavacheril et al. (2024).

BAO data reveal a characteristic acoustic scale of approximately 150 Mpc in the clustering patterns of galaxies in the late–time Universe. This feature enables precise measurements of the ratio between the sound horizon at the baryon drag epoch and a combination of the angular diameter distance and the Hubble parameter across redshifts. This ratio, which is highly sensitive to the matter density and other factors affecting the Universe's expansion history, provides crucial insights into cosmic distances [Bassett and Hlozek, 2009; Eisenstein, 2005; Weinberg et al., 2013]. Because the BAO signal arises during a phase of linear evolution of matter density perturbations, BAO measurements have become a widely used astrophysical data set to break geometric degeneracies in CMB analyses.

Previous ACT analyses relied on compilations of BAO data from various redshifts and surveys, including the BOSS survey [Alam et al., 2017] and the 6dF Galaxy Redshift Survey [Beutler et al., 2011]. In this analysis, we adopt the recent DESI Year–1 observations of the BAO feature in galaxy, quasar, and Lyman-α forest tracers [Adame et al., 2024a; b] as our baseline BAO data set. Within the collaboration, additional analyses were conducted to ensure that results were not solely driven by DESI data, particularly given the noted tension between some of the DESI Luminous Red Galaxy (LRG) data points and earlier measurements at the same redshifts. In cases where BAO data significantly influenced the constraints for a given model, alternative analyses were performed using BOSS/eBOSS BAO data instead. These alternative data sets included BOSS DR12 LRGs [Alam et al., 2017] and eBOSS DR16 LRGs [Alam et al., 2021]. However, for the models discussed in this work, the choice of DESI data does not significantly impact the results.

In the following we report the resulting constraints with the label conventions for different dataset combinations summarized in table 5.1.

Cosmological parameter constraints are derived using the ACT DR6 multi–frequency likelihood in conjunction with `Cobaya`[13] [Torrado and Lewis, 2021]. This framework is coupled to appropriately modified versions of the Einstein–

13 https://cobaya.readthedocs.io/en/latest/

Boltzmann solver CAMB[14] [Lewis et al., 2000], which computes the lensed theoretical CMB power spectra with high precision. All codes exploring extended models are benchmarked against the baseline ΛCDM results from CAMB. Specifically, two modified versions of CAMB were developed for this analysis—-one tailored to the massless mediator model and the other to the heavy mediator model. Both modifications underwent validation. Comparisons of the relative differences in CMB spectra are presented in fig. 5.6 for the massless mediator model and fig. 5.7 for the heavy mediator model. Additionally, results from full MCMC runs were tested against baseline ΛCDM results, with differences observed to be below 10% of the parameter uncertainties (σ) for all varied parameters.

Theoretical predictions are computed using CosmoRec[15] [Chluba et al., 2010], instead of Recfast [Seager et al., 1999], to achieve higher precision in recombination physics[16]. As a baseline, we use primordial helium abundance calculations from PRIMAT[17] [Pitrou et al., 2018] to compute BBN predictions. Alternative options were explored, and the impact of different helium and deuterium abundance predictions was thoroughly assessed[18].

For modeling non–linear corrections to the matter power spectrum, we employ the updated HMcode [Mead et al., 2021] instead of Halofit [Smith et al., 2003]. The analysis uses the dark–matter–only HMcode model, without baryonic feedback corrections.

```yaml
camb:
    extra_args:
        kmax: 10
        k_per_logint: 130
        nonlinear: true
        lens_potential_accuracy: 8
        lens_margin: 2050
        lAccuracyBoost: 1.2
        min_l_logl_sampling: 6000
        DoLateRadTruncation: false
        recombination_model: CosmoRec
```

Figure 5.5: High accuracy settings for CAMB.

Our parameter set consistently includes the six fundamental ΛCDM cosmological parameters: the physical densities of baryons and cold dark matter, $\Omega_b h^2$ and $\Omega_c h^2$, the reionization optical depth, τ, the amplitude and scalar

14 https://camb.readthedocs.io/en/latest/

15 https://www.jb.man.ac.uk/~jchluba/Science/CosmoRec/Welcome.html

16 The "fudge parameters" in Recfast were tuned for sufficient accuracy for Planck but do not meet the precision required for ACT DR6 data.

17 https://www2.iap.fr/users/pitrou/primat.htm

18 Differences in the helium abundance predicted by recent BBN codes have a negligible impact on the CMB primary anisotropy spectra and therefore on cosmological parameters inferred from them.

spectral index of primordial adiabatic density perturbations, A_s and n_s, both defined at a pivot scale of $k_* = 0.05\,\mathrm{Mpc}^{-1}$, and a parameter representing the absolute distance scale, θ_{MC}. The latter is an approximation of the angular scale of the acoustic horizon at decoupling as implemented in `CAMB`. For all analyses presented here, broad, flat, and uninformative priors are adopted for the ΛCDM parameters, except in cases where an `Sroll2`–informed prior on τ is applied in ACT–only fits.

Additional parameters are introduced in the theoretical model to account for astrophysical foregrounds, passband uncertainties, calibration factors, and polarization efficiency. These parameters are varied when using the multi–frequency likelihood to ensure comprehensive modeling.

MCMC chains are run with theory predictions computed up to $\ell_{\mathrm{max}} = 9000$. The chains are terminated once the Gelman–Rubin convergence criterion, $R - 1$, falls below 0.01.

5.5.2 Massless mediator limit

In this work we follow the method of Forastieri et al. (2015), 2019: we derive limits on the strength of neutrino non–standard interactions by directly modifying the Boltzmann equation in order to account for neutrino collisions, without assuming a sudden transition between the two limiting regimes (free–streaming and tight coupling).

We introduce the scattering term using the so called *Relaxation Time Approximation*, or *BGK approximation*, requiring that neutrino distribution function remains exactly thermal throughout the epoch at which neutrinos decouple and start free–streaming, implying that the only possible neutrino perturbations are local temperature fluctuations. [Bhatnagar et al., 1954; Welander, 1954]. The collisional operator at the right–hand side of the Boltzmann equation (see section 1.3.4) is replaced by[19]

$$\left(\frac{\partial f}{\partial \tau}\right)_C \sim \frac{1}{\tau_{\mathrm{coll}}}(f_0 - f), \tag{5.17}$$

where τ_{col} is the relaxation factor and $1/\tau_{\mathrm{col}} \equiv \Gamma$ is the collision frequency. Replacing it in Eq. (1.118) and in particular

$$\frac{1}{f_0}\left(\frac{\partial f}{\partial \tau}\right)_C = \frac{1}{f_0}(\Gamma(f_0 - f)) = -\frac{1}{f_0}(\Gamma f_0 \Psi)\,, \tag{5.18}$$

where Ψ is the perturbation to the phase space distribution function, defined by $f = f_0(1 + \Psi)$. The latter equation is valid in every case: massless or massive neutrinos, (pseudo)scalar or Fermi-like interaction.

19 Differently to what we have done in section 1.3.4, we are now discussing Botlzmann equations in cosmological perturbation theory. Not to overload this work with a unnecessary detailed introduction on the subject we refer to Ma and Bertschinger (1995), from which we borrow the notation for ease of comparison. In particular, in the following f_0 is the unperturbed phase space dsitribution function, τ the conformal time and $(\partial f/\partial \tau)_C$ the collision term in the right–hand side of eq. (1.88).

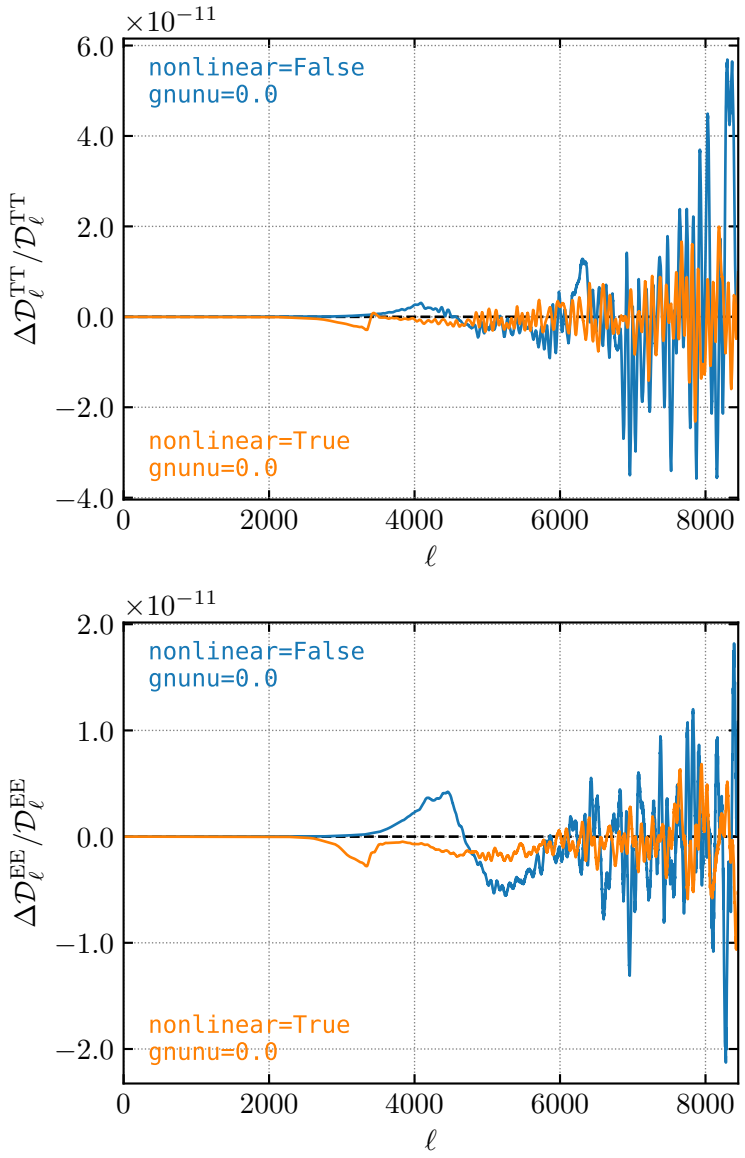

Figure 5.6: Relative difference between CMB temperature and polarization power spectra computed by our modified version of `CAMB` code implementing the massless mediator model and the reference version of the code. The parameter `gnunu` represent the effective coupling constant defined in eq. (5.23).

Thus, for massless neutrinos, the presence of $\nu\nu$ scatterings amounts, in the relaxation time approximation, to modifying the Boltzmann hierarchy as follows

$$\dot{\delta}_\nu = -\frac{4}{3}\theta_\nu - \frac{2}{3}\dot{h}\,, \tag{5.19}$$

$$\dot{\theta}_\nu = k^2\left(\frac{1}{4}\delta_\nu - \sigma_\nu\right)\,, \tag{5.20}$$

$$\dot{\sigma}_\nu = \frac{4}{15}\theta_\nu - \frac{3}{10}kF_{\nu 3} + \frac{2}{15}\dot{h} + \frac{4}{5}\dot{\eta} - a\Gamma\sigma_\nu\,, \tag{5.21}$$

$$\dot{F}_{\nu\ell} = \frac{k}{2\ell+1}\left[\ell F_{\nu(\ell-1)} - (\ell+1)F_{\nu(\ell+1)}\right] - a\Gamma F_{\nu\ell}, \quad (\ell \geq 3)\,. \tag{5.22}$$

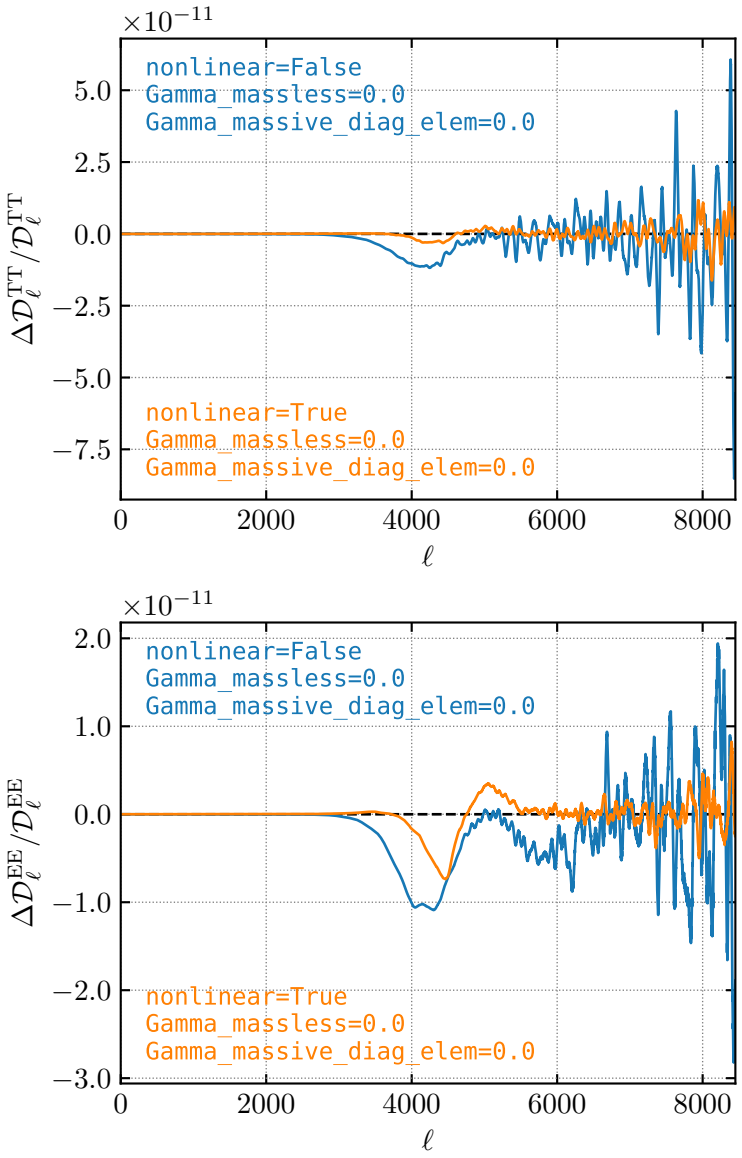

Figure 5.7: Relative difference between CMB temperature and polarization power spectra computed by our modified version of `CAMB` code implementing the heavy mediator model and the reference version of the code. The parameters `Gamma_massless` and `Gamma_massive_diag_elem` represent the effective coupling constant G_{eff} for the massless and massive neutrinos Boltzmann hierarchies, respectively.

The monopole and dipole ($\ell = 0, 1$) of the collision term are set to zero, as it follows from the conservation of particle number and momentum. The $2 \leftrightarrow 2$ collisions lead a suppression of the quadrupole ($\ell = 2$), i.e. the anisotropic stress σ_ν, and of all the highest moments of the distribution function, and to a corresponding enhancement of the monopole and dipole ($\ell = 0, 1$), i.e. the density and velocity perturbations δ_ν and θ_ν. These changes propagate to the photon distribution, and thus to the CMB spectrum, through the gravitational potentials.

We decided to parametrize the interaction using an effective coupling constant $g_{\rm eff}$; this choice guarantees the inclusion of many models attributable to a (pseudo)scalar–like interaction. Thus we rewrite the scattering rate in the following phenomenological way

$$\Gamma = 0.183 \times g_{\rm eff}^4 T_\nu^5 \,. \tag{5.23}$$

This definition of the effective coupling constant encloses such details as the precise Yukawa structure of the theory, the effect of thermal averaging, etc. Given a definite form of the Lagrangian, eq. (5.13), this can be remapped, to a good approximation, to a collision rate of the form eq. (5.23) for the purposes of its effect on the evolution of cosmological neutrino perturbations. Seen in another way, the quantity that we are actually constraining is the (temperature–independent in the high–energy limit) combination $\langle \sigma v \rangle T_\nu^2$.

The analysis has been carried out considering a simple extension of the standard cosmological model in which the effective coupling constant between self–interacting neutrino has been varied together with the standard cosmological parameters. We refer to this model as $\Lambda{\rm CDM} + g_{\rm eff}$. From Planck CMB we find $g_{\rm eff}^4 < 1.5 \times 10^{-27}$ at 95% CL. While the new ACT DR6 spectra alone give a limit about three times weaker, with $g_{\rm eff}^4 < 5.2 \times 10^{-27}$ at 95% CL. Combining the two datasets gives a $\sim 20\%$ improvement on Planck alone, with

$$g_{\rm eff}^4 < 1.2 \times 10^{-27} \quad (95\%, \text{P-ACT}), \tag{5.24}$$

$$< 1.3 \times 10^{-27} \quad (95\%, \text{P-ACT-LB}) \tag{5.25}$$

or $|g_{\rm eff}| < 1.1 \times 10^{-7}$. Neutrino couplings with a light scalar can be constrained from $0\nu2\beta$ experiments and from supernovae explosions. These constraints are usually derived in the flavor basis, as opposed to the mass basis, and expressed in terms of the couplings $g_{\alpha\beta}$, where $\alpha, \beta = e, \mu, \tau$. Currently, EXO-200 provides the most stringent laboratory limits on the electron neutrino–Majoron coupling: $|g_{ee}| < (0.4 - 0.9) \times 10^{-5}$ [Kharusi et al., 2021], where the range expresses the uncertainty due to nuclear matrix elements. Supernova data can also be used to constrain neutrino–Majoron couplings. In particular, scalar emission might shorten too much the observed neutrino signal from SN1987A. This luminosity argument excludes the range of couplings $3 \times 10^{-7} < |g_{\alpha\beta}| < 2 \times 10^{-5}$ [Kachelriess et al., 2000]. Assuming that $g_{\rm eff}$ and $g_{\alpha\beta}$ are related by a factor $\mathcal{O}(1)$, P-ACT-LB yields the strongest forecast on neutrino interactions with a light (pseudo)scalar. In fig. 5.8, we show the posterior distribution for the parameters of the $\Lambda{\rm CDM} + g_{\rm eff}$ model for various data combinations. Let us notice the mild correlation between $g_{\rm eff}$ and the scalar spectral index n_s, that we interpret as the result of the additional power at intermediate scales (i.e., left of the pivot k) for $g_{\rm eff} > 0$.

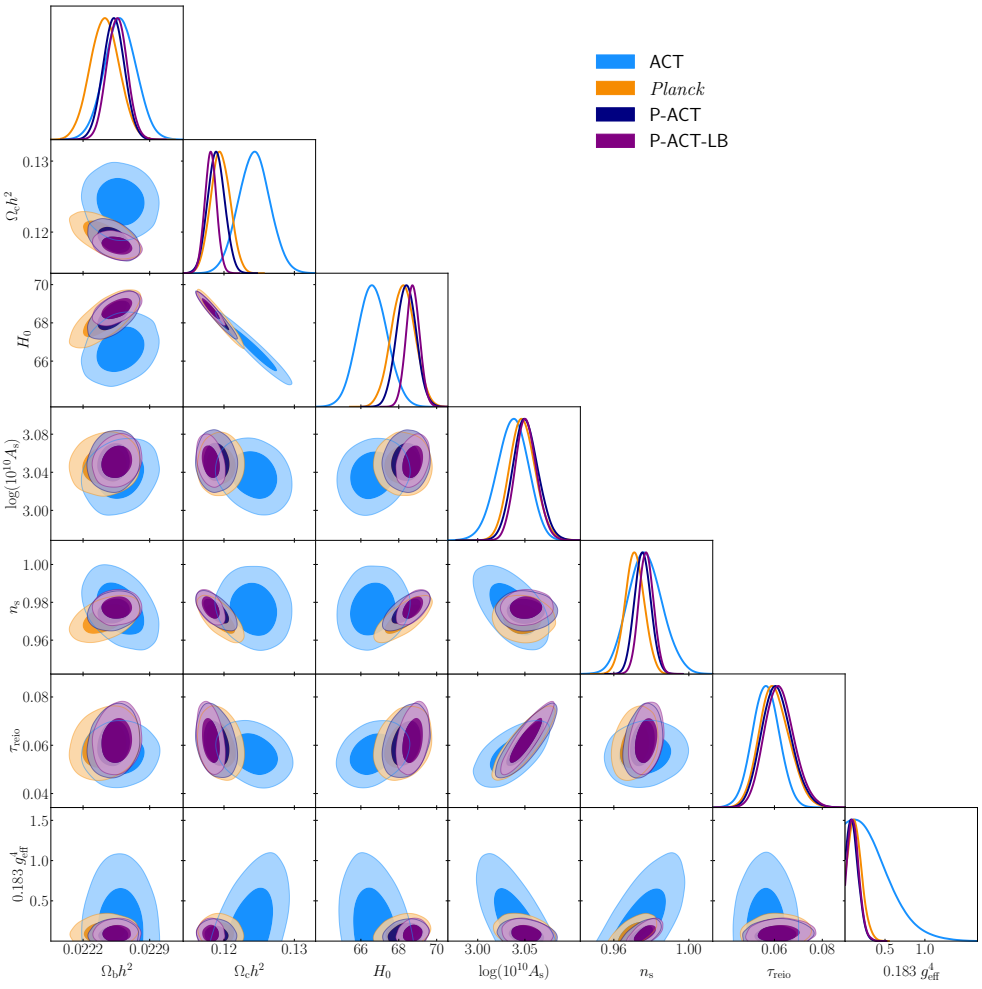

Figure 5.8: Triangle plot including one–dimensional posteriors and two-dimensional 68% and 95% credible regions for the parameters of the $\Lambda\text{CDM} + g_{\text{eff}}$ model for different data combinations. Numerical results with error bars are shown in Tab. 5.2.

Parameter	ACT	*Planck*	P-ACT	P-ACT-LB
$\mathbf{0.183}\ g_{\rm eff}^4$	< 0.866	< 0.281	< 0.227	< 0.233
$\Omega_{\rm b}h^2$	0.02259 ± 0.00033	0.02243 ± 0.00030	0.02252 ± 0.00022	$0.02256^{+0.00021}_{-0.00020}$
$\Omega_{\rm c}h^2$	$0.1243^{+0.0044}_{-0.0043}$	$0.1195^{+0.0027}_{-0.0026}$	$0.1189^{+0.0024}_{-0.0023}$	$0.1181^{+0.0017}_{-0.0016}$
$\log(10^{10}A_{\rm s})$	$3.037^{+0.031}_{-0.034}$	$3.048^{+0.028}_{-0.026}$	$3.051^{+0.027}_{-0.025}$	$3.051^{+0.023}_{-0.021}$
$n_{\rm s}$	$0.977^{+0.019}_{-0.017}$	$0.971^{+0.010}_{-0.0099}$	$0.9754^{+0.0087}_{-0.0083}$	$0.9773^{+0.0076}_{-0.0075}$
$\tau_{\rm reio}$	0.056 ± 0.011	$0.060^{+0.013}_{-0.012}$	$0.061^{+0.013}_{-0.012}$	$0.062^{+0.013}_{-0.011}$
H_0	$66.6^{+1.6}_{-1.5}$	$68.2^{+1.2}_{-1.3}$	68.4 ± 1.0	68.74 ± 0.71

Table 5.2: 95% Bayesian credible intervals for the seven parameters of the ΛCDM + $g_{\rm eff}$ model. Different columns refers to different combinations of data sets, as indicated in the table.

5.5.3 Heavy mediator limit

For the analysis of this model, modification to the standard cosmological scenario were implemented following the procedure developed in Kreisch et al. (2020), 2024. Again, collision integral computation have been simplified through the use of the relaxation time approximation, which has been shown to be particularly accurate for the model considered in this section [Oldengott et al., 2017]. Under this assumption, equations of motion for different neutrino multipoles ν_ℓ at first order in perturbation theory can be summarized in the following compact form (following now the notation of [Kreisch et al., 2020])

$$\frac{\partial \nu_\ell}{\partial \tau} + k\frac{q}{\epsilon}\left(\frac{\ell+1}{2\ell+1}\nu_{\ell+1} - \frac{\ell}{2\ell+1}\nu_{\ell-1}\right) - 4\left(\frac{\partial \phi}{\partial \tau}\delta_{\ell 0} + \frac{k}{3q}\psi\delta_{\ell 1}\right) = -a\frac{G_{\rm eff}^2 T_\nu^5 \nu_\ell f_\nu^{(0)}(q)}{f_\nu^{(0)}(q)}\left(\frac{T_{\nu,0}}{q}\right)\left[A\left(\frac{q}{T_{\nu,0}}\right) + B_\ell\left(\frac{q}{T_{\nu,0}}\right) - 2D_\ell\left(\frac{q}{T_{\nu,0}}\right)\right], \tag{5.26}$$

where we have introduced the comoving momentum $\mathbf{q} \equiv a\mathbf{p}$, $\epsilon = \sqrt{q^2 + a^2 m_\nu^2}$, a is the scale factor, δ_{mn} is the Kronecker delta function, and $T_{\nu,0}$ is the current ($a = 1$) temperature of the neutrinos. In eq. (5.26), the functions $A(x)$, $B_\ell(x)$ and $D_\ell(x)$ are integral functions whose explicit expression can be found in Appendix C of Kreisch et al. (2020). The fact that the collision term is directly proportional to ν_ℓ is a consequence of our use of the thermal approximation. We note that energy and momentum conservation ensures that $A + B_0 - 2D_0 = 0$ and $A + B_1 - 2D_1 = 0$, respectively.

In the massless case ($q = \epsilon$), it is possible to integrate eq. (5.26) over the comoving momentum to yield a simpler neutrino multipole hierarchy [Cyr-Racine and Sigurdson, 2014; Lancaster et al., 2017]

$$\frac{\partial F_\ell}{\partial \tau} + k\left(\frac{\ell+1}{2\ell+1}F_{\ell+1} - \frac{\ell}{2\ell+1}F_{\ell-1}\right) - 4\left(\frac{\partial \phi}{\partial \tau}\delta_{\ell 0} + \frac{k}{3}\psi\delta_{\ell 1}\right) = -aG_{\rm eff}^2 T_\nu^5 \alpha_\ell F_\ell\,, \tag{5.27}$$

where

$$\alpha_\ell = \frac{120}{7\pi^4}\int_0^\infty dx\, x^2[A(x) + B_l(x) - 2D_l(x)]\,, \tag{5.28}$$

and where we denoted the massless perturbations as F_ℓ to distinguish them from the massive neutrino variables ν_l.

These modified Boltzmann equations have been implemented in the code `CAMB`. For computational speed, the functions A, B_l, and D_l were precomputed on a grid of $q/T_{\nu,0}$ values and an interpolation routine was used to access them when solving the cosmological perturbation equations. The coefficient α_l was precomputed and tabulated as well. Neutrinos were assumed to have masses distributed according to the NO. All neutrinos are assumed to interact with the same coupling strength $G_{\rm eff}$. At early times, the large self–interaction rate of neutrinos renders the equations of motion for multipoles $l \geq 2$ extremely stiff. To handle this, a tight-coupling scheme was employed.

Previous analyses have shown that CMB and BAO data are compatible with, and in some cases prefer, neutrino self–interactions with $G_{\rm eff} \gg G_F$ [Archidiacono and Hannestad, 2014; Barenboim et al., 2019; Brinckmann et al., 2021; Cyr-Racine and Sigurdson, 2014; Das and Ghosh, 2021; Kreisch et al., 2020; Lancaster et al., 2017; Mazumdar et al., 2022; Oldengott et al., 2017; Park et al., 2019; Roy Choudhury et al., 2021]. In fact, the posterior for $G_{\rm eff}$ has been found to be bimodal, with probability being concentrated in two distinct regions: a moderately interacting (MIν) mode, compatible with no self–interactions, and to a strongly interacting (SIν) mode. The analysis of ACT–DR4 data found $G_{\rm eff} \lesssim 10^{-3}\,{\rm MeV}^{-2}$ for MIν, and $G_{\rm eff} \simeq 10^{-1.5}\,{\rm MeV}^{-2}$ for SIν [Kreisch et al., 2024].

We start by considering a one-parameter extension of ΛCDM, including $G_{\rm eff}$ as an extra parameter and keeping fixed $\sum m_\nu = 0.06\,{\rm eV}$ and $N_{\rm eff} = 3.044$. To check if the bimodal behavior persists with the ACT DR6 spectra, we split the parameter space in two regions, $G_{\rm eff} < 10^{-2}$ MeV^{-2} (MIν) and $G_{\rm eff} > 10^{-2}$ MeV^{-2} (SIν), and perform separate MCMC runs with flat priors on $\log_{10}\left(G_{\rm eff}\,{\rm MeV}^2\right)$:

$$-8 \leq \log_{10}\left(G_{\rm eff}\,{\rm MeV}^2\right) \leq -2 \quad ({\rm MI}\nu)\,, \tag{5.29}$$

and

$$-2 \leq \log_{10}\left(G_{\rm eff}\,{\rm MeV}^2\right) \leq 0 \quad ({\rm SI}\nu)\,. \tag{5.30}$$

The logarithmic prior allows us to explore a wide range of values of $G_{\rm eff}$, spanning several orders of magnitude.

In the MIν region, the P-ACT and P-ACT-LB combinations are compatible with $G_{\rm eff} = 0$, but show a mild preference for $\log_{10}\left(G_{\rm eff}\,{\rm MeV}^2\right) \simeq -3$. In contrast, in the SI$\nu$ region, the posteriors for the same dataset combinations peak at the lower edge of the prior range, i.e., at $\log_{10}\left(G_{\rm eff}\,{\rm MeV}^2\right) = -2.0$. We show the two posteriors in Fig. 5.9. Since we are performing separate

	ACT	P-ACT	P-ACT-LB
$\Delta\chi^2_{\mathrm{MI}\nu}$	-0.2	2.9	3.1
$\Delta\chi^2_{\mathrm{SI}\nu}$	-3.2	-10.6	-7.3
$\sigma_{\mathrm{MI}\nu}$	–	1.7	1.8
$\sigma_{\mathrm{SI}\nu}$	–	–	–

Table 5.3: $\Delta\chi^2 \equiv \chi^2_{\Lambda\mathrm{CDM}} - \chi^2_{\Lambda\mathrm{CDM}+G_{\mathrm{eff}}}$ from the MAP points of the MIν and SIν regions for different data combinations. When self-interacting neutrino models yield an improvement of the fit over ΛCDM we also report the preference for the model in units of σ. We find no statistically significant preference for neutrino self-interactions.

parameter estimation runs for MIν and SIν, we cannot use the distributions to assess the relative probability of the two scenarios. Instead we compare the effective χ^2 of Maximum A Posteriori (MAP)[20] models in the two regions to that of the ΛCDM model, as reported in Table 5.3. We find that the SIν model is never preferred over ΛCDM. The MIν model yields basically no improvement to the goodness-of-fit for the ACT DR6 data alone with respect to ΛCDM, while it gives marginal improvement for P-ACT and P-ACT-LB. Specifically, we find $\Delta\chi^2_{\mathrm{MI}\nu} = 2.9$ (P-ACT) and $\Delta\chi^2_{\mathrm{MI}\nu} = 3.1$ (P-ACT-LB), corresponding respectively to a mild 1.7σ and 1.8σ preference over ΛCDM, as computed using the likelihood-ratio test.

Since $G_{\mathrm{eff}} = 0$ is compatible with the data, the posterior for the MIν scenario ideally extends with non-zero probability down to $\log_{10}\left(G_{\mathrm{eff}}\mathrm{MeV}^2\right) \to -\infty$. The posterior is therefore ill-defined with a diverging integrated probability. This prevents the computation of meaningful Bayesian credible intervals. Previous analyses chose to arbitrarily cut the distribution at some lower bound and reported credible intervals depending on this choice. Here, we take a different approach; once the information about the position of the peaks has been acquired from the runs with a logarithmic prior, the proposal density of the MCMC can be correspondingly tuned and we repeat the runs using a uniform prior on G^2_{eff}, namely $0 \leq G^2_{\mathrm{eff}} \leq (10^{-2}\,\mathrm{MeV}^{-2})^2$, ensuring a proper posterior. We choose a uniform prior on G^2_{eff} rather than on G_{eff} because the former amounts to a uniform prior on the scattering rate $\Gamma \propto G^2_{\mathrm{eff}}$. Adopting this strategy, we find

$$G_{\mathrm{eff}}\ (\mathrm{MI}\nu) < 7.9 \times 10^{-3}\,\mathrm{MeV}^{-2}\ (95\%, \text{P-ACT-LB}). \tag{5.31}$$

We repeat the analysis for a model in which only one of the three neutrino families is self-interacting. In this case, we find that both P-ACT and P-ACT-LB yield a posterior with a well-defined peak in the SI region; in particular, $\log_{10}\left(G_{\mathrm{eff}}\,\mathrm{MeV}^2\right) = -1.33^{+0.21}_{-0.14}$ (68% P-ACT-LB). The posterior in the MI region is instead qualitatively similar to the one found in the scenario with

20 ACT DR6 likelihood includes informative priors on some nuisance parameters, and thus the MAP is used, rather than the maximum–likelihood point.

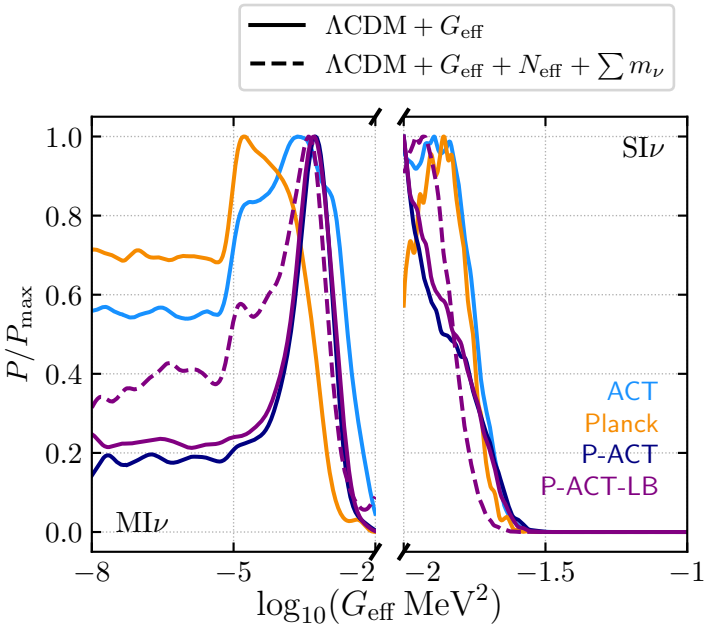

Figure 5.9: Posterior distribution of the effective coupling constant, $G_{\rm eff}$ from various data combination within the ΛCDM + $G_{\rm eff}$ model. The posterior is presented in two distinct regions of parameter space, corresponding to the MIν and SIν modes, each independently normalized due to separate sampling. Minimal smoothing is applied to the plot to preserve the features of the bimodal distribution.

three interacting neutrinos. Both these single interacting-neutrino models are however not significantly preferred over ΛCDM, with $\Delta\chi^2_{\rm MI\nu} = -1.2$ and $\Delta\chi^2_{\rm SI\nu} = -5.5$ (P-ACT-LB), corresponding respectively to a 1.1σ (MIν) and 2.3σ (SIν) preference over ΛCDM.

We further consider a 9-parameter extended model with three interacting neutrinos in which, in addition to the base ΛCDM parameters and $G_{\rm eff}$, also $N_{\rm eff}$ and $\sum m_\nu$ are allowed to vary. As in Kreisch et al. (2024), $N_{\rm eff}$ is used to rescale the neutrino temperature. We find results similar to those for the ΛCDM + $G_{\rm eff}$ model with three interacting neutrinos (see Fig. 5.9). In particular, we do not find a peak in the posterior in the SIν region, in contrast to the mild preference for such a model seen in the analysis of the ACT DR4 data [Kreisch et al., 2024]. The mild hint of SIν in the DR4 analysis was largely driven by a high fluctuation in the EE power spectrum at intermediate scales, $700 < \ell < 1000$, which is no longer present in the DR6 spectra (see Appendix of Calabrese et al. (2025)).

To summarize, we find that limits on interacting neutrino models are sensitive to the underlying assumptions used to describe the broader physics in the neutrino sector. However, neutrino self-interactions are not detected in any scenario that we consider and not preferred over ΛCDM.

This lack of evidence also limits the ability of this model to increase the value of the Hubble constant. For example, a heavy mediator in the MIν

scenario gives $H_0 = 68.2 \pm 0.4$ km/s/Mpc (ΛCDM + $G_{\rm eff}$) and $H_0 = 67.5 \pm 1.0$ km/s/Mpc (ΛCDM + $G_{\rm eff}$ + $N_{\rm eff}$ + $\sum m_\nu$) using P-ACT-LB. In general, we find no significant shift compared to ΛCDM for the ΛCDM + $G_{\rm eff}$ model. In the extended case of ΛCDM + $G_{\rm eff}$ + $N_{\rm eff}$ + $\sum m_\nu$, the H_0 distribution shifts lower by ~ 1 km/s/Mpc and has a twice larger uncertainty. This is driven by the $N_{\rm eff} - H_0$ correlation and by ACT's preference for $N_{\rm eff} < 3.044$ found in ΛCDM + $N_{\rm eff}$ (see [Calabrese et al., 2025]), which persists in this model. In the SIν scenario, we find instead $H_0 = 69.0 \pm 0.4$ km/s/Mpc (ΛCDM + $G_{\rm eff}$) and $H_0 = 67.0 \pm 0.9$ km/s/Mpc (ΛCDM + $G_{\rm eff}$ + $N_{\rm eff}$ + $\sum m_\nu$) for P-ACT-LB. The ~ 1 km/s/Mpc upward shift in H_0 in the ΛCDM + $G_{\rm eff}$ model is induced by the positive correlation between $G_{\rm eff}$ and θ_s. In the ΛCDM + $G_{\rm eff}$ + $N_{\rm eff}$ + $\sum m_\nu$ model, this effect is countered by a lower value of $N_{\rm eff}$, resulting in a lower value of H_0 with respect to the corresponding MIν scenario.

Laboratory searches, especially double-β decay experiments and observations of meson and lepton decays, severely constrain the coupling of neutrinos with a new light boson [Blinov et al., 2019]. Taken at face value, the values of $G_{\rm eff}$ in the SIν region, as well as those corresponding to the MIν peak, are excluded by these searches as shown in Fig. 5.10, unless the new scalar couples almost exclusively to τ neutrinos.

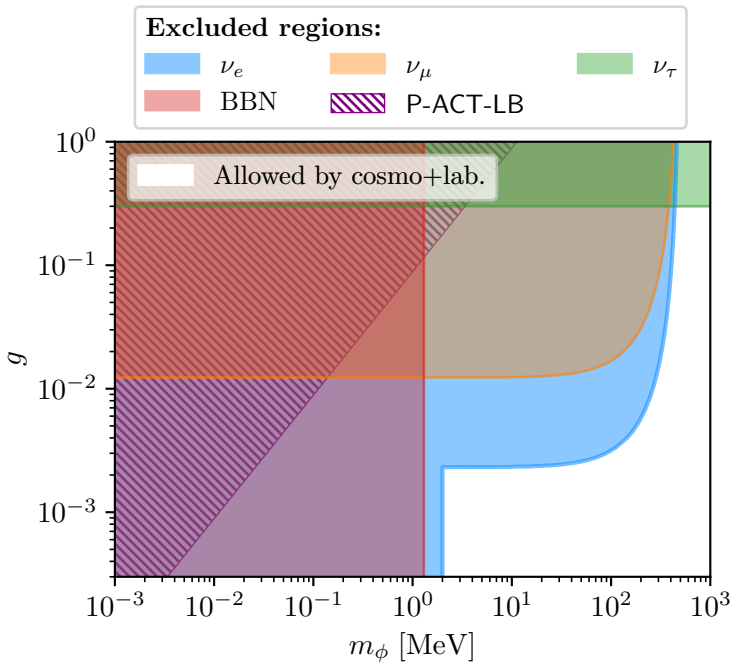

Figure 5.10: Cosmological and laboratory limits on neutrino couplings with a new scalar ϕ. The purple band with hatches in the upper left corner corresponds to the region excluded by P-ACT-LB accounting for both MI and SI neutrinos. The other overlaid color bands are excluded by particle physics and BBN limits. The shaded blue region refers to scalars coupling to electron neutrinos and is excluded by neutrinoless double β decay searches [Agostini et al., 2020; Arnold et al., 2014; Blum et al., 2018; Kharusi et al., 2021] and measurements of the ratio $\mathrm{Br}(K^+ \to e^+\nu_e)/\mathrm{Br}(K^+ \to \mu^+\nu_\mu)$ [Fiorini, 2007; Lessa and Peres, 2007]. The orange shaded region is excluded by laboratory constraints on the decay $K^+ \to \mu^+\nu_\mu\phi$ [Navas et al., 2024] that apply to scalars coupling to μ neutrinos. The green shaded region is excluded by laboratory constraints on the decay $\tau^- \to \ell_\alpha^+\bar{\nu}_\alpha\nu_\tau\phi$ [Lessa and Peres, 2007], applying to scalars coupling to τ neutrinos. The red-shaded region is excluded by BBN constraints on N_{eff} [Blinov et al., 2019]. Together, cosmology and laboratory measurements allow the parameter space remaining in the right bottom corner (in white).

Part III

SIGNATURES OF PRIMORDIAL OSCILLATORY FEATURES IN THE LSS OF THE UNIVERSE

This part of the thesis explores the theoretical and observational imprints of primordial oscillatory features in LSS of the Universe investigating how deviations from standard primordial spectra influence the formation and distribution of cosmic structures. The focus of the work is on extending traditional methodologies for incorporating oscillatory features into perturbation theory, examining their compatibility with observational data, and comparing analytical predictions with results from state–of–the–art N-body simulations.

6 NONLINEAR MODELLING OF PRIMORDIAL OSCILLATORY FEATURES

The discussion in this chapter is focused on study of features in the primordial power spectrum and it is based on the results reported in Ballardini and Barbieri (2024). In section 6.1 we review the basic technicalities and main results of the TSPT formalism. In section 6.2, we specify the main formalism to the addition of primordial oscillatory features, reproducing the results already obtained in the literature and extending them taking into account novel contributions. Detailed calculations have been carried out in sections 6.3 and 6.4 for linear and logarithmic features, respectively. Finally in section 6.6 we compare our analytical results with N–body simulations using the COLA method.

6.1 TIME–SLICED PERTURBATION THEORY

In this section, we review the core elements of the TSPT formalism, along with its main features following the work presented in Blas et al. (2016a) and b and Vasudevan et al. (2019). For the sake of generality, we begin by considering a single field variable, denoted as Θ. In cosmology, perturbative fields are dynamical variables. Therefore, without loss of generality, we assume that they satisfy deterministic equations of motion, given by

$$\dot{\Theta}_\eta\left(\mathbf{k}\right) = \mathcal{I}\left[\Theta_\eta; \eta, \mathbf{k}\right] \,, \tag{6.1}$$

where η is a generic time coordinate and the dot represents the derivative with respect to it. In the spirit of PT, the right–hand side (rhs) is given as a power series in the fields

$$\mathcal{I}\left[\Theta_\eta; \eta, \mathbf{k}\right] = \sum_{n=1}^{\infty} \frac{1}{n!} \int \prod_{i=1}^{n} \mathrm{d}^3 q_i \; \Theta_\eta\left(\mathbf{q}_i\right) I_n\left(\eta; \mathbf{q}_1, \ldots, \mathbf{q}_n\right) \delta^{(3)}\left(\mathbf{k} - \sum_{j=1}^{n} \mathbf{q}_j\right) \,. \tag{6.2}$$

The δ-function in this expression enforces the conservation of momentum, which we assume is satisfied by the system. We also assume that the latter respects parity, which is encoded by the following property

$$I_m\left(\eta; \mathbf{q}_1, \ldots, \mathbf{q}_m\right) = I_m\left(\eta; -\mathbf{q}_1, \ldots, -\mathbf{q}_m\right) \,. \tag{6.3}$$

The second key element for constructing our framework is the statistical distribution at the initial time η_0, which is set deep within the linear regime.

This choice allows us to recover the correlators of standard perturbation theory (SPT) within a path-integral formulation, using the following partition function [Carroll et al., 2014; Valageas, 2004]

$$Z\left[J;\eta\right]=\mathcal{N}^{-1}\int\mathcal{D}\Theta_{\eta_0}\exp\left\{-\frac{1}{2}\int\mathrm{d}^3k\,\frac{\Theta_{\eta_0}\left(\mathbf{k}\right)\Theta_{\eta_0}\left(-\mathbf{k}\right)}{P_{\eta_0}\left(k\right)}+\int\mathrm{d}^3k\,\Theta_{\eta}\left(\mathbf{k}\right)J\left(-\mathbf{k}\right)\right\}, \tag{6.4}$$

where P_{η_0} is the power spectrum of the initial Gaussian distribution and

$$\mathcal{N}=\int\mathcal{D}\Theta_{\eta_0}\exp\left\{-\frac{1}{2}\int\mathrm{d}^3k\,\frac{\Theta_{\eta_0}\left(\mathbf{k}\right)\Theta_{\eta_0}\left(-\mathbf{k}\right)}{P_{\eta_0}\left(k\right)}\right\} \tag{6.5}$$

is a normalization factor. It is important to note that the integration here is performed over the fields at the initial time, while the source J couples to the final values of the field. At first glance, this may seem counterintuitive: since the second term in the exponential of eq. (6.4) does not depend on the path integral variable, one might think that it could be factored out and included in the normalisation term. However, we must always remember that at any given time the field Θ_η is determined by a deterministic time evolution governed by eq. (6.1), meaning it can always be expressed as a function of the initial conditions, $\Theta_\eta\left(\mathbf{k}\right)=\Theta_\eta\left[\Theta_{\eta_0};\mathbf{k}\right]$ (see section 4.2 of Carroll et al. (2014)). We have explicitly imposed statistical homogeneity and isotropy by ensuring that, in the Gaussian weight, the momenta of the Θ-fields sum to zero, and the power spectrum $P_{\eta_0}\left(k\right)$ depends only on the magnitude of the momentum. The equal-time correlation functions are then derived by differentiating $Z\left[J;\eta\right]$ with respect to the source and then setting $J=0$

$$\left\langle\Theta_\eta\left(\mathbf{k}_1\right)\cdots\Theta_\eta\left(\mathbf{k}_n\right)\right\rangle=\left.\frac{\delta^n Z\left[J;\eta\right]}{\delta J\left(-\mathbf{k}_1\right)\cdots\delta J\left(-\mathbf{k}_n\right)}\right|_{J=0}. \tag{6.6}$$

This fact follows directly from the expansion of the second factor at the exponential in the generating functional, eq. (6.4), in power series

$$Z\left[J;\eta\right]=\sum_{n=0}^{\infty}\frac{1}{n!}\int\prod_{i=1}^{n}\mathrm{d}^3q_i\,J\left(-\mathbf{q}_i\right)\left\langle\Theta_\eta\left(\mathbf{q}_1\right)\cdots\Theta_\eta\left(\mathbf{q}_n\right)\right\rangle, \tag{6.7}$$

which, noticing that

$$\frac{\delta^n}{\delta J\left(-\mathbf{k}_1\right)\cdots\delta J\left(-\mathbf{k}_n\right)}\int\prod_{i=1}^{m}\mathrm{d}^3q_i\,J\left(-\mathbf{q}_i\right)\Bigg|_{J=0}=n!\,\delta_{mn}\int\prod_{i=1}^{n}\mathrm{d}^3q_i\,\delta^3\left(\mathbf{k}_i-\mathbf{q}_i\right), \tag{6.8}$$

gives us back exactly eq. (6.6). In particular, for the two-point function at the initial time we can explicitly calculate this formula. When $\eta=\eta_0$, the path-integral partition function of eq. (6.4) can be easily computed as a Gaussian integral giving

$$\begin{aligned}Z\left[J;\eta_0\right]&=\mathcal{N}^{-1}\int\mathcal{D}\Theta_{\eta_0}\exp\left\{-\frac{1}{2}\int\mathrm{d}^3k\left[\frac{\Theta_{\eta_0}\left(\mathbf{k}\right)\Theta_{\eta_0}\left(-\mathbf{k}\right)}{P_{\eta_0}\left(k\right)}+\Theta_{\eta_0}\left(\mathbf{k}\right)J\left(-\mathbf{k}\right)\right]\right\},\\&=\exp\left\{\frac{1}{2}\int\mathrm{d}^3k\,J\left(\mathbf{k}\right)J\left(-\mathbf{k}\right)P_{\eta_0}\left(k\right)\right\}.\end{aligned} \tag{6.9}$$

It is then easy to see that the two-point correlation function is

$$\left\langle \Theta_{\eta_0}(\mathbf{k}_1)\Theta_{\eta_0}(\mathbf{k}_2)\right\rangle \equiv \left.\frac{\delta^2 Z\left[J;\eta_0\right]}{\delta J\left(-\mathbf{k}_1\right)\delta J\left(-\mathbf{k}_2\right)}\right|_{J=0} = \delta^{(3)}\left(\mathbf{k}_1+\mathbf{k}_2\right)P_{\eta_0}\left(k\right)\,, \tag{6.10}$$

which correspond to the initial power spectrum, as expected.

In SPT, it is customary to solve the equations of motion, eq. (6.1), iteratively and express the field at final time, $\Theta_\eta\left(\mathbf{k}\right)$, as a Taylor series in powers of the initial configuration, $\Theta_{\eta_0}\left(\mathbf{k}\right)$. The key distinction between SPT and TSPT lies in the way we choose to approach this problem. Since we are generally interested in correlation functions at a specific time, say η, it is natural to use the field evaluated at that moment as the primary variable in our formalism. To implement this, we replace the integration variable in eq. (6.4) with the field at time η, which then defines a time-dependent probability density function (PDF), $\mathcal{P}\left[\Theta_\eta;\eta\right]$, as follows

$$Z\left[J;\eta\right] = \int \mathcal{D}\Theta_\eta\, \mathcal{P}\left[\Theta_\eta;\eta\right] \exp\left\{\int \mathrm{d}^3k\, \Theta_\eta\left(\mathbf{k}\right) J\left(-\mathbf{k}\right)\right\}\,. \tag{6.11}$$

Note that $\mathcal{P}\left[\Theta_\eta;\eta\right]$ not only generalises eq. (6.4), which defines a time-dependent PDF, but also takes into account deviations from the Gaussian one, if any. The equation that determines the time evolution of $\mathcal{P}$ is nothing more than the classical Liouville equation, where the value of the field at a given $\mathbf{k}$ is considered as a stochastic variable. It can be derived by performing a substitution of the integration variables in eq. (6.11) in terms of the fields at time $\eta+\delta\eta$, namely

$$\Theta_{\eta+\delta\eta}\left(\mathbf{k}\right) = \Theta_\eta\left(\mathbf{k}\right) + \delta\eta\dot{\Theta}_\eta\left(\mathbf{k}\right) \overset{(6.1)}{=} \Theta_\eta\left(\mathbf{k}\right) + \delta\eta\mathcal{I}\left[\Theta_\eta;\eta,\mathbf{k}\right]\,. \tag{6.12}$$

This change of variables affects all the factors appearing in eq. (6.11). Then, asking for the invariance of $Z\left[J;\eta\right]$ one finally obtain the following time evolution equation

$$\frac{\partial}{\partial\eta}\mathcal{P}\left[\Theta_\eta;\eta\right] + \int \mathrm{d}^3p\, \frac{\delta}{\delta\Theta_\eta\left(\mathbf{p}\right)}\left(\mathcal{I}\left[\Theta_\eta;\mathbf{p},\eta\right]\mathcal{P}\left[\Theta_\eta;\eta\right]\right) = 0\,, \tag{6.13}$$

which, as expected, is the functional version of Liouville's equation for the conservation of probability. We note that once $\mathcal{P}$ is found from eq. (6.13), it is possible to compute all the different correlation functions using eq. (6.11). In this way, TSPT allows to disentangle the time evolution of the fields from their statistical averaging. From now on we will omit the subindex η on the field Θ whenever it appears as an argument of the distribution function.

In the spirit of a perturbative expansion, in analogy of what it is usually done in QFT is it convenient to search for solution of eq. (6.13) in the form

$$\mathcal{P}[\Theta;\eta] = \mathcal{N}^{-1}\exp\left\{-\sum_{n=1}^{\infty}\frac{1}{n!}\int\prod_{i=1}^{n}\mathrm{d}^3k_i\,\Theta(\mathbf{k}_i)\Gamma_n^{\mathrm{tot}}(\eta;\mathbf{k}_1,\cdots,\mathbf{k}_n)\right\}\,, \tag{6.14}$$

where $\Gamma_n^{\rm tot}$ is reminiscent of the power expansion of the 1–Particle Irreducible (1PI) QFT effective action. This expression allows us to traslate the conservation of probability in a hierarchy of equations which replace the dynamical equation of SPT,

$$\dot{\Gamma}_n^{\rm tot}(\eta;\mathbf{k}_1,\ldots,\mathbf{k}_n) + \sum_{m=1}^{n} \frac{1}{m!(n-m)!} \times \sum_{\sigma} I_m\Big(\eta;\mathbf{k}_{\sigma(1)},\ldots,\mathbf{k}_{\sigma(m)}\Big)\Gamma_{n-m+1}^{\rm tot}\left(\eta;\sum_{l=1}^{m}\mathbf{k}_{\sigma(l)},\mathbf{k}_{\sigma(m+1)},\ldots,\mathbf{k}_{\sigma(n)}\right) = = \delta^{(3)}\left(\sum_{i=1}^{n}\mathbf{k}_i\right)\int \mathrm{d}^3p\; I_{n+1}(\eta;\mathbf{p},\mathbf{k}_1,\ldots,\mathbf{k}_n)\,, \tag{6.15}$$

where in the second term on the left–hand side (lhs) the sum runs over all permutations σ of n indices.

It is useful to decompose the solutions of this equation as

$$\Gamma_n^{\rm tot} = \Gamma_n + C_n\,, \tag{6.16}$$

where Γ_n are the solutions of the homogeneous equations with initial conditions matching the statistical distribution of the primordial fluctuations, while C_n are the solutions of the non-homogeneous equations with vanishing initial conditions. The Γ_n vertices have the physical meaning of the 1PI contributions to the tree-level correlators, and C_n are counterterms whose role is to cancel UV divergences in the loop corrections.[1] For the purposes of this work, the expressions for C_n are not needed.

In order to solve the regular part of eq. (6.15), we assume to be in an Einstein–de Sitter (EdS) universe. This is a good approximation for the study of LSS (see section 2 of Blas et al. (2016a)) and leads a great simplification of equations. For a more realistic ΛCDM cosmology, the deviations from a EdS regime can be taken into account perturbatively. These assumptions allow us to assume that the evolution kernels I_n are time-independent. By resorting to the statistical homogeneity of the fields, $\langle\Theta\rangle = 0$, it is possible to set $\Gamma_1 = 0$, while for $n \geq 2$ we use the ansatz

$$\Gamma_n(\eta,\mathbf{k}_1,\ldots,\mathbf{k}_n) = \sum_{l=2}^{n} e^{-l\eta}\Gamma_n^{(l)}(\mathbf{k}_1,\ldots,\mathbf{k}_n)\,, \tag{6.17}$$

1 To avoid confusion, let us stress that the C_n differ from the generic counterterms of QFT in that their values cannot be adjusted at will: they are uniquely fixed by the solution of the Liouville equation. They arise to cancel certain UV divergences that arise from the (singular) Jacobian describing the change in functional measure when going from eq. (6.4) to eq. (6.11). A proper UV renormalisation of the theory is likely to require additional counterterms to capture the true physical effects of the short modes.

which separates time and momentum dependence. This, together with eq. (6.15), gives the relations for $\Gamma_n^{(l)}$ with $2 < l < n$,

$$\Gamma_n^{(l)}(\mathbf{k}_1, \dots, \mathbf{k}_n) = -\frac{1}{n-l} \sum_{m=2}^{n-l+1} \frac{1}{m!(n-m)!} \times \sum_{\sigma} I_m\left(\mathbf{k}_{\sigma(1)}, \dots, \mathbf{k}_{\sigma(m)}\right) \Gamma_{n-m+1}^{(l)}\left(\sum_{i=1}^{m} \mathbf{k}_{\sigma(i)}, \mathbf{k}_{\sigma(m+1)}, \dots, \mathbf{k}_{\sigma(n)}\right). \tag{6.18}$$

The remaining vertices, $\Gamma_n^{(n)}$, should be fixed from initial conditions.

In case of Gaussian initial conditions, the problem is simplified: the PDF $\mathcal{P}[\Theta, \eta]$ must reduce to a Gaussian distribution at early times after having rescaled the fields with the linear growth factor $D(\eta) = e^{\eta}$.[2] Basically, one can require

$$\lim_{\eta \to -\infty} \mathcal{P}\left[D(\eta)\tilde{\Theta}, \eta\right] = \mathcal{N} \exp\left\{-\int \mathrm{d}^3 k \, \frac{\tilde{\Theta}_{\mathbf{k}} \tilde{\Theta}_{-\mathbf{k}}}{2P_L(k)}\right\}, \tag{6.19}$$

where $P_L(k)$ is the linear power spectrum. Under these assumptions one finds that the Γ_n vertices have a universal dependence on time

$$\Gamma_n(\eta; \mathbf{k}_1, \dots, \mathbf{k}_n) = \frac{1}{g^2(\eta)} \bar{\Gamma}_n(\mathbf{k}_1, \dots, \mathbf{k}_n), \tag{6.20}$$

where $g(\eta) \equiv D(\eta)$ plays the role of TSPT coupling constant. In particular, all the vertices are sourced by the Gaussian initial weight inherited by $P_L(k)$ and propagated from the simplest vertex $\Gamma_2^{(2)}$ to all the other through recursion relations like those of eq. (6.18). In TSPT it is possible to build a perturbative structure upon expanding the generating functional of eq. (6.11) around the Gaussian part of $\mathcal{P}$, which is equivalent to an expansion in the coupling constant. At this step the analogy with the QFT is complete and it is possible to represent this calculation as a sum of Feynman diagrams, whose first elements (for the regular vertices) are given by

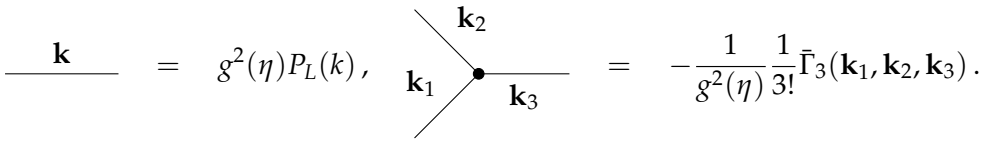

(6.21)

Let us notice that, in contrast to SPT, time does not flow along the diagrammatic elements, but is taken care of by the time dependence of the coupling constant. To calculate an n-point correlation function of the field Θ one needs

2 As the discussion now focuses on the specific problem of cosmological perturbation evolution, η is no longer just a generic time coordinate; rather, it is that which allows perturbation equations to be written without any explicit time dependence, as is customary in the study of LSS evolution. It is defined as $\eta \equiv \ln D(\tau)$, where τ is the conformal time.

to draw all diagrams with n external legs. It is straightforward to see that diagrams with higher number of loops are proportional to higher powers of $g(\eta)$. One should also include vertices corresponding to counterterms C_n, with $n \geq 1$, in order to subtract certain UV divergences in loop diagrams. In this sense counterterms appear quite naturally in TSPT.

6.2 INCLUSION OF PRIMORDIAL OSCILLATORY FEATURES

In this section, we will first outline the general procedure for incorporating primordial oscillatory features into a TSPT-like approach to perturbation theory. This procedure is completely general in the sense that it does not depend on the particular shape of the wiggly part of the power spectrum. We then focus on two cases of interest: linear and logarithmic primordial oscillations. This discussion is mainly based on Blas et al. (2016a) and Vasudevan et al. (2019) where we refer the interested reader for further details.

The key objects for describing LSS are the matter density contrast, δ, and the velocity divergence, Θ, fields. The nonlinear evolution is captured by the cosmological perturbation theory, which uses as seeds the linear fields δ_L and Θ_L evolved up to the present epoch as if the perturbations were always in the linear regime. In the case of adiabatic initial conditions corresponding to a growing mode, the two linear fields are identical, and they are related to the curvature perturbation, ζ, by a transfer function $T(\eta_0, \mathbf{k})$ which encodes the evolution of perturbations eventually from cosmic inflation, through recombination, up to a given time η_0. So we write

$$\Theta_L(\mathbf{k}) = \delta_L(k) \equiv T(\eta_0, \mathbf{k})\, \zeta(\mathbf{k})\,. \tag{6.22}$$

The statistical properties of the field δ_L are captured by the power spectrum, defined as the Fourier transform of the two-point correlation function, given by

$$\left\langle \delta_L(\mathbf{k}) \delta_L(\mathbf{k}') \right\rangle \equiv (2\pi)^3 \delta^{(3)}(\mathbf{k} + \mathbf{k}') P_L(k)\,. \tag{6.23}$$

In this way we can relate the linear matter power spectrum to the primordial power spectrum of curvature perturbations as[3]

$$P_L(k) = \left[T(\eta_0, \mathbf{k})\right]^2 P_\zeta(k)\,. \tag{6.24}$$

To start with the TSPT formalism, it is convenient to decompose the linear power spectrum into a smooth (non-wiggly, nw) and an oscillatory (wiggly, w) part, which describes the imprint of the BAO and any other oscillations, as

$$P_L(k) = P_L^{\mathrm{nw}}(k) + P_L^{\mathrm{w}}(k)\,. \tag{6.25}$$

3 From now on we will omit the time dependence of the matter power spectrum for simplicity.

The vertices (limiting ourselves to the case of Gaussian fields), $\bar{\Gamma}_n$, are functionals of the linear power spectrum. It is therefore natural to expand them to the first order in $P_L^{\rm w}$ to separate them into non-wiggly and wiggly parts

$$\bar{\Gamma}_n(\mathbf{k}_1,\ldots,\mathbf{k}_n) = \bar{\Gamma}_n^{\rm nw}(\mathbf{k}_1,\ldots,\mathbf{k}_n) + \bar{\Gamma}_n^{\rm w}(\mathbf{k}_1,\ldots,\mathbf{k}_n)\,. \tag{6.26}$$

As in Blas et al. (2016a), let us split the momenta into hard $\{\mathbf{k}_i\}$ and soft $\{\mathbf{q}_j\}$ and analyze the structure of the wiggly vertices in the limit $\varepsilon \sim q/k \ll 1$. Consider first the cubic vertex. The leading contribution in the soft limit is

$$\Gamma_3'^{\rm w}(\mathbf{k},-\mathbf{k}-\mathbf{q},\mathbf{q}) \simeq \frac{(\mathbf{q}\cdot\mathbf{k})}{q^2}\frac{P_L^{\rm w}(|\mathbf{k}+\mathbf{q}|)-P_L^{\rm w}(k)}{[P_L^{\rm nw}(k)]^2}\,. \tag{6.27}$$

The pole of the first factor cancels the numerator of the second factor at $q\to 0$. However, the cancellation does not occur if q is greater than the period of the oscillations, $q \gtrsim k/\omega$, where ω is a generic frequency describing the wiggle part of the spectrum, in which case the contribution is enhanced by $1/\varepsilon$. To keep track of this enhancement, we introduce the linear operator $\mathcal{D}_{\mathbf{q}}$ acting on the wiggly power spectrum,

$$\begin{aligned}\mathcal{D}_{\mathbf{q}}P_L^{\rm w}(\mathbf{k}) &\equiv \frac{(\mathbf{q}\cdot\mathbf{k})}{q^2}[P_L^{\rm w}(|\mathbf{k}+\mathbf{q}|)-P_L^{\rm w}(k)]\\ &= \frac{(\mathbf{q}\cdot\mathbf{k})}{q^2}[\exp(\mathbf{q}\cdot\nabla_{\mathbf{k}'})-1]P_L^{\rm w}(k')\Big|_{\mathbf{k}'=\mathbf{k}}\,.\end{aligned} \tag{6.28}$$

It is useful here to introduce a *translation operator*, $\mathcal{T}_{\mathbf{q}} \equiv \exp(\mathbf{q}\cdot\nabla_{\mathbf{k}})$, in analogy to quantum mechanics, which, acting on the linear power spectrum, shifts its evaluation point in momentum space by $\mathbf{q}$. Then, the second equality in eq. (6.28) follows by the Taylor series expansion of the power spectrum

$$\begin{aligned}P_L^{\rm w}(|\mathbf{k}+\mathbf{q}|) &= P_L^{\rm w}(k) + \mathbf{q}\cdot\nabla_{\mathbf{k}}P_L^{\rm w}(k) + q_iq_j\partial_{k_i}\partial_{k_j}P_L^{\rm w}(k)+\cdots\\ &= \exp(\mathbf{q}\cdot\nabla_{\mathbf{k}})\,P_L^{\rm w}(k) = \mathcal{T}_{\mathbf{q}}P_L^{\rm w}(k)\,.\end{aligned} \tag{6.29}$$

Each insertion of this operator is treated as a quantity of order $1/\varepsilon$. Next, it can be shown that the leading contribution in an n-point vertex with $n-2$ soft momenta is of order $(1/\varepsilon)^{n-2}$ and has the form

$$\bar{\Gamma}_n'^{\rm w}\left(\mathbf{k},-\mathbf{k}-\sum_{i=1}^{n-2}\mathbf{q}_i,\mathbf{q}_1,\ldots,\mathbf{q}_{n-2}\right) \simeq \frac{(-1)^{n-1}}{[P_L^{\rm nw}(k)]^2}\prod_{j=1}^{n-2}\mathcal{D}_{\mathbf{q}_j}P_L^{\rm w}(k)\,. \tag{6.30}$$

The proof of this formula can be found in appendix C of Vasudevan et al. (2019).

The most IR-enhanced diagrams among the loop corrections to the wiggly power spectrum are the so-called *daisy* diagrams, which are obtained by dressing the wiggly vertices with soft loops. Thus, at the leading IR order, we have

$P_{\delta\delta}^{\rm w,\,LO}(k)$ = 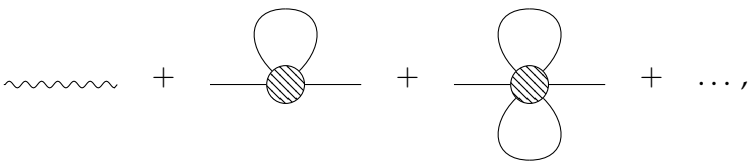 + ⋯ ,

(6.31)

where we have used a wavy line and shaded circles to denote the wiggly linear power spectrum and the wiggly vertices respectively. The smooth lines represent the non-wiggly propagator $g^2 P_L^{\rm nw}(k)$. The term with ℓ loops in this expression is of the order $g^2\left(g^2/\varepsilon^2\right)^\ell$. We see that the loop suppression represented by g^2 is partially compensated by the IR enhancement, so these contributions must be resummed. The leading part of the diagram with ℓ loops reads

$$P_{\delta\delta}^{\rm w,LO,\,\ell-loop}(\eta,k) = -\frac{1}{(2\ell+2)!}\cdot(2\ell+2)\cdot(2\ell+1)\cdot(2\ell-1)!!\cdot g^4(\eta)[P_L^{\rm nw}(k)]^2$$
$$\times\prod_{i=1}^{\ell}\left[\int {\rm d}^3q_i\, g^2(\eta)P_L^{\rm nw}(q_i)\right] g^{-2}(\eta)\bar{\Gamma}'^{\rm w}_{2\ell+2}(\mathbf{k},-\mathbf{k},\mathbf{q}_1,-\mathbf{q}_1,\ldots,\mathbf{q}_\ell,-\mathbf{q}_\ell)$$
$$\simeq \frac{g^{2\ell+2}(\eta)}{2^\ell\ell!}\prod_{i=1}^{\ell}\left[\int_{q_i\le k_{\rm S}} {\rm d}^3q_i\, P_L^{\rm nw}(q_i)\mathcal{D}_{\mathbf{q}_i}\mathcal{D}_{-\mathbf{q}_i}\right] P_L^{\rm w}(k)\,, \tag{6.32}$$

where we have used eq. (6.30) to go to the second line. We have also restricted the loop integrals to the IR domain $g \le k_{\rm S}$. The separation scale $k_{\rm S}$ defining this domain must be in the range $k/\omega < k_{\rm S} < k$. Otherwise its choice is arbitrary and represents an intrinsic freedom in the resummation scheme. The sensitivity of the final result to the precise value of $k_{\rm S}$ provides an estimate of the theoretical uncertainty due to considering only the IR part of the loops and omitting the integrals over the hard momenta $q > k_{\rm S}$. This sensitivity decreases when higher orders in the hard loops are included in the calculation; see Blas et al. (2016a) and Vasudevan et al. (2019).

Adding up the contributions eq. (6.32) with all ℓ we obtain the leading-order IR-resummed wiggly power spectrum in a closed form,

$$P_{\delta\delta}^{\rm w,LO}(\eta,k) = g^2(\eta)e^{-g^2(\eta)\mathcal{S}}P_L^{\rm w}(k)\,, \tag{6.33}$$

where we introduced a new operator

$$\mathcal{S} \equiv -\frac{1}{2}\int_{q\le k_{\rm S}} {\rm d}^3q\, P_L^{\rm nw}(q)\mathcal{D}_{\mathbf{q}}\mathcal{D}_{-\mathbf{q}}\,. \tag{6.34}$$

It should be emphasised that this operator encodes the damping of the oscillations by IR resummation of the large-scale bulk flows. The total IR-resumed power spectrum at the leading order is obtained by adding the non-wiggly contribution, which remains unchanged,

$$P_{\delta\delta}^{\rm LO}(\eta,k) = g^2(\eta)\left[P_L^{\rm nw}(k) + e^{-g^2(\eta)\mathcal{S}}P_L^{\rm w}(k)\right]. \tag{6.35}$$

The resummation procedure can be extended to include the corrections from hard loops. We will not repeat the derivation here and refer the interested reader to Blas et al. (2016a). For the next-to-leading order (NLO) in the hard loops, the result is

$$P_{\delta\delta}^{\rm NLO}(\eta,k) = g^2(\eta)\left[P_L^{\rm nw}(k) + \left(1+g^2(\eta)\mathcal{S}\right)e^{-g^2(\eta)\mathcal{S}}P_L^{\rm w}(k)\right]$$
$$+\, g^4(\eta)P_{\delta\delta}^{\rm 1-loop}\left[P_L^{\rm nw}(k) + e^{-g^2(\eta)\mathcal{S}}P_L^{\rm w}(k)\right], \tag{6.36}$$

where the last term is the usual 1-loop correction to the power spectrum evaluated using the linear spectrum with damped oscillations corresponding to the Leading Order (LO) result.

Before we look at the details of IR resummation with oscillatory features, we want to say a few words about its theoretical modelling, since we have tried to stay as general as possible so far. In the following, we will assume that the PPS can be written as

$$P_\zeta(k) = P_{\zeta,0}(k)\left[1 + \delta P_\zeta^X(k)\right], \tag{6.37}$$

where

$$P_{\zeta,0} \equiv \frac{2\pi^2}{k^3} A_s \left(\frac{k}{k_*}\right)^{n_s - 1}, \tag{6.38}$$

is the standard almost scale-invariant PPS predicted by the simplest inflationary models while $\delta P_\zeta(k)$ encodes any deviations from the scale invariance, the primordial feature. Here, A_s and n_s are the scalar amplitude and spectral index at the pivot scale k_*, which is assumed to be $k_* = 0.05\,\mathrm{Mpc}^{-1}$. We consider primordial features with linearly- and logarithmically-spaced oscillations with $X = \{\mathrm{lin}, \mathrm{log}\}$.

Within this work, we consider the following generic parameterisation

$$\delta P_\zeta^X(k) = A(k)\sin(\omega_X \Xi_X + \phi_X), \tag{6.39}$$

where $\Xi_X = \{k/k_*, \ln(k/k_*)\}$, which we refer to as *linear features* (LIN) and *logarithmic features* (LOG), respectively. On top of the sinusoidal component, one can additionally consider the presence of a scale-dependent amplitude. We consider three different cases: one with a constant amplitude and two with a scale-dependent amplitude modulated by a Gaussian function (to which we refer to as *wave packet*, WP) or by a power law (PL). We parameterise the generic amplitude appearing in eq. (6.39) as

$$A(k) = \begin{cases} A_X & \text{(6.40a)} \\ A_X^{\mathrm{WP}} \exp\left[-(k-\mu)^2/2\Delta^2\right]. & \text{(6.40b)} \\ A_X^{\mathrm{PL}} (k/k_\star)^n & \text{(6.40c)} \end{cases}$$

The templates described by eq. (6.39) cover a wide range of primordial oscillatory signals. Linear oscillations in the PPS of density perturbations can be generated by abrupt changes in the background parameters, also known as sharp features, at certain moments during the evolution of the inflationary dynamics. These sudden shifts give rise to transient oscillatory features both in single-field inflationary models [Adams et al., 2001; Bean et al., 2008; Chen et al., 2007; 2008; Miranda et al., 2012; Starobinsky, 1992] and in multi-field models [Achucarro et al., 2011; Braglia et al., 2020; Chen, 2012]. Logarithmic oscillations, also known as resonant features, can arise from periodic modulations in the inflationary potential, as seen in Chen (2010), 2012, Chen et al.

(2008), Flauger et al. (2010), and Flauger and Pajer (2011). The amplitude of these oscillatory signals is highly model dependent, influenced by the nature of the primordial feature for both case with linear and logarithmic oscillations [Achucarro et al., 2011; Adams et al., 2001; Armendariz-Picon and Lim, 2003; Chen, 2012; Starobinsky, 1992]. Starting from templates that assume oscillatory features with a constant amplitude (6.40a), we study two different cases where the envelope evolves as a Gaussian (6.40b) or as a power-law (6.40c). In addition to these behaviours, some models, such as the *classical primordial standard clock* models, predict a complex superposition of both types of linear and logarithmic features [Braglia et al., 2023; Chen, 2012] and other models like *axion monodromy inflation* [McAllister et al., 2010; Silverstein and Westphal, 2008] predict a running frequency appear, further extending the testable phenomenology.

The information in the PPS is transferred to the matter power spectrum by the evolution of eq. (6.24). Given the linearity property of the transfer function, it is natural to assume a split like that of eq. (6.37) also in the matter power spectrum. This is in perfect analogy to what has been done for the description of BAO in eq. (6.25), so it is natural to constrain the feature models as contributions to the BAO spectrum. In presence of primordial features, it is useful to further separate the wiggly component of the matter power spectrum as

$$P^{\rm w}\left(k\right) \equiv P^{\rm w}_{\rm BAO}\left(k\right) + P^{\rm w}_{X}\left(k\right) + P^{\rm w}_{\rm BAO}\left(k\right)\delta P^{X}_{\zeta}\left(k\right)\,, \tag{6.41}$$

where $P^{\rm w}_{\rm BAO}(k)$ is the standard BAO features in a flat ΛCDM cosmology, which can be parameterised as [Seo and Eisenstein, 2007]

$$P^{\rm w}_{\rm BAO}(k) = P^{\rm nw}(k)\delta P^{\rm BAO}(k) \simeq A_{\rm BAO}(k)\sin(\omega_{\rm BAO}k)\,. \tag{6.42}$$

Here, $\omega_{\rm BAO} \simeq 110\,h^{-1}\,$Mpc is the frequency of the BAO [Aghanim et al., 2020c], $A_{\rm BAO}(k)$ is the amplitude of the BAO, where the k dependence stems for the modulation originated by the diffusion damping, which start to be efficient around the Silk damping scale [Eisenstein and Hu, 1998; Hu and Sugiyama, 1996; Silk, 1968]. The component proportional to the primordial features is given by

$$P^{\rm w}_{X}(k) = P^{\rm nw}(k)\delta P^{X}_{\zeta}(k)\,. \tag{6.43}$$

Finally, the third term in eq. (6.41) is the cross-correlation term between the BAO and the primordial features. Since it is proportional to $A_{\rm BAO}\cdot A_X$, it is usually assumed to be subdominant and therefore neglected.

6.3 LINEAR OSCILLATIONS

The key ingredient to compute the damping of oscillatory features by IR resummation is to evaluate the action of the $\mathcal{S}$ operator, defined in eq. (6.34),

on the analytic expression of the wiggly part of the power spectrum. As already discussed in section 6.2, the first step is the evaluation of the translation operator, which we recall here to be defined as

$$\mathcal{T}_{\mathbf{q}}[\,.\,] = \sum_{n=0}^{\infty} \frac{1}{n!} \left(\mathbf{q} \cdot \nabla_{\mathbf{k}}\right)^n . \tag{6.44}$$

From this equation it is clear how the problem moves to the evaluation of the derivative operator $(\mathbf{q} \cdot \nabla_{\mathbf{k}})$ and its integer powers. Considering the case of linear oscillations with constant amplitude, as introduced in eq. (6.39), we have to evaluate the following quantity

$$\mathbf{q} \cdot \nabla_{\mathbf{k}} \left[A_{\rm lin} \sin\left(\omega_{\rm lin} \frac{k}{k_*} + \varphi_{\rm lin} \right) \right] . \tag{6.45}$$

The next steps become simpler by considering separately the complex exponential functions building the sine function, on which the derivative operator of our interest act as

$$\mathbf{q} \cdot \nabla_{\mathbf{k}} e^{\pm i \omega_{\rm lin} k/k_*} = \pm i \frac{\omega_{\rm lin}}{k_*} \frac{(\mathbf{q} \cdot \mathbf{k})}{k} e^{\pm i \omega_{\rm lin} k/k_*} . \tag{6.46}$$

Thanks to this relation we can now start looking to the action of the translation operator on the exponential components of our parameterisation. By explicitly carrying out the first two steps of the series we find

$$\begin{aligned} \mathcal{T}_{\mathbf{q}} \left[e^{\pm i \omega_{\rm lin} k/k_*} \right] &= \sum_{n=0}^{\infty} \left(\mathbf{q} \cdot \nabla_{\mathbf{k}}\right)^{(n-1)} \left[\pm i \frac{\omega_{\rm lin}}{k_*} \frac{(\mathbf{q} \cdot \mathbf{k})}{k} e^{\pm i \omega_{\rm lin} k/k_*} \right] \\ &= \sum_{n=0}^{\infty} \left(\mathbf{q} \cdot \nabla_{\mathbf{k}}\right)^{(n-2)} \left\{ \pm i \frac{\omega_{\rm lin}}{k_*} \left[\pm i \frac{\omega_{\rm lin}}{k_*} \frac{(\mathbf{q} \cdot \mathbf{k})^2}{k^2} + \frac{q^2}{k} - \frac{(\mathbf{q} \cdot \mathbf{k})^2}{k^3} \right] e^{\pm i \omega_{\rm lin} k/k_*} \right\} . \end{aligned} \tag{6.47}$$

The terms in the squared brackets are the second derivative of the exponential factor (analogous to the previous step) plus the derivatives of the polynomial factor in front of the exponential in the first line of eq. (6.47). We notice that it is not possible to write this sum with a closed-form because of the problem of the nth derivatives of a fraction and therefore it is not possible to write the action of the translation operator for our linear feature. The common practice here is to recall the hierarchy between soft and hard momenta, and noticing that all the corrections coming from subsequent derivatives of $(\mathbf{q} \cdot \mathbf{k})/k$ are of order $\mathcal{O}(\varepsilon)$, and thus negligible in the limit of soft momenta corrections. Under this approximation, we can finally write the action of the translation operator as

$$\mathcal{T}_{\mathbf{q}} \left[e^{\pm i \omega_{\rm lin} k/k_*} \right] = e^{\pm i \frac{\omega_{\rm lin}}{k_*} \frac{(\mathbf{q} \cdot \mathbf{k})}{k}} e^{\pm i \omega_{\rm lin} k/k_*} . \tag{6.48}$$

As we are going to show, the possibility to build this kind of relationship is fundamental to compute in an analytic way the damping due to IR resummation of the features.

To compute the 1-loop corrections to the matter power spectrum we need now to evaluate the derivative operator defined in eq. (6.34) on the wiggly part of the spectrum, corresponding to eq. (6.39). We start by noticing that using eq. (6.28), we can cast eq. (6.34) in the following way

$$\begin{aligned}\mathcal{S}P_L^{\mathrm{w}}(k) &= +\frac{1}{2}\int_{q\leq k_{\mathrm{S}}}\frac{\mathrm{d}^3q}{(2\pi)^3}\,P_L^{\mathrm{nw}}(q)\,\frac{(\mathbf{q}\cdot\mathbf{k}')^2}{q^4}\left(\mathcal{T}_{\mathbf{q}}-1\right)\left(\mathcal{T}_{-\mathbf{q}}-1\right)P_L^{\mathrm{w}}(k')\Big|_{\mathbf{k}'=\mathbf{k}} \\ &= \int_{q\leq k_{\mathrm{S}}}\frac{\mathrm{d}^3q}{(2\pi)^3}\,P_L^{\mathrm{nw}}(q)\,\frac{(\mathbf{q}\cdot\mathbf{k}')^2}{q^4}\left[1-\cosh\left(\mathbf{q}\cdot\nabla_{\mathbf{k}'}\right)\right]P_L^{\mathrm{w}}(k')\Big|_{\mathbf{k}'=\mathbf{k}}\,.\end{aligned} \tag{6.49}$$

It is now easy to show that

$$\left[1-\cosh\left(\mathbf{q}\cdot\nabla_{\mathbf{k}'}\right)\right]P_L^{\mathrm{w}}(k')|_{\mathbf{k}'=\mathbf{k}} = \left[1-\cos\left(\frac{\omega_{\mathrm{lin}}}{k_*}\frac{\mathbf{q}\cdot\mathbf{k}}{k}\right)\right]P_L^{\mathrm{w}}(k)\,, \tag{6.50}$$

which is true every time that the translation operator has exponential "eigenvalues" like in eq. (6.48). Thanks to this result it is possible to calculate the angular part of the integral in eq. (6.49) leaving us with

$$\begin{aligned}\mathcal{S}P_L^{\mathrm{w}}(k) &= P_L^{\mathrm{w}}(k)\,\frac{k^2}{6\pi^2}\int_0^{k_{\mathrm{S}}}\mathrm{d}q\,P_L^{\mathrm{nw}}(q)\left[1-j_0\left(\frac{\omega_{\mathrm{lin}}}{k_*}q\right)+2j_2\left(\frac{\omega_{\mathrm{lin}}}{k_*}q\right)\right] \\ &\equiv k^2\Sigma_{\mathrm{lin}}(k)\,P_L^{\mathrm{w}}(k)\,.\end{aligned} \tag{6.51}$$

This formula for the damping of linear oscillations coincides with that of the BAO case (up to modifications in the frequency from $\omega_{\mathrm{lin}}/k_*$ to ω_{BAO}), already present in the literature in Blas et al. (2016a). This result already appeared in the treatment of primordial linear oscillations in Beutler et al. (2019) (albeit in a slightly different formalism) and can be seen here as a test of our methodology and a summary of its main steps. Finally, let us recall that this is all we need for the calculation of the LO matter power spectrum, using eq. (6.35), but also for the calculation of the Next–to–Leading Order (NLO) in the hard loops, as shown in eq. (6.36).

6.3.1 Mixed term between baryon and primordial linear oscillations

The goal of this section is to further improve the calculation of the nonlinear matter power spectrum with linear oscillatory features by the addition of the

primordial features to BAO mixed term in eq. (6.41). Thanks to some basic trigonometric relations,[4] we can write

$$\begin{aligned} & P^{\rm w}_{\rm BAO}\left(k\right)\delta P^{\rm lin}_{\zeta}\left(k\right) = \\ & \quad = P^{\rm nw}_{L}(k) A_{\rm BAO}(k)\sin(\omega_{\rm BAO}k) A_{\rm lin}\sin\left(\omega_{\rm lin}\frac{k}{k_*}+\varphi_{\rm lin}\right) \\ & \quad = \frac{1}{2}A_{\rm BAO}(k)P^{\rm nw}_{L}\left(k\right)A_{\rm lin} \\ & \qquad \times\left\{\cos\left[\left(\omega_{\rm lin}-k_*\omega_{\rm BAO}\right)\frac{k}{k_*}+\varphi_{\rm lin}\right]-\cos\left[\left(\omega_{\rm lin}+k_*\omega_{\rm BAO}\right)\frac{k}{k_*}+\varphi_{\rm lin}\right]\right\} \\ & \quad \equiv \frac{1}{2}A_{\rm BAO}(k)\left[P^{\rm w}_{\rm lin}\left(k\right)|^{\varphi_{\rm lin}+\pi/2}_{\omega_{\rm lin}-k_*\omega_{\rm BAO}} - P^{\rm w}_{\rm lin}\left(k\right)|^{\varphi_{\rm lin}+\pi/2}_{\omega_{\rm lin}+k_*\omega_{\rm BAO}}\right]. \end{aligned} \tag{6.53}$$

From the previous equation we notice that it is possible to describe the mixed term as interference between linear waves of different frequencies. Let us notice that the shift in the phase has been introduced to recover the initial expression of the wiggly power spectrum.

Given that all operators needed to compute the damping are linear operators and that eq. (6.53) is linear as well, we can easily compute the damping sourced by the mixed term using the results of section 6.3. In particular, thanks to eq. (6.51), we can write

$$\begin{aligned} & \mathcal{S}\left[P^{\rm w}_{\rm BAO}\left(k\right)\delta P^{\rm lin}_{\zeta}\left(k\right)\right] = \\ & \quad = \frac{k^2}{2}A_{\rm BAO}(k)\left[\Sigma_{\rm lin}\left(k\right)P^{\rm w}_{\rm lin}\left(k\right)|^{\varphi_{\rm lin}+\pi/2}_{\omega_{\rm lin}-k_*\omega_{\rm BAO}} - \Sigma_{\rm lin}\left(k\right)P^{\rm w}_{\rm lin}\left(k\right)|^{\varphi_{\rm lin}+\pi/2}_{\omega_{\rm lin}+k_*\omega_{\rm BAO}}\right]. \end{aligned} \tag{6.54}$$

In this case, it is not possible to define a single damping factor for mixed term (in our terminology we could say that it is not an "eigenfunction" of the $\mathcal{S}$ operator). However, to proceed with our evaluations we just need to know what has been reported in eq. (6.54). The approximations underlying this result are exactly the same used in the case of a single component of linear oscillations. In addition, we neglected corrections coming from the derivatives of the BAO amplitude, which shows a weak dependence on k. Thanks to this result, and those of the previous section, we can finally write the LO matter power spectrum with linear oscillatory features as

$$\begin{aligned} P^{\rm LO}_{\delta\delta}(\eta,k) = g^2(\eta)\Bigg\{ & P^{\rm nw}_{L}(k) + e^{-g^2(\eta)k^2\Sigma_{\rm BAO}(k)}P^{\rm w}_{\rm BAO}(k) + e^{-g^2(\eta)k^2\Sigma_{\rm lin}(k)}P^{\rm w}_{\rm lin}(k) \\ & + \frac{1}{2}A_{\rm BAO}(k)\left[e^{-g^2(\eta)k^2\Sigma_{\rm lin}(k)}P^{\rm w}_{\rm lin}\left(k\right)\Big|^{\varphi_{\rm lin}+\pi/2}_{\omega_{\rm lin}-k_*\omega_{\rm BAO}} - e^{-g^2(\eta)k^2\Sigma_{\rm lin}(k)}P^{\rm w}_{\rm lin}\left(k\right)\Big|^{\varphi_{\rm lin}+\pi/2}_{\omega_{\rm lin}+k_*\omega_{\rm BAO}}\right]\Bigg\}, \end{aligned} \tag{6.55}$$

4 From addition and subtraction relations one finds

$$\sin\alpha\sin\beta = \frac{1}{2}\left[\cos\left(\alpha+\beta\right)-\cos\left(\alpha-\beta\right)\right]. \tag{6.52}$$

where $\Sigma_{\rm lin}$ is defined in eq. (6.51) while $\Sigma_{\rm BAO}$ can be obtained from the latter by substitution of $\omega_{\rm lin}/k_*$ with $\omega_{\rm BAO}$. From now on, the vertical line on the side of factors within an equation indicates that all factors to its left should be evaluated using the values to its right. For example, in eq. (6.55),

$$e^{-g^2(\eta)k^2\Sigma_{\rm lin}(k)}P^{\rm w}_{\rm lin}(k)\Big|^{\varphi_{\rm lin}+\pi/2}_{\omega_{\rm lin}-k_*\omega_{\rm BAO}}, \tag{6.56}$$

means that both the damping and the wiggly power spectrum must be evaluated with frequency $\omega_{\rm lin}-k_*\omega_{\rm BAO}$ and phase $\varphi_{\rm lin}+\pi/2$. Using the same ingredients, it is possible to compute also the NLO matter power spectrum, that is

$$\begin{aligned}
P^{\rm NLO}_{\delta\delta}(\eta,k) = g^2(\eta)\Big\{ & P^{\rm nw}_L(k) + g^2(\eta)P^{\text{1-loop}}_{\delta\delta}\left[g^{-2}(\eta)P^{\rm LO}_{\delta\delta}(\eta,k)\right] \\
& + \left(1+g^2(\eta)k^2\Sigma_{\rm BAO}(k)\right)e^{-g^2(\eta)k^2\Sigma_{\rm BAO}(k)}P^{\rm w}_{\rm BAO}(k) \\
& + \left(1+g^2(\eta)k^2\Sigma_{\rm lin}(k)\right)e^{-g^2(\eta)k^2\Sigma_{\rm lin}(k)}P^{\rm w}_{\rm lin}(k) \\
& + \frac{1}{2}A_{\rm BAO}(k)\Big[\left(1+g^2(\eta)k^2\Sigma_{\rm lin}(k)\right)e^{-g^2(\eta)k^2\Sigma_{\rm lin}(k)}P^{\rm w}_{\rm lin}(k)\Big|^{\varphi+\pi/2}_{\omega-k_*\omega_{\rm BAO}} \\
& - \left(1+g^2(\eta)k^2\Sigma_{\rm lin}(k)\right)e^{-g^2(\eta)k^2\Sigma_{\rm lin}(k)}P^{\rm w}_{\rm lin}(k)\Big|^{\varphi+\pi/2}_{\omega+k_*\omega_{\rm BAO}}\Big]\Big\}.
\end{aligned} \tag{6.57}$$

This formula, together with eq. (6.55), shows how the addition of the mixed term between baryon and primordial linear oscillations affects the calculation of the matter power spectrum, which has never been explicitly calculated. While these corrections are clearly sub-dominant compared to the main signal, we found it useful to perform a full derivation of this contribution to quantitatively assess its impact.

6.4 LOGARITHMIC OSCILLATIONS

The case of logarithmic oscillations, besides some subtleties that we are going to discuss later, is analogous to that of linear oscillations. Again, the key ingredient is the evaluation of the translation operator, which passes through the computation of the integer powers of $(\mathbf{q}\cdot\nabla_{\mathbf{k}})$ on the wiggly power spectrum of eq. (6.39), namely

$$\mathbf{q}\cdot\nabla_{\mathbf{k}}\left[A_{\log}\sin\left(\omega_{\log}\ln\frac{k}{k_*}+\varphi_{\log}\right)\right]. \tag{6.58}$$

As before, we consider separately the exponential components of the sine function, on which the derivative operator acts as

$$\mathbf{q}\cdot\nabla_{\mathbf{k}}e^{\pm i\omega_{\log}\ln(k/k_*)} = \pm i\omega_{\log}\frac{(\mathbf{q}\cdot\mathbf{k})}{k^2}e^{\pm i\omega_{\log}\ln(k/k_*)}. \tag{6.59}$$

To find a suitable form for the eigenvalues of the translation operator is necessary to operate some approximations. The natural choice, in analogy to what we have done in the previous section, is to neglect derivatives of the factor $(\mathbf{q}\cdot\mathbf{k})/k^2$ in front of the oscillating exponential; as it was done in Beutler et al. (2019) and Vasudevan et al. (2019). For logarithmic oscillations, this approximation is stronger than for the linear ones, since we are neglecting the derivatives of an additional $1/k$ factor in the first term. We will refer to this prescription, which only applies to the logarithmic case, as *strong approximation*. Under this assumption, we thus have

$$\mathcal{T}_{\mathbf{q}}\left[e^{\pm i\omega_{\log}\ln(k/k_*)}\right] = e^{\pm i\omega_{\log}\frac{(\mathbf{q}\cdot\mathbf{k})}{k^2}} e^{\pm i\omega_{\log}\ln(k/k_*)}\,. \tag{6.60}$$

The effect of this approximation can be assessed with the same argument used in the calculation of eq. (6.47) for linear oscillations. In the present case we obtain

$$\begin{aligned}\mathcal{T}_{\mathbf{q}}\left[e^{\pm i\omega_{\log}\ln(k/k_*)}\right] &= \sum_{n=0}^{\infty}(\mathbf{q}\cdot\nabla_{\mathbf{k}})^{(n-1)}\left[\pm i\omega_{\log}\frac{(\mathbf{q}\cdot\mathbf{k})}{k^2}e^{\pm i\omega_{\log}\ln(k/k_*)}\right]\\ &= \sum_{n=0}^{\infty}(\mathbf{q}\cdot\nabla_{\mathbf{k}})^{(n-2)}\left\{\pm i\omega_{\log}\left[\pm i\omega_{\log}\frac{(\mathbf{q}\cdot\mathbf{k})^2}{k^4}+\frac{q^2}{k^2}-2\frac{(\mathbf{q}\cdot\mathbf{k})^2}{k^4}\right]e^{\pm i\omega_{\log}\ln(k/k_*)}\right\},\end{aligned} \tag{6.61}$$

from which it is easy to see that in this case the corrections (those coming from the derivatives of the rational factor) are of the same order in ε as the first term (those coming from the subsequent derivatives of the exponential). However, we avoid inconsistency in our approximation because, by choosing sufficiently large feature frequencies, we can distinguish these oscillations from the broadband shape of the power spectrum, such as the BAO. This choice improves the first term of eq. (6.61) with respect to the derivative corrections. To complete the analogy with the linear case, we conclude the evaluation of the damping within this approximation, leaving further comments on possible strategies to overcome this strong approximation in appendix E.

Following the steps shown in eqs. (6.49) and (6.50), we end up with the following result for the calculation of the 1-loop corrected matter power spectrum

$$\begin{aligned}\mathcal{S}P_L^{\mathrm{w}}(k) &= P_L^{\mathrm{w}}(k)\frac{k^2}{6\pi^2}\int_0^{k_{\mathrm{S}}}\mathrm{d}q\; P_L^{\mathrm{nw}}(q)\left[1-j_0\left(\frac{\omega_{\log}}{k}q\right)+2j_2\left(\frac{\omega_{\log}}{k}q\right)\right]\\ &\equiv k^2\Sigma_{\log}(k)\,P_L^{\mathrm{w}}(k)\,.\end{aligned} \tag{6.62}$$

This result is similar to the linear case except replacing $\omega_{\log}/k$ with $\omega_{\mathrm{lin}}/k_*$.[5] This result already appeared explicitly in the framework of TSPT in Vasudevan et al. (2019) and, with a slightly different formalism, in Beutler et al.

5 This is valid only under the hypothesis $q/k \ll 1$. In fact, as shown in appendix E, when this hypothesis is not strictly satisfied, one must start to take into account corrections like the one in eq. (E.15), which make impossible to map the linear case into the logarithmic one with a simple redefinition of the frequency.

(2019). Finally, it should be emphasised that, for the purpose of calculating the LO and NLO matter power spectra, it is sufficient to replace this result by eqs. (6.35) and (6.36), respectively.

6.4.1 Mixed term between baryon and primordial logarithmic oscillations

The inclusion of the mixed term for the case of logarithmic oscillation is more subtle than for the linear case because it cannot be seen as a superposition of linear waves due to the additional k dependence arising from the logarithmic term. It is useful to exploit the same idea of the linear case and write the mixed term as

$$\begin{aligned} P^{\rm w}_{\rm BAO}(k)\,\delta P^{\rm log}_{\zeta}(k) &= P^{\rm nw}_{L}(k)\,A_{\rm BAO}(k)\sin(\omega_{\rm BAO}k)A_{\log}\sin\left(\omega_{\log}\ln\frac{k}{k_*}+\varphi_{\log}\right) \\ &= \frac{1}{2}P^{\rm nw}_{L}(k)\,A_{\rm BAO}(k)A_{\log}\left\{\cos\left(\omega_{\log}\ln\frac{k}{k_*}-\omega_{\rm BAO}k+\varphi_{\log}\right)\right. \\ &\quad \left.-\cos\left(\omega_{\log}\ln\frac{k}{k_*}+\omega_{\rm BAO}k+\varphi_{\log}\right)\right\}. \end{aligned} \tag{6.63}$$

This expression does not represent a limitation to our purposes, it just leads to more cumbersome calculations. Indeed, also for this exotic oscillatory term is possible to prove that (under the same hypotheses assumed in the case of logarithmic oscillations)

$$\mathbf{q}\cdot\nabla_{\mathbf{k}}\left[e^{i\left(\omega_{\log}\ln(k/k_*)\pm\omega_{\rm BAO}k\right)}\right] = i\frac{(\mathbf{q}\cdot\mathbf{k})}{k^2}\left(\omega_{\log}\pm\omega_{\rm BAO}k\right)e^{i\left(\omega_{\log}\ln(k/k_*)\pm\omega_{\rm BAO}k\right)}. \tag{6.64}$$

To build the translation operator here, we need to specify a power counting. As a first approximation we can neglect all the k dependence that is not coming from the exponential term, thus finding

$$\mathcal{T}_{\mathbf{q}}\left[e^{i\left(\omega_{\log}\ln(k/k_*)\pm\omega_{\rm BAO}k\right)}\right] = e^{i\frac{(\mathbf{q}\cdot\mathbf{k})}{k^2}\left(\omega_{\log}\pm\omega_{\rm BAO}k\right)}e^{i\left(\omega_{\log}\ln(k/k_*)\pm\omega_{\rm BAO}k\right)}. \tag{6.65}$$

However, differently from the pure logarithmic case, we do not have only the polynomial factor in front of the exponential, but also an additional k factor in the frequency term coming from the differences between linear and logarithmic oscillations in the mixed term.

Thanks to eq. (6.65), we can compute also in this case the damping coming from the IR resummation, obtaining

$$\begin{aligned} \mathcal{S}\left[P^{\rm w}_{\rm BAO}(k)\,\delta P^{\rm log}_{\zeta}(k)\right] &= \frac{k^2}{2}A_{\rm BAO}(k)P^{\rm nw}_{L}(k)\,A_{\log} \\ &\quad\times\left[\Sigma_{\log}(k)\big|_{\omega_{\log}-\omega_{\rm BAO}k}\cos\left(\omega_{\log}\ln\frac{k}{k_*}-\omega_{\rm BAO}k+\varphi_{\log}\right)\right. \\ &\quad\left.-\Sigma_{\log}(k)\big|_{\omega_{\log}+\omega_{\rm BAO}k}\cos\left(\omega_{\log}\ln\frac{k}{k_*}+\omega_{\rm BAO}k+\varphi_{\log}\right)\right]. \end{aligned} \tag{6.66}$$

Then, from eq. (6.35), we obtain at LO

$$
\begin{aligned}
P^{\rm LO}_{\delta\delta}(\eta,k) = g^2(\eta)\Big\{ & P^{\rm nw}_L(k) + e^{-g^2(\eta)k^2\Sigma_{\rm BAO}(k)}P^{\rm w}_{\rm BAO}(k) \\
& + e^{-g^2(\eta)k^2\Sigma_{\log}(k)}P^{\rm w}_{\log}(k) + \frac{1}{2}A_{\rm BAO}(k)P^{\rm nw}_L(k)A_{\log} \\
& \times \Bigg[e^{-g^2(\eta)k^2\Sigma_{\log}(k)}\Big|_{\omega_{\log}-k\omega_{\rm BAO}} \cos\left(\omega_{\log}\ln\frac{k}{k_*} - \omega_{\rm BAO}k + \varphi_{\log}\right) \\
& - e^{-g^2(\eta)k^2\Sigma_{\log}(k)}\Big|_{\omega_{\log}+k\omega_{\rm BAO}} \cos\left(\omega_{\log}\ln\frac{k}{k_*} + \omega_{\rm BAO}k + \varphi_{\log}\right)\Bigg]\Big\}\,,
\end{aligned}
\tag{6.67}
$$

where $\Sigma_{\log}$ is defined in eq. (6.62). With the same ingredients, it is possible to compute also the NLO matter power spectrum, namely

$$
\begin{aligned}
P^{\rm NLO}_{\delta\delta}(\eta,k) = g^2(\eta)\Big\{ & P^{\rm nw}_L(k) + P^{\text{1-loop}}_{\delta\delta}\left[g^{-2}(\eta)P^{\rm LO}_{\delta\delta}(\eta,k)\right] \\
& + \left(1 + g^2(\eta)k^2\Sigma_{\rm BAO}(k)e^{-g^2(\eta)k^2\Sigma_{\rm BAO}(k)}P^{\rm w}_{\rm BAO}(k)\right) \\
& + \left(1 + g^2(\eta)k^2\Sigma_{\log}(k)e^{-g^2(\eta)k^2\Sigma_{\log}(k)}P^{\rm w}_{\log}(k)\right) \\
& + \frac{1}{2}A_{\rm BAO}(k)P^{\rm nw}_L(k)A_{\log} \\
& \qquad \times \Bigg[\left(1 + g^2(\eta)k^2\Sigma_{\log}(k)\right)e^{-g^2(\eta)k^2\Sigma_{\log}(k)}\Big|_{\omega_{\log}-k\omega_{\rm BAO}} \\
& \qquad\quad \times \cos\left(\omega_{\log}\ln\frac{k}{k_*} - \omega_{\rm BAO}k + \varphi_{\log}\right) \\
& \qquad - \left(1 + g^2(\eta)k^2\Sigma_{\log}(k)\right)e^{-g^2(\eta)k^2\Sigma_{\log}(k)}\Big|_{\omega_{\log}+k\omega_{\rm BAO}} \\
& \qquad\quad \times \cos\left(\omega_{\log}\ln\frac{k}{k_*} + \omega_{\rm BAO}k + \varphi_{\log}\right)\Bigg]\Big\}\,.
\end{aligned}
\tag{6.68}
$$

Eq. (6.67) and eq. (6.68) show the calculation of the matter power spectrum at LO and NLO, respectively, including the mixed term between baryon and primordial logarithmic oscillations, in analogy to eqs. (6.55) and (6.57). They currently represent the state of the art of this calculation. We note that it is still possible to extend this result by partially relaxing the $q \ll k$ assumption used in the derivation of eq. (6.60), as shown in Beutler et al. (2019). In appendix E we present the calculation of the mixed term that relaxes the $q \ll k$ assumption. Note that the contribution from relaxing this assumption is consistently subdominant compared to the effect of including the mixed term discussed in this section. Although the magnitude of the $q \ll k$ contribution increases as the frequency is lowered, we have checked that the cross term remains larger across the range of scales of interest for all frequencies considered. In particular, we find that the cross term is an order of magnitude larger than the $q \ll k$ corrections for $\omega \sim \mathcal{O}(100)$ and about a factor of 3 for $\omega \sim \mathcal{O}(1)$.

6.5 GAUSSIAN WAVE PACKETS

In this section, we examine both linear and logarithmic features modulated by a Gaussian distribution, using the same methodology as in the previous sections. These templates are particularly useful for assessing the effects of a scale-dependent amplitude on the description of primordial oscillatory features. This is usually the case in realistic models. The perturbations to the primordial power spectrum can be expressed as in eq. (6.39), namely

$$\delta P_\zeta^{\mathrm{WP,lin}}(k) = A_{\mathrm{lin}}^{\mathrm{WP}} \exp\left[-\frac{(k-\mu)^2}{2\Delta^2}\right] \sin\left(\omega_{\mathrm{lin}} \frac{k}{k_*} + \varphi_{\mathrm{lin}}\right), \tag{6.69}$$

and

$$\delta P_\zeta^{\mathrm{WP,log}}(k) = A_{\mathrm{log}}^{\mathrm{WP}} \exp\left[-\frac{(k-\mu)^2}{2\Delta^2}\right] \sin\left(\omega_{\mathrm{log}} \ln \frac{k}{k_*} + \varphi_{\mathrm{log}}\right), \tag{6.70}$$

for linear and logarithmic oscillations, respectively. Let us briefly comment on the structure of these equations: the first factor is the Gaussian weight, while the second is the standard oscillatory term introduced in eq. (6.39) for linear and logarithmic oscillations, respectively. Here, μ is the centre of the Gaussian envelope of the oscillations and Δ is its width.

As with other parameterisations, the initial step is to examine the effect of the translation operator, $\mathcal{T}_{\mathbf{q}}$, on the oscillatory component of the power spectrum. For a single application of the operator $\mathbf{q}\cdot\nabla_{\mathbf{k}}$, we have

$$\mathbf{q}\cdot\nabla_{\mathbf{k}}\left[e^{-\frac{(k-\mu)^2}{2\Delta^2}} e^{\pm i\omega_{\mathrm{lin}} k/k_*}\right] = i\left[\pm\frac{\omega_{\mathrm{lin}}}{k_*} + \frac{i}{\Delta^2}(k-\mu)\right]\frac{(\mathbf{q}\cdot\mathbf{k})}{k} e^{-\frac{(k-\mu)^2}{2\Delta^2}} e^{\pm i\omega_{\mathrm{lin}} k/k_*}, \tag{6.71}$$

and

$$\mathbf{q}\cdot\nabla_{\mathbf{k}}\left[e^{-\frac{(k-\mu)^2}{2\Delta^2}} e^{\pm i\omega_{\mathrm{log}} \ln(k/k_*)}\right] = i\left[\pm\omega_{\mathrm{log}} + \frac{ik}{\Delta^2}(k-\mu)\right]\frac{(\mathbf{q}\cdot\mathbf{k})}{k^2} e^{-\frac{(k-\mu)^2}{2\Delta^2}} e^{\pm i\omega_{\mathrm{log}} \ln(k/k_*)}. \tag{6.72}$$

In order to extend these relationships to n-evaluations of the operator and thereby construct the translation operator, it is necessary to establish a power counting scheme between successive applications of the derivative operator. It should be noted that while it is always possible to compute the action of n-copies of the derivative operator exactly, it is not possible to obtain a closed-form expression for their sum, as found previously for linear and logarithmic oscillations. An alternative method for evaluating the impact of this approximation would be to truncate the sum after a specified number of terms and compare it to the approximated version. This approach is analogous to that employed in sections 6.3 and 6.4, with the key distinction being that, in this case, the power counting is determined not only by the oscillation frequency but also by the amplitude of the Gaussian weights. Indeed, depending on the amplitude of the Gaussian, these corrections may render the

perturbative approach to the problem inapplicable, as they could exceed the damping effects caused by the oscillatory component. Therefore, this method is valid only within a specific range of Gaussian weight parameters. Within this approximation, we can express the translation operator as

$$\mathcal{T}_{\mathbf{q}}\left[e^{-\frac{(k-\mu)^2}{2\Delta^2}}e^{\pm i\omega_{\rm lin}k/k_*}\right] = e^{i\left[\pm\frac{\omega_{\rm lin}}{k_*}+\frac{i}{\Delta^2}(k-\mu)\right]\frac{(\mathbf{q}\cdot\mathbf{k})}{k}}e^{-\frac{(k-\mu)^2}{2\Delta^2}}e^{\pm i\omega_{\rm lin}k/k_*}\,, \tag{6.73}$$

and

$$\mathcal{T}_{\mathbf{q}}\left[e^{-\frac{(k-\mu)^2}{2\Delta^2}}e^{\pm i\omega_{\log}\ln(k/k_*)}\right] = e^{i\left[\pm\omega_{\log}+\frac{ik}{\Delta^2}(k-\mu)\right]\frac{(\mathbf{q}\cdot\mathbf{k})}{k^2}}e^{-\frac{(k-\mu)^2}{2\Delta^2}}e^{\pm i\omega_{\log}\ln(k/k_*)}\,. \tag{6.74}$$

In order to complete the computation of the 1-loop corrections to the matter power spectrum, it is sufficient to follow the steps outlined in eqs. (6.49) and (6.50). Here, however, the presence of an additional imaginary factor in the frequency results in a significant alteration to the computation. The subsequent steps are illustrated for the linear case only; the logarithmic case differs solely in terms containing the frequency, which can be reinterpreted from the linear one. In this context, the analogue of eq. (6.50) is

$$\begin{aligned}
&[1-\cosh(\mathbf{q}\cdot\nabla_{\mathbf{k}})]P^{\rm w}_{\rm WP,lin}(k) = \\
&\quad = \frac{1}{2}\left\{1-\cos\left[\left(\frac{\omega_{\rm lin}}{k_*}+\frac{ik}{\Delta^2}(k-\mu)\right)\frac{(\mathbf{q}\cdot\mathbf{k})}{k}\right]\left[\sin\left(\omega_{\rm lin}\frac{k}{k_*}\right)-i\cos\left(\omega_{\rm lin}\frac{k}{k_*}\right)\right]\right. \\
&\qquad \left.-\cos\left[\left(\frac{\omega_{\rm lin}}{k_*}-\frac{ik}{\Delta^2}(k-\mu)\right)\frac{(\mathbf{q}\cdot\mathbf{k})}{k}\right]\left[\sin\left(\omega_{\rm lin}\frac{k}{k_*}\right)+i\cos\left(\omega_{\rm lin}\frac{k}{k_*}\right)\right]\right\}e^{-\frac{(k-\mu)^2}{2\Delta^2}}\,,
\end{aligned} \tag{6.75}$$

which, by means of relationships between trigonometric and hyperbolic functions can be casted in a manifestly real expression, namely

$$\begin{aligned}
&[1-\cosh(\mathbf{q}\cdot\nabla_{\mathbf{k}})]P^{\rm w}_{\rm WP,lin}(k) = \\
&\quad = \left\{1-\cos\left[\frac{\omega_{\rm lin}}{k_*}\frac{(\mathbf{q}\cdot\mathbf{k})}{k}\right]\cosh\left[\frac{(k-\mu)}{\Delta^2}\frac{(\mathbf{q}\cdot\mathbf{k})}{k}\right]\right\}P^{\rm w}_{\rm WP,lin}(k) \\
&\qquad +\sin\left[\frac{\omega_{\rm lin}}{k_*}\frac{(\mathbf{q}\cdot\mathbf{k})}{k}\right]\sinh\left[\frac{(k-\mu)}{\Delta^2}\frac{(\mathbf{q}\cdot\mathbf{k})}{k}\right]P^{\rm w}_{\rm WP,lin}(k)\big|_{\phi+\pi/2}\,.
\end{aligned} \tag{6.76}$$

It is evident from this expression that the inclusion of a scale-dependent amplitude in the computation of the damping factor introduces an out-of-phase contribution, as seen in eq. (6.76). This result is to be expected: derivative operators induce a phase shift when acting on oscillatory functions. However, when acting on the scale-dependent amplitude, the derivative does not introduce any phase shift in the oscillatory component. This results in the emergence of two oscillatory factors that are out of phase. It is crucial to highlight that in order to compute the oscillatory component of the matter power spectrum at LO, the operator defined in eq. (6.76) must be applied multiple times. In light of the out-of-phase contribution, the application of eq. (6.76) alone is not enough. Consequently, the computation must be

repeated in order to determine how the operator acts upon the phase-shifted power spectrum. It can be demonstrated that

$$\begin{aligned}
&\left[1-\cosh(\mathbf{q}\cdot\nabla_{\mathbf{k}})\right]P^{\mathrm{w}}_{\mathrm{WP,lin}}(k)\big|_{\phi+\pi/2} = \\
&\quad=\left\{1-\cos\left[\frac{\omega_{\mathrm{lin}}}{k_*}\frac{(\mathbf{q}\cdot\mathbf{k})}{k}\right]\cosh\left[\frac{(k-\mu)}{\Delta^2}\frac{(\mathbf{q}\cdot\mathbf{k})}{k}\right]\right\}P^{\mathrm{w}}_{\mathrm{WP,lin}}(k)\big|_{\phi+\pi/2} \\
&\qquad-\sin\left[\frac{\omega_{\mathrm{lin}}}{k_*}\frac{(\mathbf{q}\cdot\mathbf{k})}{k}\right]\sinh\left[\frac{(k-\mu)}{\Delta^2}\frac{(\mathbf{q}\cdot\mathbf{k})}{k}\right]P^{\mathrm{w}}_{\mathrm{WP,lin}}(k)\,. \qquad (6.77)
\end{aligned}$$

Now, following what has been shown in appendix A.2 of Beutler et al. (2019), we find the ℓ-loop contribution to the matter power spectrum to be

$$\begin{aligned}
P^{\mathrm{w}}_{\ell-\mathrm{loop,LO}}(\eta,k) = \frac{[ikg(\eta)]^{2\ell}}{\ell!}\Bigg\{&\frac{1}{2}\left[\left(\Sigma^2_{\mathrm{lin}}(k)+i\hat{\Sigma}^2_{\mathrm{lin}}(k)\right)^{\ell}+\left(\Sigma^2_{\mathrm{lin}}(k)-i\hat{\Sigma}^2_{\mathrm{lin}}(k)\right)^{\ell}\right]P^{\mathrm{w}}_{\mathrm{WP,lin}}(k) \\
&+\frac{1}{2i}\left[\left(\Sigma^2_{\mathrm{lin}}(k)+i\hat{\Sigma}^2_{\mathrm{lin}}(k)\right)^{\ell}-\left(\Sigma^2_{\mathrm{lin}}(k)-i\hat{\Sigma}^2_{\mathrm{lin}}(k)\right)^{\ell}\right]P^{\mathrm{w}}_{\mathrm{WP,lin}}(k)\big|_{\phi+\pi/2}\Bigg\}\,. \qquad (6.78)
\end{aligned}$$

Adding together the contributions from eq. (6.78) for all ℓ, we obtain the leading-order IR-resummed wiggly power spectrum

$$\begin{aligned}
P^{\mathrm{w,LO}}_{\delta\delta}(\eta,k) = g^2(\eta)\Big\{&e^{-g^2(\eta)k^2\Sigma^{\mathrm{WP}}_{\mathrm{lin}}(k)}\cos\left[g^2(\eta)k^2\hat{\Sigma}^{\mathrm{WP}}_{\mathrm{lin}}(k)\right]P^{\mathrm{w}}_{\mathrm{WP,lin}}(k) \\
&-e^{-g^2(\eta)k^2\Sigma^{\mathrm{WP}}_{\mathrm{lin}}(k)}\sin\left[g^2(\eta)k^2\hat{\Sigma}^{\mathrm{WP}}_{\mathrm{lin}}(k)\right]P^{\mathrm{w}}_{\mathrm{WP,lin}}(k)\big|_{\phi+\pi/2}\Big\}\,, \qquad (6.79)
\end{aligned}$$

where

$$\begin{aligned}
\Sigma^{\mathrm{WP}}_{\mathrm{lin}}(k) \equiv \frac{1}{6\pi^2}\int_0^{k_{\mathrm{S}}}\mathrm{d}q\;P_{\mathrm{nw}}(q)\Bigg\{&1-\frac{3\Delta^2}{q^3\left((k-\mu)^2+\Delta^4\tilde{\omega}^2_{\mathrm{lin}}\right)^3} \\
&\times\Bigg[\Delta^2\cosh\left(\frac{q(k-\mu)}{\Delta^2}\right)\Big(-2q\cos(\tilde{\omega}_{\mathrm{lin}}q)\left((k-\mu)^4-\Delta^8\tilde{\omega}^4_{\mathrm{lin}}\right) \\
&+\tilde{\omega}_{\mathrm{lin}}\sin(\tilde{\omega}_{\mathrm{lin}}q)\left(q^2(k-\mu)^4+6(k-\mu)^2\Delta^4+q^2\Delta^8\tilde{\omega}^4_{\mathrm{lin}}\right. \\
&\left.-2\Delta^4\tilde{\omega}^2_{\mathrm{lin}}\left(\Delta^4-q^2(k-\mu)^2\right)\right)\Big) \\
&+(k-\mu)\sinh\left(\frac{q(k-\mu)}{\Delta^2}\right)\Big(-4q\Delta^4\tilde{\omega}_{\mathrm{lin}}\sin(q\tilde{\omega}_{\mathrm{lin}})\left((k-\mu)^2+\Delta^4\tilde{\omega}^2_{\mathrm{lin}}\right) \\
&+\cos(\tilde{\omega}_{\mathrm{lin}}q)\left(q^2(k-\mu)^4+2(k-\mu)^2\Delta^4+q^2\Delta^8\tilde{\omega}^4_{\mathrm{lin}}\right. \\
&\left.\left.-2\Delta^4\tilde{\omega}^2_{\mathrm{lin}}\left(3\Delta^4-q^2(k-\mu)^2\right)\right)\Big)\Bigg]\Bigg\}\,, \qquad (6.80)
\end{aligned}$$

and

$$\hat{\Sigma}^{\rm WP}_{\rm lin}(k) \equiv -\frac{1}{6\pi^2}\int_0^{k_{\rm S}} {\rm d}q\; P_{\rm nw}(q)\frac{3\Delta^2}{q^3\left((k-\mu)^2+\Delta^4\tilde{\omega}^2_{\rm lin}\right)^3}$$
$$\times\left\{(k-\mu)\cosh\left[\frac{q(k-\mu)}{\Delta^2}\right]\left[4q\Delta^4\tilde{\omega}_{\rm lin}\cos(q\tilde{\omega}_{\rm lin})\left((k-\mu)^2+\Delta^4\tilde{\omega}^2_{\rm lin}\right)\right.\right.$$
$$+\sin(\tilde{\omega}_{\rm lin}q)\left(q^2(k-\mu)^4+2(k-\mu)^2\Delta^4+q^2\Delta^8\tilde{\omega}^4_{\rm lin}\right.$$
$$\left.-2\Delta^4\tilde{\omega}^2_{\rm lin}\left(3\Delta^4-q^2(k-\mu)^2\right)\right)\Big]$$
$$-\Delta^2\sinh\left[\frac{q(k-\mu)}{\Delta^2}\right]\left[2q\sin(\tilde{\omega}_{\rm lin}q)\left((k-\mu)^4-\Delta^8\tilde{\omega}^4_{\rm lin}\right)\right.$$
$$+\tilde{\omega}_{\rm lin}\cos(\tilde{\omega}_{\rm lin}q)\left(q^2(k-\mu)^4+6(k-\mu)^2\Delta^4+q^2\Delta^8\tilde{\omega}^4_{\rm lin}\right.$$
$$\left.\left.\left.-2\Delta^4\tilde{\omega}^2_{\rm lin}\left(\Delta^4-q^2(k-\mu)^2\right)\right)\right]\right\}, \tag{6.81}$$

are the two contributions to the damping. Here we used for simplicity $\tilde{\omega}_{\rm lin} \equiv \omega_{\rm lin}/k_*$. Finally, in this case, we can include the NLO corrections in the hard loops by analogy with eq. (6.36). With minor adjustments to the procedure used in the previous case, we now find

$$P^{\rm w,NLO}_{\delta\delta}(\eta,k) = g^2(\eta)e^{-g^2(\eta)k^2\Sigma^{\rm WP}_{\rm lin}(k)}\left\{\left(1+k^2\Sigma^{\rm WP}_{\rm lin}(k)\right)\right.$$
$$\times\left[\cos\left(g^2(\eta)k^2\hat{\Sigma}^{\rm WP}_{\rm lin}(k)\right)P^{\rm w}_{\rm WP,lin}(k)\right.$$
$$\left.-\sin\left(g^2(\eta)k^2\hat{\Sigma}^{\rm WP}_{\rm lin}(k)\right)P^{\rm w}_{\rm WP,lin}(k)\big|_{\phi+\pi/2}\right]$$
$$+k^2\hat{\Sigma}^{\rm WP}_{\rm lin}(k)\left[\sin\left(g^2(\eta)k^2\hat{\Sigma}^{\rm WP}_{\rm lin}(k)\right)P^{\rm w}_{\rm WP,lin}(k)\right.$$
$$\left.\left.+\cos\left(g^2(\eta)k^2\hat{\Sigma}^{\rm WP}_{\rm lin}(k)\right)P^{\rm w}_{\rm WP,lin}(k)\big|_{\phi+\pi/2}\right]\right\}$$
$$+g^4(\eta)P^{\rm 1-loop}_{\delta\delta}\left[g^{-2}(\eta)P^{\rm LO}_{\delta\delta}(k)\right]. \tag{6.82}$$

Eq. (6.79) and eq. (6.82) hold for the LO and NLO wave packets with logarithmic oscillations, respectively. In this case the two damping factors are given by

$$\Sigma^{\rm WP}_{\rm log}(k) \equiv \frac{1}{6\pi^2}\int_0^{k_{\rm S}} {\rm d}q\; P_{\rm nw}(q)\left\{1-\frac{3k\Delta^2}{q^3\left(k^2(k-\mu)^2+\Delta^4\omega^2_{\rm log}\right)^3}\right.$$
$$\times\left[\Delta^2\cosh\left(\frac{q(k-\mu)}{\Delta^2}\right)\left(-2kq\cos\left(\omega_{\rm log}\frac{q}{k}\right)\left(k^4(k-\mu)^4-\Delta^8\omega^4_{\rm log}\right)\right.\right.$$
$$+\omega_{\rm log}\sin\left(\omega_{\rm log}\frac{q}{k}\right)\left(k^4(k-\mu)^2\left(q^2(k-\mu)^2+6\Delta^4\right)+q^2\Delta^8\omega^4_{\rm log}\right.$$
$$\left.-2k^2\Delta^4\omega^2_{\rm log}\left(\Delta^4-q^2(k-\mu)^2\right)\right)\Big)$$
$$+k(k-\mu)\sinh\left(\frac{q(k-\mu)}{\Delta^2}\right)\left(-4kq\Delta^4\omega_{\rm log}\sin\left(\omega_{\rm log}\frac{q}{k}\right)\left(k^2(k-\mu)^2+\Delta^4\omega^2_{\rm log}\right)\right.$$
$$+\cos\left(\omega_{\rm log}\frac{q}{k}\right)\left(k^4(k-\mu)^2\left(q^2(k-\mu)^2+2\Delta^4\right)+q^2\Delta^8\omega^4_{\rm log}\right.$$
$$\left.\left.\left.\left.-2k^2\Delta^4\omega^2_{\rm log}\left(3\Delta^4-q^2(k-\mu)^2\right)\right)\right)\right]\right\}, \tag{6.83}$$

and

$$\hat{\Sigma}^{\rm WP}_{\rm log}(k) \equiv -\frac{1}{6\pi^2}\int_0^{k_{\rm S}} {\rm d}q\; P_{\rm nw}(q)\frac{3k\Delta^2}{q^3\left(k^2(k-\mu)^2+\Delta^4\omega_{\rm log}^2\right)^3}$$
$$\times\left\{k(k-\mu)\cosh\left[\frac{q(k-\mu)}{\Delta^2}\right]\left[4kq\Delta^4\omega_{\rm log}\cos\left(\omega_{\rm log}\frac{q}{k}\right)\left(k^2(k-\mu)^2+\Delta^4\omega_{\rm log}^2\right)\right.\right.$$
$$+\sin\left(\omega_{\rm log}\frac{q}{k}\right)\left(k^4(k-\mu)^2\left(q^2(k-\mu)^2+2\Delta^4\right)+q^2\Delta^8\omega_{\rm log}^4\right.$$
$$\left.-2k^2\Delta^4\omega_{\rm log}^2\left(3\Delta^4-q^2(k-\mu)^2\right)\right)\Big]$$
$$-\Delta^2\sinh\left[\frac{q(k-\mu)}{\Delta^2}\right]\left[2kq\sin\left(\omega_{\rm log}\frac{q}{k}\right)\left(k^4(k-\mu)^4-\Delta^8\omega_{\rm log}^4\right)\right.$$
$$+\omega_{\rm log}\cos\left(\omega_{\rm log}\frac{q}{k}\right)\left(k^4(k-\mu)^2\left(q^2(k-\mu)^2+6\Delta^4\right)+q^2\Delta^8\omega_{\rm log}^4\right.$$
$$\left.\left.\left.-2k^2\Delta^4\omega_{\rm log}^2\left(\Delta^4-q^2(k-\mu)^2\right)\right)\right]\right\}. \tag{6.84}$$

These formulas represent the main result of this section and provide a generalisation of eqs. (6.51) and (6.62) when a scale-dependent Gaussian amplitude is introduced. In the limit of $\Delta\to\infty$, corresponding to oscillations with constant amplitude, we recover

$$\lim_{\Delta\to\infty}\Sigma^{\rm WP}_{\rm lin}(k)=\Sigma_{\rm lin}(k)\qquad\text{and}\qquad\lim_{\Delta\to\infty}\hat{\Sigma}^{\rm WP}_{\rm lin}(k)=0\,, \tag{6.85}$$

from which it is straightforward to see how eqs. (6.79) and (6.82) reduce to eqs. (6.35) and (6.36). The same behaviour occurs for logarithmic oscillations. The key parameter governing the size of the corrections to the damping, arising from the scale-dependent amplitude, is Δ. A Taylor expansion around $\Delta\to\infty$ can be used to assess the impact of these corrections on linear and logarithmic oscillations. In particular, we find

$$\Sigma^{\rm WP}_{\rm lin}(k)=\Sigma_{\rm lin}(k)+\frac{1}{\Delta^4}\delta\Sigma^{(4)}_{\rm lin}(k)+\mathcal{O}\left(\frac{1}{\Delta^8}\right), \tag{6.86}$$

$$\hat{\Sigma}^{\rm WP}_{\rm lin}(k)=\frac{1}{\Delta^2}\delta\hat{\Sigma}^{(2)}_{\rm lin}(k)+\mathcal{O}\left(\frac{1}{\Delta^6}\right). \tag{6.87}$$

The largest corrections come from the out-of-phase spectrum term. It would be useful to establish a criterion to assess the impact of corrections and to define the region of the parameter space where our methodology is valid. As emphasised throughout this work, our analysis relies on certain approximations. When these break down, the results are no longer reliable. This means that we can ignore the derivatives in eq. (6.71) if we assume that Δ is large enough. If Δ is too small, the assumption fails and the corrections are unreliable. We need to find a safe range for Δ where our formulas still work. It is difficult to establish this range based on the damping terms. It would be easier to check if this is right by looking at the LO wiggly power spectrum.

By propagating the corrections from eqs. (6.86) and (6.87) into eq. (6.79), we obtain a series expansion in Δ, with the first three terms given by

$$\Delta^0 \quad \to \quad e^{-k^2\Sigma_{\rm lin}(k)} P_L^{\rm w}(k) \tag{6.88}$$

$$\Delta^{-2} \quad \to \quad k^2 e^{-k^2\Sigma_{\rm lin}(k)} \delta\hat{\Sigma}^{(2)}_{\rm lin}(k)\, P_L^{\rm w}(k)|_{\phi+\pi/2} \tag{6.89}$$

$$\Delta^{-4} \quad \to \quad -k^2 e^{-k^2\Sigma_{\rm lin}(k)} \left[\frac{k^2}{2}\delta\hat{\Sigma}^{(2)}_{\rm lin}(k) + \delta\Sigma^{(4)}_{\rm lin}(k)\right] P_L^{\rm w}(k)\,. \tag{6.90}$$

Finally, we can compute the relative impact of the corrections to the LO power spectrum as

$$\frac{P^{\rm w,LO}_{\delta\delta}(k) - P^{\rm w,LO}_{\delta\delta}(k)\Big|_{\Delta\to\infty}}{P^{\rm w,LO}_{\delta\delta}(k)\Big|_{\Delta\to\infty}} = \frac{k^2}{\Delta^2}\delta\hat{\Sigma}^{(2)}_{\rm lin}(k)\frac{P_L^{\rm w}(k)|_{\phi+\pi/2}}{P_L^{\rm w}(k)}\,, \tag{6.91}$$

where

$$\begin{aligned}\delta\hat{\Sigma}^{(2)}_{\rm lin}(k) \equiv \frac{1}{6\pi^2}\int_0^{k_{\rm S}} {\rm d}q\; P_{\rm nw}(q)\frac{3(k-\mu)}{q^3\tilde{\omega}^4_{\rm lin}} \\ \times\left[q\tilde{\omega}_{\rm lin}\left(-6+q^2\tilde{\omega}^2_{\rm lin}\right)\cos(q\tilde{\omega}_{\rm lin}) - 3\left(-2+q^2\tilde{\omega}^2_{\rm lin}\right)\sin(q\tilde{\omega}_{\rm lin})\right]\,.\end{aligned} \tag{6.92}$$

This formula can be used to determine the range of Δ where our method is valid, given other fixed parameters. Analogous considerations hold for the case with logarithmic oscillations, with the terms arising from the corrections to the damping given by

$$\begin{aligned}\delta\hat{\Sigma}^{(2)}_{\rm log}(k) \equiv \frac{1}{6\pi^2}\int_0^{k_{\rm S}} {\rm d}q\; P_{\rm nw}(q)\frac{3k(k-\mu)}{q^3\omega^4_{\rm log}} \\ \times\left[q\omega_{\rm log}\left(-6k^2+q^2\omega^2_{\rm log}\right)\cos\left(\frac{q\omega_{\rm log}}{k}\right) + 3k\left(2k^2-q^2\omega^2_{\rm log}\right)\sin\left(\frac{q\omega_{\rm log}}{k}\right)\right]\,.\end{aligned} \tag{6.93}$$

While these equations suggest that an analytical determination could be attempted, we find that empirical validation through simulation provides the most reliable approach. We have verified that our approximations hold in all cases analysed, and extending this analysis to more general scenarios would require a dedicated study beyond our purposes. We find that for the Gaussian wave packet the calculations work well for $\Delta > 0.1$, while for lower values such as $\Delta \sim 0.01$ they only work for high frequencies such as $\omega > 10$ and $\omega > 100$ for linear and logarithmic oscillations, respectively.

6.5.1 Power-law amplitude

In this section, we study models of linear and logarithmic oscillations modulated by a power-law, scale-dependent amplitude. The motivation for this,

beyond providing a more comprehensive analysis of feature models, is that these templates allow a broader assessment of the impact of scale-dependent amplitudes, complementing the Gaussian models studied in the previous section. The two templates we intend to explore can be written as

$$\delta P_\zeta^{\rm PL,lin}(k) = A_{\rm lin}^{\rm PL}\left(\frac{k}{k_\star}\right)^n \sin\left(\omega_{\rm lin}\frac{k}{k_*}+\varphi_{\rm lin}\right), \tag{6.94}$$

and

$$\delta P_\zeta^{\rm PL,log}(k) = A_{\rm log}^{\rm PL}\left(\frac{k}{k_\star}\right)^n \sin\left(\omega_{\rm log}\ln\frac{k}{k_*}+\varphi_{\rm log}\right), \tag{6.95}$$

for linear and logarithmic oscillations, respectively.

Note the presence of two distinct pivot scales in eqs. (6.94) and (6.95) (namely $k_\star$ and k_*). The scale in the amplitude can be chosen independently of the other since, as we will see, it never enters explicitly into the computation of the damping factors. These templates are conceptually analogous to the wave packets discussed in the previous section, differing only in the function used to represent the scale-dependent amplitude. Therefore, we will not detail every step of the computation. Instead, we will proceed by drawing analogies with the main equations and focus more on general insights.

The evaluation of the translation operator can be carried out under the same assumptions discussed above eqs. (6.73) and (6.74). In particular, any model with a scale-dependent amplitude represented by a regular function will show a similar issue: applying the derivative operator within the translation operator introduces an additional scale dependence that cannot be fully addressed analytically. Typically, this dependence is weaker than that of the oscillatory factor and can be neglected within a certain range of the parameters that model the envelope. This confines the effect of the amplitude's shape to a modification in the eigenvalues of the translation operator. Specifically, for the model of interest in this section, we find

$$\mathcal{T}_{\mathbf{q}}\left[e^{n\ln(k/k_*)\pm i\omega_{\rm lin}k/k_*}\right] = e^{\left(\frac{n}{k}\pm i\frac{\omega_{\rm lin}}{k_*}\right)\frac{(\mathbf{q}\cdot\mathbf{k})}{k}} e^{n\ln(k/k_*)\pm i\omega_{\rm lin}k/k_*}, \tag{6.96}$$

and

$$\mathcal{T}_{\mathbf{q}}\left[e^{\left(n\pm i\omega_{\rm log}\right)\ln k/k_*}\right] = e^{\left(n\pm i\omega_{\rm log}\right)\frac{(\mathbf{q}\cdot\mathbf{k})}{k^2}} e^{\left(n\pm i\omega_{\rm log}\right)\ln k/k_*}. \tag{6.97}$$

This change will, of course, impact the computation of the damping factors. Whenever a non-oscillatory envelope is used, it will introduce the out-of-phase contribution discussed in the previous section due to the separation of derivatives. In such a case we need to resort again to eq. (6.79) for the computation of the damping. In this particular case we do not show all the passages leading to the final expression which can be recovered from the previous section through the substitution

$$\frac{(k-\mu)}{\Delta^2} \quad \to \quad \frac{n}{k} \tag{6.98}$$

in all the arguments of hyperbolic functions. We finally give the expression for the damping factors which are

$$\Sigma^{\rm PL}_{\rm lin}(k) \equiv \frac{1}{6\pi^2}\int_0^{k_{\rm S}} {\rm d}q\; P_{\rm nw}(q)\left\{1-\frac{3k}{q^3\left(n^2+k^2\tilde{\omega}^2_{\rm lin}\right)^3}\right.$$
$$\times\left[k\cosh\left(\frac{nq}{k}\right)\left(-2q\cos(q\tilde{\omega}_{\rm lin})\left(n^4-k^4\tilde{\omega}^4_{\rm lin}\right)\right.\right.$$
$$\left.+\tilde{\omega}_{\rm lin}\sin(q\tilde{\omega}_{\rm lin})\left(n^4q^2+k^4\tilde{\omega}^2_{\rm lin}\left(-2+q^2\tilde{\omega}^2_{\rm lin}\right)+2k^2n^2\left(3+q^2\tilde{\omega}^2_{\rm lin}\right)\right)\right)$$
$$+n\sinh\left(\frac{nq}{k}\right)\left(-4k^2q\tilde{\omega}_{\rm lin}\sin(q\tilde{\omega}_{\rm lin})\left(n^2+k^2\tilde{\omega}^2_{\rm lin}\right)\right.$$
$$\left.\left.\left.+\cos(q\tilde{\omega}_{\rm lin})\left(n^4q^2+k^4\tilde{\omega}^2_{\rm lin}\left(-6+q^2\tilde{\omega}^2_{\rm lin}\right)+2k^2n^2\left(1+q^2\tilde{\omega}^2_{\rm lin}\right)\right)\right)\right]\right\}, \tag{6.99}$$

and

$$\hat{\Sigma}^{\rm PL}_{\rm lin}(k) \equiv -\frac{1}{6\pi^2}\int_0^{k_{\rm S}} {\rm d}q\; P_{\rm nw}(q)\frac{3k}{q^3\left(n^2+k^2\tilde{\omega}^2_{\rm lin}\right)^3}$$
$$\times\left\{n\cosh\left(\frac{nq}{k}\right)\left[4k^2q\tilde{\omega}_{\rm lin}\cos(q\tilde{\omega}_{\rm lin})\left(n^2+k^2\tilde{\omega}^2_{\rm lin}\right)\right.\right.$$
$$\left.+\sin(q\tilde{\omega}_{\rm lin})\left(n^4q^2+k^4\tilde{\omega}^2_{\rm lin}\left(-6+q^2\tilde{\omega}^2_{\rm lin}\right)+2k^2n^2\left(1+q^2\tilde{\omega}^2_{\rm lin}\right)\right)\right]$$
$$-k\sinh\left(\frac{nq}{k}\right)\left[2q\sin(q\tilde{\omega}_{\rm lin})\left(n^4-k^4\tilde{\omega}^4_{\rm lin}\right)\right.$$
$$\left.\left.+\tilde{\omega}_{\rm lin}\cos(q\tilde{\omega}_{\rm lin})\left(n^4q^2+k^4\tilde{\omega}^2_{\rm lin}\left(-2+q^2\tilde{\omega}^2_{\rm lin}\right)+2k^2n^2\left(3+q^2\tilde{\omega}^2_{\rm lin}\right)\right)\right]\right\}, \tag{6.100}$$

for the linear oscillations model. Also here we used $\tilde{\omega}_{\rm lin} \equiv \omega_{\rm lin}/k_*$. Instead, for the logarithmic case we have

$$\Sigma^{\rm PL}_{\rm log}(k) \equiv \frac{1}{6\pi^2}\int_0^{k_{\rm S}} {\rm d}q\; P_{\rm nw}(q)\left\{1-\frac{3k}{q^3\left(n^2+\omega^2_{\rm log}\right)^3}\right.$$
$$\times\left[\cosh\left(\frac{nq}{k}\right)\left(-2kq\cos\left(\omega_{\rm log}\frac{q}{k}\right)\left(n^4-\omega^4_{\rm log}\right)\right.\right.$$
$$\left.+\omega_{\rm log}\sin\left(\omega_{\rm log}\frac{q}{k}\right)\left(k^2\left(6n^2-2\omega^2_{\rm log}\right)+q^2\left(n^2+\omega^2_{\rm log}\right)^2\right)\right)$$
$$+n\sinh\left(\frac{nq}{k}\right)\left(-4kq\omega_{\rm log}\sin\left(\omega_{\rm log}\frac{q}{k}\right)\left(n^2+\omega^2_{\rm log}\right)\right.$$
$$\left.\left.\left.+\cos\left(\omega_{\rm log}\frac{q}{k}\right)\left(2k^2\left(n^2-3\omega^2_{\rm log}\right)+q^2\left(n^2+\omega^2_{\rm log}\right)^2\right)\right)\right]\right\}, \tag{6.101}$$

and

$$\hat{\Sigma}^{\rm PL}_{\rm log}(k) \equiv -\frac{1}{6\pi^2}\int_0^{k_{\rm S}} {\rm d}q\; P_{\rm nw}(q)\frac{3k}{q^3\left(n^2+\omega_{\rm log}^2\right)^3}$$
$$\times\Big[n\cosh\Big(\frac{nq}{k}\Big)\Big(4kq\omega_{\rm log}\cos\Big(\omega_{\rm log}\frac{q}{k}\Big)\left(n^2+\omega_{\rm log}^2\right)$$
$$+\sin\Big(\omega_{\rm log}\frac{q}{k}\Big)\left(2k^2\left(n^2-3\omega_{\rm log}^2\right)+q^2\left(n^2+\omega_{\rm log}^2\right)^2\right)\Big)$$
$$-\sinh\Big(\frac{nq}{k}\Big)\Big(2kq\sin\Big(\omega_{\rm log}\frac{q}{k}\Big)\left(n^4-\omega_{\rm log}^4\right)$$
$$+\omega_{\rm log}\cos\Big(\omega_{\rm log}\frac{q}{k}\Big)\left(k^2(6n^2-2\omega_{\rm log})+q^2\left(n^2+\omega_{\rm log}^2\right)^2\right)\Big)\Big]\,. \tag{6.102}$$

Finally, these new sets of damping factors, evaluated for the case of the power-law envelope, can be used in combination to eqs. (6.79) and (6.82) to obtain the nonlinear matter power spectra at LO and NLO, respectively.

6.6 COSMOLOGICAL SIMULATIONS

To quantify the accuracy of the analytic templates based on perturbation theory of the dark matter clustering in the nonlinear regime, we produce sets of large-scale N-body simulations. In particular, we explore the following primordial features models:

LIN with $\mathcal{A}_{\rm lin}=0.1$, $\log_{10}(\omega_{\rm lin})=[0.6,1.0,1.4,1.8]$, and $\varphi_{\rm lin}=0$;

LOG with $\mathcal{A}_{\rm log}=0.1$, $\log_{10}(\omega_{\rm log})=[0.6,1.0,1.4,1.8]$, and $\varphi_{\rm log}=0$;

WPLIN with $\mathcal{A}_{\rm lin}=0.1$, $\mu=[0.1,0.3]$, $\Delta=[0.01,0.1]$, $\log_{10}(\omega_{\rm lin})=[0.8,1.4]$, and $\varphi_{\rm lin}=0$;

WPLOG with $\mathcal{A}_{\rm log}=0.1$, $\mu=[0.1,0.3]$, $\Delta=[0.01,0.1]$, $\log_{10}(\omega_{\rm log})=[0.8,1.4]$, and $\varphi_{\rm log}=0$;

PLLIN with $\mathcal{A}_{\rm lin}=0.1$, $n=[-0.5,0.5]$, $\log_{10}(\omega_{\rm lin})=[0.8,1.4]$, and $\varphi_{\rm lin}=0$;

PLLOG $\mathcal{A}_{\rm log}=0.1$, $n=0.5$, $\log_{10}(\omega_{\rm log})=[0.8,1.4]$, and $\varphi_{\rm log}=0$.

Here μ and Δ have the dimension of $h\,{\rm Mpc}^{-1}$ while n is a dimensionless number. We consider an amplitude for the primordial features $\mathcal{A}_{\rm X}=0.1$ larger compared to the one allowed by current constraints for most of the template considered here, see Akrami et al. (2020), Ballardini and Finelli (2022), and Beutler et al. (2019). We fix the value of the standard cosmological parameters to [Aghanim et al., 2020c]

$$\Omega_{\rm m}=0.31377,\;\Omega_{\rm b}=0.04930,\;h=0.6736,\;\sigma_8=0.8107,\;n_{\rm s}=0.9649\,. \tag{6.103}$$

The value of σ_8 corresponds to the value for a flat ΛCDM cosmological model with one massive neutrinos with minimal mass of 60 meV with $\ln\left(10^{10}A_s\right) = 3.044$. Note that high frequency oscillations are averaged to zero and do not modify the value of σ_8. Vice versa, cases with a low frequency modify σ_8 with respect the ΛCDM model. We keep it fixed to make the comparison on small scales clearer.

The simulations produced in this study make use of the `COLA` (COmoving Lagrangian Acceleration) method [Tassev et al., 2015; 2013; Winther et al., 2017; Wright et al., 2017], an approximate N-body method alternative to full N-body simulations that combines second-order Lagrangian Perturbation Theory (2LPT) with a Particle-Mesh (PM) algorithm. The main advantage of this hybrid approach is its ability to efficiently evolve large-scale and intermediate-scale structures using 2LPT, while the PM algorithm handles the small-scale evolution. This combination allows for a significant reduction in the number of time-steps required compared to conventional N-body simulations, without compromising the accuracy of the large-scale dynamics.

In traditional N-body simulations, particle positions and velocities are updated using the equations of motion

$$\frac{\mathrm{d}\mathbf{x}}{\mathrm{d}t} = \mathbf{v}\,, \tag{6.104a}$$

$$\frac{\mathrm{d}\mathbf{v}}{\mathrm{d}t} = -\nabla\Phi\,, \tag{6.104b}$$

where $\mathbf{x}$ and $\mathbf{v}$ represent the position and velocity of a particle, and Φ is the gravitational potential. In the COLA framework, the particle displacement is expressed as $\mathbf{x}_{\mathrm{COLA}} = \mathbf{x} - \mathbf{x}_{\mathrm{LPT}}$, where $\mathbf{x}_{\mathrm{LPT}}$ denotes the trajectory determined by 2LPT. Consequently, the equations of motion are modified to

$$\frac{\mathrm{d}\mathbf{x}}{\mathrm{d}t} = \mathbf{v}_{\mathrm{COLA}} + \frac{\mathrm{d}\mathbf{x}_{\mathrm{LPT}}}{\mathrm{d}t}\,, \tag{6.105a}$$

$$\frac{\mathrm{d}\mathbf{v}_{\mathrm{COLA}}}{\mathrm{d}t} = -\nabla\Phi - \frac{\mathrm{d}^2\mathbf{x}_{\mathrm{LPT}}}{\mathrm{d}t^2}\,, \tag{6.105b}$$

where the variables $\mathbf{x}$ and $\mathbf{v}_{\mathrm{COLA}}$ are evolved over time. At the start of the simulation $\mathbf{v}_{\mathrm{COLA}} = 0$, ensuring that the particle trajectories closely follow the LPT evolution on large scales. This method effectively functions as a Particle-Mesh N-body code in the COLA frame, binding particles to LPT trajectories at large scales.

COLA-based simulations, as well as full N-body ones, have been already used to study the nonlinear dynamics in the presence of primordial features in Ballardini et al. (2024), Ballardini and Finelli (2022), Ballardini et al. (2020), Chen et al. (2020), and Li et al. (2022).

6.6.1 Simulation settings

We executed COLA simulations using a modified version of the publicly available code `L-PICOLA` [Howlett et al., 2015][6] evolving 2048 particles in a simulation box of $(2048\,h^{-1}\,\mathrm{Mpc})^3$ and a mesh grid of $N_{\mathrm{mesh}} = 1024$.

All simulations commenced from an initial redshift of $z_{\mathrm{ini}} = 9$ using 2LPT to generate the initial displacement fields, ensuring that transient effects from initial conditions are minimized. The simulations were performed with 50 time-steps across five redshift intervals, each with a time resolution of $\Delta a \approx 0.02$, with 10 time-steps for each of the following interval $9 \geq z > 2$, $2 \geq z > 1.5$, $1.5 \geq z > 1$, $1 \geq z > 0.5$, and $0.5 \geq z > 0$.

To suppress the undersamples large modes, due to the finite volume of the simulations, we use spectra averaged over pairs of simulations with the same initial seeds and inverted initial conditions, and with amplitude fixing in order to minimise the cosmic variance [Viel et al., 2010; Villaescusa-Navarro et al., 2018]. Finally, we generate 5 realisations with different initial seed for each pairs of cosmological model studied.

6.6.2 Comparing predictions of perturbation theory with N-body simulations

In this section, we present a comparison between the results from TSPT and N-body simulations for the nonlinear matter power spectrum at redshift $z = 0$. We analyse all six different types of primordial feature modelled, with linear and logarithmic oscillations and with constant and scale-dependent amplitudes.[7]

In fig. 6.1 we show the comparison for primordial linear oscillations with constant amplitude, focusing on the results at NLO. At LO, differences between TSPT spectra and N-body simulations are reduced and closer to the NLO results by choosing the separation scale $k_{\mathrm{S}} = 0.2\,h\,\mathrm{Mpc}^{-1}$; see in Ballardini et al. (2024) and Ballardini et al. (2020) for a comparison between LO and NLO with a wider range of values for k_{S}. At NLO, however, the comparison improves and the dependence on the separation scale k_{S} is minimal. This suggests that higher-order corrections are critical to accurately capture the nonlinear behaviour, especially at smaller scales where nonlinear damping becomes important. A comparable trend is observed when logarithmic oscillations are taken into account, as shown in fig. 6.2. However, for both LO and NLO, discrepancies with N-body simulations are more pronounced, particularly for low primordial frequencies such as $\log_{10}(\omega_{\log}) = 0.6$, as already pointed out in Ballardini et al. (2024), Ballardini et al. (2020), Beutler et al. (2019), and Vasudevan et al. (2019). This is due to the different correlation length in real space between linear and logarithmic oscillations, from $\omega_{\mathrm{lin}}/k_*$

6 https://github.com/CullanHowlett/l-picola, https://github.com/HAWinther/MG-PICOLA-PUBLIC

7 We used `FastPT` Fang et al., 2017; McEwen et al., 2016 to compute the 1-loop power spectrum; https://github.com/JoeMcEwen/FAST-PT.

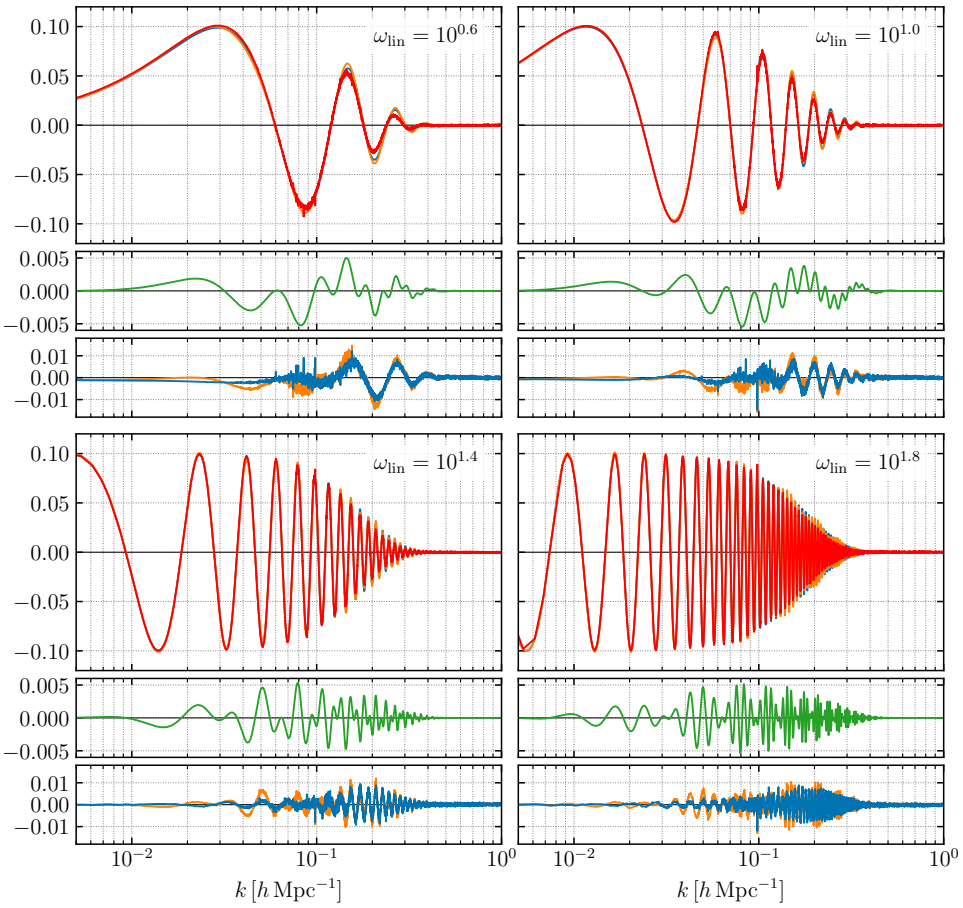

Figure 6.1: In each of the the four panels we show: the relative differences between the matter power spectra computed for a model with primordial linear oscillations and the one with power-law PPS divided by the non-wiggly power spectrum with (orange line) and without (blue line) the mixed term at NLO and the one obtained from the N-body simulations (red line), the relative differences of the NLO matter power spectrum with mixed term to that without (green line), and the differences between the theoretical spectra at NLO, with (orange line) and without (blue line) the mixed term, and the simulations. All the matter power spectra are computed at redshift $z = 0$.

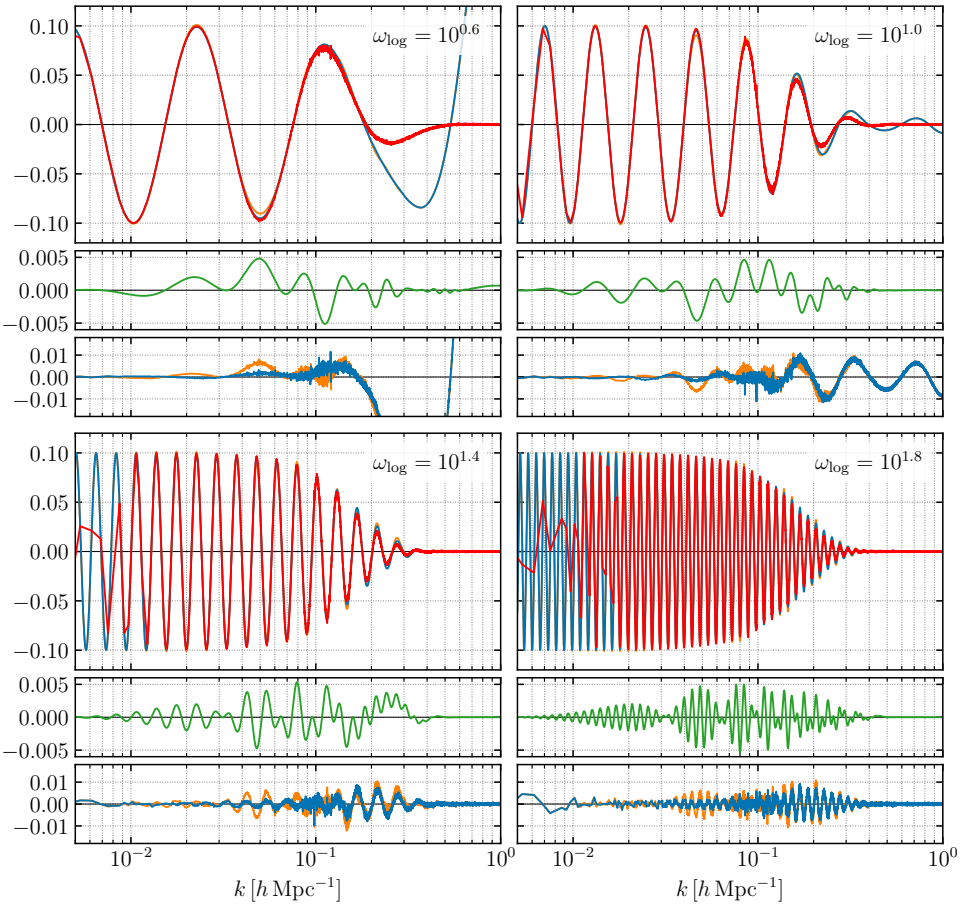

Figure 6.2: As in fig. 6.1 for the primordial logarithmic oscillations.

to $\omega_{\log}/k$. The TSPT results at NLO are in agreement with the findings of the simulations for both linear and logarithmic oscillations with constant amplitude, with discrepancies of less than 1% observed, with the exception of the logarithmic model at the lower frequency.

We explore the addition of nonlinear modelling of the mixed term between baryon and primordial oscillations, neglected in previous studies, to further refine the TSPT predictions. Given the relative small amplitude of this term, with the amplitude of the BAO feature accounting for approximately 7% of the total matter power spectrum and the amplitude of the primordial features expected to be less than 10% depending on the specific model, the effect is almost undetectable when compared to the simulation results; see figs. 6.1 and 6.2.

Furthermore, in addition to the oscillatory models with constant amplitude, we present the comparison with N-body simulations for the wave-packet and power-law models, see figs. 6.3 to 6.5. These scale-dependent amplitudes, which are closer to the expected primordial features produced by exact models, result in distinctive signatures within the matter power spectrum. In this case, the TSPT predictions show reasonable agreement with simulations at larger scales, but the inclusion of NLO corrections is crucial to improve accuracy over a wider range of scales. The results demonstrate the efficacy of TSPT in capturing the physics of primordial features, particularly when higher-order terms are considered.

For all models considered, the power spectrum at $z = 0$ shows that nonlinearities on small scales tend to wash out the primordial oscillations, especially at wavenumbers beyond $k = 0.3\,h\,\mathrm{Mpc}^{-1}$. In summary, the comparison between TSPT and N-body simulations shows that NLO corrections significantly improve the agreement for both linear and logarithmic oscillations, as well as for the scale-dependent amplitude case. This highlights the importance of going beyond the LO to capture the complexity of nonlinear structure formation, especially when studying primordial features in the matter power spectrum, in order to reduce the theoretical uncertainties arising from the modelling of nonlinear damping.

It should be noted that the discrepancies observed at large scales, particularly for logarithmically-spaced high frequencies, are numerical artefacts resulting from the finite number of samples from the nonlinear matter power spectrum of the N-body simulations. These discrepancies have no impact on the conclusions drawn in this study.

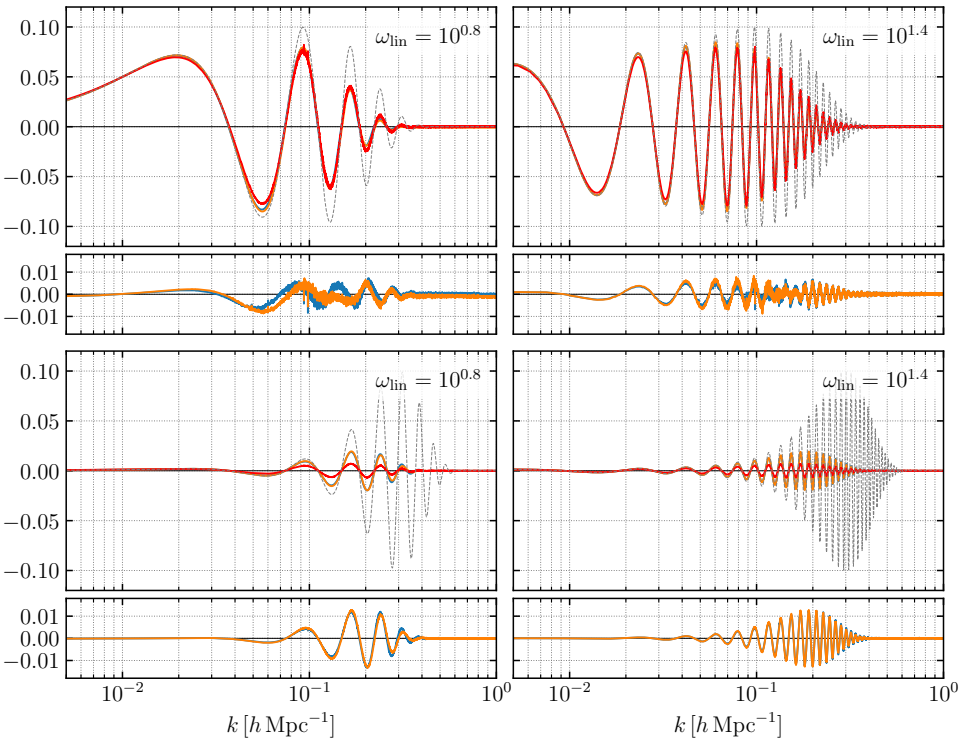

Figure 6.3: In each of the the four panels we show: in the upper subpanel the relative differences between the matter power spectra computed for a model with primordial linear oscillations, with Gaussian amplitude, and the one with power-law PPS divided by the non-wiggly power spectrum at NLO (orange line) and LO (blue line), for the simulations (red line) and for the linear theory (dashed grey line), and in the lower subpanel the relative differences between the theoretical spectra, at NLO (orange line) and LO (blue line), and the N-body simulations. The two upper panels correspond to $\mu = 0.1\,h\,{\rm Mpc}^{-1}$ while the lower ones to $\mu = 0.3\,h\,{\rm Mpc}^{-1}$; here we always assume $\Delta = 0.1\,h\,{\rm Mpc}^{-1}$. All the matter power spectra are computed at redshift $z = 0$.

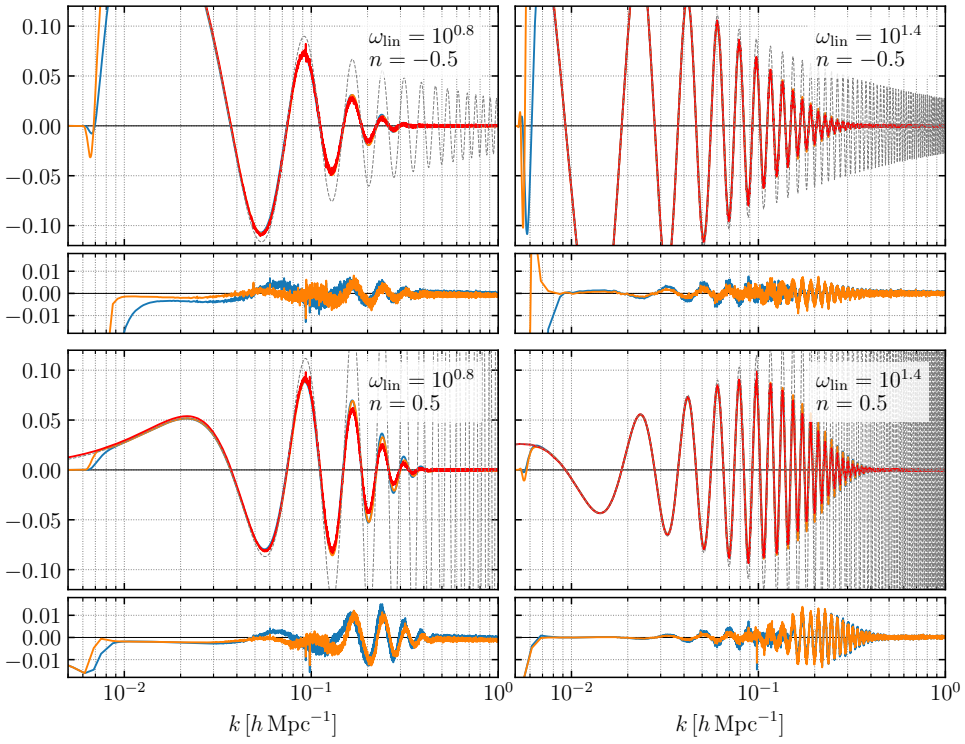

Figure 6.4: As in fig. 6.3 for the primordial linear oscillations with power-law amplitude with $n = \pm 0.5$, $k_\star = 0.05\,{\rm Mpc}^{-1}$, and $\log_{10}\left(\omega_{\log}\right) = 0.8, 1.4$.

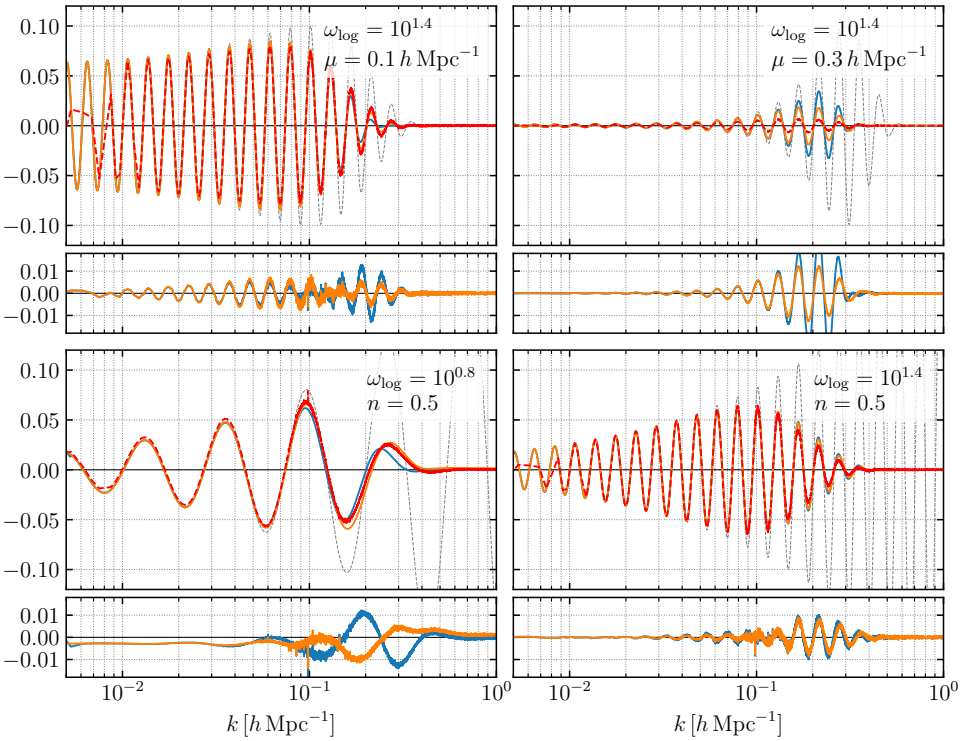

Figure 6.5: In each of the the four panels we show: in the upper subpanel the relative differences between the matter power spectra computed for a model with primordial logarithmic oscillations, with power-law amplitude, and the one with power-law PPS divided by the non-wiggly power spectrum at NLO (orange line) and LO (blue line), for the simulations (red line) and for the linear theory (dashed grey line), and in the lower subpanel the differences between the theoretical spectra, at NLO (orange line) and LO (blue line), and the simulations. The two upper panels correspond to the case with Gaussian wave-packet amplitude with $\log_{10}\left(\omega_{\log}\right) = 1.4$, $\Delta = 0.1\,h\,\mathrm{Mpc}^{-1}$, and $\mu = 0.1\,(0.3)\,h\,\mathrm{Mpc}^{-1}$ on the left (right). The two lower panels correspond to the power-law amplitude with $n = 0.5$, $k_\star = 0.1\,\mathrm{Mpc}^{-1}$, and $\log_{10}\left(\omega_{\log}\right) = 0.8\ (1.4)$ and the left (right). All the matter power spectra are computed at redshift $z = 0$.

CONCLUSIONS

The central purpose of this thesis has been to investigate the interplay between cosmological observations and particle physics, with a particular focus on the role of neutrinos and the imprints of early–Universe dynamics on observables. Through a detailed study of non–standard neutrino properties, low–reheating scenarios, and primordial features in the power spectrum, this work provides all–round new insights into Beyond the Standard Model (BSM) physics. The thesis combines theoretical modeling, analytical techniques, and numerical simulations to address key questions about the evolution of the Universe, such as the generation of neutrino masses, the properties of reheating, and the impact of inflationary physics on Large–Scale Structure (LSS) formation. These contributions are designed to interpret and maximize the scientific return from upcoming high–precision cosmological data, offering robust tools and predictions to probe the Universe's fundamental physics.

We started, in chapter 1, by providing a pedagogical description of the standard cosmological model, focusing on details and tools related to its thermal history, which are of central importance for the subsequent developments within this work. Then, in chapter 2, we turned our attention to the main historical and current puzzling aspects that have motivated the strong demand for new physics, as well as some of the extensions studied within this thesis.

Subsequent chapters contain the original work of this thesis.

In chapter 3, we studied the possibility of placing cosmological constraints on the reheating temperature. We considered some models, called low reheating models, in which reheating occurs for temperatures $T_{\rm RH} < 20\,\text{MeV}$. Assuming the massive scalar field that dominates the energy density decays exclusively into electromagnetic particles, neutrinos are populated only via weak interactions with charged leptons. Therefore, neutrinos can achieve thermal equilibrium with the rest of the plasma only if the scalar decays occur sufficiently early. For sufficiently low reheating temperatures, neutrinos are produced with non–thermal distributions, which we proved to have a deep impact on Big Bang Nucleosynthesis (BBN) and Cosmic Microwave Background (CMB) physics. Specifically, concerning BBN, we found that the energy density of all neutrino states contributes to both the Hubble expansion rate and the continuity equation for the radiation energy density, while the energy distribution of electron neutrinos directly affects the Charged–Current (CC) weak rates that govern neutron–proton chemical equilibrium. In the case of CMB, the main effect is the reduction of neutrino energy density, with consequent modifications to the expansion history before recombination.

We successfully computed non–thermal neutrino distribution functions with a properly modified version of the `FortEPiaNO` code, ensuring our computations align with the state–of–the–art in neutrino decoupling. Then, we performed a Bayesian analysis on the latest light element abundance data [Workman et al., 2022], the most recent CMB temperature and polarization anisotropy data from the Planck collaboration with lensing reconstruction [Aghanim et al., 2020c; d], and geometric information from Baryon Acoustic Oscillations (BAO) measurements from BOSS/eBOSS and DESI surveys. The analysis was carried out using properly modified versions of the `PArthENoPE` , `MontePython`, and `CLASS` codes, alongside a new methodology shown to allow a more efficient exploration of the parameter space of these models. Our main result is represented by the lower bounds on the reheating temperatures on the full benchmark data set Planck+lensing+DESI: $T_{\rm RH} > 6.75\,\text{MeV}$ when sampling on $T_{\rm RH}$ and $T_{\rm RH} > 5.85\,\text{MeV}$ when sampling on $N_{\rm eff}^{FP}$ (see section 3.5.3 for details).

Finally, let us mention that our results are also important for scenarios with additional relativistic particles, whose contribution to the radiation energy density could be reduced for very low values of $T_{\rm RH}$. In particular, when light sterile neutrinos exist with non-zero mixing with the active states, low reheating temperatures could relax the tight cosmological bounds in the standard ΛCDM model [Abazajian, 2017; Gelmini et al., 2019; Gelmini et al., 2008; 2004; Hasegawa et al., 2020; Yaguna, 2007]. The study of this follow-up possibility is part of a project currently under development.

In chapter 4, we studied the optical activity induced by Non–Standard Interactions (NSI) interactions in the neutrino sector. We focused our attention on a phenomenological model with couplings motivated by neutrino mass generation. The additional coupling to photons was then required to ensure some degree of optical activity. We handled the problem using the formalism of Quantum Boltzmann Equation (QBE). The application of this tool, originally developed for the study of neutrino oscillations, allowed us to separately follow the different polarization states of a photon throughout its propagation in a medium. The application to CMB photons allowed us to obtain theoretical predictions that can be constrained using the latest data on CMB polarization anisotropies.

We studied both the forward scattering (tree–level + 1–loop corrections) and collision terms (tree–level) of the QBE. Our work includes the full procedure for the reduction of the collision integrals. The main results are represented by Boltzmann equations for the Stokes parameters of linear polarization in the two limiting cases of Light Mediator Limit (LML), eq. (4.123), and Heavy Mediator Limit (HML), eq. (4.125). A further qualitative study of these equations shows how they provide two main effects: a correction to the photon visibility function and a variation of the linear polarization angle of the CMB, i.e., cosmic birefringence. Thanks to current measurements, it is then possible to place constraints on the couplings of our model.

This study demonstrated how fundamental parameters like couplings can be directly linked to CMB observables to obtain bounds and study phenomenology without relying on effective descriptions. However, our final qualitative analysis shows that bounds derived from these effects are not competitive with those from other searches in the case of this specific model. A natural follow-up would be to study different types of interactions. Particular interest has been shown toward the case of neutrinos with electromagnetic properties [Bartolo et al., 2019; Giunti et al., 2024; Khodagholizadeh et al., 2023], which we are currently exploring in the first stages of development.

In chapter 5, we analyzed the impact of neutrino self–interactions on cosmological observables, focusing on constraints derived from the latest Atacama Cosmology Telescope (ACT) DR6 simulated data combined with other cosmological probes. Two scenarios were considered: a massless mediator model and a heavy mediator model, each with distinct effects on neutrino dynamics and their imprints on the CMB power spectra and matter power spectrum. Using modified versions of the Boltzmann solver `CAMB`, we implemented the effects of neutrino self–interactions in the equations governing cosmological perturbations.

In the massless mediator case, neutrino–neutrino scattering was parametrized using an effective coupling constant $g_{\rm eff}$, which impacts the free–streaming nature of neutrinos and modifies the anisotropic stress and photon perturbations. The most stringent constraint on $g_{\rm eff}$ was found to be $g_{\rm eff}^4 < 1.17 \times 10^{-27}$ (95%, P-ACT-LB) achieving upper bound competitive with existing constraints. For the heavy mediator model, the self–interaction strength was expressed in terms of $G_{\rm eff}$, and modifications to the Boltzmann hierarchy were implemented to account for the collisional regime of neutrinos at early times. The analysis revealed a bimodal posterior distribution for $G_{\rm eff}$ (see fig. 5.9), corresponding to moderately and strongly interacting neutrino scenarios. Separate parameter estimations for these two regions provided constraints on the interaction strength whose, however, a more precise determination is left for the full data analysis because of subtleties in the statistical procedure.

This work demonstrates the sensitivity of CMB and LSS data to neutrino self–interactions, highlighting the role of advanced instruments like ACT in probing new physics. Forecasts derived from ACT DR6 simulated data consistently improve previous results. Combination with complementary datasets also indicate potential preference for non–zero interactions in certain regions of parameter space. Future analysis on real data could further refine these predictions and better explore the implications of neutrino self–interactions in the broader context of cosmology.

In chapter 6, we presented a comprehensive analysis of the impact of primordial oscillatory features on the matter power spectrum within the framework of Time–Slice Perturbation Theory (TSPT). Our results extend previous studies by including a detailed treatment of the nonlinear evolution

of these features, providing new analytical insights into their behavior at different scales, and comparing these predictions with results from N–body simulations using the COLA method. We derived new contributions to the nonlinear matter power spectrum, particularly the mixed term between primordial oscillations and BAO, as well as corrections arising from a scale–dependent envelope modulating the oscillation patterns. These corrections, although small, represent an important refinement of current theoretical models, bringing us closer to a full characterization of the nonlinear imprints of primordial features.

The inclusion of IR resummation techniques, as implemented in TSPT, proved essential for handling long–wavelength perturbations that significantly affect the power spectrum, especially in the presence of oscillatory features. The good agreement between our analytical results and N–body simulations underlines the robustness of the formalism and highlights the importance of using such perturbative techniques for future analyses of primordial features. It has been shown that, in both the cases of linear and logarithmic oscillatory features, contributions arise from small–scale inhomogeneities in the nonlinear region of the power spectrum [Baumann et al., 2017; Beutler et al., 2019]. Corrections due to the mixed term do not spoil the argument used to prove this statement, which still holds without additional issues. However, when considering scale–dependent amplitudes, additional scales (such as the amplitude of the Gaussian shape in our GAUSSLIN and GAUSSLOG models) enter the discussion. We found that when these scales become too small, the power counting developed between derivatives of the oscillatory template breaks down, making the computation unstable and unreliable. These additional constraints on the allowed parameter space can be derived through eq. (6.91) or analogous.

Our results are relevant for upcoming LSS surveys, such as DESI [Adame et al., 2024b] and *Euclid* [Ballardini et al., 2024; Mellier et al., 2024], which are expected to provide more precise measurements of the matter power spectrum at small scales, potentially revealing subtle signatures of new physics in the early Universe. By considering the nonlinear regime of structure formation, our analysis provides an improved theoretical framework for interpreting these future data.

Part IV

APPENDICES

A THE KULLBACK-LEIBLER DIVERGENCE

In this appendix, we aim to revisit some concepts related to the notion of relative entropy, or Kullback–Leibler (KL) divergence, $D_{\mathrm{KL}}(P \parallel Q)$. We recall that this tool has been used in section 3.5.3 to asses the impact of different priors on the reheating temperature when sampling extended $\Lambda\mathrm{CDM} + T_{\mathrm{RH}}$ models.

A.1 FORMAL DEFINITION AND PROPERTIES

In its most general formulation, the KL divergence between two probability distributions $P(x)$ and $Q(x)$, on the same sample space $\mathcal{X}$, can be defined as [MacKay, 2002]

$$D_{\mathrm{KL}}(P \parallel Q) \equiv \sum_{x \in \mathcal{X}} P(x) \log\left[\frac{P(x)}{Q(x)}\right] . \tag{A.1}$$

In other words, it is the expected value of the logarithmic difference (or Shannon information [Shannon and Weaver, 1949]) between the probabilities P and Q, where the expectation is calculated with respect to the probabilities P. In particular, it quantifies the information loss when approximating one distribution with another. For continuous distributions, the definition can be repurposed as

$$D_{\mathrm{KL}}(P \parallel Q) = \int_{-\infty}^{\infty} dx\, P(x) \log\left[\frac{P(x)}{Q(x)}\right] . \tag{A.2}$$

Let us notice that, even if we referred to the KL divergence as a "distance", it is not truly a metric in the sense of mathematics, which is the most familiar and formal way to introduce a notion of distance in a given space. This can be easily deduced from the definition of Eq. (A.2), which is not symmetric in the two distributions and does not satisfy the triangle inequality. Rather, it is called a divergence in the sense of information geometry. Divergences can be viewed as generalizations of the squared Euclidean distance; in particular, given a differentiable manifold M of dimension n (typically the space of parameters of a family of PDFs), a divergence on M is a C^2-function $D : M \times M \to [0, \infty)$ satisfying the following properties

1. $D(p, q) \geq 0$ for all $p, q \in M$ (non-negativity or Gibb's inequality),
2. $D(p, q) = 0$ if and only if $p = q$ (positivity),

3. For every point $p \in M$, $D(p, p+dp)$ is a positive-definite quadratic form for any infinitesimal displacement dp from p.

Unlike metrics, divergences are not required to be symmetric, and this asymmetry is important in practical applications. Consequently, divergences are often referred to asymmetrically as the divergence "of q from p" or "from p to q", rather than simply "between p and q" as it happens for the metrics. This is reflected by the introduction of the concept of dual divergence, $D^*(p,q) \equiv D(q,p)$. Moreover, as divergences generalize squared distances, and not linear distances, they do not satisfy the triangle inequality. On the contrary, in some cases, like that of the KL divergence, they satisfy a generalized Pythagorean theorem, which allow them to be minimized through geometric tools.

A.2 APPLICATION TO BAYESIAN ANALYSIS

In cosmology, Bayesian inference is frequently employed to extract information from observational data, often involving high-dimensional parameter spaces. Here, KL divergence is particularly useful in the context of comparing different posterior distributions or priors [Gariazzo et al., 2022b; Handley and Lemos, 2019]. When conducting Bayesian analysis, the choice of priors can significantly impact the results. The KL divergence can quantify the difference between the prior, $\Pi(\theta)$, and posterior, $\mathcal{P}(\theta \mid D)$, distributions,

$$D_{\mathrm{KL}}(\mathcal{P}(\theta \mid D) \parallel \Pi(\theta)) = \int d\theta\, \mathcal{P}(\theta \mid D) \log\left[\frac{\mathcal{P}(\theta \mid D)}{\Pi(\theta)}\right], \tag{A.3}$$

where θ represents the parameters vector and D the data. This divergence measures the information gain provided by the data D in updating the prior to the posterior, often referred to as the Bayesian surprise. A higher KL divergence indicates that the data significantly alters our prior knowledge, making this tool valuable in evaluating the effectiveness of different priors. The KL can also be used in Bayesian model comparison and averaging. In the former case one can compute the KL divergence between posterior distributions corresponding to different models, providing insights into how distinguishable the models are given the data. In the latter case the KL divergence it is used to determine the relative weight of different models to the final averaged prediction.

The KL divergence, the Bayesian evidence Z and the mean log-likelihood,

$$\langle \log \mathcal{L} \rangle_{\mathcal{P}} \equiv \int d\theta\, \mathcal{P} \log \mathcal{L}\,, \tag{A.4}$$

are closely connected through the following relationship [Gariazzo et al., 2022b; Hergt et al., 2021]

$$\log Z = \langle \ln \mathcal{L} \rangle_P - D_{\mathrm{KL}}\,. \tag{A.5}$$

From this relation we can obtain insights on the meaning of the KL divergence thanks to what we know about the Bayesian evidence. In Bayesian inference, this quantity is used to the purpose of model comparison to go further the simple criterion of quality of fit to choose the most realistic among different models. The key feature is the addition of a penalty based on the number of parameters of a given model, preventing the possibility of over-fitting the data with a real increase in the quality of the fit. These two terns in the right-hand side of Eq. (A.5) represent exactly these two effects: the first term represents the average goodness-of-fit of the model, while the second one reflects, in a general sense, the extent to which the prior volume has been "contracted" after incorporating the data, what it is usually referred as the "Occam penalty". To go deeper with this interpretation we can recall the definition of Bayesian evidence as

$$Z \equiv \langle \mathcal{L} \rangle_{\Pi} = \int d\theta \; \mathcal{L}(\theta)\Pi(\theta) \; , \tag{A.6}$$

namely the average likelihood over the prior. It is thus easy now to notice the analogy between $\log Z$ and the first term on the right-hand side of Eq. (A.5). To get a fair comparison between these two quantities we can resort to the Jensen's inequality, which allow us to write [Gariazzo et al., 2022b]

$$D_{\mathrm{KL}} = \langle \log \mathcal{L} \rangle_{\mathcal{P}} - \log \langle \mathcal{L} \rangle_{\Pi} \leq \langle \log \mathcal{L} \rangle_{\mathcal{P}} - \langle \log \mathcal{L} \rangle_{\Pi} \; , \tag{A.7}$$

leading us to the interpretation of the KL divergence as a minimum threshold on the improvement in the expected goodness-of-fit when moving from the prior to the posterior.

B COMPUTATION OF THE FEYNMAN RULES

B.1 NEUTRINO–PSEUDOSCALAR COUPLING

The 1st order term in the S–matrix expansion related to this vertex can be written as

$$\begin{aligned} S^{(1)}_{\nu\phi} &= -i\int d^4x\, \mathcal{T}\left\{\mathcal{H}_{\nu\phi}(x)\right\} = i\int d^4x\, \mathcal{T}\left\{\mathcal{L}_{\nu\phi}(x)\right\} \\ &= i\int d^4x\, \mathrm{N}\left[-ig_{\nu\nu\phi}\bar{\nu}(x)\gamma_5\nu(x)\phi(x)\right] \\ &= g_{\nu\nu\phi}\int d^4x\, \mathrm{N}\left[\bar{\nu}(x)\gamma_5\nu(x)\phi(x)\right] , \end{aligned} \tag{B.1}$$

where $N[\,.\,]$ is the normal order product operator. We notice that the first equality follows from the fact that $\mathcal{H}_{\nu\phi} = -\mathcal{L}_{\nu\phi}$ when no derivative interactions are present. Moreover, we were able to pass from the first to the second line thanks to the Wick's theorem and its corollary concerning fields evaluated in the same spacetime point. Assuming now, for example, $|i\rangle = |\nu_s(p)\rangle$ and $|f\rangle = |\nu_r(q)\,\phi(k)\rangle$, we find the matrix element related to the vertex to be

$$\begin{aligned} S^{(1)}_{\nu\phi,fi} &\equiv \langle f|\, S^{(1)}_{\nu\phi}\, |i\rangle \\ &= g_{\nu\nu\phi}\,\langle \nu_r(q)\,\phi(k)|\int d^4x\, \mathrm{N}\left[\bar{\nu}\gamma_5\nu\phi\right]_x |\nu_s(p)\rangle \\ &= g_{\nu\nu\phi}\,\langle \nu_r(q)\,\phi(k)|\int d^4x\, \mathrm{N}\left[\bar{\nu}_-\gamma_5\nu_+\phi_-\right] |\nu_s(p)\rangle \\ &= g_{\nu\nu\phi}\left(\bar{u}_r(q)\gamma_5 u_s(p)\right)\int d^4x\, e^{i(q+k-p)\cdot x}\,\langle 0|0\rangle \\ &\equiv (2\pi)^4\,\delta^{(4)}(q+k-p)\,\mathcal{M}_{\nu\to\nu\phi} , \end{aligned} \tag{B.2}$$

where $\mathcal{M}_{\nu\to\nu\phi} \equiv g_{\nu\nu\phi}\left[\bar{u}_r(q)\gamma_5 u_s(p)\right]$ is the amplitude. So we can write the following Feynman rule

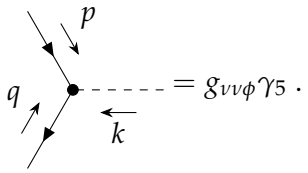

$$= g_{\nu\nu\phi}\gamma_5 . \tag{B.3}$$

B.2 PHOTON–PSEUDOSCALAR COUPLING

In this case, before taking the S–matrix expansion, it is convenient to cast the interaction Lagrangian in the following way

$$\mathcal{L}_{\gamma\phi} = \frac{1}{4} g_{\gamma\gamma\phi} F_{\mu\nu} \tilde{F}^{\mu\nu} \phi = \frac{1}{2} g_{\gamma\gamma\phi} \varepsilon^{\mu\nu\rho\sigma} \left(\partial_\mu A_\nu\right) \left(\partial_\rho A_\sigma\right) \phi \, . \tag{B.4}$$

Then we evaluate again the 1st order term of the corresponding S–matrix to obtain

$$\begin{aligned} S^{(1)}_{\gamma\phi} &= -i \int d^4x \, \mathcal{T} \left\{ \mathcal{H}_{\gamma\phi} \left(x\right) \right\} = i \int d^4x \, \mathcal{T} \left\{ \mathcal{L}_{\gamma\phi} \left(x\right) \right\} \\ &= \frac{i}{2} g_{\gamma\gamma\phi} \varepsilon^{\mu\nu\rho\sigma} \int d^4x \, \mathrm{N} \left[\left(\partial_\mu A_\nu \left(x\right)\right) \left(\partial_\rho A_\sigma \left(x\right)\right) \phi \left(x\right) \right] \, . \end{aligned} \tag{B.5}$$

Here in the first equality we exploited again the fact that $\mathcal{H}_{\gamma\phi} = -\mathcal{L}_{\gamma\phi}$, even if now the interaction Hamiltonian contains derivative terms. When this kind of terms are present, the Hamiltonian and the opposite of the Lagrangian typically differ by a noncovariant term. However, it is possible to recover the usual relation by a redefinition of the action of the time ordered product on the derivative couplings which allow to recover the usual Wick's expansion. Here we make an abuse of notation and we inidicate both the old and the new definition of the time ordered product with $\mathcal{T}\left[\,.\,\right]$. A rigorous proof of this fact can be found in [Itzykson and Zuber, 1980]. Now, by repeating what done in the previous case, we can assume $|i\rangle = |\phi\left(k\right)\rangle$ and $|f\rangle = \left|\gamma_\lambda\left(p\right)\gamma_\eta\left(q\right)\right\rangle$, and we find

$$\begin{aligned} S^{(1)}_{\gamma\phi,fi} &\equiv \langle f | \, S^{(1)}_{\gamma\phi} \, | i \rangle \\ &= \frac{i}{2} g_{\gamma\gamma\phi} \varepsilon^{\mu\nu\rho\sigma} \left\langle \gamma_\lambda\left(p\right) \gamma_\eta\left(q\right) \right| \int d^4x \, \mathrm{N} \left[\left(\partial_\mu A^-_\nu\right) \left(\partial_\rho A^-_\sigma\right) \phi_+ \right] \left| \phi\left(k\right) \right\rangle \\ &= -\frac{i}{2} g_{\gamma\gamma\phi} \varepsilon^{\mu\nu\rho\sigma} \int d^4x \, e^{i(p+q-k)\cdot x} \, \langle 0|0\rangle \\ &\quad \times \left[q_\mu \varepsilon^{\eta *}_\nu\left(q\right) p_\rho \varepsilon^{\lambda *}_\sigma\left(p\right) + p_\mu \varepsilon^{\lambda *}_\nu\left(p\right) q_\rho \varepsilon^{\eta *}_\sigma\left(q\right) \right] \\ &\equiv \left(2\pi\right)^4 \delta^{(4)}\left(q+k-p\right) \mathcal{M}_{\phi\to\gamma\gamma} \, , \end{aligned} \tag{B.6}$$

where $\mathcal{M}_{\phi\to\gamma\gamma} = -i g_{\gamma\phi\phi} \varepsilon^{\mu\nu\rho\sigma} p_\mu \varepsilon^{\lambda *}_\nu\left(p\right) q_\rho \varepsilon^{\eta *}_\sigma\left(q\right)$ is the amplitude. In particular, we notice that the shaded lines indicate an alternative choice of contractions due to the presence of identical particles in the final state. At the end of the computation this peculiarity appears as a symmetry factor, 2 in this particular case, by multiplicating the amplitude of the process, that must be carefully added whenever calculating matrix elements without the explicit

computation showed before. Finally, as in the previous case, we can write the following Feynman rule

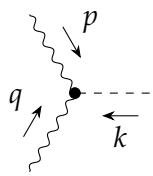

$$= -ig_{\gamma\phi\phi}\varepsilon^{\mu\nu\rho\sigma}p_\mu q_\rho \ . \tag{B.7}$$

C

SCHRÖDINGER, HEISENBERG AND INTERACTION PICTURES

Within this appendix, we would like to remind the reader of basic properties of the Schrödinger, Heisenberg and interaction picture. In chapter 4, we will often switch between these different descriptions of quantum mechanics.

In the usual description of quantum mechanics, time–independent operators correspond to the observables of the system. The time evolution is entirely contained in that of the state vector $|\psi(t)\rangle$, here written $|\psi_S(t)\rangle$, and it is obtained from the Schrödinger equation. This way to approach the problem is called the *Schrödinger picture*. Nevertheless, we know that all the predictions of quantum mechanics are expressed in terms of scalar products of bra and ket or matrix element of operators. These quantities are invariant when the same unitary transformation is performed on the states and on the operators. By appropriately choosing this transformation is possibile to make the trasform of $|\psi_S(t)\rangle$ as a time–independent ket. Of course, the transforms of the observables cited above then depends on time. This alternative approach is called the *Heisenberg picture*.

To avoid confusion, from now on, we shall sistematically assign an index S to the states and operators in the Schrödinger picture and an index H to those in the Heisenberg picture when more of them come into the discussion.

The state vector $|\psi_S(t)\rangle$ is at the instant t is expressed in terms of the initial state as

$$|\psi_S(t)\rangle = U(t,t_0)\,|\psi_S(t_0)\rangle \ , \tag{C.1}$$

where the time–evolution operator $U(t,t_0)$ with initial time t_0, takes the form

$$U(t,t_0) = \mathcal{T}\left[\exp\left(-i\int_{t_0}^{t} dt'\hat{H}(t')\right)\right] \ , \tag{C.2}$$

with $\mathcal{T}$ being the time ordering operator. This general solution can be simplified to give $U(t,t_0) = \exp\left[-iH(t-t_0)\right]$ if the Hamiltonian is time–independent, as we will assume in the following if not otherwise stated. Thanks to the unitarity of this operator, it is sufficient to perform the unitary transformation associated with its adjoint to obtain a constant transformed vector

$$|\psi_H(t)\rangle \equiv U^{\dagger}(t,t_0)\,|\psi_S(t)\rangle = U(t,t_0)\,U^{\dagger}(t,t_0)\,|\psi_S(t_0)\rangle = |\psi_S(t_0)\rangle \ , \tag{C.3}$$

which is the representation of the state of the system in the Heisenberg picture. Notice that it is constantly equal to the initial condition as anticipated in the beginning.

Now, how to recover the transformation law for operators in the Heisenberg picture? To make good our description of the physics by the Heisenberg picture we want it to match physical predictions computed by the Schrödinger's one. In particular we want to ask the equivalence of the average value of a given observable $\hat{A}$ computed in both cases

$$\left\langle \hat{A} \right\rangle (t) = \langle \psi_S (t)| \, \hat{A}_S (t_0) \, |\psi_S (t)\rangle = \langle \psi_H (t)| \, \hat{A}_H (t) \, |\psi_H (t)\rangle \ . \tag{C.4}$$

Using now the inverse of (C.3) on the l.h.s. of the equivalence above, is easy to see that we obtain

$$\hat{A}_H (t) \equiv U^\dagger (t, t_0) \, A_S (t) \, U (t, t_0) \ . \tag{C.5}$$

Give that in the Heisenberg picture the opertor is time–dependent, is possibile to compute an evolution equation, as happens for states in the Schrödinger picture. By taking the time derivative of (C.5), with some easy manipulations one obtains

$$i \frac{\mathrm{d}}{\mathrm{d}t} \hat{A}_H (t) = \left[\hat{A}_H (t) \, , \hat{H}_H (t) \right] \ . \tag{C.6}$$

Although the Schrödinger and Heisenberg pictures are conceptually simple, it is not so easy to actually calculate expectation values of field operators, like two–point functions, for arbitrary times. If we know how to diagonalize the Hamiltonian in (C.5), the exponentials in the evolution operator can be computed straightforwardly and we are able to obtain an explicit representation of a field operator $\hat{\phi} (\mathbf{x}, t)$ in terms of creation and annihilation operators. These are eigenmodes of the Hamiltonian [Peskin and Schroeder, 1995]

$$\hat{\phi}_H (\mathbf{x}, t) = \int \frac{d^3 \mathbf{p}}{(2\pi)^3 \, 2E_{\mathbf{p}}} \left[\hat{a}_H (\mathbf{p}, t_0) \, e^{-ip \cdot x} + \hat{a}_H^\dagger (\mathbf{p}, t_0) \, e^{ip \cdot x} \right] \ , \tag{C.7}$$

where for the sake of simplicity we assumed a real scalar field. The operators $\hat{a}_H$ and $\hat{a}_H^\dagger (\mathbf{p}, t_0)$ are the familiar annihilation and creation operators. The excitations that are created by $\hat{a}_H^\dagger (\mathbf{p}, t_0)$ are eigenstates of the Hamiltonian, and thus have well–defined energies. They can be interpreted as particles, as usual, and it is the evolution of these operators that we aim to describe.

If the Hamiltonian incorporates interactions which cannot be diagonalized, the representation of the field in (C.7) in terms of eigenstates of the Hamiltonian breaks down. However, we can split the Hamiltonian into a diagonalizable part $\hat{H}_0$ and an interaction piece $\hat{H}_{\text{int}}$ that contains the non–diagonalizable parts. If the product $\hat{H}_{\text{int}} (t - t_0) \ll 1$, we can expand the non–diagonal part of (C.5) through the usual method of the Dyson series [Dyson, 1949]. This approach leads to the definition of the *interaction picture* in which we defined the transformed states as

$$|\psi_I (t)\rangle \equiv U_0^\dagger (t, t_0) \, |\psi_S (t)\rangle \ , \tag{C.8}$$

and the operators as

$$\hat{A}_I (t) \equiv U_0^\dagger (t, t_0) \, \hat{A}_S (t) \, U_0 (t, t_0) \ . \tag{C.9}$$

It is possible to check that the interaction picture is well defined by the equations above by computing the mean value of a generic operator $\hat{A}$. In particular one easily finds that

$$\begin{aligned}\left\langle \hat{A} \right\rangle (t) &= \langle \psi_S (t)| \hat{A}_S (t_0) |\psi_S (t)\rangle \\ &= \langle \psi_H (t)| \hat{A}_H (t) |\psi_H (t)\rangle \\ &= \langle \psi_I (t)| \hat{A}_I (t) |\psi_I (t)\rangle \ . \end{aligned} \tag{C.10}$$

The key feature of the interaction picture is that the time evolution of the interaction picture field operators is only due to the diagonalizable part of the Hamiltonian. Indeed, by taking the time derivative of (C.9) one gets the following evolution equation

$$i \frac{\mathrm{d}}{\mathrm{d}t} \hat{A}_I (t) = \left[\hat{A}_I (t) , \hat{H}_0 \right] \ . \tag{C.11}$$

This fact allows us to use the standard expansion in creation and annihilation operators of (C.7) to compute observables and correlation functions in Quantum Field Theory (QFT), thus representing a substantial simplification in calculations.

The density matrix can be shown to transform to the interaction picture in the same way as any other operator. It is interesting to show the von Neumann equation in the interaction picture [Blum, 2012]

$$i \frac{\mathrm{d}}{\mathrm{d}t} \hat{\rho}_i (t) = \left[\hat{H}_{\mathrm{int},I} (t) , \hat{\rho}_I (t) \right] \ . \tag{C.12}$$

Thus, the time evolution of the interaction picture density matrix is controlled by the interaction part of the Hamiltonian. In particular, thanks to the weak coupling hypothesis, this form of the von Neumann equation can be used as a starting point of a perturbative approach to the construction of approximate solutions.

D

ROTATION OF REFERENCE FRAME

When Thomson scattering is the only process modifying the geodesic propagation of the photons, then the transfer problem for the polarization matrix considerably simplifies [Chandrasekhar, 1960]. For a given plane wave, the polarization matrix is diagonal it the unit vectors

$$\hat{e}_1(\hat{\mathbf{k}}, \hat{\mathbf{q}}) \equiv \frac{\hat{\mathbf{k}} - \mu \hat{\mathbf{q}}}{\sqrt{1-\mu^2}}\,, \qquad \hat{e}_2(\hat{\mathbf{k}}, \hat{\mathbf{q}}) \equiv \frac{\hat{\mathbf{k}} \times \hat{\mathbf{q}}}{\sqrt{1-\mu^2}}\,, \tag{D.1}$$

where $\mu \equiv \hat{\mathbf{k}} \cdot \hat{\mathbf{q}}$, are used to describe the polarization vectors. In this case the only non–zero Stokes's parameters are I and $Q = \Delta_P^+ = \Delta_P^-$. In CMB polarization literature collision integrals are usually solved in this basis with the unit vector $\hat{\mathbf{k}}$ laying on the z axis [Kosowsky, 1996]. Indeded, it is easy to note that, when $\hat{\mathbf{k}} = (0, 0, 1)$, the k–dependent polarization vectors in (D.1) reduce to

$$\hat{e}_\theta(\hat{\mathbf{z}}, \hat{\mathbf{q}}) = \begin{pmatrix} -\cos\theta_q \cos\phi_q \\ -\cos\theta_q \sin\phi_q \\ \sin\theta_q \end{pmatrix}\,, \qquad \hat{e}_\phi(\hat{\mathbf{z}}, \hat{\mathbf{q}}) = \begin{pmatrix} -\sin\theta_q \\ \cos\theta_q \\ 0 \end{pmatrix}\,, \tag{D.2}$$

which are exactly those appearing in eq. (6.2) of Kosowsky (1996) employed for the solution of the Compton scattering integrals. However, to match the frame in which we solved the collision integral related to neutrino–photon scattering, we need to rotate this k–dependent basis to a fixed basis, let's say $\hat{e}_i(\hat{\mathbf{q}})$, in the plane perpendicular to the photon direction (see Figure D.1). This can be done following the standard reconstruction of polarization distribution at the present time when summing over all wavenumbers [Bond and Efstathiou, 1987]. In that case we have the fixed basis of polarization vectors to be the canonical one induced by the spherical coordinates system in the 3D-space

$$\hat{\varepsilon}_\theta(\hat{\mathbf{q}}) = \begin{pmatrix} \cos\theta_q \cos\phi_q \\ \cos\theta_q \sin\phi_q \\ -\sin\theta_q \end{pmatrix}\,, \qquad \hat{\varepsilon}_\phi(\hat{\mathbf{q}}) = \begin{pmatrix} -\sin\theta_q \\ \cos\theta_q \\ 0 \end{pmatrix}\,, \tag{D.3}$$

while the k-dependent basis now becomes

$$\hat{e}_\theta(\hat{\mathbf{k}}, \hat{\mathbf{q}}) = \frac{1}{\sqrt{1-\mu^2}} \begin{pmatrix} -\sin\theta_k \cos\phi_k + \mu \sin\theta_q \cos\phi_q \\ -\sin\theta_k \sin\phi_k + \mu \sin\theta_q \sin\phi_q \\ -\cos\theta_k + \mu \cos\theta_q \end{pmatrix}\,, \tag{D.4}$$

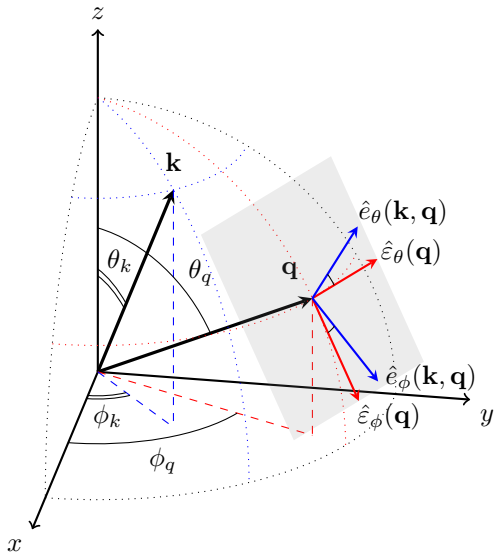

Figure D.1: Rotation of polarization vectors induced by the change of frame from the k–dependent to the fixed one. Everything here is embedded in a global 3D frame with spherical coordinates. The polarization vectors live on the tangent plane to the sphere whose normal vector is the direction of view of the photon with momentum $\mathbf{q}$.

$$\hat{e}_\phi(\hat{\mathbf{k}},\hat{\mathbf{q}}) = \frac{1}{\sqrt{1-\mu^2}} \begin{pmatrix} \cos\theta_q \sin\theta_k \sin\phi_k - \cos\theta_k \sin\theta_q \sin\phi_q \\ -\cos\theta_q \sin\theta_k \cos\phi_k + \cos\theta_k \sin\theta_q \cos\phi_q \\ -\sin\theta_q \sin\theta_k \sin(\phi_k - \phi_q) \end{pmatrix} , \quad \text{(D.5)}$$

where now $\mu = \cos\theta_k \cos\theta_q + \sin\theta_k \sin\theta_q \cos(\phi_k - \phi_q)$. Now, given our thos basis of polarization vectors, we can define the rotation matrix connecting them as

$$R(\hat{\mathbf{k}},\hat{\mathbf{q}}) = \begin{pmatrix} \hat{e}_\theta(\hat{\mathbf{k}},\hat{\mathbf{q}}) \cdot \hat{\varepsilon}_\theta(\hat{\mathbf{q}}) & \hat{e}_\theta(\hat{\mathbf{k}},\hat{\mathbf{q}}) \cdot \hat{\varepsilon}_\phi(\hat{\mathbf{q}}) \\ \hat{e}_\phi(\hat{\mathbf{k}},\hat{\mathbf{q}}) \cdot \hat{\varepsilon}_\theta(\hat{\mathbf{q}}) & \hat{e}_\phi(\hat{\mathbf{k}},\hat{\mathbf{q}}) \cdot \hat{\varepsilon}_\phi(\hat{\mathbf{q}}) \end{pmatrix} , \quad \text{(D.6)}$$

which explicitly reads

$$R(\hat{\mathbf{k}},\hat{\mathbf{q}}) = \frac{1}{1-\mu^2} \begin{pmatrix} \cos\theta_k \sin\theta_q - \cos\theta_q \sin\theta_k \cos(\Delta\phi) & -\sin\theta_k \sin(\Delta\phi) \\ \sin\theta_k \sin(\Delta\phi) & \cos\theta_k \sin\theta_q - \cos\theta_q \sin\theta_k \cos(\Delta\phi) \end{pmatrix} , \quad \text{(D.7)}$$

where $\Delta\phi \equiv \phi_k - \phi_q$. It is easy to prove that this matrix represent a rotation because $R(\hat{\mathbf{k}},\hat{\mathbf{q}})R^T(\hat{\mathbf{k}},\hat{\mathbf{q}}) = R^T(\hat{\mathbf{k}},\hat{\mathbf{q}})R(\hat{\mathbf{k}},\hat{\mathbf{q}}) = 1$.

To our purposes it is interesting to note that in the limit in which $\hat{\mathbf{q}}$ lays on the z axis (corresponding to the reference frame in which we solved the neutrino-photon scattering collision integrals), the rotation matrix reduces to

$$R(\phi_k) \equiv R(\hat{\mathbf{k}}, \hat{\mathbf{z}}) = \begin{pmatrix} -\cos\phi_k & -\sin\phi_k \\ \sin\phi_k & -\cos\phi_k \end{pmatrix} . \tag{D.8}$$

Thus, in the new basis, the polarization matrix is $\rho'_{ij}(\mathbf{q}, \phi_k) = R^{\dagger}(\phi_k)\rho_{kl}(\mathbf{q})R(\phi_k)$ which explicitly corresponds to a mixing of the Q and U Stokes' parameters as

$$Q'(\mathbf{q}, \phi_k) = Q\cos(2\phi_k) - U\sin(2\phi_k) \tag{D.9}$$

$$U'(\mathbf{q}, \phi_k) = Q\sin(2\phi_k) + U\cos(2\phi_k) \tag{D.10}$$

E

PARTIAL RELAXATION OF $q \ll k$ LIMIT

In this appendix, following the approach of Beutler et al. (2019), we aim to demonstrate how it is possible to include some of the terms neglected in eq. (6.60) due to the assumption of working in the limit $q \ll k$. Note beforehand that the intermediate results and steps in this subsection differ from those in Beutler et al. (2019), while the final result for the damping factor matches when integrated via eq. (6.62). In contrast to the strong approximation used in the main text, we will refer to this approach as the *weak approximation*. To avoid overloading the text with unnecessary derivation steps, we assume a phase $\varphi_{\log} = 0$, and will provide comments on this assumption at the end of the computation.

E.1 LOGARITHMIC OSCILLATIONS

The crucial point is writing $2n$-th element in the sum defining the translation operator, see eq. (6.44), stripped of the momenta $\mathbf{q}$ and evaluated on the oscillating function in the wiggle part of the spectrum as

$$\begin{aligned}
&\partial_{k_{i_n}} \cdots \partial_{k_{i_{2n}}} \sin\left[\omega_{\log} \ln\left(\frac{k}{k_*}\right)\right] = \\
&\quad = \frac{1}{2i} \frac{\hat{k}_{i_1} \cdots \hat{k}_{i_{2n}}}{k^{2n}} \left[f_n(i\omega_{\log}) \left(\frac{k}{k_*}\right)^{i\omega_{\log}} - f_n(-i\omega_{\log}) \left(\frac{k}{k_*}\right)^{-i\omega_{\log}} \right] \\
&\quad = \frac{1}{2} \frac{\hat{k}_{i_1} \cdots \hat{k}_{i_{2n}}}{k^{2n}} \left\{ \left[f_n(i\omega_{\log}) + f_n(-i\omega_{\log}) \right] \sin\left(\omega_{\log} \ln \frac{k}{k_*}\right) \right. \\
&\qquad \left. - i \left[f_n(i\omega_{\log}) - f_n(-i\omega_{\log}) \right] \cos\left(\omega_{\log} \ln \frac{k}{k_*}\right) \right\} ,
\end{aligned} \tag{E.1}$$

where we employed the following decomposition of the sine

$$\sin(y \ln x) = \frac{1}{2i}\left(e^{iy \ln x} - e^{-iy \ln x}\right) = \frac{1}{2i}\left(x^{iy} - x^{-iy}\right) , \tag{E.2}$$

and we defined the function

$$f_n(i\omega_{\log}) \equiv \frac{(i\omega_{\log})!}{(i\omega_{\log} - 2n)!} . \tag{E.3}$$

In these terms the action of the operator appearing in eq. (6.50) now is

$$\begin{aligned}
&[1-\cosh(\mathbf{q}\cdot\nabla_{\mathbf{k}})]P^{\mathrm{w}}_{\log}(k) = \\
&\quad= \left[1-\sum_{n=0}^{\infty}\frac{1}{(2n)!}(\mathbf{q}\cdot\nabla_{\mathbf{k}})^{2n}\right]P^{\mathrm{nw}}(k)A_{\log}\sin\left(\omega_{\log}\ln\frac{k}{k_*}\right) \\
&\quad= P^{\mathrm{nw}}(k)A_{\log}\left\{\sin\left(\omega_{\log}\ln\frac{k}{k_*}\right)-\frac{1}{2}\sum_{n=0}^{\infty}\frac{1}{(2n)!}q_{i_1}\cdots q_{i_{2n}}\frac{\hat{k}_{i_1}\cdots\hat{k}_{i_{2n}}}{k^{2n}}\right. \\
&\qquad\times\left[\left(f_n(i\omega_{\log})+f_n(-i\omega_{\log})\right)\sin\left(\omega_{\log}\ln\frac{k}{k_*}\right)\right. \\
&\qquad\left.\left.-i\left(f_n(i\omega_{\log})-f_n(-i\omega_{\log})\right)\cos\left(\omega_{\log}\ln\frac{k}{k_*}\right)\right]\right\}. \qquad \text{(E.4)}
\end{aligned}$$

As anticipated, the computation was performed with a phase of $\varphi_{\log} \neq 0$. While this would have resulted in a more extensive calculation, it would not have been significantly more challenging or different from what we have done. In that case, one simply needs to express the oscillating function in eq. (E.1) as

$$\begin{aligned}
&\sin\left(\omega_{\log}\ln\frac{k}{k_*}+\varphi_{\log}\right) = \\
&\quad=\cos(\varphi_{\log})\sin\left(\omega_{\log}\ln\frac{k}{k_*}\right)+\sin(\varphi_{\log})\cos\left(\omega_{\log}\ln\frac{k}{k_*}\right). \qquad \text{(E.5)}
\end{aligned}$$

The initial term is identical to that which was previously studied, with the exception of the multiplication by the constant $\cos(\varphi_{\log})$. The second term is analogous to the first, differing only in the sign changes. Given that the operator in eq. (E.4) is linear, it is feasible to compute the two terms separately and subsequently add the results together. By summing the two results, weighted by the corresponding phase functions, and combining the trigonometric functions using eq. (E.5), it is possible to recast the result in the same form as eq. (E.4), with the phase appearing in the argument of the sine and cosine functions in the second line, showing that this result is unaffected by the phase.

For the next step of the computation, let us break eq. (E.4) into two parts. We begin by analyzing the first term, namely

$$\textcircled{1} \equiv \frac{1}{2}\sum_{n=0}^{\infty}\frac{1}{(2n)!}q_{i_1}\cdots q_{i_{2n}}\frac{\hat{k}_{i_1}\cdots\hat{k}_{i_{2n}}}{k^{2n}}\left[f_n(i\omega_{\log})+f_n(-i\omega_{\log})\right]. \qquad \text{(E.6)}$$

The $2n$ scalar products in eq. (E.6) can be rewritten as

$$\frac{(\mathbf{q}\cdot\hat{\mathbf{k}})}{k} = \frac{q}{k}(\hat{\mathbf{q}}\cdot\hat{\mathbf{k}}) = \frac{q\mu}{k}, \qquad \text{(E.7)}$$

and we can also notice that

$$\frac{1}{(2n)!}f_n(i\omega_{\log}) = \binom{i\omega_{\log}}{i\omega_{\log}-2n} = \binom{i\omega_{\log}}{2n}. \qquad \text{(E.8)}$$

Using eqs. (E.7) and (E.8) then, our sum can be rewritten as

$$① = \frac{1}{2}\sum_{n=0}^{\infty}\left\{\binom{i\omega_{\log}}{2n}\left(\frac{q\mu}{k}\right)^{2n} + \binom{-i\omega_{\log}}{2n}\left(\frac{q\mu}{k}\right)^{2n}\right\}. \tag{E.9}$$

Here it is easy to recognize that each terms has the same form of a Newton's series with only even powers. In particular, it is possible to build such a series by means of the following trick

$$(1+x)^{\alpha} + (1-x)^{\alpha} = \sum_{n=0}^{+\infty}\binom{\alpha}{n}\left[1+(-1)^n\right]x^n = 2\sum_{n=0}^{+\infty}\binom{\alpha}{2n}x^{2n}, \tag{E.10}$$

where, the second equality comes just from the fact that all the elements corresponding to odd indices in the sum are identically vanishing. Thanks to this observations, the first term in eq. (E.4) can be finally written as

$$\begin{aligned} ① &= \frac{1}{4}\left\{\left(1+\frac{q\mu}{k}\right)^{i\omega_{\log}} + \left(1-\frac{q\mu}{k}\right)^{i\omega_{\log}} + \left(1+\frac{q\mu}{k}\right)^{-i\omega_{\log}} + \left(1-\frac{q\mu}{k}\right)^{-i\omega_{\log}}\right\} \\ &= \frac{1}{2}\left\{\cos\left[\omega_{\log}\ln\left(1+\frac{q\mu}{k}\right)\right] + \cos\left[\omega_{\log}\ln\left(1-\frac{q\mu}{k}\right)\right]\right\}. \end{aligned} \tag{E.11}$$

Concerning the second term of eq. (E.4) instead we have

$$② \equiv \frac{i}{2}\sum_{n=0}^{+\infty}\frac{1}{(2n)!}q_{i_1}\cdots q_{i_{2n}}\frac{\hat{k}_{i_1}\cdots\hat{k}_{i_{2n}}}{k^{2n}}\left[f_n(i\omega_{\log}) - f_n(-i\omega_{\log})\right]. \tag{E.12}$$

The analysis is completely analogous to that of ① indeed, following what has been done before, we can write

$$② = \frac{i}{2}\sum_{n=0}^{\infty}\left\{\binom{i\omega_{\log}}{2n}\left(\frac{q\mu}{k}\right)^{2n} - \binom{-i\omega_{\log}}{2n}\left(\frac{q\mu}{k}\right)^{2n}\right\}, \tag{E.13}$$

and then

$$\begin{aligned} ② &= \frac{i}{4}\left\{\left(1+\frac{q\mu}{k}\right)^{i\omega_{\log}} + \left(1-\frac{q\mu}{k}\right)^{i\omega_{\log}} - \left(1+\frac{q\mu}{k}\right)^{-i\omega_{\log}} - \left(1-\frac{q\mu}{k}\right)^{-i\omega_{\log}}\right\} \\ &= -\frac{1}{2}\left\{\sin\left[\omega_{\log}\ln\left(1+\frac{q\mu}{k}\right)\right] + \sin\left[\omega_{\log}\ln\left(1-\frac{q\mu}{k}\right)\right]\right\}. \end{aligned} \tag{E.14}$$

Putting everything back together in eq. (E.4), we finally have

$$\begin{aligned} &[1-\cosh(\mathbf{q}\cdot\nabla_{\mathbf{k}})]P^{\mathrm{w}}_{\log}(k) = \\ &\quad= \left\{1 - \frac{1}{2}\left[\cos\left(\omega_{\log}\ln\left(1+\frac{q\mu}{k}\right)\right) + \cos\left(\omega_{\log}\ln\left(1-\frac{q\mu}{k}\right)\right)\right]\right\}P^{\mathrm{w}}_{\log}(k) \\ &\qquad - \left\{\frac{1}{2}\left[\sin\left(\omega_{\log}\ln\left(1+\frac{q\mu}{k}\right)\right) + \sin\left(\omega_{\log}\ln\left(1-\frac{q\mu}{k}\right)\right)\right]\right\}\frac{P^{\mathrm{nw}}(k)}{\omega_{\log}}\frac{\mathrm{d}\delta P^{\log}_{\zeta}(k)}{\mathrm{d}\ln k}. \end{aligned} \tag{E.15}$$

Here we notice that a term with the derivative of the spectrum appeared. This is analogous to what we found in the case of scale dependent amplitudes

when a term with a phase shift appeared in our computation of the damping. In this case it was possible to write it as derivative of the spectrum because, given the absence of a scale dependent amplitude, all the scale dependence is concentrated within the oscillatory function. We decided to keep this notation to facilitate a direct comparison with Beutler et al. (2019) and for an easier interpretation of this object. At this point we can compute the damping factors with the formula in eq. (6.79) finding

$$\begin{aligned}\Sigma_{\log}(k) \equiv \frac{1}{6\pi^2}\int_0^{k_S} \mathrm{d}q\; P_{\rm nw}(q)\Bigg\{1 - \frac{3}{2q^3\left(36+49\omega_{\log}^2+14\omega_{\log}^4+\omega_{\log}^6\right)} \\ \times\Bigg[-(k+q)\cos\left(\omega_{\log}\log\left(1+\frac{q}{k}\right)\right) \\ \times\left(12k^2\left(-1+\omega_{\log}^2\right)-2kq\left(-6-5\omega_{\log}^2+\omega_{\log}^4\right)-3q^2\left(4+5\omega_{\log}^2+\omega_{\log}^4\right)\right) \\ +(k-q)\cos\left(\omega_{\log}\log\left(1-\frac{q}{k}\right)\right) \\ \times\left(12k^2\left(-1+\omega_{\log}^2\right)+2kq\left(-6-5\omega_{\log}^2+\omega_{\log}^4\right)-3q^2\left(4+5\omega_{\log}^2+\omega_{\log}^4\right)\right) \\ -(k+q)\omega_{\log}\sin\left(\omega_{\log}\log\left(1+\frac{q}{k}\right)\right) \\ \times\left(2k^2\left(-11+\omega_{\log}^2\right)+10kq\left(1+\omega_{\log}^2\right)-q^2\left(4+5\omega_{\log}^2+\omega_{\log}^4\right)\right) \\ +(k-q)\omega_{\log}\sin\left(\omega_{\log}\log\left(1-\frac{q}{k}\right)\right) \\ \times\left(2k^2\left(-11+\omega_{\log}^2\right)-10kq\left(1+\omega_{\log}^2\right)-q^2\left(4+5\omega_{\log}^2+\omega_{\log}^4\right)\right)\Bigg]\Bigg\}, \end{aligned} \tag{E.16}$$

and

$$\begin{aligned}\hat{\Sigma}_{\log}(k) \equiv -\frac{1}{6\pi^2}\int_0^{k_S} \mathrm{d}q\; P_{\rm nw}(q)\frac{3}{2q^3\left(36+49\omega_{\log}^2+14\omega_{\log}^4+\omega_{\log}^6\right)} \\ \times\Bigg\{(k+q)\omega_{\log}\cos\left[\omega_{\log}\log\left(1+\frac{q}{k}\right)\right] \\ \times\left[2k^2\left(-11+\omega_{\log}^2\right)+10kq\left(1+\omega_{\log}^2\right)-q^2\left(4+5\omega_{\log}^2+\omega_{\log}^4\right)\right] \\ -(k-q)\omega_{\log}\cos\left[\omega_{\log}\log\left(1-\frac{q}{k}\right)\right] \\ \times\left[2k^2\left(-11+\omega_{\log}^2\right)-10kq\left(1+\omega_{\log}^2\right)-q^2\left(4+5\omega_{\log}^2+\omega_{\log}^4\right)\right] \\ -(k+q)\sin\left[\omega_{\log}\log\left(1+\frac{q}{k}\right)\right] \\ \times\left[12k^2\left(-1+\omega_{\log}^2\right)-2kq\left(-6-5\omega_{\log}^2+\omega_{\log}^4\right)-3q^2\left(4+5\omega_{\log}^2+\omega_{\log}^4\right)\right] \\ +(k-q)\sin\left[\omega_{\log}\log\left(1-\frac{q}{k}\right)\right] \\ \times\left[12k^2\left(-1+\omega_{\log}^2\right)+2kq\left(-6-5\omega_{\log}^2+\omega_{\log}^4\right)-3q^2\left(4+5\omega_{\log}^2+\omega_{\log}^4\right)\right]\Bigg\}. \end{aligned} \tag{E.17}$$

Finally let us briefly comment on how the appearance of the additional term in eq. (E.15) is due to a minor loss, in terms of powers of k, when taking

the $2n$ gradients on the wiggle power spectrum. Indeed in Vasudevan et al. (2019) just the derivatives of a factor $(\mathbf{q}\cdot\mathbf{k})/k^2$, in contrast to the derivatives of a factor $(\mathbf{q}\cdot\mathbf{k})/k$ in Beutler et al. (2019), are neglected. As a proof of this fact we can follow the steps in the derivation of Beutler et al. (2019) factorizing the whole $(\mathbf{q}\cdot\mathbf{k})/k^2$, and we will find a result analogous to the one of Vasudevan et al. (2019), that is eq. (6.50). The trick is, at each iteration, to rewrite the action of the derivative as follows

$$\begin{aligned}\partial_{k_i}\left[\sin\left(\omega_{\log}\ln\frac{k}{k_*}\right)\right] &= \frac{1}{2i}\left[\frac{i\omega_{\log}}{k_*}\left(\frac{k}{k_*}\right)^{i\omega_{\log}-1} - \frac{(-i\omega_{\log})}{k_*}\left(\frac{k}{k_*}\right)^{-i\omega_{\log}-1}\right]\frac{k_i}{k}\\ &= \frac{1}{2i}\left[i\omega_{\log}\left(\frac{k}{k_*}\right)^{i\omega_{\log}} - (-i\omega_{\log})\left(\frac{k}{k_*}\right)^{-i\omega_{\log}}\right]\frac{k_i}{k^2}\,,\end{aligned} \tag{E.18}$$

so that, in this approximation, the analogous of eq. (E.1) will be

$$\begin{aligned}&\partial_{k_{i_n}}\cdots\partial_{k_{i_{2n}}}\sin\left[\omega_{\log}\ln\frac{k}{k_*}\right] =\\ &\quad= \frac{1}{2i}\frac{k_{i_1}\cdots k_{i_{2n}}}{k^{4n}}\left[(i\omega_{\log})^{2n}\left(\frac{k}{k_*}\right)^{i\omega_{\log}} - (-i\omega_{\log})^{2n}\left(\frac{k}{k_*}\right)^{-i\omega_{\log}}\right].\end{aligned} \tag{E.19}$$

And finally, we can write

$$\begin{aligned}&[1-\cosh(\mathbf{q}\cdot\nabla_{\mathbf{k}})]P^{\rm w}_{\log}(k) =\\ &\quad= P^{\rm nw}(k)A_{\log}\left\{\sin\left(\omega_{\log}\ln\frac{k}{k_*}\right)\right.\\ &\qquad\left.-\frac{1}{2i}\sum_{n=0}^{\infty}\frac{1}{(2n)!}q_{i_1}\cdots q_{i_{2n}}\frac{k_{i_1}\cdots k_{i_{2n}}}{k^{4n}}\left[(i\omega_{\log})^{2n}\left(\frac{k}{k_*}\right)^{i\omega_{\log}} - (-i\omega_{\log})^{2n}\left(\frac{k}{k_*}\right)^{-i\omega_{\log}}\right]\right\}\\ &\quad= P^{\rm nw}(k)A_{\log}\left\{\sin\left(\omega_{\log}\ln\frac{k}{k_*}\right)\right.\\ &\qquad\left.-\sum_{n=0}^{\infty}\frac{1}{(2n)!}(-1)^n\left[\frac{(\mathbf{q}\cdot\mathbf{k})}{k^2}\omega_{\log}\right]^{2n}\times\frac{1}{2i}\left[\left(\frac{k}{k_*}\right)^{i\omega_{\log}} - \left(\frac{k}{k_*}\right)^{-i\omega_{\log}}\right]\right\}\\ &\quad= \left[1-\cos\left(\frac{\mathbf{q}\cdot\mathbf{k}}{k^2}\omega_{\log}\right)\right]P^{\rm w}_{\log}(k)\,,\end{aligned} \tag{E.20}$$

which is exactly analogous to eq. (6.50).

E.2 MIXED TERM BETWEEN BARYON AND PRIMORDIAL LOGARITHMIC OSCILLATIONS

We can use a similar method to compute a more detailed version of eq. (6.66). The $2n$-th derivative of the mixed oscillatory term can be calculated using induction. For example, for $n = 1$, we have that[1]

$$\begin{aligned}
&\partial_{k_{i_1}}\partial_{k_{i_2}}\left[\cos\left(\omega_{\log}\ln\frac{k}{k_*}-\omega_{\rm BAO}k\right)\right] = \\
&\quad=\frac{1}{2}\frac{k_{i_1}k_{i_2}}{k^2}\left\{\left[\frac{i\omega_{\log}}{k_*}\frac{(i\omega_{\log}-1)}{k_*}\left(\frac{k}{k_*}\right)^{i\omega_{\log}-2}+2(-i\omega_{\rm BAO})\left(\frac{k}{k_*}\right)^{i\omega_{\log}-1}\right.\right. \\
&\qquad\left.\left.+(-i\omega_{\rm BAO})^2\left(\frac{k}{k_*}\right)^{i\omega_{\log}}\right]e^{-i\omega_{\rm BAO}k}+\begin{pmatrix}\omega_{\log}\to-\omega_{\log}\\ \omega_{\rm BAO}\to-\omega_{\rm BAO}\end{pmatrix}\right\}. \qquad \text{(E.21)}
\end{aligned}$$

Now, assuming this to be true for any number of derivatives, we have

$$\begin{aligned}
&\partial_{k_{i_1}}\cdots\partial_{k_{i_n}}\left[\cos\left(\omega_{\log}\ln\frac{k}{k_*}-\omega_{\rm BAO}k\right)\right] = \\
&\quad=\frac{1}{2}\frac{k_{i_1}\cdots k_{i_n}}{k^n}\left\{\sum_{m=0}^{n}\binom{n}{m}\frac{1}{k_*^{n-m}}\frac{(i\omega_{\log})!}{(i\omega_{\log}-n+m)!}\left(\frac{k}{k_*}\right)^{i\omega_{\log}-n+m}(-i\omega_{\rm BAO})^m\right\}e^{-i\omega_{\rm BAO}k} \\
&\qquad+\begin{pmatrix}\omega_{\log}\to-\omega_{\log}\\ \omega_{\rm BAO}\to-\omega_{\rm BAO}\end{pmatrix}. \qquad \text{(E.22)}
\end{aligned}$$

To check the proof, we add another derivative to the previous expression

$$\begin{aligned}
&\partial_{k_j}\partial_{k_{i_1}}\cdots\partial_{k_{i_n}}\left[\cos\left(\omega_{\log}\ln\frac{k}{k_*}-\omega_{\rm BAO}k\right)\right] = \\
&\quad=\frac{1}{2}\frac{k_{i_1}\cdots k_{i_n}k_j}{k^{n+1}}\left\{\sum_{m=0}^{n}\binom{n}{m}\frac{1}{k_*^{n-m+1}}\frac{(i\omega_{\log})!}{(i\omega_{\log}-n-1+m)!}\left(\frac{k}{k_*}\right)^{i\omega_{\log}-n-1+m}(-i\omega_{\rm BAO})^m\right. \\
&\qquad\left.+\sum_{m=0}^{n}\binom{n}{m}\frac{1}{k_*^{n-m}}\frac{(i\omega_{\log})!}{(i\omega_{\log}-n+m)!}\left(\frac{k}{k_*}\right)^{i\omega_{\log}-n+m}(-i\omega_{\rm BAO})^{m+1}\right\}e^{-i\omega_{\rm BAO}k} \\
&\qquad+\begin{pmatrix}\omega_{\log}\to-\omega_{\log}\\ \omega_{\rm BAO}\to-\omega_{\rm BAO}\end{pmatrix}. \qquad \text{(E.23)}
\end{aligned}$$

1 we carry out our computation only on the first term of the wiggle power spectrum. We will sum everything together at the end.

For the first line we have

$$\begin{aligned}
\textcircled{1} &= \frac{1}{2}\frac{k_{i_1}\cdots k_{i_n}k_j}{k^{n+1}}\left\{\binom{n}{0}\frac{1}{k_*^{n+1}}\frac{(i\omega_{\log})!}{(i\omega_{\log}-n-1)!}\left(\frac{k}{k_*}\right)^{i\omega_{\log}-n-1}\right.\\
&\quad\left.+\sum_{m=1}^{n}\binom{n}{m}\frac{1}{k_*^{n-m+1}}\frac{(i\omega_{\log})!}{(i\omega_{\log}-n-1+m)!}\left(\frac{k}{k_*}\right)^{i\omega_{\log}-n-1+m}(-i\omega_{\mathrm{BAO}})^m\right\}e^{-i\omega_{\mathrm{BAO}}k}\\
&= \frac{1}{2}\frac{k_{i_1}\cdots k_{i_n}k_j}{k^{n+1}}\left\{\binom{n}{0}\frac{1}{k_*^{n+1}}\frac{(i\omega_{\log})!}{(i\omega_{\log}-n-1)!}\left(\frac{k}{k_*}\right)^{i\omega_{\log}-n-1}\right.\\
&\quad\left.+\sum_{m=0}^{n}\binom{n-1}{m}\frac{1}{k_*^{n-m}}\frac{(i\omega_{\log})!}{(i\omega_{\log}-n)!}\left(\frac{k}{k_*}\right)^{i\omega_{\log}-n}(-i\omega_{\mathrm{BAO}})^{m+1}\right\}e^{-i\omega_{\mathrm{BAO}}k}.
\end{aligned}\tag{E.24}$$

For the second line instead we have

$$\begin{aligned}
\textcircled{2} &= \frac{1}{2}\frac{k_{i_1}\cdots k_{i_n}k_j}{k^{n+1}}\left\{\sum_{m=0}^{n-1}\binom{n}{m}\frac{1}{k_*^{n-m}}\frac{(i\omega_{\log})!}{(i\omega_{\log}-n+m)!}\left(\frac{k}{k_*}\right)^{i\omega_{\log}-n+m}(-i\omega_{\mathrm{BAO}})^{m+1}\right.\\
&\quad\left.+\binom{n}{n}\left(\frac{k}{k_*}\right)^{i\omega_{\log}}(-i\omega_{\mathrm{BAO}})^{n+1}\right\}e^{-i\omega_{\mathrm{BAO}}k}.
\end{aligned}\tag{E.25}$$

By merging the two terms we obtain[2]

$$\begin{aligned}
\textcircled{1}+\textcircled{2} &= \frac{1}{2}\frac{k_{i_1}\cdots k_{i_n}k_j}{k^{n+1}}\left\{\binom{n}{0}\frac{1}{k_*^{n+1}}\frac{(i\omega_{\log})!}{(i\omega_{\log}-n-1)!}\left(\frac{k}{k_*}\right)^{i\omega_{\log}-n-1}\right.\\
&\quad+\sum_{m=0}^{n-1}\binom{n+1}{m+1}\frac{1}{k_*^{n-m}}\frac{(i\omega_{\log})!}{(i\omega_{\log}-n+m)!}\left(\frac{k}{k_*}\right)^{i\omega_{\log}-n+m}(-i\omega_{\mathrm{BAO}})^{m+1}\\
&\quad\left.+\binom{n}{n}\left(\frac{k}{k_*}\right)^{i\omega_{\log}}(-i\omega_{\mathrm{BAO}})^{n+1}\right\}e^{-i\omega_{\mathrm{BAO}}}\\
&= \frac{1}{2}\frac{k_{i_1}\cdots k_{i_n}k_j}{k^{n+1}}\left\{\binom{n}{0}\frac{1}{k_*^{n+1}}\frac{(i\omega_{\log})!}{(i\omega_{\log}-n-1)!}\left(\frac{k}{k_*}\right)^{i\omega_{\log}-n-1}\right.\\
&\quad+\sum_{m=1}^{n}\binom{n+1}{m}\frac{1}{k_*^{n+1-m}}\frac{(i\omega_{\log})!}{(i\omega_{\log}-n-1+m)!}\left(\frac{k}{k_*}\right)^{i\omega_{\log}-n-1+m}(-i\omega_{\mathrm{BAO}})^{m}\\
&\quad\left.+\binom{n}{n}\left(\frac{k}{k_*}\right)^{i\omega_{\log}}(-i\omega_{\mathrm{BAO}})^{n+1}\right\}e^{-i\omega_{\mathrm{BAO}}k}.
\end{aligned}\tag{E.27}$$

Now, since

$$\binom{n}{0}=\binom{n+1}{0}=1\,,\qquad \binom{n}{n}=\binom{n+1}{n+1}=1\,,\tag{E.28}$$

2 We recall that

$$\binom{n+1}{m+1}=\binom{n}{m+1}+\binom{n}{m}.\tag{E.26}$$

we have that

$$
\begin{aligned}
\textcircled{1}+\textcircled{2} = \frac{1}{2}\frac{k_{i_1}\cdots k_{i_n}k_j}{k^{n+1}}\Bigg\{ & \binom{n+1}{0}\frac{1}{k_*^{n+1}}\frac{(i\omega_{\log})!}{(i\omega_{\log}-n-1)!}\left(\frac{k}{k_*}\right)^{i\omega_{\log}-n-1} \\
& + \sum_{m=1}^{n}\binom{n+1}{m}\frac{1}{k_*^{n+1-m}}\frac{(i\omega_{\log})!}{(i\omega_{\log}-n-1+m)!}\left(\frac{k}{k_*}\right)^{i\omega_{\log}-n-1+m}(-i\omega_{\mathrm{BAO}})^m \\
& + \binom{n+1}{n+1}\left(\frac{k}{k_*}\right)^{i\omega_{\log}}(-i\omega_{\mathrm{BAO}})^{n+1}\Bigg\} e^{-i\omega_{\mathrm{BAO}}k} \\
= \frac{1}{2}\frac{k_{i_1}\cdots k_{i_n}k_j}{k^{n+1}} & e^{-i\omega_{\mathrm{BAO}}k} \\
\times \Bigg\{ & \sum_{m=0}^{n+1}\binom{n+1}{m}\frac{1}{k_*^{n+1-m}}\frac{(i\omega_{\log})!}{(i\omega_{\log}-n-1+m)!}\left(\frac{k}{k_*}\right)^{i\omega_{\log}-n-1+m}(-i\omega_{\mathrm{BAO}})^m\Bigg\},
\end{aligned}
\tag{E.29}
$$

which is exactly eq. (E.22) at the $n+1$ iteration, fact that completes our inductive proof.

As we did done before, now we can rewrite the action of the operator appearing in eq. (6.50) now as[3]

$$
\begin{aligned}
& [1-\cos(\mathbf{q}\cdot\nabla_{\mathbf{k}})]P^{\mathrm{w}}_{\mathrm{BAO}}(k)\,\delta P^{\log}_{\zeta}(k) = \\
& = \left[1-\sum_{n=0}^{\infty}\frac{1}{(2n)!}(\mathbf{q}\cdot\nabla_{\mathbf{k}})^{2n}\right]P^{\mathrm{w}}_{\mathrm{BAO}}(k)\,\delta P^{\log}_{\zeta}(k) \\
& = P_L^{\mathrm{nw}}A_{\mathrm{BAO}}(k)\,(k)\,A_{\log}\Bigg\{\sin(\omega_{\mathrm{BAO}}k)\sin\left(\omega_{\log}\ln\frac{k}{k_*}\right) \\
& \quad - \frac{e^{i\omega_{\mathrm{BAO}}k}}{2}\sum_{n=0}^{\infty}\frac{1}{(2n)!}\frac{(i\omega_{\log})!}{(-2n+i\omega_{\log})!}\left(\frac{q\mu}{k_*}\right)^{2n} \\
& \qquad \times {}_1F_1(-2n,1-2n+i\omega_{\log},ik\omega_{\mathrm{BAO}})\left(\frac{k}{k_*}\right)^{-2n+i\omega_{\log}} \\
& \quad + \begin{pmatrix}\omega_{\log}\to-\omega_{\log}\\ \omega_{\mathrm{BAO}}\to-\omega_{\mathrm{BAO}}\end{pmatrix} - \begin{pmatrix}\omega_{\log}\to\omega_{\log}\\ \omega_{\mathrm{BAO}}\to-\omega_{\mathrm{BAO}}\end{pmatrix} - \begin{pmatrix}\omega_{\log}\to-\omega_{\log}\\ \omega_{\mathrm{BAO}}\to\omega_{\mathrm{BAO}}\end{pmatrix}\Bigg\}
\end{aligned}
\tag{E.30}
$$

where ${}_pF_q$ is the hypergeometric function, defined as

$${}_pF_q(a_1,a_2,\ldots,a_p;b_1,b_2,\ldots,b_q;z) = \sum_{n=0}^{\infty}\frac{(a_1)_n(a_2)_n\cdots(a_p)_n}{(b_1)_n(b_2)_n\cdots(b_q)_n}\frac{z^n}{n!}, \tag{E.31}$$

with $(a)_n$ representing the Pochhammer symbol

$$(a)_n = a(a+1)(a+2)\cdots(a+n-1) = \frac{\Gamma(a+n)}{\Gamma(a)}, \tag{E.32}$$

3 Here the two additional terms in the third line are due to the presence of the second cosine term in the wiggle mixed power spectrum, neglected during the computation of this appendix as mentioned in the previous footnote.

with an analogous expression for $(b)_n$. Unfortunately this expression does not admit any closed representation and thus we are not able to give a single formula for the damping in this case which, to be computed require the use of specific numeric methods. However, given the small magnitude of this correction observed in the strong approximation, we do not pursue a precise evaluation in this weak approximation, which is beyond the purposes of this work.

ACRONYMS

1PI	1–Particle Irreducible
2HDM	Two–Higgs–Doublet Model
ACT	Atacama Cosmology Telescope
BAO	Baryon Acoustic Oscillations
BBGKY	Bogoljubov–Born–Green–Kirkwood–Yvon
BBN	Big Bang Nucleosynthesis
BOSS	Baryon Oscillation Spectroscopic Survey
BSM	Beyond the Standard Model
CC	Charged–Current
CDM	Cold Dark Matter
CKM	Cabibbo–Kobayashi–Maskawa
CMB	Cosmic Microwave Background
CNB	Cosmic Neutrino Background
COBE	COsmic Background Explorer
DES	Dark Energy Survey
DESI	Dark Energy Spectroscopic Instrument
DM	Dark Matter
DUNE	Deep Underground Neutrino Experiment
EdS	Einstein–de Sitter
EFT	Effective Field Theory
eBOSS	extended Baryon Oscillation Spectroscopic Survey
EW	ElectroWeak
EWSB	ElectroWeak Simmetry Breaking
FRW	Friedmann–Robertson–Walker
GUT	Grand Unified Theory
HML	Heavy Mediator Limit
IO	Inverted Ordering
IRs	Irreducible Representations
ISW	Integrated Sach–Wolfe
KiDS	Kilo–Degree Survey
KL	Kullback–Leibler
lhs	left–hand side
LH	Left–Handed
LML	Light Mediator Limit
LO	Leading Order
LRG	Luminous Red Galaxy
LSS	Large–Scale Structure
LSST	Vera C. Rubin Observatory's Legacy Survey of Space and Time
MAP	Maximum A Posteriori
MBAC	Millimeter Bolometric Array Camera
MCMC	Markov Chain Monte Carlo
MSW	Micheev–Smirnov–Wolfenstein
NC	Neutral–Current
NCDM	Non–Cold Dark Matter
NO	Normal Ordering
NSI	Non–Standard Interactions
NLO	Next–to–Leading Order
PDF	Probability Density Function
PGWs	Primordial Gravitational Waves
PMNS	Pontecorvo–Maki–Nakagawa–Sakata
QBE	Quantum Boltzmann Equation
QCD	Quantum ChromoDynamics
QED	Quantum ElectroDynamics
QFT	Quantum Field Theory
RH	Right–Handed
rhs	right–hand side
SNO	Sudbury Neutrino Observatory
SNR	Signal–to–Noise Ratio
SKAO	Square Kilometer Array Observatory
SM	Standard Model
SSB	Spontaneous Symmetry Breaking
SUSY	SUperSYmmetry
TSPT	Time–Slice Perturbation Theory

vev vacuum expectation value

WIMPs Weakly–Interacting Massive Particles

WMAP Wilkinson Microwave Anisotropy Probe

BIBLIOGRAPHY

Abazajian, K. N. (2017). "Sterile neutrinos in cosmology." In: *Phys. Rept.* **711-712**, pp. 1–28. DOI: 10.1016/j.physrep.2017.10.003. arXiv: 1705.01837 [hep-ph] (cit. on p. 210).

Abazajian, K. N. et al. (Oct. 2016). "CMB-S4 Science Book, First Edition." In: arXiv: 1610.02743 [astro-ph.CO] (cit. on p. xix).

Acciarri, R. et al. (Dec. 2015). "Long-Baseline Neutrino Facility (LBNF) and Deep Underground Neutrino Experiment (DUNE): Conceptual Design Report, Volume 2: The Physics Program for DUNE at LBNF." In: arXiv: 1512.06148 [physics.ins-det] (cit. on p. 148).

Achucarro, A., J.-O. Gong, S. Hardeman, G. A. Palma, and S. P. Patil (2011). "Features of heavy physics in the CMB power spectrum." In: *JCAP* **01**, p. 030. DOI: 10.1088/1475-7516/2011/01/030. arXiv: 1010.3693 [hep-ph] (cit. on pp. 183, 184).

Adame, A. G. et al. (Apr. 2024a). "DESI 2024 III: Baryon Acoustic Oscillations from Galaxies and Quasars." In: arXiv: 2404.03000 [astro-ph.CO] (cit. on p. 160).

– (Apr. 2024b). "DESI 2024 VI: Cosmological Constraints from the Measurements of Baryon Acoustic Oscillations." In: arXiv: 2404.03002 [astro-ph.CO] (cit. on pp. 98, 160, 212).

– (2024c). "Validation of the Scientific Program for the Dark Energy Spectroscopic Instrument." In: *Astron. J.* **167**.2, p. 62. DOI: 10.3847/1538-3881/ad0b08. arXiv: 2306.06307 [astro-ph.CO] (cit. on p. xx).

Adams, J. A., B. Cresswell, and R. Easther (2001). "Inflationary perturbations from a potential with a step." In: *Phys. Rev. D* **64**, p. 123514. DOI: 10.1103/PhysRevD.64.123514. arXiv: astro-ph/0102236 (cit. on pp. 183, 184).

Ade, P. A. R. et al. (2016). "Planck 2015 results. XV. Gravitational lensing." In: *Astron. Astrophys.* **594**, A15. DOI: 10.1051/0004-6361/201525941. arXiv: 1502.01591 [astro-ph.CO] (cit. on p. 160).

– (2021). "Improved Constraints on Primordial Gravitational Waves using Planck, WMAP, and BICEP/Keck Observations through the 2018 Observing Season." In: *Phys. Rev. Lett.* **127**.15, p. 151301. DOI: 10.1103/PhysRevLett.127.151301. arXiv: 2110.00483 [astro-ph.CO] (cit. on p. 42).

Aghanim, N. et al. (2020a). "Planck 2018 results. I. Overview and the cosmological legacy of Planck." In: *Astron. Astrophys.* **641**, A1. DOI: 10.1051/0004-6361/201833880. arXiv: 1807.06205 [astro-ph.CO] (cit. on pp. ii, xix).

– (2020b). "Planck 2018 results. V. CMB power spectra and likelihoods." In: *Astron. Astrophys.* **641**, A5. DOI: 10.1051/0004-6361/201936386. arXiv: 1907.12875 [astro-ph.CO] (cit. on pp. 93, 97, 98).

Aghanim, N. et al. (2020c). "Planck 2018 results. VI. Cosmological parameters." In: *Astron. Astrophys.* **641**. [Erratum: Astron.Astrophys. 652, C4 (2021)], A6. DOI: 10.1051/0004-6361/201833910. arXiv: 1807.06209 [astro-ph.CO] (cit. on pp. xix, 18, 31, 97, 160, 184, 200, 210).

– (2020d). "Planck 2018 results. VIII. Gravitational lensing." In: *Astron. Astrophys.* **641**, A8. DOI: 10.1051/0004-6361/201833886. arXiv: 1807.06210 [astro-ph.CO] (cit. on pp. 97, 210).

Agostini, M. et al. (2020). "Final Results of GERDA on the Search for Neutrinoless Double-β Decay." In: *Phys. Rev. Lett.* **125**.25, p. 252502. DOI: 10.1103/PhysRevLett.125.252502. arXiv: 2009.06079 [nucl-ex] (cit. on p. 172).

Aiola, S. et al. (2020). "The Atacama Cosmology Telescope: DR4 Maps and Cosmological Parameters." In: *JCAP* **12**, p. 047. DOI: 10.1088/1475-7516/2020/12/047. arXiv: 2007.07288 [astro-ph.CO] (cit. on pp. 157, 158).

Akrami, Y. et al. (2020). "Planck 2018 results. X. Constraints on inflation." In: *Astron. Astrophys.* **641**, A10. DOI: 10.1051/0004-6361/201833887. arXiv: 1807.06211 [astro-ph.CO] (cit. on pp. 42, 200).

Alam, S. et al. (2017). "The clustering of galaxies in the completed SDSS-III Baryon Oscillation Spectroscopic Survey: cosmological analysis of the DR12 galaxy sample." In: *Mon. Not. Roy. Astron. Soc.* **470**.3, pp. 2617–2652. DOI: 10.1093/mnras/stx721. arXiv: 1607.03155 [astro-ph.CO] (cit. on pp. 97, 160).

– (2021). "Completed SDSS-IV extended Baryon Oscillation Spectroscopic Survey: Cosmological implications from two decades of spectroscopic surveys at the Apache Point Observatory." In: *Phys. Rev. D* **103**.8, p. 083533. DOI: 10.1103/PhysRevD.103.083533. arXiv: 2007.08991 [astro-ph.CO] (cit. on pp. 97, 160).

Alvey, J., M. Escudero, and N. Sabti (2022). "What can CMB observations tell us about the neutrino distribution function?" In: *JCAP* **02**.02, p. 037. DOI: 10.1088/1475-7516/2022/02/037. arXiv: 2111.12726 [astro-ph.CO] (cit. on p. 95).

Alvi, S., T. Brinckmann, M. Gerbino, M. Lattanzi, and L. Pagano (2022). "Do you smell something decaying? Updated linear constraints on decaying dark matter scenarios." In: *JCAP* **11**, p. 015. DOI: 10.1088/1475-7516/2022/11/015. arXiv: 2205.05636 [astro-ph.CO] (cit. on p. 98).

Archidiacono, M. and S. Hannestad (2014). "Updated constraints on non-standard neutrino interactions from Planck." In: *JCAP* **07**, p. 046. DOI: 10.1088/1475-7516/2014/07/046. arXiv: 1311.3873 [astro-ph.CO] (cit. on p. 168).

Armendariz-Picon, C. and E. A. Lim (2003). "Vacuum choices and the predictions of inflation." In: *JCAP* **12**, p. 006. DOI: 10.1088/1475-7516/2003/12/006. arXiv: hep-th/0303103 (cit. on p. 184).

Arnold, R. et al. (2014). "Search for neutrinoless double-beta decay of ^{100}Mo with the NEMO-3 detector." In: *Phys. Rev. D* **89**.11, p. 111101. DOI: 10.1103/PhysRevD.89.111101. arXiv: 1311.5695 [hep-ex] (cit. on p. 172).

Audren, B., J. Lesgourgues, K. Benabed, and S. Prunet (2013). "Conservative Constraints on Early Cosmology: an illustration of the Monte Python cosmological parameter inference code." In: *JCAP* **02**, p. 001. DOI: 10.1088/1475-7516/2013/02/001. arXiv: 1210.7183 [astro-ph.CO] (cit. on pp. 96, 98).

Bacon, D. J. et al. (2020). "Cosmology with Phase 1 of the Square Kilometre Array: Red Book 2018: Technical specifications and performance forecasts." In: *Publ. Astron. Soc. Austral.* **37**, e007. DOI: 10.1017/pasa.2019.51. arXiv: 1811.02743 [astro-ph.CO] (cit. on p. xx).

Ballardini, M. et al. (2024). "Euclid: The search for primordial features." In: *Astron. Astrophys.* **683**, A220. DOI: 10.1051/0004-6361/202348162. arXiv: 2309.17287 [astro-ph.CO] (cit. on pp. 201, 202, 212).

Ballardini, M. and N. Barbieri (Nov. 2024). "Refining the nonlinear modelling of primordial oscillatory features." In: arXiv: 2411.02261 [astro-ph.CO] (cit. on pp. xxii, 175).

Ballardini, M. and F. Finelli (2022). "On the primordial origin of the smoothing excess in the Planck temperature power spectrum in light of LSS data." In: *JCAP* **10**, p. 083. DOI: 10.1088/1475-7516/2022/10/083. arXiv: 2207.14410 [astro-ph.CO] (cit. on pp. 200, 201).

Ballardini, M., R. Murgia, M. Baldi, F. Finelli, and M. Viel (2020). "Non-linear damping of superimposed primordial oscillations on the matter power spectrum in galaxy surveys." In: *JCAP* **04**.04, p. 030. DOI: 10.1088/1475-7516/2020/04/030. arXiv: 1912.12499 [astro-ph.CO] (cit. on pp. 201, 202).

Ballesteros, G., J. Redondo, A. Ringwald, and C. Tamarit (2017). "Standard Model—axion—seesaw—Higgs portal inflation. Five problems of particle physics and cosmology solved in one stroke." In: *JCAP* **08**, p. 001. DOI: 10.1088/1475-7516/2017/08/001. arXiv: 1610.01639 [hep-ph] (cit. on p. 115).

– (2019). "Several Problems in Particle Physics and Cosmology Solved in One SMASH." In: *Front. Astron. Space Sci.* **6**, p. 55. DOI: 10.3389/fspas.2019.00055. arXiv: 1904.05594 [hep-ph] (cit. on p. 115).

Barbieri, N., N. Bartolo, M. Lattanzi, and M. Zarei (2025a). "Testing neutrino NSI through CMB polarization." In preparation (cit. on pp. xxi, 109).

Barbieri, N., T. Brinckmann, S. Gariazzo, M. Lattanzi, S. Pastor, and O. Pisanti (Jan. 2025b). "Current constraints on cosmological scenarios with very low reheating temperatures." In: arXiv: 2501.01369 [astro-ph.CO] (cit. on pp. xxi, 77).

Barbieri, R. and A. Dolgov (1991). "Neutrino oscillations in the early universe." In: *Nucl. Phys. B* **349**, pp. 743–753. DOI: 10.1016/0550-3213(91)90396-F (cit. on p. 109).

Barenboim, G., P. B. Denton, and I. M. Oldengott (2019). "Constraints on inflation with an extended neutrino sector." In: *Phys. Rev. D* **99**.8, p. 083515. DOI: 10.1103/PhysRevD.99.083515. arXiv: 1903.02036 [astro-ph.CO] (cit. on p. 168).

Barenboim, G., P. Ko, and W.-i. Park (Mar. 2024a). "The minimal cosmological standard model." In: arXiv: 2403.05390 [hep-ph] (cit. on p. 115).

Barenboim, G., P. Ko, and W.-i. Park (Mar. 2024b). "Axi-majoron for almost everything." In: arXiv: 2403.08675 [hep-ph] (cit. on p. 115).

Bartolo, N., A. Hoseinpour, S. Matarrese, G. Orlando, and M. Zarei (2019). "CMB Circular and B-mode Polarization from New Interactions." In: *Phys. Rev. D* **100**.4, p. 043516. DOI: 10.1103/PhysRevD.100.043516. arXiv: 1903.04578 [hep-ph] (cit. on pp. 110, 211).

Bartolo, N., A. Hoseinpour, G. Orlando, S. Matarrese, and M. Zarei (2018). "Photon-graviton scattering: A new way to detect anisotropic gravitational waves?" In: *Phys. Rev. D* **98**.2, p. 023518. DOI: 10.1103/PhysRevD.98.023518. arXiv: 1804.06298 [gr-qc] (cit. on p. 110).

Bashinsky, S. and U. Seljak (2004). "Neutrino perturbations in CMB anisotropy and matter clustering." In: *Phys. Rev. D* **69**, p. 083002. DOI: 10.1103/PhysRevD.69.083002. arXiv: astro-ph/0310198 (cit. on pp. 94, 95, 145, 152, 154).

Bassett, B. A. and R. Hlozek (Oct. 2009). "Baryon Acoustic Oscillations." In: arXiv: 0910.5224 [astro-ph.CO] (cit. on p. 160).

Baumann, D. (2011). "Inflation." In: *Theoretical Advanced Study Institute in Elementary Particle Physics: Physics of the Large and the Small*, pp. 523–686. DOI: 10.1142/9789814327183_0010. arXiv: 0907.5424 [hep-th] (cit. on p. 38).

– (July 2022). *Cosmology*. Cambridge University Press. ISBN: 978-1-108-93709-2, 978-1-108-83807-8. DOI: 10.1017/9781108937092 (cit. on pp. 3, 22, 25).

Baumann, D., D. Green, and M. Zaldarriaga (2017). "Phases of New Physics in the BAO Spectrum." In: *JCAP* **11**, p. 007. DOI: 10.1088/1475-7516/2017/11/007. arXiv: 1703.00894 [astro-ph.CO] (cit. on p. 212).

Bautista, J. E. et al. (2020). "The Completed SDSS-IV extended Baryon Oscillation Spectroscopic Survey: measurement of the BAO and growth rate of structure of the luminous red galaxy sample from the anisotropic correlation function between redshifts 0.6 and 1." In: *Mon. Not. Roy. Astron. Soc.* **500**.1, pp. 736–762. DOI: 10.1093/mnras/staa2800. arXiv: 2007.08993 [astro-ph.CO] (cit. on p. 97).

Beacom, J. F., N. F. Bell, and S. Dodelson (2004). "Neutrinoless universe." In: *Phys. Rev. Lett.* **93**, p. 121302. DOI: 10.1103/PhysRevLett.93.121302. arXiv: astro-ph/0404585 (cit. on p. 152).

Bean, R., X. Chen, G. Hailu, S. H. H. Tye, and J. Xu (2008). "Duality Cascade in Brane Inflation." In: *JCAP* **03**, p. 026. DOI: 10.1088/1475-7516/2008/03/026. arXiv: 0802.0491 [hep-th] (cit. on p. 183).

Becker, M. R. et al. (2016). "Cosmic shear measurements with Dark Energy Survey Science Verification data." In: *Phys. Rev. D* **94**.2, p. 022002. DOI: 10.1103/PhysRevD.94.022002. arXiv: 1507.05598 [astro-ph.CO] (cit. on p. xx).

Bennett, C. L. et al. (2003). "The Microwave Anisotropy Probe (MAP) mission." In: *Astrophys. J.* **583**, pp. 1–23. DOI: 10.1086/345346. arXiv: astro-ph/0301158 (cit. on p. xix).

– (2013). "Nine-Year Wilkinson Microwave Anisotropy Probe (WMAP) Observations: Final Maps and Results." In: *Astrophys. J. Suppl.* **208**, p. 20. DOI: 10.1088/0067-0049/208/2/20. arXiv: 1212.5225 [astro-ph.CO] (cit. on p. xix).

Bennett, J. J., G. Buldgen, P. F. De Salas, M. Drewes, S. Gariazzo, S. Pastor, and Y. Y. Y. Wong (2021). "Towards a precision calculation of N_{eff} in the Standard Model II: Neutrino decoupling in the presence of flavour oscillations and finite-temperature QED." In: *JCAP* **04**, p. 073. DOI: 10.1088/1475-7516/2021/04/073. arXiv: 2012.02726 [hep-ph] (cit. on pp. 80, 86, 87).

Berryman, J. M. (2019). "Constraining Sterile Neutrino Cosmology with Terrestrial Oscillation Experiments." In: *Phys. Rev. D* **100**.2, p. 023540. DOI: 10.1103/PhysRevD.100.023540. arXiv: 1905.03254 [hep-ph] (cit. on p. 79).

Bethe, H. A. (1986). "A Possible Explanation of the Solar Neutrino Puzzle." In: *Phys. Rev. Lett.* **56**, p. 1305. DOI: 10.1103/PhysRevLett.56.1305 (cit. on p. 60).

Beutler, F., M. Biagetti, D. Green, A. Slosar, and B. Wallisch (2019). "Primordial Features from Linear to Nonlinear Scales." In: *Phys. Rev. Res.* **1**.3, p. 033209. DOI: 10.1103/PhysRevResearch.1.033209. arXiv: 1906.08758 [astro-ph.CO] (cit. on pp. 186, 189, 191, 194, 200, 202, 212, 231, 234, 235).

Beutler, F., C. Blake, M. Colless, D. H. Jones, L. Staveley-Smith, L. Campbell, Q. Parker, W. Saunders, and F. Watson (2011). "The 6dF Galaxy Survey: Baryon Acoustic Oscillations and the Local Hubble Constant." In: *Mon. Not. Roy. Astron. Soc.* **416**, pp. 3017–3032. DOI: 10.1111/j.1365-2966.2011.19250.x. arXiv: 1106.3366 [astro-ph.CO] (cit. on pp. 97, 160).

Bhatnagar, P. L., E. P. Gross, and M. Krook (1954). "A Model for Collision Processes in Gases. 1. Small Amplitude Processes in Charged and Neutral One-Component Systems." In: *Phys. Rev.* **94**, pp. 511–525. DOI: 10.1103/PhysRev.94.511 (cit. on p. 162).

Bilenky, S. M., J. Hosek, and S. T. Petcov (1980). "On Oscillations of Neutrinos with Dirac and Majorana Masses." In: *Phys. Lett. B* **94**, pp. 495–498. DOI: 10.1016/0370-2693(80)90927-2 (cit. on p. 60).

Bilenky, S. M. and B. Pontecorvo (1976a). "Again on Neutrino Oscillations." In: *Lett. Nuovo Cim.* **17**, p. 569. DOI: 10.1007/BF02746567 (cit. on p. 53).

– (1976b). "The Quark-Lepton Analogy and the Muonic Charge." In: *Yad. Fiz.* **24**, pp. 603–608 (cit. on p. 53).

– (1978). "Lepton Mixing and Neutrino Oscillations." In: *Phys. Rept.* **41**, pp. 225–261. DOI: 10.1016/0370-1573(78)90095-9 (cit. on p. 53).

Birrell, J., C.-T. Yang, and J. Rafelski (2014). "Relic Neutrino Freeze-out: Dependence on Natural Constants." In: *Nucl. Phys. B* **890**, pp. 481–517. DOI:

10.1016/j.nuclphysb.2014.11.020. arXiv: 1406.1759 [nucl-th] (cit. on p. 81).

Blas, D., M. Garny, M. M. Ivanov, and S. Sibiryakov (2016a). "Time-Sliced Perturbation Theory II: Baryon Acoustic Oscillations and Infrared Resummation." In: *JCAP* **07**, p. 028. DOI: 10.1088/1475-7516/2016/07/028. arXiv: 1605.02149 [astro-ph.CO] (cit. on pp. 175, 178, 180–182, 186).

– (2016b). "Time-Sliced Perturbation Theory for Large Scale Structure I: General Formalism." In: *JCAP* **07**, p. 052. DOI: 10.1088/1475-7516/2016/07/052. arXiv: 1512.05807 [astro-ph.CO] (cit. on p. 175).

Blas, D., J. Lesgourgues, and T. Tram (2011). "The Cosmic Linear Anisotropy Solving System (CLASS) II: Approximation schemes." In: *JCAP* **07**, p. 034. DOI: 10.1088/1475-7516/2011/07/034. arXiv: 1104.2933 [astro-ph.CO] (cit. on p. 96).

Blinov, N., K. J. Kelly, G. Z. Krnjaic, and S. D. McDermott (2019). "Constraining the Self-Interacting Neutrino Interpretation of the Hubble Tension." In: *Phys. Rev. Lett.* **123**.19, p. 191102. DOI: 10.1103/PhysRevLett.123.191102. arXiv: 1905.02727 [astro-ph.CO] (cit. on pp. 171, 172).

Blum, K. (2012). *Density Matrix Theory and Applications*. Vol. 64. Springer Series on Atomic, Optical and Plasma Physics. Berlin, Heidelberg: Springer. ISBN: 978-3-642-20560-6, 978-3-642-20561-3. DOI: 10.1007/978-3-642-20561-3 (cit. on p. 225).

Blum, K., Y. Nir, and M. Shavit (2018). "Neutrinoless double-beta decay with massive scalar emission." In: *Phys. Lett. B* **785**, pp. 354–361. DOI: 10.1016/j.physletb.2018.08.022. arXiv: 1802.08019 [hep-ph] (cit. on p. 172).

Boggess, N. W. et al. (1992). "The COBE mission - Its design and performance two years after launch." In: *Astrophys. J.* **397**, pp. 420–429. DOI: 10.1086/171797 (cit. on p. xix).

Bond, J. R. and G. Efstathiou (1987). "The statistics of cosmic background radiation fluctuations." In: *Mon. Not. Roy. Astron. Soc.* **226**, pp. 655–687 (cit. on p. 227).

Bourboux, H. du Mas des et al. (2020). "The Completed SDSS-IV Extended Baryon Oscillation Spectroscopic Survey: Baryon Acoustic Oscillations with Lyα Forests." In: *Astrophys. J.* **901**.2, p. 153. DOI: 10.3847/1538-4357/abb085. arXiv: 2007.08995 [astro-ph.CO] (cit. on p. 97).

Braglia, M., X. Chen, D. K. Hazra, and L. Pinol (2023). "Back to the features: assessing the discriminating power of future CMB missions on inflationary models." In: *JCAP* **03**, p. 014. DOI: 10.1088/1475-7516/2023/03/014. arXiv: 2210.07028 [astro-ph.CO] (cit. on p. 184).

Braglia, M., D. K. Hazra, L. Sriramkumar, and F. Finelli (2020). "Generating primordial features at large scales in two field models of inflation." In: *JCAP* **08**, p. 025. DOI: 10.1088/1475-7516/2020/08/025. arXiv: 2004.00672 [astro-ph.CO] (cit. on p. 183).

Brinckmann, T., J. H. Chang, and M. LoVerde (2021). "Self-interacting neutrinos, the Hubble parameter tension, and the cosmic microwave background." In: *Phys. Rev. D* **104**.6, p. 063523. DOI: 10.1103/PhysRevD.104.063523. arXiv: 2012.11830 [astro-ph.CO] (cit. on p. 168).

Brinckmann, T. and J. Lesgourgues (2019). "MontePython 3: boosted MCMC sampler and other features." In: *Phys. Dark Univ.* **24**, p. 100260. DOI: 10.1016/j.dark.2018.100260. arXiv: 1804.07261 [astro-ph.CO] (cit. on pp. 96, 98).

Calabrese, E. et al. (Mar. 2025). "The Atacama Cosmology Telescope: DR6 Constraints on Extended Cosmological Models." In: arXiv: 2503.14454 [astro-ph.CO] (cit. on pp. xxi, 143, 170, 171).

Cannoni, M. (2014). "Relativistic $< \sigma v_{\rm rel} >$ in the calculation of relics abundances: a closer look." In: *Phys. Rev. D* **89**.10, p. 103533. DOI: 10.1103/PhysRevD.89.103533. arXiv: 1311.4508 [astro-ph.CO] (cit. on p. 30).

Carroll, S. M., S. Leichenauer, and J. Pollack (2014). "Consistent effective theory of long-wavelength cosmological perturbations." In: *Phys. Rev. D* **90**.2, p. 023518. DOI: 10.1103/PhysRevD.90.023518. arXiv: 1310.2920 [hep-th] (cit. on p. 176).

Carron, J., M. Mirmelstein, and A. Lewis (2022). "CMB lensing from Planck PR4 maps." In: *JCAP* **09**, p. 039. DOI: 10.1088/1475-7516/2022/09/039. arXiv: 2206.07773 [astro-ph.CO] (cit. on p. 159).

Chandrasekhar, S. (1960). *Radiative Transfer*. Dover Books on Intermediate and Advanced Mathematics. Dover Publications. ISBN: 9780486605906. URL: https://books.google.es/books?id=K7YLRcTP_XUC (cit. on p. 227).

Chen, S.-F., Z. Vlah, and M. White (2020). "Modeling features in the redshift-space halo power spectrum with perturbation theory." In: *JCAP* **11**, p. 035. DOI: 10.1088/1475-7516/2020/11/035. arXiv: 2007.00704 [astro-ph.CO] (cit. on p. 201).

Chen, X. (2010). "Folded Resonant Non-Gaussianity in General Single Field Inflation." In: *JCAP* **12**, p. 003. DOI: 10.1088/1475-7516/2010/12/003. arXiv: 1008.2485 [hep-th] (cit. on p. 183).

– (2012). "Primordial Features as Evidence for Inflation." In: *JCAP* **01**, p. 038. DOI: 10.1088/1475-7516/2012/01/038. arXiv: 1104.1323 [hep-th] (cit. on pp. 183, 184).

Chen, X., R. Easther, and E. A. Lim (2007). "Large Non-Gaussianities in Single Field Inflation." In: *JCAP* **06**, p. 023. DOI: 10.1088/1475-7516/2007/06/023. arXiv: astro-ph/0611645 (cit. on p. 183).

– (2008). "Generation and Characterization of Large Non-Gaussianities in Single Field Inflation." In: *JCAP* **04**, p. 010. DOI: 10.1088/1475-7516/2008/04/010. arXiv: 0801.3295 [astro-ph] (cit. on p. 183).

Chikashige, Y., R. N. Mohapatra, and R. D. Peccei (1980). "Spontaneously Broken Lepton Number and Cosmological Constraints on the Neutrino Mass Spectrum." In: *Phys. Rev. Lett.* **45**, p. 1926. DOI: 10.1103/PhysRevLett.45.1926 (cit. on p. 150).

Chikashige, Y., R. N. Mohapatra, and R. D. Peccei (1981). "Are There Real Goldstone Bosons Associated with Broken Lepton Number?" In: *Phys. Lett. B* **98**, pp. 265–268. DOI: 10.1016/0370-2693(81)90011-3 (cit. on pp. 114, 150).

Chluba, J., G. M. Vasil, and L. J. Dursi (2010). "Recombinations to the Rydberg States of Hydrogen and Their Effect During the Cosmological Recombination Epoch." In: *Mon. Not. Roy. Astron. Soc.* **407**, p. 599. DOI: 10.1111/j.1365-2966.2010.16940.x. arXiv: 1003.4928 [astro-ph.CO] (cit. on p. 161).

Choi, S. K. et al. (2020). "The Atacama Cosmology Telescope: a measurement of the Cosmic Microwave Background power spectra at 98 and 150 GHz." In: *JCAP* **12**, p. 045. DOI: 10.1088/1475-7516/2020/12/045. arXiv: 2007.07289 [astro-ph.CO] (cit. on pp. 157, 158).

Cyr-Racine, F.-Y. and K. Sigurdson (2014). "Limits on Neutrino-Neutrino Scattering in the Early Universe." In: *Phys. Rev. D* **90**.12, p. 123533. DOI: 10.1103/PhysRevD.90.123533. arXiv: 1306.1536 [astro-ph.CO] (cit. on pp. 154, 167, 168).

Danielewicz, P. (1984). "Quantum Theory of Nonequilibrium Processes. 1." In: *Annals Phys.* **152**, pp. 239–304. DOI: 10.1016/0003-4916(84)90092-7 (cit. on p. 116).

Darwish, O. et al. (2020). "The Atacama Cosmology Telescope: A CMB lensing mass map over 2100 square degrees of sky and its cross-correlation with BOSS-CMASS galaxies." In: *Mon. Not. Roy. Astron. Soc.* **500**.2, pp. 2250–2263. DOI: 10.1093/mnras/staa3438. arXiv: 2004.01139 [astro-ph.CO] (cit. on pp. 157, 158).

Das, A. and S. Ghosh (2021). "Flavor-specific interaction favors strong neutrino self-coupling in the early universe." In: *JCAP* **07**, p. 038. DOI: 10.1088/1475-7516/2021/07/038. arXiv: 2011.12315 [astro-ph.CO] (cit. on p. 168).

Das, S. et al. (2011). "The Atacama Cosmology Telescope: A Measurement of the Cosmic Microwave Background Power Spectrum at 148 and 218 GHz from the 2008 Southern Survey." In: *Astrophys. J.* **729**, p. 62. DOI: 10.1088/0004-637X/729/1/62. arXiv: 1009.0847 [astro-ph.CO] (cit. on pp. 157–159).

Davidson, S., E. Nardi, and Y. Nir (2008). "Leptogenesis." In: *Phys. Rept.* **466**, pp. 105–177. DOI: 10.1016/j.physrep.2008.06.002. arXiv: 0802.2962 [hep-ph] (cit. on pp. 72, 73).

Dawson, K. S. et al. (2013). "The Baryon Oscillation Spectroscopic Survey of SDSS-III." In: *Astron. J.* **145**, p. 10. DOI: 10.1088/0004-6256/145/1/10. arXiv: 1208.0022 [astro-ph.CO] (cit. on p. xx).

– (2016). "The SDSS-IV extended Baryon Oscillation Spectroscopic Survey: Overview and Early Data." In: *Astron. J.* **151**, p. 44. DOI: 10.3847/0004-6256/151/2/44. arXiv: 1508.04473 [astro-ph.CO] (cit. on p. xx).

Dodelson, S. (2003). *Modern Cosmology*. Amsterdam: Academic Press. ISBN: 978-0-12-219141-1 (cit. on p. 3).

Doi, M., T. Kotani, H. Nishiura, K. Okuda, and E. Takasugi (1981). "CP Violation in Majorana Neutrinos." In: *Phys. Lett. B* **102**, pp. 323–326. DOI: 10.1016/0370-2693(81)90627-4 (cit. on p. 60).

Dolgov, A. D. (1981). "Neutrinos in the Early Universe." In: *Sov. J. Nucl. Phys.* **33**, pp. 700–706 (cit. on p. 109).

Dolgov, A. D., S. H. Hansen, S. Pastor, S. T. Petcov, G. G. Raffelt, and D. V. Semikoz (2002). "Cosmological bounds on neutrino degeneracy improved by flavor oscillations." In: *Nucl. Phys. B* **632**, pp. 363–382. DOI: 10.1016/S0550-3213(02)00274-2. arXiv: hep-ph/0201287 (cit. on p. 81).

Dolgov, A. D., S. H. Hansen, and D. V. Semikoz (1997). "Nonequilibrium corrections to the spectra of massless neutrinos in the early universe." In: *Nucl. Phys. B* **503**, pp. 426–444. DOI: 10.1016/S0550-3213(97)00479-3. arXiv: hep-ph/9703315 (cit. on pp. 80, 81).

– (1999). "Nonequilibrium corrections to the spectra of massless neutrinos in the early universe: Addendum." In: *Nucl. Phys. B* **543**, pp. 269–274. DOI: 10.1016/S0550-3213(98)00818-9. arXiv: hep-ph/9805467 (cit. on p. 81).

Drewes, M., Y. Georis, M. Klasen, L. P. Wiggering, and Y. Y. Y. Wong (2024). "Towards a precision calculation of N_{eff} in the Standard Model. Part III. Improved estimate of NLO contributions to the collision integral." In: *JCAP* **06**, p. 032. DOI: 10.1088/1475-7516/2024/06/032. arXiv: 2402.18481 [hep-ph] (cit. on p. 80).

Dunkley, J. et al. (2011). "The Atacama Cosmology Telescope: Cosmological Parameters from the 2008 Power Spectra." In: *Astrophys. J.* **739**, p. 52. DOI: 10.1088/0004-637X/739/1/52. arXiv: 1009.0866 [astro-ph.CO] (cit. on p. 157).

Dunner, R. et al. (2013). "The Atacama Cosmology Telescope: Data Characterization and Map Making." In: *Astrophys. J.* **762**, p. 10. DOI: 10.1088/0004-637X/762/1/10. arXiv: 1208.0050 [astro-ph.IM] (cit. on p. 157).

Dyson, F. J. (1949). "The S matrix in quantum electrodynamics." In: *Phys. Rev.* **75**, pp. 1736–1755. DOI: 10.1103/PhysRev.75.1736 (cit. on p. 224).

Eisenstein, D. J. (2005). "Dark energy and cosmic sound." In: *New Astron. Rev.* **49**.7-9, pp. 360–365. DOI: 10.1016/j.newar.2005.08.005 (cit. on p. 160).

Eisenstein, D. J. and W. Hu (1998). "Baryonic features in the matter transfer function." In: *Astrophys. J.* **496**, p. 605. DOI: 10.1086/305424. arXiv: astro-ph/9709112 (cit. on p. 184).

Eliezer, S. and A. R. Swift (1976). "Experimental Consequences of electron Neutrino-Muon-neutrino Mixing in Neutrino Beams." In: *Nucl. Phys. B* **105**, pp. 45–51. DOI: 10.1016/0550-3213(76)90059-6 (cit. on p. 53).

Engelen, A. van et al. (2015). "The Atacama Cosmology Telescope: Lensing of CMB Temperature and Polarization Derived from Cosmic Infrared Background Cross-Correlation." In: *Astrophys. J.* **808**.1, p. 7. DOI: 10.1088/0004-637X/808/1/7. arXiv: 1412.0626 [astro-ph.CO] (cit. on p. 158).

Escudero, M. (2019). "Neutrino decoupling beyond the Standard Model: CMB constraints on the Dark Matter mass with a fast and precise $N_{\rm eff}$

evaluation." In: *JCAP* **02**, p. 007. DOI: 10.1088/1475-7516/2019/02/007. arXiv: 1812.05605 [hep-ph] (cit. on p. 17).

Esposito, S., G. Miele, S. Pastor, M. Peloso, and O. Pisanti (2000). "Nonequilibrium spectra of degenerate relic neutrinos." In: *Nucl. Phys. B* **590**, pp. 539–561. DOI: 10.1016/S0550-3213(00)00554-X. arXiv: astro-ph/0005573 (cit. on p. 81).

Fang, X., J. A. Blazek, J. E. McEwen, and C. M. Hirata (2017). "FAST-PT II: an algorithm to calculate convolution integrals of general tensor quantities in cosmological perturbation theory." In: *JCAP* **02**, p. 030. DOI: 10.1088/1475-7516/2017/02/030. arXiv: 1609.05978 [astro-ph.CO] (cit. on p. 202).

Fidler, C. and C. Pitrou (2017). "Kinetic theory of fermions in curved spacetime." In: *JCAP* **06**, p. 013. DOI: 10.1088/1475-7516/2017/06/013. arXiv: 1701.08844 [cond-mat.stat-mech] (cit. on p. 112).

Fiorini, L. (2007). "Testing LFV measuring the ratio R(K) between the branching ratio of K+- —> e+- nu (gamma) and K+- —> mu+- nu (gamma) in NA48/2 experiment: Measurement and perspectives." In: *Nucl. Phys. B Proc. Suppl.* **169**. Ed. by F. Cei, I. Ferrante, and A. Lusiani, pp. 205–209. DOI: 10.1016/j.nuclphysbps.2007.03.030 (cit. on p. 172).

Fixsen, D. J. (2009). "The Temperature of the Cosmic Microwave Background." In: *Astrophys. J.* **707**, pp. 916–920. DOI: 10.1088/0004-637X/707/2/916. arXiv: 0911.1955 [astro-ph.CO] (cit. on pp. 4, 25).

Flauger, R., L. McAllister, E. Pajer, A. Westphal, and G. Xu (2010). "Oscillations in the CMB from Axion Monodromy Inflation." In: *JCAP* **06**, p. 009. DOI: 10.1088/1475-7516/2010/06/009. arXiv: 0907.2916 [hep-th] (cit. on pp. 183, 184).

Flauger, R. and E. Pajer (2011). "Resonant Non-Gaussianity." In: *JCAP* **01**, p. 017. DOI: 10.1088/1475-7516/2011/01/017. arXiv: 1002.0833 [hep-th] (cit. on pp. 183, 184).

Foot, R., H. Lew, X. G. He, and G. C. Joshi (1989). "Seesaw Neutrino Masses Induced by a Triplet of Leptons." In: *Z. Phys. C* **44**, p. 441. DOI: 10.1007/BF01415558 (cit. on p. 72).

Forastieri, F., M. Lattanzi, and P. Natoli (2015). "Constraints on secret neutrino interactions after Planck." In: *JCAP* **07**, p. 014. DOI: 10.1088/1475-7516/2015/07/014. arXiv: 1504.04999 [astro-ph.CO] (cit. on p. 162).

– (2019). "Cosmological constraints on neutrino self-interactions with a light mediator." In: *Phys. Rev. D* **100**.10, p. 103526. DOI: 10.1103/PhysRevD.100.103526. arXiv: 1904.07810 [astro-ph.CO] (cit. on pp. 152, 162).

Fowler, J. M. et al. (2007). "Optical Design of the Atacama Cosmology Telescope and the Millimeter Bolometric Array Camera." In: *Appl. Opt.* **46**, pp. 3444–3454. DOI: 10.1364/AO.46.003444. arXiv: astro-ph/0701020 (cit. on p. 156).

Fritzsch, H., M. Gell-Mann, and H. Leutwyler (1973). "Advantages of the Color Octet Gluon Picture." In: *Phys. Lett. B* **47**, pp. 365–368. DOI: 10.1016/0370-2693(73)90625-4 (cit. on p. 61).

Fritzsch, H. and P. Minkowski (1976). "Vector-Like Weak Currents, Massive Neutrinos, and Neutrino Beam Oscillations." In: *Phys. Lett. B* **62**, pp. 72–76. DOI: 10.1016/0370-2693(76)90051-4 (cit. on p. 53).

Galitzki, N. et al. (2018). "The Simons Observatory: Instrument Overview." In: *Proc. SPIE Int. Soc. Opt. Eng.* **10708**. Ed. by G. Z. Angeli and P. Dierickx, p. 1070804. DOI: 10.1117/12.2312985. arXiv: 1808.04493 [astro-ph.IM] (cit. on p. xix).

Gariazzo, S., P. F. de Salas, and S. Pastor (2019). "Thermalisation of sterile neutrinos in the early Universe in the 3+1 scheme with full mixing matrix." In: *JCAP* **07**, p. 014. DOI: 10.1088/1475-7516/2019/07/014. arXiv: 1905.11290 [astro-ph.CO] (cit. on p. 86).

Gariazzo, S., P. F. de Salas, O. Pisanti, and R. Consiglio (2022a). "PArthENoPE revolutions." In: *Comput. Phys. Commun.* **271**, p. 108205. DOI: 10.1016/j.cpc.2021.108205. arXiv: 2103.05027 [astro-ph.IM] (cit. on p. 88).

Gariazzo, S. et al. (2022b). "Neutrino mass and mass ordering: no conclusive evidence for normal ordering." In: *JCAP* **10**, p. 010. DOI: 10.1088/1475-7516/2022/10/010. arXiv: 2205.02195 [hep-ph] (cit. on pp. 216, 217).

Ge, S.-F. and S. J. Parke (2019). "Scalar Nonstandard Interactions in Neutrino Oscillation." In: *Phys. Rev. Lett.* **122**.21, p. 211801. DOI: 10.1103/PhysRevLett.122.211801. arXiv: 1812.08376 [hep-ph] (cit. on p. 149).

Gelmini, G. B. and M. Roncadelli (1981). "Left-Handed Neutrino Mass Scale and Spontaneously Broken Lepton Number." In: *Phys. Lett. B* **99**, pp. 411–415. DOI: 10.1016/0370-2693(81)90559-1 (cit. on p. 114).

Gelmini, G. B., P. Lu, and V. Takhistov (2019). "Cosmological Dependence of Non-resonantly Produced Sterile Neutrinos." In: *JCAP* **12**, p. 047. DOI: 10.1088/1475-7516/2019/12/047. arXiv: 1909.13328 [hep-ph] (cit. on p. 210).

Gelmini, G., E. Osoba, S. Palomares-Ruiz, and S. Pascoli (2008). "MeV sterile neutrinos in low reheating temperature cosmological scenarios." In: *JCAP* **10**, p. 029. DOI: 10.1088/1475-7516/2008/10/029. arXiv: 0803.2735 [astro-ph] (cit. on p. 210).

Gelmini, G., S. Palomares-Ruiz, and S. Pascoli (2004). "Low reheating temperature and the visible sterile neutrino." In: *Phys. Rev. Lett.* **93**, p. 081302. DOI: 10.1103/PhysRevLett.93.081302. arXiv: astro-ph/0403323 (cit. on p. 210).

Gerbino, M. (Mar. 2018). "Neutrino properties from cosmology." In: *Prospects in Neutrino Physics*, pp. 52–52. arXiv: 1803.11545 [astro-ph.CO] (cit. on p. 148).

Gil-Marin, H. et al. (2020). "The Completed SDSS-IV extended Baryon Oscillation Spectroscopic Survey: measurement of the BAO and growth rate of structure of the luminous red galaxy sample from the anisotropic power spectrum between redshifts 0.6 and 1.0." In: *Mon. Not. Roy. Astron. Soc.* **498**.2, pp. 2492–2531. DOI: 10.1093/mnras/staa2455. arXiv: 2007.08994 [astro-ph.CO] (cit. on p. 97).

Giudice, G. F., E. W. Kolb, and A. Riotto (2001). "Largest temperature of the radiation era and its cosmological implications." In: *Phys. Rev. D* **64**, p. 023508. DOI: 10.1103/PhysRevD.64.023508. arXiv: hep-ph/0005123 (cit. on p. 85).

Giunti, C. and C. W. Kim (2007). *Fundamentals of Neutrino Physics and Astrophysics*. ISBN: 978-0-19-850871-7. DOI: 10.1093/acprof:oso/9780198508717.001.0001 (cit. on p. 45).

Giunti, C., K. Kouzakov, Y.-F. Li, and A. Studenikin (Nov. 2024). "Neutrino Electromagnetic Properties." In: DOI: 10.1146/annurev-nucl-102122-023242. arXiv: 2411.03122 [hep-ph] (cit. on p. 211).

Glashow, S. L. (1961). "Partial Symmetries of Weak Interactions." In: *Nucl. Phys.* **22**, pp. 579–588. DOI: 10.1016/0029-5582(61)90469-2 (cit. on p. 61).

Gnedin, N. Y. and O. Y. Gnedin (1998). "Cosmological neutrino background revisited." In: *Astrophys. J.* **509**, pp. 11–15. DOI: 10.1086/306469. arXiv: astro-ph/9712199 (cit. on p. 81).

Gralla, M. B. et al. (2014). "A measurement of the millimetre emission and the Sunyaev–Zel'dovich effect associated with low-frequency radio sources." In: *Mon. Not. Roy. Astron. Soc.* **445**.1, pp. 460–478. DOI: 10.1093/mnras/stu1592. arXiv: 1310.8281 [astro-ph.CO] (cit. on p. 158).

– (2020). "Atacama Cosmology Telescope: Dusty star-forming galaxies and active galactic nuclei in the equatorial survey." In: *Astrophys. J.* **893**.2, p. 104. DOI: 10.3847/1538-4357/ab7915. arXiv: 1905.04592 [astro-ph.GA] (cit. on p. 157).

Grohs, E., G. M. Fuller, C. T. Kishimoto, M. W. Paris, and A. Vlasenko (2016). "Neutrino energy transport in weak decoupling and big bang nucleosynthesis." In: *Phys. Rev. D* **93**.8, p. 083522. DOI: 10.1103/PhysRevD.93.083522. arXiv: 1512.02205 [astro-ph.CO] (cit. on p. 81).

Gross, D. J. and F. Wilczek (1973). "Ultraviolet Behavior of Nonabelian Gauge Theories." In: *Phys. Rev. Lett.* **30**. Ed. by J. C. Taylor, pp. 1343–1346. DOI: 10.1103/PhysRevLett.30.1343 (cit. on p. 61).

Guth, A. H. (1981). "The Inflationary Universe: A Possible Solution to the Horizon and Flatness Problems." In: *Phys. Rev. D* **23**. Ed. by L.-Z. Fang and R. Ruffini, pp. 347–356. DOI: 10.1103/PhysRevD.23.347 (cit. on p. 32).

Han, D. et al. (2021). "The Atacama Cosmology Telescope: delensed power spectra and parameters." In: *JCAP* **01**, p. 031. DOI: 10.1088/1475-7516/2021/01/031. arXiv: 2007.14405 [astro-ph.CO] (cit. on pp. 157, 158).

Hand, N. et al. (2012). "Evidence of Galaxy Cluster Motions with the Kinematic Sunyaev-Zel'dovich Effect." In: *Phys. Rev. Lett.* **109**, p. 041101. DOI: 10.1103/PhysRevLett.109.041101. arXiv: 1203.4219 [astro-ph.CO] (cit. on p. 158).

Handley, W. and P. Lemos (2019). "Quantifying dimensionality: Bayesian cosmological model complexities." In: *Phys. Rev. D* **100**.2, p. 023512. DOI: 10.1103/PhysRevD.100.023512. arXiv: 1903.06682 [astro-ph.CO] (cit. on p. 216).

Hannestad, S. (2004). "What is the lowest possible reheating temperature?" In: *Phys. Rev. D* **70**, p. 043506. DOI: 10.1103/PhysRevD.70.043506. arXiv: astro-ph/0403291 (cit. on p. 88).

– (2010). "Neutrino physics from precision cosmology." In: *Prog. Part. Nucl. Phys.* **65**, pp. 185–208. DOI: 10.1016/j.ppnp.2010.07.001. arXiv: 1007.0658 [hep-ph] (cit. on p. 143).

Hannestad, S. and J. Madsen (1995). "Neutrino decoupling in the early universe." In: *Phys. Rev. D* **52**, pp. 1764–1769. DOI: 10.1103/PhysRevD.52.1764. arXiv: astro-ph/9506015 (cit. on p. 81).

Hasegawa, T., N. Hiroshima, K. Kohri, R. S. L. Hansen, T. Tram, and S. Hannestad (2020). "MeV-scale reheating temperature and cosmological production of light sterile neutrinos." In: *JCAP* **08**, p. 015. DOI: 10.1088/1475-7516/2020/08/015. arXiv: 2003.13302 [hep-ph] (cit. on p. 210).

Henderson, S. W. et al. (2016). "Advanced ACTPol Cryogenic Detector Arrays and Readout." In: *J. Low Temp. Phys.* **184**.3-4. Ed. by P. Camus, A. Juillard, and A. Monfardini, pp. 772–779. DOI: 10.1007/s10909-016-1575-z. arXiv: 1510.02809 [astro-ph.IM] (cit. on p. 156).

Hergt, L. T., W. J. Handley, M. P. Hobson, and A. N. Lasenby (2021). "Bayesian evidence for the tensor-to-scalar ratio r and neutrino masses m_ν: Effects of uniform vs logarithmic priors." In: *Phys. Rev. D* **103**, p. 123511. DOI: 10.1103/PhysRevD.103.123511. arXiv: 2102.11511 [astro-ph.CO] (cit. on p. 216).

Hoseinpour, A., M. Zarei, G. Orlando, N. Bartolo, and S. Matarrese (2020). "CMB V modes from photon-photon forward scattering revisited." In: *Phys. Rev. D* **102**.6, p. 063501. DOI: 10.1103/PhysRevD.102.063501. arXiv: 2006.14418 [hep-ph] (cit. on p. 110).

Hou, J. et al. (2020). "The Completed SDSS-IV extended Baryon Oscillation Spectroscopic Survey: BAO and RSD measurements from anisotropic clustering analysis of the Quasar Sample in configuration space between redshift 0.8 and 2.2." In: *Mon. Not. Roy. Astron. Soc.* **500**.1, pp. 1201–1221. DOI: 10.1093/mnras/staa3234. arXiv: 2007.08998 [astro-ph.CO] (cit. on p. 97).

Hou, Z., R. Keisler, L. Knox, M. Millea, and C. Reichardt (2013). "How Massless Neutrinos Affect the Cosmic Microwave Background Damping Tail." In: *Phys. Rev. D* **87**, p. 083008. DOI: 10.1103/PhysRevD.87.083008. arXiv: 1104.2333 [astro-ph.CO] (cit. on pp. 94, 95, 145, 154).

Howlett, C., M. Manera, and W. J. Percival (2015). "L-PICOLA: A parallel code for fast dark matter simulation." In: *Astron. Comput.* **12**, pp. 109–126. DOI: 10.1016/j.ascom.2015.07.003. arXiv: 1506.03737 [astro-ph.CO] (cit. on p. 202).

Hu, W. T. (Aug. 1995). "Wandering in the Background: A CMB Explorer." Other thesis. arXiv: astro-ph/9508126 (cit. on p. 145).

Hu, W. and N. Sugiyama (1996). "Small scale cosmological perturbations: An Analytic approach." In: *Astrophys. J.* **471**, pp. 542–570. DOI: 10.1086/177989. arXiv: astro-ph/9510117 (cit. on p. 184).

Ichikawa, K., M. Kawasaki, and F. Takahashi (2005). "The Oscillation effects on thermalization of the neutrinos in the Universe with low reheating temperature." In: *Phys. Rev. D* **72**, p. 043522. DOI: 10.1103/PhysRevD.72.043522. arXiv: astro-ph/0505395 (cit. on p. 79).

– (2007). "Constraint on the Effective Number of Neutrino Species from the WMAP and SDSS LRG Power Spectra." In: *JCAP* **05**, p. 007. DOI: 10.1088/1475-7516/2007/05/007. arXiv: astro-ph/0611784 (cit. on p. 88).

Itzykson, C. and J. B. Zuber (1980). *Quantum Field Theory*. International Series In Pure and Applied Physics. New York: McGraw-Hill. ISBN: 978-0-486-44568-7 (cit. on p. 220).

Ivezić, v. et al. (2019). "LSST: from Science Drivers to Reference Design and Anticipated Data Products." In: *Astrophys. J.* **873**.2, p. 111. DOI: 10.3847/1538-4357/ab042c. arXiv: 0805.2366 [astro-ph] (cit. on p. xx).

Jackson, G. and M. Laine (2024). "QED corrections to the thermal neutrino interaction rate." In: *JHEP* **05**, p. 089. DOI: 10.1007/JHEP05(2024)089. arXiv: 2312.07015 [hep-ph] (cit. on p. 80).

Kachelriess, M., R. Tomas, and J. W. F. Valle (2000). "Supernova bounds on Majoron emitting decays of light neutrinos." In: *Phys. Rev. D* **62**, p. 023004. DOI: 10.1103/PhysRevD.62.023004. arXiv: hep-ph/0001039 (cit. on p. 165).

Kawasaki, M., K. Kohri, and N. Sugiyama (2000). "MeV scale reheating temperature and thermalization of neutrino background." In: *Phys. Rev. D* **62**, p. 023506. DOI: 10.1103/PhysRevD.62.023506. arXiv: astro-ph/0002127 (cit. on p. 87).

Kharusi, S. A. et al. (2021). "Search for Majoron-emitting modes of ^{136}Xe double beta decay with the complete EXO-200 dataset." In: *Phys. Rev. D* **104**.11, p. 112002. DOI: 10.1103/PhysRevD.104.112002. arXiv: 2109.01327 [hep-ex] (cit. on pp. 165, 172).

Khodagholizadeh, J., S. Mahmoudi, R. Mohammadi, and M. Sadegh (2023). "Cosmic birefringence as a probe of the nature of dark matter: Sterile neutrino and dipolar dark matter." In: *Phys. Rev. D* **108**.2, p. 023023. DOI: 10.1103/PhysRevD.108.023023. arXiv: 2307.16286 [hep-ph] (cit. on p. 211).

Kolb, E. W. and M. S. Turner (May 2019). *The Early Universe*. Vol. 69. Taylor and Francis. ISBN: 978-0-429-49286-0, 978-0-201-62674-2. DOI: 10.1201/9780429492860 (cit. on pp. 3, 85).

Kosowsky, A. (1996). "Cosmic microwave background polarization." In: *Annals Phys.* **246**, pp. 49–85. DOI: 10.1006/aphy.1996.0020. arXiv: astro-ph/9501045 (cit. on pp. 112, 114, 227).

Kreisch, C. D., F.-Y. Cyr-Racine, and O. Doré (2020). "Neutrino puzzle: Anomalies, interactions, and cosmological tensions." In: *Phys. Rev. D*

101.12, p. 123505. DOI: 10.1103/PhysRevD.101.123505. arXiv: 1902.00534 [astro-ph.CO] (cit. on pp. 167, 168).

Kreisch, C. D. et al. (2024). "Atacama Cosmology Telescope: The persistence of neutrino self-interaction in cosmological measurements." In: *Phys. Rev. D* **109**.4, p. 043501. DOI: 10.1103/PhysRevD.109.043501. arXiv: 2207.03164 [astro-ph.CO] (cit. on pp. 167, 168, 170).

Kuijken, K. et al. (2015). "Gravitational Lensing Analysis of the Kilo Degree Survey." In: *Mon. Not. Roy. Astron. Soc.* **454**.4, pp. 3500–3532. DOI: 10.1093/mnras/stv2140. arXiv: 1507.00738 [astro-ph.CO] (cit. on p. xx).

Lancaster, L., F.-Y. Cyr-Racine, L. Knox, and Z. Pan (2017). "A tale of two modes: Neutrino free-streaming in the early universe." In: *JCAP* **07**, p. 033. DOI: 10.1088/1475-7516/2017/07/033. arXiv: 1704.06657 [astro-ph.CO] (cit. on pp. 167, 168).

Langacker, P., S. T. Petcov, G. Steigman, and S. Toshev (1987). "Implications of the Mikheev-Smirnov-Wolfenstein (MSW) Mechanism of Amplification of Neutrino Oscillations in Matter." In: *Nucl. Phys. B* **282**, pp. 589–609. DOI: 10.1016/0550-3213(87)90699-7 (cit. on p. 60).

Lattanzi, M. and M. Gerbino (2018). "Status of neutrino properties and future prospects - Cosmological and astrophysical constraints." In: *Front. in Phys.* **5**, p. 70. DOI: 10.3389/fphy.2017.00070. arXiv: 1712.07109 [astro-ph.CO] (cit. on pp. 143, 148).

Laureijs, R. et al. (Oct. 2011). "Euclid Definition Study Report." In: arXiv: 1110.3193 [astro-ph.CO] (cit. on pp. xix, xx).

Lazarides, G., Q. Shafi, and C. Wetterich (1981). "Proton Lifetime and Fermion Masses in an SO(10) Model." In: *Nucl. Phys. B* **181**, pp. 287–300. DOI: 10.1016/0550-3213(81)90354-0 (cit. on p. 72).

Lesgourgues, J., G. Mangano, G. Miele, and S. Pastor (Feb. 2013). *Neutrino Cosmology*. Cambridge University Press. ISBN: 978-1-108-70501-1, 978-1-139-60341-6 (cit. on pp. 45, 79, 95, 145, 146).

Lesgourgues, J. and S. Pastor (2006). "Massive neutrinos and cosmology." In: *Phys. Rept.* **429**, pp. 307–379. DOI: 10.1016/j.physrep.2006.04.001. arXiv: astro-ph/0603494 (cit. on pp. 143, 146–148).

Lesgourgues, J. and T. Tram (2011). "The Cosmic Linear Anisotropy Solving System (CLASS) IV: efficient implementation of non-cold relics." In: *JCAP* **09**, p. 032. DOI: 10.1088/1475-7516/2011/09/032. arXiv: 1104.2935 [astro-ph.CO] (cit. on pp. 92, 96).

Lessa, A. P. and O. L. G. Peres (2007). "Revising limits on neutrino-Majoron couplings." In: *Phys. Rev. D* **75**, p. 094001. DOI: 10.1103/PhysRevD.75.094001. arXiv: hep-ph/0701068 (cit. on p. 172).

Lewis, A. (Oct. 2019). "GetDist: a Python package for analysing Monte Carlo samples." In: arXiv: 1910.13970 [astro-ph.IM] (cit. on p. 96).

Lewis, A. and A. Challinor (2006). "Weak gravitational lensing of the CMB." In: *Phys. Rept.* **429**, pp. 1–65. DOI: 10.1016/j.physrep.2006.03.002. arXiv: astro-ph/0601594 (cit. on p. 147).

Lewis, A., A. Challinor, and A. Lasenby (2000). "Efficient computation of CMB anisotropies in closed FRW models." In: *Astrophys. J.* **538**, pp. 473–476. DOI: 10.1086/309179. arXiv: astro-ph/9911177 (cit. on p. 161).

Li, Y., H.-M. Zhu, and B. Li (2022). "Non-linear reconstruction of features in the primordial power spectrum from large-scale structure." In: *Mon. Not. Roy. Astron. Soc.* **514**.3, pp. 4363–4378. DOI: 10.1093/mnras/stac1544. arXiv: 2102.09007 [astro-ph.CO] (cit. on p. 201).

Louis, T. et al. (2017). "The Atacama Cosmology Telescope: Two-Season ACTPol Spectra and Parameters." In: *JCAP* **06**, p. 031. DOI: 10.1088/1475-7516/2017/06/031. arXiv: 1610.02360 [astro-ph.CO] (cit. on p. 157).

Ma, C.-P. and E. Bertschinger (1995). "Cosmological perturbation theory in the synchronous and conformal Newtonian gauges." In: *Astrophys. J.* **455**, pp. 7–25. DOI: 10.1086/176550. arXiv: astro-ph/9506072 (cit. on p. 162).

Ma, E. (1998). "Pathways to naturally small neutrino masses." In: *Phys. Rev. Lett.* **81**, pp. 1171–1174. DOI: 10.1103/PhysRevLett.81.1171. arXiv: hep-ph/9805219 (cit. on p. 72).

Ma, E. and D. P. Roy (2002). "Heavy triplet leptons and new gauge boson." In: *Nucl. Phys. B* **644**, pp. 290–302. DOI: 10.1016/S0550-3213(02)00815-5. arXiv: hep-ph/0206150 (cit. on pp. 72, 73).

MacCrann, N. et al. (2024). "The Atacama Cosmology Telescope: reionization kSZ trispectrum methodology and limits." In: *Mon. Not. Roy. Astron. Soc.* **532**.4, pp. 4247–4260. DOI: 10.1093/mnras/stae1746. arXiv: 2405.01188 [astro-ph.CO] (cit. on p. 159).

MacKay, D. J. C. (2002). *Information Theory, Inference & Learning Algorithms*. USA: Cambridge University Press. ISBN: 0521642981 (cit. on p. 215).

Madhavacheril, M. S. et al. (2020). "Atacama Cosmology Telescope: Component-separated maps of CMB temperature and the thermal Sunyaev-Zel'dovich effect." In: *Phys. Rev. D* **102**.2, p. 023534. DOI: 10.1103/PhysRevD.102.023534. arXiv: 1911.05717 [astro-ph.CO] (cit. on pp. 157, 158).

– (2024). "The Atacama Cosmology Telescope: DR6 Gravitational Lensing Map and Cosmological Parameters." In: *Astrophys. J.* **962**.2, p. 113. DOI: 10.3847/1538-4357/acff5f. arXiv: 2304.05203 [astro-ph.CO] (cit. on pp. 158–160).

Madhavacheril, M. et al. (2015). "Evidence of Lensing of the Cosmic Microwave Background by Dark Matter Halos." In: *Phys. Rev. Lett.* **114**.15. [Addendum: Phys.Rev.Lett. 114, 189901 (2015)], p. 151302. DOI: 10.1103/PhysRevLett.114.151302. arXiv: 1411.7999 [astro-ph.CO] (cit. on p. 158).

Magg, M. and C. Wetterich (1980). "Neutrino Mass Problem and Gauge Hierarchy." In: *Phys. Lett. B* **94**, pp. 61–64. DOI: 10.1016/0370-2693(80)90825-4 (cit. on p. 72).

Mallaby-Kay, M. et al. (2021). "The Atacama Cosmology Telescope: Summary of DR4 and DR5 Data Products and Data Access." In: *Astrophys. J. Supp.* **255**.1, p. 11. DOI: 10.3847/1538-4365/abfcc4. arXiv: 2103.03154 [astro-ph.CO] (cit. on p. 157).

Mangano, G., G. Miele, S. Pastor, and M. Peloso (2002). "A Precision calculation of the effective number of cosmological neutrinos." In: *Phys. Lett. B* **534**, pp. 8–16. DOI: 10.1016/S0370-2693(02)01622-2. arXiv: astro-ph/0111408 (cit. on pp. 78, 81).

Mangano, G., G. Miele, S. Pastor, T. Pinto, O. Pisanti, and P. D. Serpico (2005). "Relic neutrino decoupling including flavor oscillations." In: *Nucl. Phys. B* **729**, pp. 221–234. DOI: 10.1016/j.nuclphysb.2005.09.041. arXiv: hep-ph/0506164 (cit. on p. 81).

Matsumura, T. et al. (2014). "Mission design of LiteBIRD." In: *J. Low Temp. Phys.* **176**, p. 733. DOI: 10.1007/s10909-013-0996-1. arXiv: 1311.2847 [astro-ph.IM] (cit. on p. xix).

Mattia, A. de et al. (2021). "The Completed SDSS-IV extended Baryon Oscillation Spectroscopic Survey: measurement of the BAO and growth rate of structure of the emission line galaxy sample from the anisotropic power spectrum between redshift 0.6 and 1.1." In: *Mon. Not. Roy. Astron. Soc.* **501**.4, pp. 5616–5645. DOI: 10.1093/mnras/staa3891. arXiv: 2007.09008 [astro-ph.CO] (cit. on p. 97).

Mazumdar, A., S. Mohanty, and P. Parashari (2022). "Flavour specific neutrino self-interaction: H $_0$ tension and IceCube." In: *JCAP* **10**, p. 011. DOI: 10.1088/1475-7516/2022/10/011. arXiv: 2011.13685 [hep-ph] (cit. on p. 168).

McAllister, L., E. Silverstein, and A. Westphal (2010). "Gravity Waves and Linear Inflation from Axion Monodromy." In: *Phys. Rev. D* **82**, p. 046003. DOI: 10.1103/PhysRevD.82.046003. arXiv: 0808.0706 [hep-th] (cit. on p. 184).

McEwen, J. E., X. Fang, C. M. Hirata, and J. A. Blazek (2016). "FAST-PT: a novel algorithm to calculate convolution integrals in cosmological perturbation theory." In: *JCAP* **09**, p. 015. DOI: 10.1088/1475-7516/2016/09/015. arXiv: 1603.04826 [astro-ph.CO] (cit. on p. 202).

McKellar, B. H. J. and M. J. Thomson (1994). "Oscillating doublet neutrinos in the early universe." In: *Phys. Rev. D* **49**, pp. 2710–2728. DOI: 10.1103/PhysRevD.49.2710 (cit. on pp. 77, 78).

Mead, A., S. Brieden, T. Tröster, and C. Heymans (2021). "hmcode-2020: improved modelling of non-linear cosmological power spectra with baryonic feedback." In: *Mon. Not. Roy. Astron. Soc.* **502**.1, pp. 1401–1422. DOI: 10.1093/mnras/stab082. arXiv: 2009.01858 [astro-ph.CO] (cit. on p. 161).

Mellier, Y. et al. (May 2024). "Euclid. I. Overview of the Euclid mission." In: arXiv: 2405.13491 [astro-ph.CO] (cit. on p. 212).

Menanteau, F. et al. (2012). "The Atacama Cosmology Telescope: ACT-CL J0102-4215 'El Gordo,' a Massive Merging Cluster at Redshift 0.87." In: *Astrophys. J.* **748**, p. 7. DOI: 10.1088/0004-637X/748/1/7. arXiv: 1109.0953 [astro-ph.CO] (cit. on p. 158).

Mikheev, S. P. and A. Y. Smirnov (1986). "Resonant amplification of neutrino oscillations in matter and solar neutrino spectroscopy." In: *Nuovo Cim. C* **9**, pp. 17–26. DOI: 10.1007/BF02508049 (cit. on p. 60).

Mikheyev, S. P. and A. Y. Smirnov (1985). "Resonance Amplification of Oscillations in Matter and Spectroscopy of Solar Neutrinos." In: *Sov. J. Nucl. Phys.* **42**, pp. 913–917 (cit. on p. 60).

Minkowski, P. (1977). "$\mu \to e\gamma$ at a Rate of One Out of 10^9 Muon Decays?" In: *Phys. Lett. B* **67**, pp. 421–428. DOI: 10.1016/0370-2693(77)90435-X (cit. on p. 70).

Miranda, V., W. Hu, and P. Adshead (2012). "Warp Features in DBI Inflation." In: *Phys. Rev. D* **86**, p. 063529. DOI: 10.1103/PhysRevD.86.063529. arXiv: 1207.2186 [astro-ph.CO] (cit. on p. 183).

Mirizzi, A., N. Saviano, G. Miele, and P. D. Serpico (2012). "Light sterile neutrino production in the early universe with dynamical neutrino asymmetries." In: *Phys. Rev. D* **86**, p. 053009. DOI: 10.1103/PhysRevD.86.053009. arXiv: 1206.1046 [hep-ph] (cit. on p. 78).

Mohammadi, R. (2014). "Evidence for cosmic neutrino background form CMB circular polarization." In: *Eur. Phys. J. C* **74**.10, p. 3102. DOI: 10.1140/epjc/s10052-014-3089-7. arXiv: 1312.2199 [astro-ph.CO] (cit. on p. 119).

Mohapatra, R. N. and P. B. Pal (1998). *Massive neutrinos in physics and astrophysics. Second edition*. Vol. 60 (cit. on pp. 45, 54).

Mohapatra, R. N. and G. Senjanovic (1980). "Neutrino Mass and Spontaneous Parity Nonconservation." In: *Phys. Rev. Lett.* **44**, p. 912. DOI: 10.1103/PhysRevLett.44.912 (cit. on p. 70).

– (1981). "Neutrino Masses and Mixings in Gauge Models with Spontaneous Parity Violation." In: *Phys. Rev. D* **23**, p. 165. DOI: 10.1103/PhysRevD.23.165 (cit. on p. 72).

Naess, S. et al. (2014). "The Atacama Cosmology Telescope: CMB Polarization at $200 < \ell < 9000$." In: *JCAP* **10**, p. 007. DOI: 10.1088/1475-7516/2014/10/007. arXiv: 1405.5524 [astro-ph.CO] (cit. on pp. 157, 158).

– (2020). "The Atacama Cosmology Telescope: arcminute-resolution maps of 18 000 square degrees of the microwave sky from ACT 2008–2018 data combined with Planck." In: *JCAP* **12**, p. 046. DOI: 10.1088/1475-7516/2020/12/046. arXiv: 2007.07290 [astro-ph.IM] (cit. on p. 157).

Namikawa, T. et al. (2020). "Atacama Cosmology Telescope: Constraints on cosmic birefringence." In: *Phys. Rev. D* **101**.8, p. 083527. DOI: 10.1103/PhysRevD.101.083527. arXiv: 2001.10465 [astro-ph.CO] (cit. on pp. 157, 158).

Navas, S. et al. (2024). "Review of particle physics." In: *Phys. Rev. D* **110**.3, p. 030001. DOI: 10.1103/PhysRevD.110.030001 (cit. on pp. 47, 146, 148, 172).

Neveux, R. et al. (2020). "The completed SDSS-IV extended Baryon Oscillation Spectroscopic Survey: BAO and RSD measurements from the anisotropic power spectrum of the quasar sample between redshift 0.8 and 2.2." In: *Mon. Not. Roy. Astron. Soc.* **499**.1, pp. 210–229. DOI: 10.1093/mnras/staa2780. arXiv: 2007.08999 [astro-ph.CO] (cit. on p. 97).

Niemack, M. D. et al. (2010). "ACTPol: a polarization-sensitive receiverfor the Atacama Cosmology Telescope." In: *Proc. SPIE Int. Soc. Opt. Eng.* **7741**. Ed. by A. D. Holland, 77411S. DOI: 10.1117/12.857464. arXiv: 1006.5049 [astro-ph.IM] (cit. on p. 156).

Oldengott, I. M., C. Rampf, and Y. Y. Y. Wong (2015). "Boltzmann hierarchy for interacting neutrinos I: formalism." In: *JCAP* **04**, p. 016. DOI: 10.1088/1475-7516/2015/04/016. arXiv: 1409.1577 [astro-ph.CO] (cit. on p. 152).

Oldengott, I. M., T. Tram, C. Rampf, and Y. Y. Y. Wong (2017). "Interacting neutrinos in cosmology: exact description and constraints." In: *JCAP* **11**, p. 027. DOI: 10.1088/1475-7516/2017/11/027. arXiv: 1706.02123 [astro-ph.CO] (cit. on pp. 167, 168).

Pagano, L., J. M. Delouis, S. Mottet, J. L. Puget, and L. Vibert (2020). "Reionization optical depth determination from Planck HFI data with ten percent accuracy." In: *Astron. Astrophys.* **635**, A99. DOI: 10.1051/0004-6361/201936630. arXiv: 1908.09856 [astro-ph.CO] (cit. on p. 159).

Park, M., C. D. Kreisch, J. Dunkley, B. Hadzhiyska, and F.-Y. Cyr-Racine (2019). "ΛCDM or self-interacting neutrinos: How CMB data can tell the two models apart." In: *Phys. Rev. D* **100**.6, p. 063524. DOI: 10.1103/PhysRevD.100.063524. arXiv: 1904.02625 [astro-ph.CO] (cit. on p. 168).

Pastor, S., T. Pinto, and G. G. Raffelt (2009). "Relic density of neutrinos with primordial asymmetries." In: *Phys. Rev. Lett.* **102**, p. 241302. DOI: 10.1103/PhysRevLett.102.241302. arXiv: 0808.3137 [astro-ph] (cit. on p. 86).

Peskin, M. E. and D. V. Schroeder (1995). *An Introduction to quantum field theory*. Reading, USA: Addison-Wesley. ISBN: 978-0-201-50397-5, 978-0-429-50355-9, 978-0-429-49417-8. DOI: 10.1201/9780429503559 (cit. on p. 224).

Piattella, O. F. (2018). *Lecture Notes in Cosmology*. UNITEXT for Physics. Cham: Springer. ISBN: 978-3-319-95569-8, 978-3-030-07060-1, 978-3-319-95570-4. DOI: 10.1007/978-3-319-95570-4. arXiv: 1803.00070 [astro-ph.CO] (cit. on p. 3).

Pitrou, C. (2021). "Radiative transport of relativistic species in cosmology." In: *Astropart. Phys.* **125**, p. 102494. DOI: 10.1016/j.astropartphys.2020.102494. arXiv: 1902.09456 [astro-ph.CO] (cit. on p. 112).

Pitrou, C., A. Coc, J.-P. Uzan, and E. Vangioni (2018). "Precision big bang nucleosynthesis with improved Helium-4 predictions." In: *Phys. Rept.* **754**, pp. 1–66. DOI: 10.1016/j.physrep.2018.04.005. arXiv: 1801.08023 [astro-ph.CO] (cit. on pp. 22, 161).

Politzer, H. D. (1973). "Reliable Perturbative Results for Strong Interactions?" In: *Phys. Rev. Lett.* **30**. Ed. by J. C. Taylor, pp. 1346–1349. DOI: 10.1103/PhysRevLett.30.1346 (cit. on p. 61).

Qu, F. J. et al. (2024). "The Atacama Cosmology Telescope: A Measurement of the DR6 CMB Lensing Power Spectrum and Its Implications for Structure Growth." In: *Astrophys. J.* **962**.2, p. 112. DOI: 10.3847/1538-4357/acfe06. arXiv: 2304.05202 [astro-ph.CO] (cit. on pp. 158, 159).

Raffelt, G., G. Sigl, and L. Stodolsky (1993). "NonAbelian Boltzmann equation for mixing and decoherence." In: *Phys. Rev. Lett.* **70**. [Erratum: Phys.Rev.Lett. 98, 069902 (2007)], pp. 2363–2366. DOI: 10.1103/PhysRevLett.70.2363. arXiv: hep-ph/9209276 (cit. on p. 109).

Ringwald, A. (2024). "Prospects to scrutinise or smash SM*A*S*H." In: *PoS* **COSMICWISPers**, p. 003. DOI: 10.22323/1.454.0003. arXiv: 2312.14679 [hep-ph] (cit. on p. 115).

Rodejohann, W. and J. W. F. Valle (2011). "Symmetrical Parametrizations of the Lepton Mixing Matrix." In: *Phys. Rev. D* **84**, p. 073011. DOI: 10.1103/PhysRevD.84.073011. arXiv: 1108.3484 [hep-ph] (cit. on p. 57).

Ross, A. J., L. Samushia, C. Howlett, W. J. Percival, A. Burden, and M. Manera (2015). "The clustering of the SDSS DR7 main Galaxy sample – I. A 4 per cent distance measure at $z = 0.15$." In: *Mon. Not. Roy. Astron. Soc.* **449**.1, pp. 835–847. DOI: 10.1093/mnras/stv154. arXiv: 1409.3242 [astro-ph.CO] (cit. on p. 97).

Roulet, E. and F. Vissani (Oct. 2022). *Neutrinos in Physics and Astrophysics*. World Scientific. ISBN: 978-981-12-6093-3, 978-981-12-6095-7. DOI: 10.1142/12982 (cit. on p. 45).

Roy Choudhury, S., S. Hannestad, and T. Tram (2021). "Updated constraints on massive neutrino self-interactions from cosmology in light of the H_0 tension." In: *JCAP* **03**, p. 084. DOI: 10.1088/1475-7516/2021/03/084. arXiv: 2012.07519 [astro-ph.CO] (cit. on p. 168).

Rubakov, V. A. and D. S. Gorbunov (2017). *Introduction to the Theory of the Early Universe: Hot big bang theory*. Singapore: World Scientific. ISBN: 978-981-320-987-9, 978-981-320-988-6, 978-981-322-005-8. DOI: 10.1142/10447 (cit. on pp. 3, 91).

Rudzsky, M. A. (1990). "Kinetic equations for neutrino spin- and type-oscillations in a medium." In: *Astrophys. Space Sci.* **165**.1, pp. 65–81. DOI: 10.1007/bf00653658 (cit. on p. 109).

Salam, A. (1968). "Weak and Electromagnetic Interactions." In: *Conf. Proc. C* **680519**, pp. 367–377. DOI: 10.1142/9789812795915_0034 (cit. on p. 61).

Salas, P. F. de, D. V. Forero, S. Gariazzo, P. Martínez-Miravé, O. Mena, C. A. Ternes, M. Tórtola, and J. W. F. Valle (2021). "2020 global reassessment of the neutrino oscillation picture." In: *JHEP* **02**, p. 071. DOI: 10.1007/JHEP02(2021)071. arXiv: 2006.11237 [hep-ph] (cit. on pp. 57, 78, 93).

Salas, P. F. de, M. Lattanzi, G. Mangano, G. Miele, S. Pastor, and O. Pisanti (2015). "Bounds on very low reheating scenarios after Planck." In: *Phys. Rev. D* **92**.12, p. 123534. DOI: 10.1103/PhysRevD.92.123534. arXiv: 1511.00672 [astro-ph.CO] (cit. on pp. 84, 86, 88, 90, 99).

Salas, P. F. de and S. Pastor (2016). "Relic neutrino decoupling with flavour oscillations revisited." In: *JCAP* **07**, p. 051. DOI: 10.1088/1475-7516/2016/07/051. arXiv: 1606.06986 [hep-ph] (cit. on pp. 78, 81).

Saviano, N., A. Mirizzi, O. Pisanti, P. D. Serpico, G. Mangano, and G. Miele (2013). "Multi-momentum and multi-flavour active-sterile neutrino oscil-

lations in the early universe: role of neutrino asymmetries and effects on nucleosynthesis." In: *Phys. Rev. D* **87**, p. 073006. DOI: 10.1103/PhysRevD.87.073006. arXiv: 1302.1200 [astro-ph.CO] (cit. on p. 78).

Schechter, J. and J. W. F. Valle (1980). "Neutrino Masses in SU(2) x U(1) Theories." In: *Phys. Rev. D* **22**, p. 2227. DOI: 10.1103/PhysRevD.22.2227 (cit. on pp. 70, 72).

– (1982). "Neutrino Decay and Spontaneous Violation of Lepton Number." In: *Phys. Rev. D* **25**, p. 774. DOI: 10.1103/PhysRevD.25.774 (cit. on pp. 114, 150).

Schmidt, M. A. (2007). "Renormalization group evolution in the type I+ II seesaw model." In: *Phys. Rev. D* **76**. [Erratum: Phys.Rev.D 85, 099903 (2012)], p. 073010. DOI: 10.1103/PhysRevD.76.073010. arXiv: 0705.3841 [hep-ph] (cit. on p. 72).

Schwartz, M. D. (Mar. 2014). *Quantum Field Theory and the Standard Model*. Cambridge University Press. ISBN: 978-1-107-03473-0, 978-1-107-03473-0 (cit. on p. 110).

Seager, S., D. D. Sasselov, and D. Scott (1999). "A new calculation of the recombination epoch." In: *Astrophys. J. Lett.* **523**, pp. L1–L5. DOI: 10.1086/312250. arXiv: astro-ph/9909275 (cit. on p. 161).

Seljak, U. and M. Zaldarriaga (1996). "A Line of sight integration approach to cosmic microwave background anisotropies." In: *Astrophys. J.* **469**, pp. 437–444. DOI: 10.1086/177793. arXiv: astro-ph/9603033 (cit. on p. 137).

Seo, H.-J. and D. J. Eisenstein (2007). "Improved forecasts for the baryon acoustic oscillations and cosmological distance scale." In: *Astrophys. J.* **665**, pp. 14–24. DOI: 10.1086/519549. arXiv: astro-ph/0701079 (cit. on p. 184).

Serreau, J. and C. Volpe (2014). "Neutrino-antineutrino correlations in dense anisotropic media." In: *Phys. Rev. D* **90**.12, p. 125040. DOI: 10.1103/PhysRevD.90.125040. arXiv: 1409.3591 [hep-ph] (cit. on p. 109).

Shannon, C. and W. Weaver (1949). *The Mathematical Theory of Communication*. Illini books v. 1. University of Illinois Press. ISBN: 9780252725487. URL: https://books.google.it/books?id=MSJDwAEACAAJ (cit. on p. 215).

Sherwin, B. D. et al. (2011). "Evidence for dark energy from the cosmic microwave background alone using the Atacama Cosmology Telescope lensing measurements." In: *Phys. Rev. Lett.* **107**, p. 021302. DOI: 10.1103/PhysRevLett.107.021302. arXiv: 1105.0419 [astro-ph.CO] (cit. on pp. 158, 159).

Sievers, J. L. et al. (2013). "The Atacama Cosmology Telescope: Cosmological parameters from three seasons of data." In: *JCAP* **10**, p. 060. DOI: 10.1088/1475-7516/2013/10/060. arXiv: 1301.0824 [astro-ph.CO] (cit. on pp. 157, 158).

Sigl, G. and G. Raffelt (1993). "General kinetic description of relativistic mixed neutrinos." In: *Nucl. Phys. B* **406**, pp. 423–451. DOI: 10.1016/0550-3213(93)90175-O (cit. on pp. 77, 79, 109–111).

Silk, J. (1968). "Cosmic black body radiation and galaxy formation." In: *Astrophys. J.* **151**, pp. 459–471. DOI: 10.1086/149449 (cit. on p. 184).

Silverstein, E. and A. Westphal (2008). "Monodromy in the CMB: Gravity Waves and String Inflation." In: *Phys. Rev. D* **78**, p. 106003. DOI: 10.1103/PhysRevD.78.106003. arXiv: 0803.3085 [hep-th] (cit. on p. 184).

Smith, R. E., J. A. Peacock, A. Jenkins, S. D. M. White, C. S. Frenk, F. R. Pearce, P. A. Thomas, G. Efstathiou, and H. M. P. Couchmann (2003). "Stable clustering, the halo model and nonlinear cosmological power spectra." In: *Mon. Not. Roy. Astron. Soc.* **341**, p. 1311. DOI: 10.1046/j.1365-8711.2003.06503.x. arXiv: astro-ph/0207664 (cit. on p. 161).

Smoot, G. F. (1999). "COBE observations and results." In: *AIP Conf. Proc.* **476**.1. Ed. by L. Maiani, F. Melchiorri, and N. Vittorio, pp. 1–10. DOI: 10.1063/1.59326. arXiv: astro-ph/9902027 (cit. on p. xix).

Springel, V. et al. (2005). "Simulating the joint evolution of quasars, galaxies and their large-scale distribution." In: *Nature* **435**, pp. 629–636. DOI: 10.1038/nature03597. arXiv: astro-ph/0504097 (cit. on p. ii).

Starobinsky, A. A. (1992). "Spectrum of adiabatic perturbations in the universe when there are singularities in the inflation potential." In: *JETP Lett.* **55**, pp. 489–494 (cit. on pp. 183, 184).

Storer, E. R. (Mar. 2023). "From Raw Data to Cosmology with the Atacama Cosmology Telescope." PhD thesis. Princeton U., Princeton U. (main) (cit. on p. 157).

Swetz, D. S. et al. (2011). "Overview of the Atacama Cosmology Telescope: Receiver, instrumentation, and telescope systems." In: *Astrophys. J. Suppl.* **194**, p. 41. DOI: 10.1088/0067-0049/194/2/41. arXiv: 1007.0290 [astro-ph.IM] (cit. on p. 156).

Tamone, A. et al. (2020). "The Completed SDSS-IV extended Baryon Oscillation Spectroscopic Survey: Growth rate of structure measurement from anisotropic clustering analysis in configuration space between redshift 0.6 and 1.1 for the Emission Line Galaxy sample." In: *Mon. Not. Roy. Astron. Soc.* **499**.4, pp. 5527–5546. DOI: 10.1093/mnras/staa3050. arXiv: 2007.09009 [astro-ph.CO] (cit. on p. 97).

Tassev, S., D. J. Eisenstein, B. D. Wandelt, and M. Zaldarriaga (Feb. 2015). "sCOLA: The N-body COLA Method Extended to the Spatial Domain." In: arXiv: 1502.07751 [astro-ph.CO] (cit. on p. 201).

Tassev, S., M. Zaldarriaga, and D. Eisenstein (2013). "Solving Large Scale Structure in Ten Easy Steps with COLA." In: *JCAP* **06**, p. 036. DOI: 10.1088/1475-7516/2013/06/036. arXiv: 1301.0322 [astro-ph.CO] (cit. on p. 201).

"The Scientific programme of Planck" (Apr. 2006). In: ed. by J. Tauber et al. arXiv: astro-ph/0604069 (cit. on p. xix).

Torrado, J. and A. Lewis (2021). "Cobaya: Code for Bayesian Analysis of hierarchical physical models." In: *JCAP* **05**, p. 057. DOI: 10.1088/1475-7516/2021/05/057. arXiv: 2005.05290 [astro-ph.IM] (cit. on p. 160).

Valageas, P. (2004). "A new approach to gravitational clustering: a path-integral formalism and large-n expansions." In: *Astron. Astrophys.* **421**, pp. 23–40. DOI: 10.1051/0004-6361:20040125. arXiv: astro-ph/0307008 (cit. on p. 176).

Valle, J. W. F. and J. C. Romao (2015). *Neutrinos in high energy and astroparticle physics*. Physics textbook. Weinheim: Wiley-VCH. ISBN: 978-3-527-41197-9, 978-3-527-67102-1 (cit. on pp. 45, 114).

Vasudevan, A., M. M. Ivanov, S. Sibiryakov, and J. Lesgourgues (2019). "Time-sliced perturbation theory with primordial non-Gaussianity and effects of large bulk flows on inflationary oscillating features." In: *JCAP* **09**, p. 037. DOI: 10.1088/1475-7516/2019/09/037. arXiv: 1906.08697 [astro-ph.CO] (cit. on pp. 175, 180–182, 189, 202, 235).

Viel, M., M. G. Haehnelt, and V. Springel (2010). "The effect of neutrinos on the matter distribution as probed by the Intergalactic Medium." In: *JCAP* **06**, p. 015. DOI: 10.1088/1475-7516/2010/06/015. arXiv: 1003.2422 [astro-ph.CO] (cit. on p. 202).

Villaescusa-Navarro, F., S. Naess, S. Genel, A. Pontzen, B. Wandelt, L. Anderson, A. Font-Ribera, N. Battaglia, and D. N. Spergel (2018). "Statistical properties of paired fixed fields." In: *Astrophys. J.* **867**.2, p. 137. DOI: 10.3847/1538-4357/aae52b. arXiv: 1806.01871 [astro-ph.CO] (cit. on p. 202).

Vlasenko, A., G. M. Fuller, and V. Cirigliano (2014). "Neutrino Quantum Kinetics." In: *Phys. Rev. D* **89**.10, p. 105004. DOI: 10.1103/PhysRevD.89.105004. arXiv: 1309.2628 [hep-ph] (cit. on p. 109).

Volpe, C. (2015). "Neutrino Quantum Kinetic Equations." In: *Int. J. Mod. Phys. E* **24**.09, p. 1541009. DOI: 10.1142/S0218301315410098. arXiv: 1506.06222 [astro-ph.SR] (cit. on p. 117).

Weinberg, D. H., M. J. Mortonson, D. J. Eisenstein, C. Hirata, A. G. Riess, and E. Rozo (2013). "Observational Probes of Cosmic Acceleration." In: *Phys. Rept.* **530**, pp. 87–255. DOI: 10.1016/j.physrep.2013.05.001. arXiv: 1201.2434 [astro-ph.CO] (cit. on p. 160).

Weinberg, S. (1967). "A Model of Leptons." In: *Phys. Rev. Lett.* **19**, pp. 1264–1266. DOI: 10.1103/PhysRevLett.19.1264 (cit. on p. 61).

– (1979). "Baryon and Lepton Nonconserving Processes." In: *Phys. Rev. Lett.* **43**, pp. 1566–1570. DOI: 10.1103/PhysRevLett.43.1566 (cit. on p. 69).

Welander, P (Jan. 1954). "On the temperature jump in a rarefied gas." In: *Arkiv Fysik* **Vol: 7**. URL: https://www.osti.gov/biblio/4395580 (cit. on p. 162).

Wetterich, C. (1981). "Neutrino Masses and the Scale of B-L Violation." In: *Nucl. Phys. B* **187**, pp. 343–375. DOI: 10.1016/0550-3213(81)90279-0 (cit. on p. 72).

Winther, H. A., K. Koyama, M. Manera, B. S. Wright, and G.-B. Zhao (2017). "COLA with scale-dependent growth: applications to screened modified

gravity models." In: *JCAP* **08**, p. 006. DOI: 10.1088/1475-7516/2017/08/006. arXiv: 1703.00879 [astro-ph.CO] (cit. on p. 201).

Wolfenstein, L. (1978). "Neutrino Oscillations in Matter." In: *Phys. Rev. D* **17**, pp. 2369–2374. DOI: 10.1103/PhysRevD.17.2369 (cit. on pp. 57, 149).

Wong, Y. Y. Y. (2011). "Neutrino mass in cosmology: status and prospects." In: *Ann. Rev. Nucl. Part. Sci.* **61**, pp. 69–98. DOI: 10.1146/annurev-nucl-102010-130252. arXiv: 1111.1436 [astro-ph.CO] (cit. on p. 143).

Workman, R. L. et al. (2022). "Review of Particle Physics." In: *PTEP* **2022**, p. 083C01. DOI: 10.1093/ptep/ptac097 (cit. on pp. 88, 89, 98, 210).

Wright, B. S., H. A. Winther, and K. Koyama (2017). "COLA with massive neutrinos." In: *JCAP* **10**, p. 054. DOI: 10.1088/1475-7516/2017/10/054. arXiv: 1705.08165 [astro-ph.CO] (cit. on p. 201).

Yaguna, C. E. (2007). "Sterile neutrino production in models with low reheating temperatures." In: *JHEP* **06**, p. 002. DOI: 10.1088/1126-6708/2007/06/002. arXiv: 0706.0178 [hep-ph] (cit. on p. 210).

Zaldarriaga, M. and U. Seljak (1997). "An all sky analysis of polarization in the microwave background." In: *Phys. Rev. D* **55**, pp. 1830–1840. DOI: 10.1103/PhysRevD.55.1830. arXiv: astro-ph/9609170 (cit. on p. 137).

Zarei, M., N. Bartolo, D. Bertacca, A. Ricciardone, and S. Matarrese (2021). "Non-Markovian open quantum system approach to the early Universe: Damping of gravitational waves by matter." In: *Phys. Rev. D* **104**.8, p. 083508. DOI: 10.1103/PhysRevD.104.083508. arXiv: 2104.04836 [astro-ph.CO] (cit. on pp. 110, 112).

This document was typeset using the typographical look-and-feel `classicthesis` developed by André Miede and Ivo Pletikosić. The style was inspired by Robert Bringhurst's seminal book on typography "*The Elements of Typographic Style*". `classicthesis` is available for both LaTeX and LyX:

https://bitbucket.org/amiede/classicthesis/

Final Version as of March 30, 2025 (classicthesis v4.6).

Summary

This thesis investigates the interplay between fundamental physics and cosmological observables, offering a comprehensive examination of how cutting-edge cosmological data can constrain extensions of current theories. The work begins with a detailed exploration of the standard framework of particle cosmology, encompassing the thermal history of the Universe, the inflationary paradigm, and neutrino phenomenology. In the second part, particular emphasis is placed on non-standard neutrino physics in the early Universe. Specifically, we study their behavior in very low reheating scenarios and their optical activity when the neutrino sector is extended with non-standard interactions. Finally, the focus moves to the late Universe observables, extending the study to signatures of primordial oscillatory features in the Large-Scale Structure (LSS) of the Universe, employing advanced techniques in perturbation theory and N-body simulations to assess their imprints on observables.

The results of this work contribute to the refinement of theoretical understanding of the Universe's evolution, highlighting potential deviations in standard predictions and offering insights into physical mechanisms possibly opening new avenues for future observations to test models of physics Beyond the Standard Model (BSM).

Università degli Studi di Ferrara

Tests of fundamental physics with cosmological observables

Nicola Barbieri